VARIABILITY AND DRIVERS OF AEROSOL PARTICLE CHARACTERISTICS AND NEW PARTICLE FORMATION FROM IN SITU AND REMOTE SENSING MEASUREMENTS, AND NUMERICAL SIMULATIONS

A Dissertation

Presented to the Faculty of the Graduate School

of Cornell University

In Partial Fulfillment of the Requirements for the Degree of

Doctor of Philosophy

by

Ryan Christopher Sullivan

August 2017

VARIABILITY AND DRIVERS OF AEROSOL PARTICLE CHARACTERISTICS AND NEW PARTICLE FORMATION FROM IN SITU AND REMOTE SENSING MEASUREMENTS, AND NUMERICAL SIMULATIONS

Ryan Christopher Sullivan, Ph. D

Cornell University 2017

ABSTRACT

Aerosol-climate interactions are the leading uncertainty in understanding anthropogenic climate forcing, and aerosol particles negatively impact human and ecosystem health. First, ground- and satellite-based remote sensing measurements are used to quantify the spatiotemporal coherence of mean and extreme aerosol properties, and identify the drivers of the observed aerosol variability. This analysis is extended to quantify the spatiotemporal coherence of aerosol precursors and species associated with new particle formation (NPF), develop a proxy using satellite-based measurements of aerosol and precursor concentrations to predict and diagnose controls of occurrence and intensity of NPF at a forest site in Indiana, and apply the satellite-based proxy to five long-terms sites in N. America to examine spatiotemporal scales and variability of drivers of new particle formation. Next, climate indicators are developed to track changes in aerosol optical properties using satellite-constrained reanalysis products, and applied to the U.S.A. to identify trends in characteristics of aerosol populations, and attribute these changes to changes in natural and anthropogenic emissions, and meteorological conditions. Finally, the WRF-Chem model is modified to simulate NPF and run simulations at cloud-resolving resolution to quantify the impact of NPF on indirect aerosol forcing (i.e. changes in cloud brightness and lifetimes).

BIOGRAPHICAL SKETCH

Ryan Sullivan earned an Associate's of Science from William Rainey Harper College in 2010, a Bachelor's of Science in Meteorology from Northern Illinois University in 2012, a Master's of Science in Geological Sciences – Atmospheric Sciences from Indiana University in 2014, a Master's of Science in Atmospheric Science from Cornell University in 2016, and a Doctorate of Philosophy in Atmospheric Science from Cornell University in 2017.

This dissertation is dedicated to Prof. Sara Pryor. Without her dedication and commitment to my development as a researcher, and her persistent motivation and encouragement, I would not be the scientist I am today.

ACKNOWLEDGMENTS

This research was funded by the NASA Earth and Space Science Fellowship Program - Grant “14-EARTH14F-0207”. Additional funding to SCP is indicated in the individual papers below.

TABLE OF CONTENTS

CHAPTER 1

INTRODUCTION

Atmospheric aerosol particles are a source of major uncertainty in understanding past climate change and in modeling to generate robust climate projections [*Flato et al.*, 2013]. They also present a major public health burden [*Pope et al.*, 2004]. Anthropogenic activities significantly impact the concentration, composition, and size distribution of aerosols, but direct measurements of these properties are limited in space and time, limiting our ability to validate Earth System Science models [*Flato et al.*, 2013] and to understand and quantify human exposure [*Sullivan and Pryor*, 2014]. Fortunately, remote sensing observations from satellite borne instruments, along with high-resolution numerical models provide an opportunity to fill this critical data gap. A key novelty in my research is integration of direct observation and remotely-sensed properties (drawn directly from satellite-based radiometers, ground-based sensors, and a new satellite-constrained reanalysis products) with high-resolution numerical modeling in order to characterize aerosol populations and key components of aerosol particle dynamics.

Atmospheric aerosol particles range in size from a few nanometers to many micrometers in diameter (D_p) (Figure 1.1). My research focuses principally on:

- Improved characterization of the formation mechanisms and concentrations of ultrafine particles (UFP, $D_p < 0.1$ μm). UFP concentrations are a function of new particle formation (NPF) through nucleation, and primary particle emissions, particularly those derived from anthropogenic origin. It is estimated that ~50 – 70% (spatially variable) of cloud condensation nuclei (CCN) are from NPF globally [*Yu and Luo*, 2009], with ~50% of CCN over eastern N. America from NPF [*Pierce et al.*, 2014]; thus, NPF is potentially an

important contributor to indirect aerosol forcing. Although the process of NPF is not fully understood, evidence suggests NPF (and elevated UFP concentrations) is frequently observed over the eastern half of North America [*Pryor et al.*, 2010, 2014; *Pierce et al.*, 2014], and exhibits some degree of coherence on large spatial scales (of up to hundreds of km) and a substantial 1-day autocorrelation [*Crippa and Pryor*, 2013]. Over eastern North America sulfuric acid (H_2SO_4) is a key NPF precursor [*Sipilä et al.*, 2010], NPF is increased under high solar ultraviolet (UV) flux [*Pryor et al.*, 2010], and the rate of NPF is dependent on ammonia (NH_3) concentrations (leading to the inference that NPF in the eastern North America is dominated by ternary nucleation) [*Crippa et al.*, 2012]. In some environments NPF (and particle growth) is also dependent on condensation of low volatility organic compounds (VOCs) [*Zhang et al.*, 2004]. The importance of direct particle emissions to UFP concentrations is spatiotemporally variable [*Reddington et al.*, 2011]. UFP play a significant role in indirect climate forcing (e.g. UFP dominate aerosol number concentrations and thus, with sufficient growth contribute significantly to cloud condensation nuclei concentrations and may alter cloud lifetimes and albedo, leading to a change in net radiation of between -0.77 and +0.23 W m^{-2}) and may be especially toxic to public health [*Knol et al.*, 2009; *Rückerl et al.*, 2011].

- Improved quantification of the spatiotemporal scales of variability of accumulation mode particles ($0.1 < D_p < 1$ μm). Particles in this mode dominate direct radiative forcing (estimates of the global mean radiative forcing are -1.33 to -0.06 W m^{-2}) [*Bauer and Menon*, 2012; *Myhre et al.*, 2013].

The study region of my research is eastern N. America, where anthropogenic enhancement of aerosol particle concentrations was responsible for reducing near-surface air

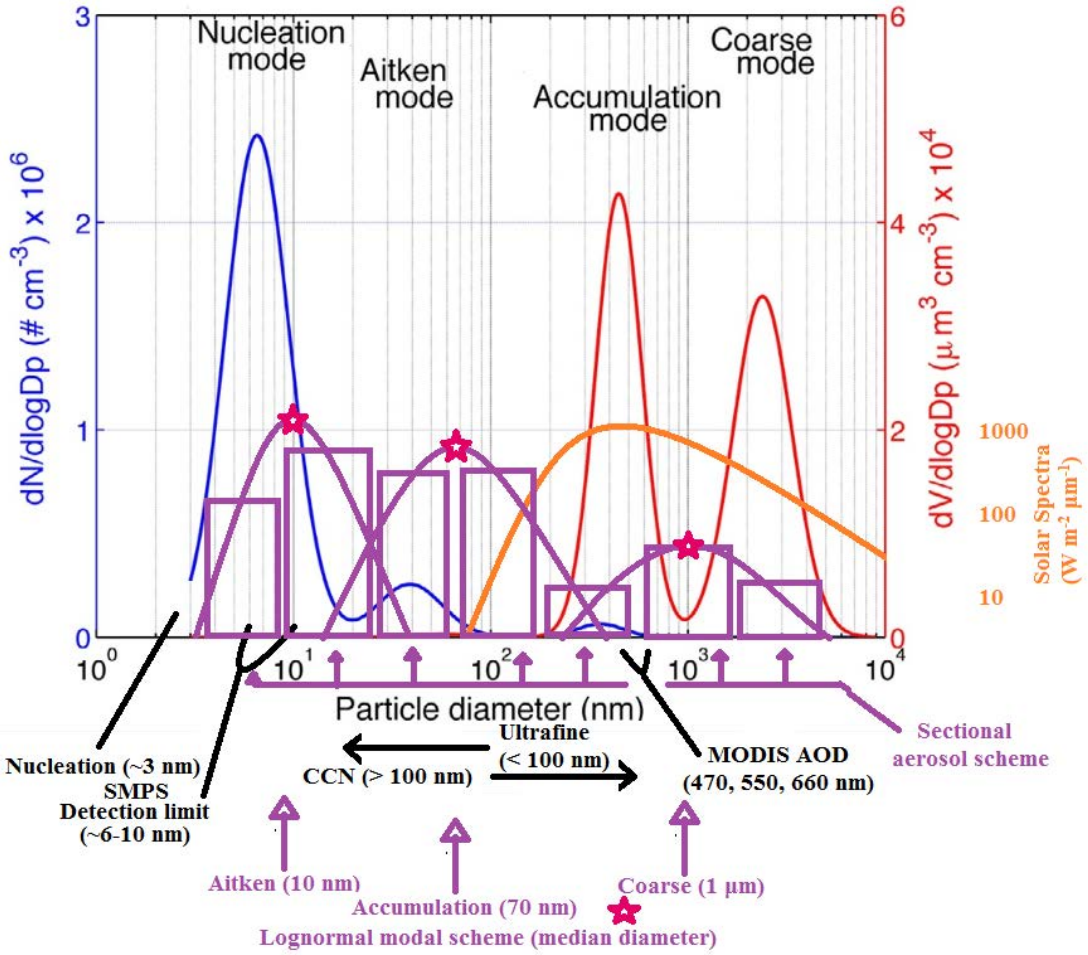

Figure 1.1 Example particle size distribution shown in terms of number (blue) and volume (red) concentrations, adapted from [*Pryor et al.*, 2015]. *Also shown is the approx. blackbody spectra of solar radiation (orange), and the diameter of nucleated particles (~3 nm), Scanning Mobility Particle Sizers' minimum detection limit (~6 – 10 nm), and wavelengths of satellite-borne radiometer aerosol optical depth measurements (470, 550, 660 nm). The purple schematic illustrates two aerosol schemes used in atmospheric chemistry models: modal (e.g. Modal Aerosol Dynamics model for Europe (MADE), where 3 lognormal modes are used* [*Ackermann et al.*, 1998]*), and sectional (e.g. Model for Simulating Aerosol Interactions and Chemistry (MOSAIC)) where aerosol concentrations are discretized into 8 bins* [*Zaveri et al.*, 2008].

temperatures by 0.5 – 1.0 °C during 1970–1990, with near equal contributions from direct and indirect effects [*Leibensperger et al.*, 2012].

My research addresses two primary, linked research objectives, and the research methods and primary results are described in the chapters noted by each objective.

Research objective 1: Improved quantification of the spatial scales of the columnar burden of optically-active (i.e. accumulation mode) aerosol particles. My initial research on the

spatiotemporal scales of coherence and variability of aerosol particle properties is described in Chapter 2, while the development of comprehensive climate indicators relevant to aerosol direct climate forcing is presented in Chapter 5. This research theme is motivated by the need to provide (i) improved metrics for evaluating model simulations, (ii) to develop inferences regarding dominant causes of variability, and (iii) to develop the information necessary to determine improved estimates of direct aerosol climate forcing at the regional scale and to track changes in that forcing through time. Additional collaborative research within this research is presented in two co-authored publications provided in the Appendices. Our research in this arena addresses a key topic within regionalization of aerosol climate forcing estimates. Specifically we seek to quantify the impact on simulation fidelity that derives from increased resolution and to attribute model skill.

Research objective 2: Improved quantification of the spatial scales of new particle formation and their potential impact on cloud properties using in situ, satellite-based observations, and numerical modeling. While accumulation mode particles have a strong radiative signature and can be measured using satellite-based radiometers, UFP have little direct interaction with atmospheric radiation transfer and cannot be observed directly with any current satellite products. However, just prior to me commencing my research, *Crippa et al.* [2013] developed a proxy estimate for UFP concentrations over eastern North America from remotely sensed data, that 'predicts' UFP concentrations based on atmospheric properties measured by satellite-borne radiometers which are associated with NPF:

- Particle loading (aerosol optical depth, AOD; wavelength, $\lambda = 550$ nm), and fraction of fine particles (Ångström exponent, AE; λ's = 470/660 nm over land), which suppress NPF by acting as a sink for precursor gases.

- Ultraviolet radiation (UV), ammonia (NH_3), and sulfur dioxide (SO_2), which act as NPF precursors and enhance NPF.

The research presented herein expands on this research by extending the satellite-based proxy to predict NPF occurrence and intensity (Chapter 3) and using the satellite-based proxy to explore spatiotemporal scales and variability of NPF (Chapter 4). In chapter 6 I present high-resolution numerical simulations that explicitly simulate convection, cloud droplet number concentrations, and NPF to quantify the indirect aerosol radiative effects due to NPF.

Additional research projects and products in which I have participated during my PhD, but that are not directly related to this dissertation, are presented in the Appendices. All of chapters 2-6 have been published in international scientific journal or are currently under consideration for publication. Full-text, copy-edited versions of these chapters are available on request.

REFERENCES

Ackermann, I. J., H. Hass, M. Memmesheimer, A. Ebel, F. S. Binkowski, and U. Shankar (1998), Modal aerosol dynamics model for Europe: Development and first applications, *Atmos. Environ.*, *32*(17), 2981–2999.

Bauer, S. E., and S. Menon (2012), Aerosol direct, indirect, semidirect, and surface albedo effects from sector contributions based on the IPCC AR5 emissions for preindustrial and present-day conditions, *J. Geophys. Res. Atmos.*, *117*(D1), doi:10.1029/2011JD016816.

Crippa, P., and S. C. Pryor (2013), Spatial and temporal scales of new particle formation events in eastern North America, *Atmos. Environ.*, *75*, 257–264, doi:10.1016/j.atmosenv.2013.04.051.

Crippa, P., T. Petäjä, H. Korhonen, Gse. Afandi, and S. C. Pryor (2012), Evidence of an elevated source of nucleation based on model simulations and data from the NIFTy experiment, *Atmos. Chem. Phys.*, *12*(17), 8021–8036, doi:10.5194/acp-12-8021-2012.

Crippa, P., D. Spracklen, and S. C. Pryor (2013), Satellite-derived estimates of ultrafine particle concentrations over eastern North America, *J. Geophys. Res. Atmos.*, *118*(17), 9968–9981, doi:10.1002/jgrd.50707.

Flato, G. et al. (2013), Evaluation of Climate Models, in *Climate Change 2013: The Physical Science Basis. Contribution of Working Group I to the Fifth Assessment Report of the Intergovernmental Panel on Climate Change*, Cambridge University Press, Cambridge, United Kingdom and New York, NY, USA.

Knol, A. B., J. J. de Hartog, H. Boogaard, P. Slottje, J. P. van der Sluijs, E. Lebret, F. R. Cassee, J. A. Wardekker, J. G. Ayres, and P. J. Borm (2009), Expert elicitation on ultrafine particles: likelihood of health effects and causal pathways, *Part. Fibre Toxicol.*, *6*(1), 19, doi:10.1186/1743-8977-6-19.

Leibensperger, E. M., L. J. Mickley, D. J. Jacob, W.-T. Chen, J. H. Seinfeld, A. Nenes, P. J. Adams, D. G. Streets, N. Kumar, and D. Rind (2012), Climatic effects of 1950–2050 changes in US anthropogenic aerosols–Part 1: Aerosol trends and radiative forcing, *Atmos. Chem. Phys.*, *12*(7), 3333–3348.

Myhre, G., D. Shindell, F. M. Bréon, W. Collins, J. Fuglestvedt, J. Huang, D. Koch, J. F. Lamarque, D. Lee, and B. Mendoza (2013), *Anthropogenic and natural radiative forcing*, edited by S. K. A. Stocker, T.F., D. Qin, G.-K. Plattner, M. Tignor and V. B. and P. M. M. J. Boschung, A. Nauels, Y. Xia, Cambridge University Press, Cambridge, United Kingdom and New York, NY, USA.

Pierce, J. R., D. M. Westervelt, S. A. Atwood, E. A. Barnes, and W. R. Leaitch (2014), New-particle formation, growth and climate-relevant particle production in Egbert, Canada: analysis from 1 year of size-distribution observations, *Atmos. Chem. Phys.*, *14*(16), 8647–8663.

Pope, C. A., R. T. Burnett, G. D. Thurston, M. J. Thun, E. E. Calle, D. Krewski, and J. J. Godleski (2004), Cardiovascular mortality and long-term exposure to particulate air pollution epidemiological evidence of general pathophysiological pathways of disease, *Circulation*, *109*(1), 71–77.

Pryor, S. C., A. M. Spaulding, and R. J. Barthelmie (2010), New particle formation in the Midwestern USA: Event characteristics, meteorological context and vertical profiles, *Atmos. Environ.*, *44*(35), 4413–4425, doi:10.1016/j.atmosenv.2010.07.045.

Pryor, S. C., K. E. Hornsby, and K. A. Novick (2014), Forest canopy interactions with nucleation mode particles, *Atmos. Chem. Phys.*, *14*(21), 11985–11996, doi:10.5194/acp-14-11985-2014.

Pryor, S. C., P. Crippa, and R. C. Sullivan (2015), Atmospheric Chemistry, in *an Elsevier online reference module "Earth Systems and Environmental Sciences" (http://www.sciencedirect.com/science/referenceworks/9780124095489)*, Elsevier.

Reddington, C. L., K. S. Carslaw, D. V Spracklen, M. G. Frontoso, L. Collins, J. Merikanto, A. Minikin, T. Hamburger, H. Coe, and M. Kulmala (2011), Primary versus secondary contributions to particle number concentrations in the European boundary layer, *Atmos. Chem. Phys.*, *11*(23), 12007–12036.

Rückerl, R., A. Schneider, S. Breitner, J. Cyrys, and A. Peters (2011), Health effects of particulate air pollution: a review of epidemiological evidence, *Inhal. Toxicol.*, *23*(10), 555–592.

Sipilä, M., T. Berndt, T. Petäjä, D. Brus, J. Vanhanen, F. Stratmann, J. Patokoski, R. L. Mauldin, A.-P. Hyvärinen, and H. Lihavainen (2010), The role of sulfuric acid in atmospheric nucleation, *Science*, *327*(5970), 1243–1246.

Sullivan, R. C., and S. C. Pryor (2014), Quantifying spatiotemporal variability of fine particles in an urban environment using combined fixed and mobile measurements, *Atmos. Environ.*, *89*, 664–671, doi:10.1016/j.atmosenv.2014.03.007.

Yu, F., and G. Luo (2009), Simulation of particle size distribution with a global aerosol model: contribution of nucleation to aerosol and CCN number concentrations, *Atmos. Chem. Phys.*, *9*(20), 7691–7710.

Zaveri, R. A., R. C. Easter, J. D. Fast, and L. K. Peters (2008), Model for simulating aerosol interactions and chemistry (MOSAIC), *J. Geophys. Res. Atmos.*, *113*(D13), doi:10.1029/2007JD008782.

Zhang, R., I. Suh, J. Zhao, D. Zhang, E. C. Fortner, X. Tie, L. T. Molina, and M. J. Molina (2004), Atmospheric new particle formation enhanced by organic acids, *Science*, *304*(5676), 1487–1490.

CHAPTER 2

SPATIOTEMPORAL COHERENCE OF MEAN AND EXTREME AEROSOL PARTICLE EVENTS OVER EASTERN NORTH AMERICA AS OBSERVED FROM SATELLITE

Sullivan, R. C., R. C. Levy, and S. C. Pryor (2015), Spatiotemporal coherence of mean and extreme aerosol particle events over eastern North America as observed from satellite, *Atmos. Environ.*, *112*, 126–135, doi:10.1016/j.atmosenv.2015.04.026.

Abstract

Quantifying spatiotemporal scales of coherence and variability of aerosol particle properties provides (i) metrics for evaluating observational data sets and model simulations, (ii) inferences regarding dominant causes of variability, and (iii) information that is necessary to determine their climate forcing and air quality impacts. Accordingly, analyses of columnar aerosol optical depth (AOD) and Ångström exponent (AE) from the MODerate resolution Imaging Spectroradiometer (MODIS) on the Aqua and Terra satellites, and AErosol RObotic NETwork (AERONET) stations are used to evaluate the spatially averaged (Level-3) MODIS products, and to characterize the spatiotemporal scales of variability (and coherence) of aerosol particles over eastern North America (2000-2013). Results show a high degree of consistency in AOD retrievals from the different data sets but larger discrepancies in AE estimates, highest mean AOD and lowest day-to-day variability during the summer, and largest scales of spatial coherence in summer and fall. Consistent with the scales of spatial coherence from MODIS data, in both data sets power spectra indicate AOD variability is manifest primarily on synoptic and annual time scales. Conversely, AE variability in MODIS data is primarily focused on seasonal, semiannual, and annual time scales, and there is an additional mode of AE variability at ~ 30 days in the AERONET measurements. The frequency of co-occurrence of extreme AOD values (> local 90th percentile) decreases to below 50% at ~ 150 km from a central grid cell, but

is above that expected by random chance over almost all of eastern North America, indicating supra-regional scale extreme events.

Introduction and motivation

Enhanced concentrations of aerosol particles (aerosols) alter Earth's radiation balance (*Boucher et al.*, 2013) and cause an estimated 800,000 premature deaths per year (*Brook et al.*, 2010). However, because aerosol populations exhibit high spatiotemporal variability (*Boucher et al.*, 2013), it is challenging to quantify their impact on air quality and regional climate forcing. Aerosols frequently exhibit complex vertical profiles and thus surface measurements do not fully represent the aerosol properties responsible for aerosol-climate impacts (*Alston et al.,* 2012*; Ford and Heald,* 2013). Satellite-borne instruments are an important source of information regarding the columnar aerosol properties that are more strongly linked to climate forcing, and cover a large, nearly continuous spatial domain (*Hollmann et al.*, 2013; *Levy et al.*, 2013). However, there are challenges in the analysis and interpretation of satellite measurements due to retrieval uncertainties, and sparse and disjunct sampling in both the temporal and spatial domains (e.g. due to their orbits and clouds).

Aerosol optical depth (AOD) is the column-integrated aerosol extinction coefficient and is proportional to total column aerosol loading. AOD is measured directly by sun photometers (e.g. AErosol RObotic NETwork (AERONET)), and can be retrieved by passive measurements of reflected solar radiation (e.g. MODerate resolution Imaging Spectroradiometer (MODIS)). AOD retrieved from MODIS instruments over dark land is highly correlated ($r > 0.8$) with AOD from sun photometers distributed globally (*Anderson et al., 2013; Levy et al.*, 2010). The Ångström exponent (AE) describes the aerosol extinction coefficient's dependence on particle size (e.g. spectral AOD). It is a qualitative descriptor of dominant aerosol size, and is retrieved

with higher uncertainty.

In this study MODIS measurements of AOD and AE, supplemented by data from AERONET ground-based radiometers, are used to characterize the spatial and temporal scales of variability in climate relevant aerosol properties (AOD and AE) over eastern North America (Figure 2.1A), and to draw inferences regarding the processes driving this variability (*Anderson et al., 2003*). The analyses presented herein are additionally designed to (i) deliver an evaluation of the spatially averaged (L3) MODIS product, (ii) characterize sub-grid scale variability in L3 MODIS products, and (iii) provide possible metrics that can be used to diagnose aerosol simulations by global and regional atmospheric chemistry models.

Data and methods

Data

MODIS is aboard two sun-synchronous polar-orbiting satellites (Terra and Aqua). The "dark–target" retrieval algorithm uses observations in seven wavelengths (0.47 – 2.11 μm) to obtain aerosol particle properties over ocean and land during clear sky conditions. Over land, dark pixels (low reflectance at 2.11 μm) are used to estimate surface radiances at 0.47 μm and 0.65 μm, and along with top of atmosphere radiance at those wavelengths, these dark pixels are used to infer AOD at 0.55 μm as well as 0.47 μm and 0.65 μm (AOD_λ). Lookup tables, representing realistic assumptions about surface and atmospheric contributions, are used to match aerosol properties with measurements. Over oceans, the primary product is also AOD at 0.55 μm, but surface properties are modeled as a function of wind speed, and more wavelengths can be used in the retrieval (*Levy et al.*, 2007). Since a product of both retrievals is spectral dependence of AOD, the Ångström power law can be used to derive the AE between pairs of

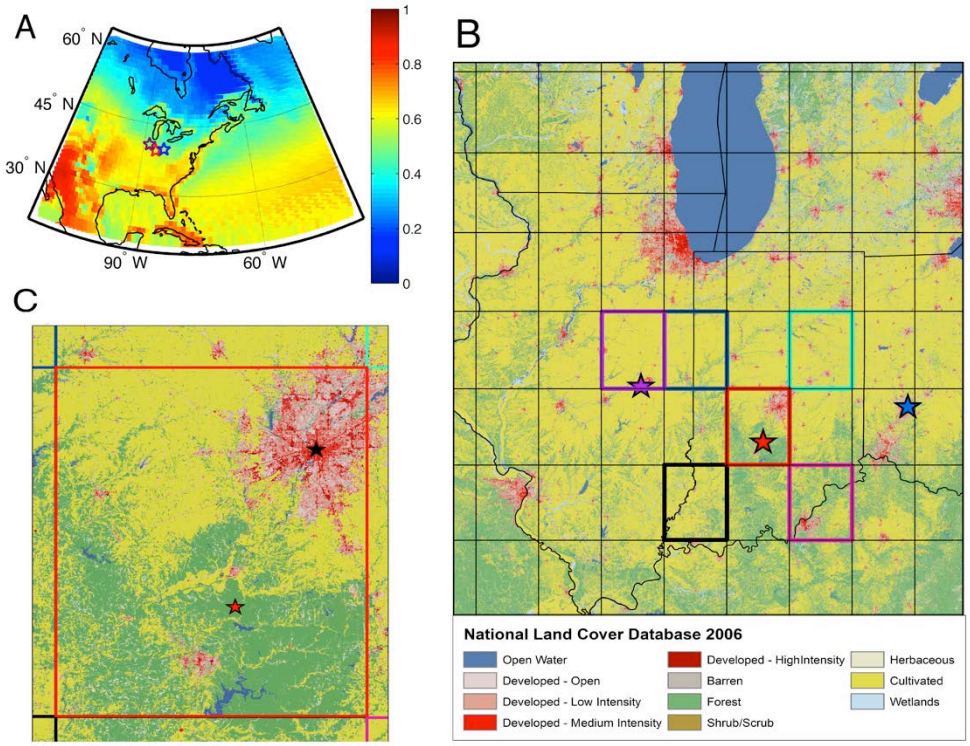

Figure 2.1 A) Retrieval frequency of daily aerosol optical depth at 0.55 μm in the MODIS L3 data set from Terra (2000-2013) over the study area (110 °W to 40 °W, 20 °N to 60 °N), and locations of Bondville, IL (violet), Dayton, OH (blue), and Morgan-Monroe State Forest (MMSF), IN (red). B) Locations of Bondville (violet), Dayton (blue), and MMSF (red); grid cells used in Terra vs. Aqua analysis (Figure 2.2, blue, cyan, black and magenta boxes); and underlying land use. The grid shows the resolution of the MODIS Level-3 aerosol product used herein (1º × 1º). Underlay of land cover is from the National Land Cover Database 2006 (downloaded from http://www.mrlc.gov/nlcd06_data.php). C) Heterogeneity of land use within the L3 MMSF grid cell (centroid 39.5ºN 86.5ºW), and locations of the urban footprint pixel (Indianapolis, 39.767ºN 86.158ºW, black) and the deciduous forest pixel (MMSF, 39.317ºN 86.417 ºW, red) used in the sub-grid cell analysis.

wavelengths (here $AOD_{0.47}$ and $AOD_{0.65}$). The uncertainty in MODIS Level 2 (L2) AOD derived from global comparisons with AERONET sun photometer data is $\pm 0.03 \pm 0.05 \times AOD$ (over ocean) and $\pm 0.05 \pm 0.15 \times AOD$ (over land) (*Remer et al.*, 2005). Due to the bimodal nature of MODIS estimates of AE, quantifying uncertainty is inherently more difficult (*Levy et al.*, 2010).

The above discussion of AOD and AE uncertainty pertains to L2 data, which are collected along the satellite orbits. Level 3 (L3) data are created by aggregating and averaging the L2 data, provided that particular retrieved values meet certain quality assurance criteria

(*Hubanks et al.*, 2008). Since the nominal resolution of the MODIS L2 aerosol product is ~10 km, a 1°x1° L3 grid may contain up to ~100 such retrievals. However, not all L3 grids are equally densely sampled due to clouds or non-retrievable surface properties, and to qualify a grid as being "filled", only > 5 retrievals are required (*Levy et al*., 2009).

Analyses presented here use L3 MODIS Terra (equatorial overpass ~1030 local standard time (LST) at nadir) and Aqua (overpass ~1330 LST) daily satellite-derived AOD and AE from 2000-2013 and 2002-2013, respectively (collection 051 downloaded from the GIOVANNI data base; http://disc.sci.gsfc.nasa.gov/giovanni), over eastern North America (110° to 40°W, 20° to 60°N; Figure 2.1A). The overpasses of the eastern U.S. occur between 15 UTC (near coast) and 18 UTC (towards Rockies) for Terra, and 17 and 20 UTC for Aqua.

Averaged over all L3 grid cells within the study region, Terra AOD values are available for 48% of days (47% for Aqua) (Figure 2.1A). Retrieval frequency is a function of cloud cover, surface brightness and solar angle, and thus is dependent on latitude and season, with the lowest retrieval frequency in winter. This study uses Morgan-Monroe State Forest (MMSF) (*Pryor et al.*, 2010) in southern Indiana (Figure 2.1B) as a central grid for the spatial analyses, and integrates ground-based radiometer measurements from AERONET (*Holben et al.*, 2001) sites across the domain, with Bondville, IL and Dayton, OH (~185 km west and 205 km east of MMSF, respectively) providing foci for the temporal analyses.

To test the dependence of the spatial coherence of extreme AOD on synoptic-scale meteorological conditions we employ the classification of *Sheridan* (2002). In this classification each day is defined as: dry polar (DP), dry moderate (DM), dry tropical (DT), moist polar (MP), moist moderate (MM), moist tropical (MT), moist tropical plus (MT+), moist tropical plus plus (MT++), or transitional (T; which reflects substantial time-evolution of conditions during a given

day such as those associated with frontal passages) based on four-times daily near-surface observations of temperature, dew point, wind speed, pressure, and cloud cover at an individual station. The classification is fully inclusive (i.e. each day at each station is allocated to a type) and is based on similarity to seed days (days that typify a particular weather type) selected within each time of the year. Conditions in the seed day for any type are a function both of the specific station and the time of the year, and thus can occur year round (see example given in Supplemental Materials (SM) Figure SM2.1). The classification incorporates some degree of spatial coherence, such that a single classification type is typically observed on the regional scale (e.g. the Midwest), but a one-day lag in classification type maybe observed downwind (e.g. eastern US). In this analysis the synoptic weather type is described using data from Indianapolis, IN, ~55 km north of MMSF (data from http://sheridan.geog.kent.edu/ssc.html). Due to the low frequency of aerosol extreme values during DM and MM days, analyses for these weather types are not presented. Conditions in the MT+ and MT++ classes are indistinguishable in the mid-latitudes, and so are merged into a single class.

Statistical methods

Analyses in both the temporal and spatial domains are used to resolve dominant scales in observed variability of AOD and AE. Temporal variability of AOD and AE in each of the MODIS L3 grids is quantified using coefficients of variation (*COV*):

$$COV = \sigma/\bar{X} \ldots (1)$$

Where σ is the standard deviation of daily measurements and $\bar{X}$ is the mean AOD or AE in each grid cell. Higher *COV* indicates greater variability within a time series.

While AOD and AE from both Terra and Aqua for grid cells containing MMSF (39.5ºN 86.5ºW) and Bondville, IL (40.5ºN 88.5ºW) (Figure 2.1B) are also subject to a Fast Fourier

Transform (FFT) to quantify dominant temporal modes of variability. On average 50% (44%) of days at MMSF (Bondville) have "good" L3 retrievals. The missing observations are approximately randomly distributed throughout the time series, and the majority of missing data periods last only 1 day (Figure SM2.2). Because application of FFT requires a continuous time series, days without valid data are filled with average values from closest preceding and succeeding good retrievals, with a higher weighting the nearest day. While this may not accurately reflect conditions during non-retrieval days (e.g. enhanced AOD due to cloud processes in non-precipitating clouds or reduced AOD due to rainout), this in-fill method was selected to minimize artificial variance modification. For comparative purposes power spectra are also computed using AERONET data from Bondville at 12:30 LST (mean of 12:15 – 12:45 retrievals). Missing observations are also approximately random in the AERONET data (Figure SM2.3), but the frequency of missing data at periods > 1 day is higher (Figure SM2.2). Thus the procedure used to derive the complete time series will tend to reduce variability at short time scales (e.g. the synoptic scale).

The spatial coherence of aerosol properties is derived by relating daily time series of AOD in the L3 grid cell containing MMSF to that in all other grid cells for all days of simultaneous good retrievals. The large sample size and high temporal autocorrelation renders estimation of significant spatial correlation difficult (*Wilks*, 1997). Thus, semivariograms computed using the correlation coefficient (r) and the coefficient of divergence (*COD*) are used to quantify the distance at which AOD measurements cease to be coherent. While r describes the mutual variability, *COD* is a measure of the magnitude of difference between daily time series from two locations:

$$COD_{ab} = \sqrt{1/n \sum_{i=1}^{n} ((X_{ai} - X_{bi})/(X_{ai} + X_{bi}))^2} \ldots (2)$$

Where n is number of observations, and X_{ai} and X_{bi} are the values at time = i at locations a and b, respectively. $COD \rightarrow 1$ indicates a more heterogeneous field.

Semivariograms are created using (3) and modeled using an exponential fit (4):

$$\gamma(h) = \frac{\sum_{i=1}^{N(h)}[Z(x_i) - Z(x_i+h)]^2}{2N(h)} \ldots (3)$$

Where $\gamma(h)$ is the empirical semivariogram, $N(h)$ is the number of grid cells with a centroid at a distance, h, from MMSF (binned by 100 km, or ~ 1°), $Z(x_i)$ is the statistical metric (e.g. r and COD) at MMSF (i.e. 1 and 0, respectively), and $Z(x_i + h)$ is the metric between MMSF and the *ith* grid cell at a distance, h, from MMSF.

$$\gamma'(h) = C_n + C_p(1 - e^{-\frac{3h}{a}}) \ldots (4)$$

Where $\gamma'(h)$ is the semivariogram model fit, C_n is the nugget (i.e. the value at distance = 0 representing experimental error and variability on scales finer than the data resolution (*Liebhold and Sharov*, 1998)), C_p is the partial sill (i.e. $C_n + C_p$ = the upper bound of the semivariogram), and a is the range of the semivariogram (where 95% of the sill has been reached (*Wade et al.*, 2006)). The range describes the relative scales of spatial autocorrelation. Note: $\gamma'(h)$ as defined here is a measure of the decay in a statistical metric (e.g. r, COD) with distance from MMSF, and is thus unitless. An exponential fit is used because:

(i) Other models cannot be estimated statistically or assume correlations approach zero at large h (*Clark, 1979*), and the exponential model coefficients are amenable to physical interpretation (*Liebhold and Sharov*, 1998; *Wade et al.*, 2006).

(ii) Assuming a single first-order removal process, concentrations from a point source exhibit exponential decay with distance.

The spatial coherence of extreme AOD is quantified using a percentile-based approach. Considering only days with retrievals at both MMSF and each other individual grid cell, dates on

which AOD in the grid cell containing MMSF exceeded the 90th percentile are found and then it is determined if data from each other grid cells also exceeded that threshold (i.e. locally determined 90th percentile) on the same day. The threshold for determining statistical significance of co-occurrence of extremes is derived using 10,000 pairs of simulated time-series created by randomly selecting from a binomial distribution with a 10% probability of selecting a 'true' value representing an extreme (> 90th percentile) event, and calculating the probability that an extreme occurs simultaneously in both time series.

Results

Evaluation of MODIS L3 products

The homogeneous nature of the L3 product makes it well-suited to regional analyses (*Levy et al.*, 2009). Further, our statistical methodology requires repeated measurements at each location, which is inherent in the gridded L3 product. Nevertheless, L3 estimates of AOD and AE are sensitive to the spatial averaging methodology employed and spatial sampling bias within each grid cell. Thus prior to application of the statistical tools described above, an evaluation of the L3 data product was undertaken.

A least-squares linear regression fit to daily AOD in the MMSF grid cell from Terra and Aqua L3 data sets has a variance explanation (r^2) of 0.75, and a root mean square difference (RMSD) = 0.09, which is comparable to the mutual uncertainty on each day's measurements. Empirical quantile-quantile plots of daily AOD and AE from Terra and Aqua for the MMSF grid cell and four diagonally adjacent grid cells (Figure 2.2) also indicate good accord. Absolute discrepancies increase with AOD (*Ichoku et al.*, 2005): $AOD_{Terra} > AOD_{Aqua}$ when AOD > 0.6 (Figure 2.2A). Upper percentiles of AOD in AERONET data from Bondville and Dayton are slightly higher at the time of the Terra satellite overpass than at the time of the Aqua satellite

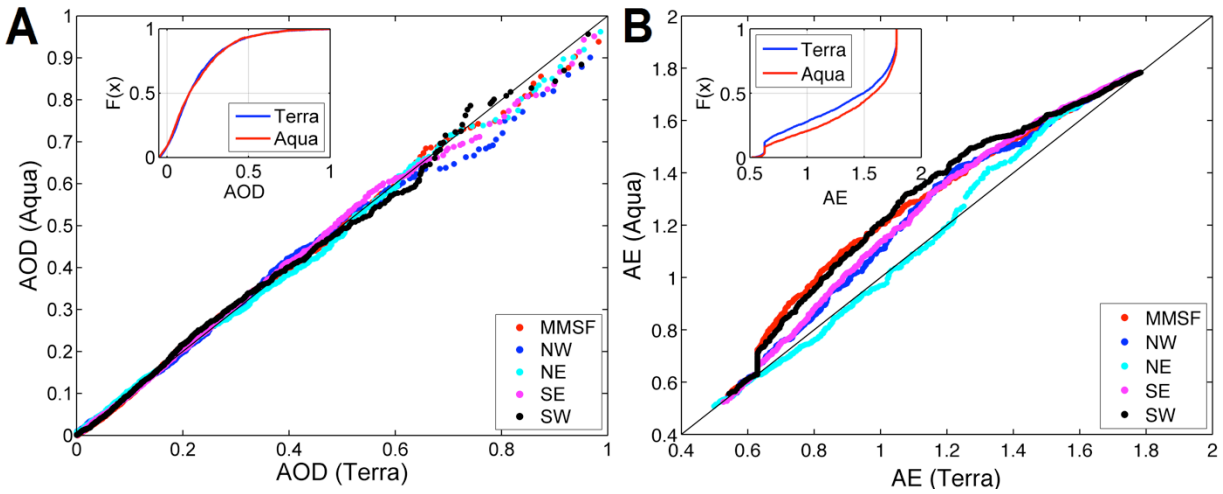

Figure 2.2 Empirical quantile-quantile plots of A) aerosol optical depth (AOD) at 0.55 μm and B) Ångström exponent (AE) at 0.47 μm – 0.65 μm from Terra (2000-2013) and Aqua (2002-2013) for the L3 grid cell containing Morgan-Monroe State Forest (MMSF, 39.5ºN 86.5ºW) and the four diagonally adjacent grid cells (location of grid cells is shown in Figure 2.1B). Also shown for reference is the 1:1 relationship (y = x). Inset shows empirical cumulative distribution function (F(x)) plots of A) AOD and B) AE for the grid cell containing MMSF. Note: Negative AOD result from the uncertainty in the retrievals (±0.05) in near zero AOD conditions, and are thus considered valid.

overpass (Figure SM2.3). L3 AE retrievals from Terra and Aqua for the MMSF grid cell exhibit lower accord (r^2 = 0.33, RMSD = 0.38). This is expected from prior research at Bondville, IL (*Green et al.*, 2009) and the high uncertainty of MODIS AE (*Levy et al.*, 2010). However, the agreement is improved when only days where AOD > 0.2 are considered (r^2 = 0.49). AE from Aqua (afternoon) is general higher than from Terra (morning) except in the lowest ~ 5% and highest ~ 5% of values (Figure 2.2B). In situ aerosol concentrations and size distributions frequently exhibit a diurnal cycle (*Ford and Heald*, 2013; *Sullivan and Pryor*, 2014) and thus the implied larger median particle diameter from Terra measurements may reflect physically consistent drivers. However, AERONET data do not exhibit a clear diurnal cycle in AE (Figure SM2.3) and thus the difference between the two MODIS instruments may be due to calibration bias (*Levy et al.*, 2013).

AE in the L3 product is the arithmetic mean of all valid L2 AE retrievals in the grid cell. However, the arithmetic mean is not a robust statistic for variables such as AE that are not

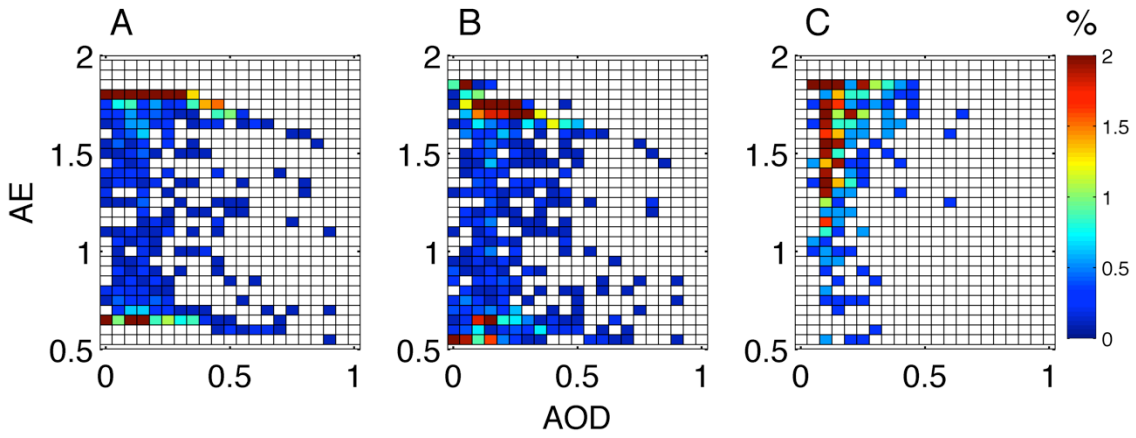

Figure 2.3 Joint probability distribution for aerosol optical depth (AOD) at 0.55 μm and Ångström exponent (AE) at 0.47 μm – 0.65 μm for Bondville, IL from (A) the MODIS L3 product from the Terra satellite (n = 926), (B) AE calculated from L3 AOD_{470} and AOD_{660} (n = 1003) from Terra, and (C) AERONET data (12:15-12:45 LST average; n = 366). Data used to construct these plots are for the period 2008-2013. For consistency with the L3 product, AE from AOD_{470} and AOD_{660} and AERONET are constrained to $0.5 \leq AE \leq 1.8$.

normally distributed and exhibit high estimation error and outliers. Accordingly, the L3 AE values are correlated with, but an imperfect estimate of, AE derived from spatially averaged AOD_{470} and AOD_{660} (Figure SM2.4). AOD and AE joint probability distributions differ markedly in MODIS data (both taken directly from L3 and computed from AOD_{470} and AOD_{660}) and AERONET observations (Figure 2.3). Although the MODIS AOD and AE values vary across the same parameter space as those from AERONET, their mutual variability is not well represented. Consistent with this evaluation, AE validation has been discontinued in the MODIS collection 6 release (*Levy et al.*, 2013), and although analyses of AE are presented herein, caution is exercised in interpreting the results.

The spatial averaging inherent in the L3 datasets inevitably masks some scales of variability (i.e. scales < 100 km). This is illustrated using a heterogeneous L3 grid cell in central Indiana (centroid 39.5ºN 86.5ºW) and quality-assured L2 data (resolution of 10 km × 10 km) (*Levy et al.*, 2010). L2 data from Terra for the pixels nearest to Indianapolis (39.767ºN 86.158ºW) and MMSF (39.317ºN 86.417ºW; Figure 2.1C) had simultaneous valid retrievals on

15% of days. These AOD retrievals indicate a high degree of co-variability, although urban enhancement of AOD is indicated by a regression analysis in which L2 data from MMSF is used to predict L2 data from Indianapolis (regression slope = 1.03 and intercept = 0.19, r^2 = 0.635, and RMSD = 0.227). Thus, although the L3 averaging may mask some variability at the mesoscale (e.g. *Anderson et al., 2003*), even in a grid cell with enormous variability in land use (Figure 2.1C) the AOD varies only modestly, supporting use of L3 in regional scale analysis. Consistent with the discussion above, there is a weaker association between AE from the two locations (r^2 = 0.069 and RMSD = 0.827), and the probability distribution indicates a higher prevalence of coarse mode aerosol in the urban environment.

For the reasons given above, only L3 data are used in analyses presented below. Nevertheless, these analyses provide important context for interpreting the analysis results, and also indicate that, although AOD and AE L3 estimates from Terra and Aqua exhibit many similarities, there are sufficient discrepancies that they are analyzed independently. In the following we focus predominantly on results from Terra because it is a slightly longer dataset.

Spatial patterns of AOD and AE

Annual mean AOD ($\overline{\text{AOD}}$) is highest (> 0.4) over Mexico/Texas (Figure 2.4A). The causes of this feature are unclear and while it may reflect physical conditions (e.g. high AOD associated with smoke transport into the area; *Wang et al.*, 2006), it may also be an artifact of poor retrieval over bright surfaces. Consistent with non-urban in situ $PM_{2.5}$ measurements that indicate a summertime maximum in the eastern U.S. (*Hand et al.*, 2012), AOD in both MODIS and AERONET data also exhibits high values in summer over the Midwestern (MODIS summer $\overline{\text{AOD}}$ ~ 0.2) and Southeast U.S. (MODIS summer $\overline{\text{AOD}} \rightarrow$ 0.3 – 0.4) (Figure 2.4D, Figure 2.4F, and Figure SM2.6). These data also indicate highest AOD persistence (low COV) in summer

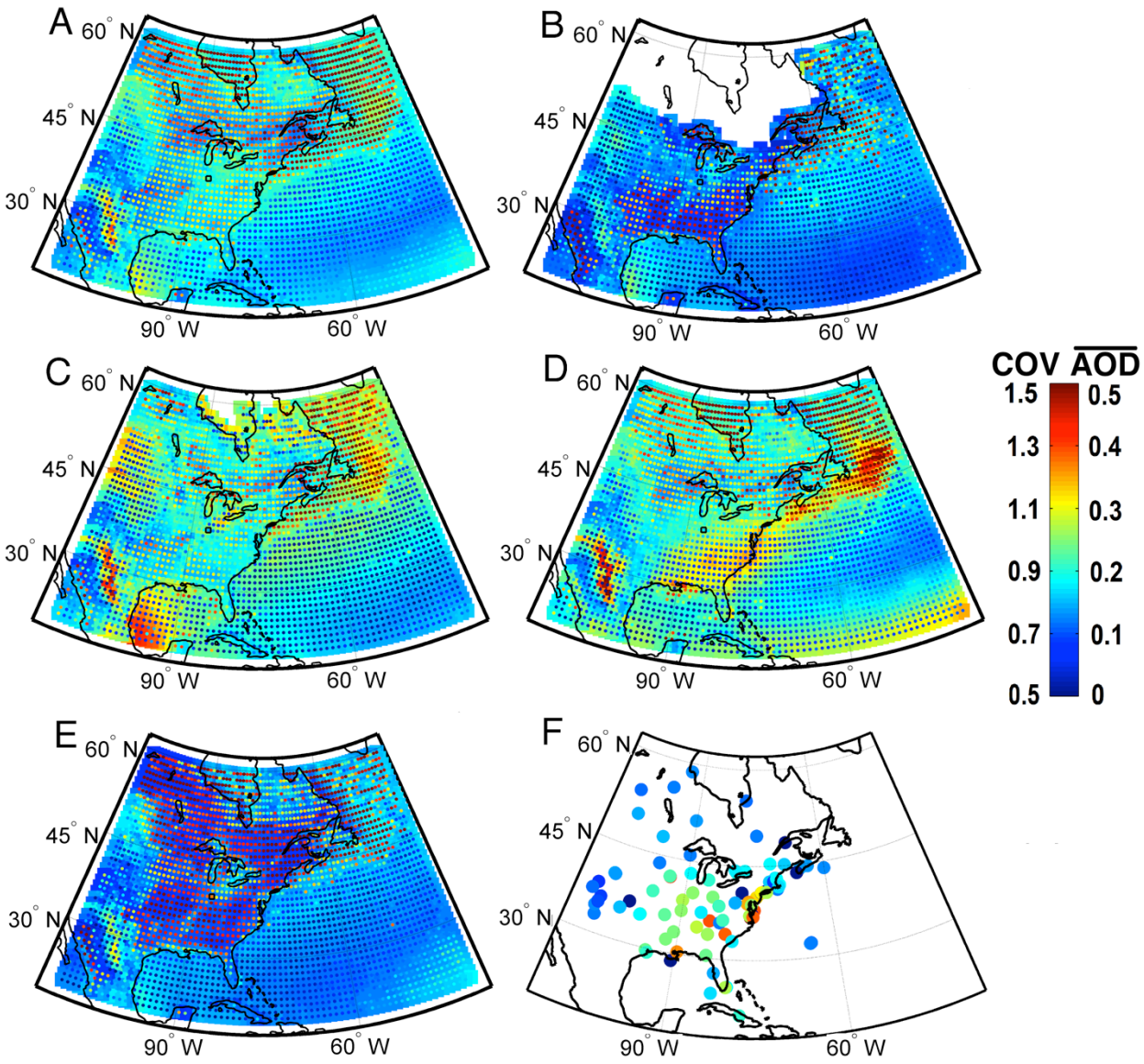

Figure 2.4 Mean aerosol optical depth (AOD) at 0.55 μm (background) and the COV of daily AOD values (stippling) A) for all seasons, B) winter (Dec – Feb), C) spring (Mar – May), D) summer (Jun – Aug), and E) fall (Sep – Nov). Data used to construct these plots derive from Terra and are for the period 2000-2013. F) Mean summer AOD at 0.5 μm from all available AERONET measurements 2000-2013 (see Figure SM2.5 for the data sample density and Figure SM2.6 for mean AOD in all seasons from the AERONET observations).

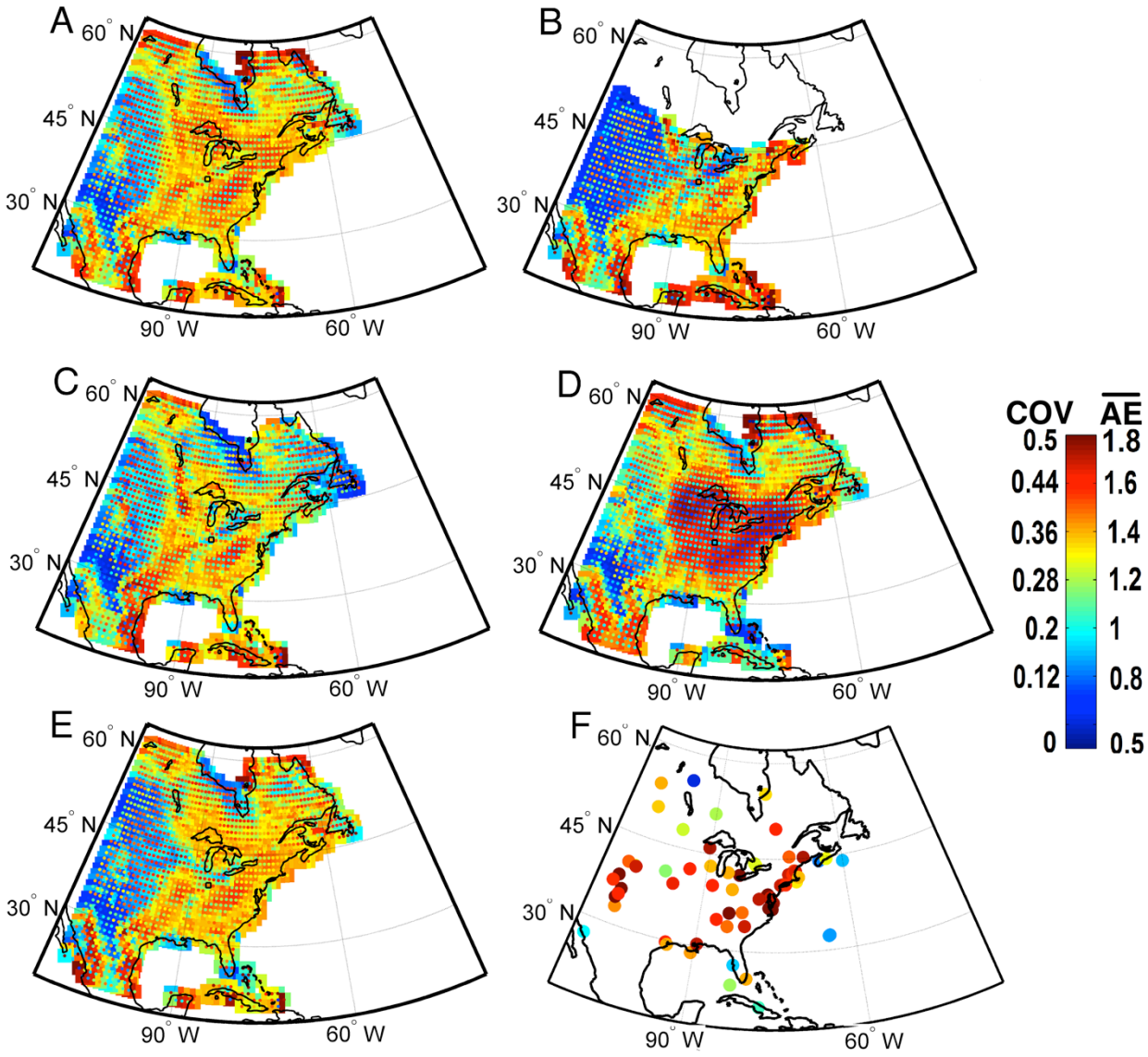

Figure 2.5 Mean Ångström exponent (AE) at 0.47 μm – 0.65 μm (background) and the COV of daily AE (stippling) A) for all seasons, B) winter (Dec – Feb), C) spring (Mar – May), D) summer (Jun – Aug), and E) fall (Sep – Nov). Data used to construct these plots derive from Terra and are for the data period 2000-2013. F) Mean winter AE 0.44 μm – 0.675 μm from all available AERONET measurements 2000-2013 (see Figure SM2.7 for mean AE in all seasons from the AERONET observations).

over the Southeast when $\overline{AOD}$ and radiative flux are highest. With the exception of the lower Great Lakes, lowest AOD is observed during the fall and winter ($\overline{AOD} < 0.1$) (Figure 2.4B, E). Although higher variability in AOD typically occurs over land (COV > 1.0 over the eastern U.S.) than over oceans (COV < 0.7), AOD also exhibits high COV off the northeast coast of North America (COV $\rightarrow$ 1.5) (Figure 2.4A), consistent with advection of aerosols from a high primary aerosol and precursor gas source region (*Jamieson and Wadleigh*, 2000; *Song et al.*, 2001).

Mean spatial patterns of AE derived from Aqua and Terra exhibit some discrepancies, but both indicate marked spatial gradients in AE and thus the dominant aerosol mode over eastern North America, which is also evident in ground measurements (*Li et al.*, 2013), and at AERONET sites (Figure SM2.7). There is a greater prevalence of coarse mode aerosols west of ~ 95 – 100º W (Figure 2.5A), coincident with the boundary at which different aerosol types are assumed in the MODIS retrieval algorithm (Levy et al., 2007). Fine mode aerosols dominate the Midwest/eastern U.S. (i.e. mean AE $\rightarrow$ 1.8, e.g. Figure 2.5A, D). AE also exhibits marked temporal variability, particularly during winter (COV ~ 0.5, Figure 2.5B), indicating alternating periods of high and low AE. Winter AE values from MODIS over portions of the Midwest are typically lower than during other seasons (Figure 2.5B). Although a winter decrease in AE is not measured at the Bondville AERONET site and AE is highly uncertain, lower mean AE during winter is observed at other AERONET sites in the region (Figure 2.5F, Figure SM2.7), and may reflect an increase in the relative abundance of coarse mode aerosols. Surface observations in the Midwest also indicate a strong seasonality in aerosol composition, with a marked increase in ammonium nitrate abundance in the winter (*Chu*, 2004; *Pitchford et al.*, 2009).

Spatial and temporal variability of aerosol particle properties

MMSF and Bondville are located in a region that experiences high AOD (Figure 2.4),

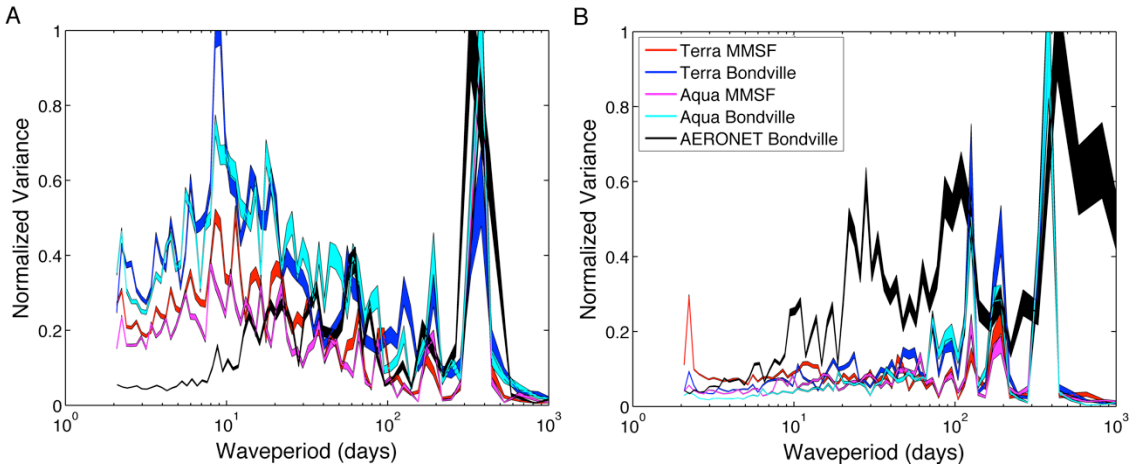

Figure 2.6 Normalized power spectra of daily A) aerosol optical depth (AOD) at 0.55 μm and B) Ångström exponent (AE) at 0.47 μm – 0.65 μm for the MODIS L3 grid cells containing Morgan-Monroe State Forest and Bondville from Terra (2000-2013) and Aqua (2002-2013). The power spectra have been normalized by maximum variance at any frequency (wave period). Shading represents statistical uncertainty under the assumption that each Fourier mode from the fast Fourier transformation (FFT) is normally distributed and uncorrelated with other modes. Thus, the uncertainty is solely a function of the sample size (time series length) and the number of modes over which the FFT is averaged. Also shown is the normalized power spectrum of AERONET measurements from Bondville, IL. The data period used to compute the power spectra from the AERONET time series is restricted to 01/2000-05/2007 due to the large data gap subsequent to 05/2007 (see Figure SM2.3).

and a high frequency of mid-latitude cyclone passages (*Coleman and Klink*, 2009). Accordingly, the annual and synoptic time scales (waveperiods ~ 1 – 2 weeks, and spatial scales of ~ O(1000 km)) dominate AOD variability (Figure 2.6A). In accord with our analyses that showed AOD in the L3 grid cell containing MMSF are also influenced by Indianapolis (Figure 2.1C), the variance maximum of AOD at the synoptic time scale is less marked in this grid cell, possibly due to the confounding effect of hebdomadal variability in primary emissions from this metropolis (Xia et al., 2008) (Figure 2.6A). Comparable AOD variability is captured in the AERONET data set from Bondville, with the exception of periods < 10 days where, as discussed in section 2.2, the variance is dampened by the high volume of missing data. The annual timescale is more dominant in AE, which also exhibits variability on seasonal and semiannual timescales, but relatively little variance on synoptic time scales (Figure 2.6B). The time series of AE from AERONET measurements at Bondville exhibit similar temporal variability (Figure

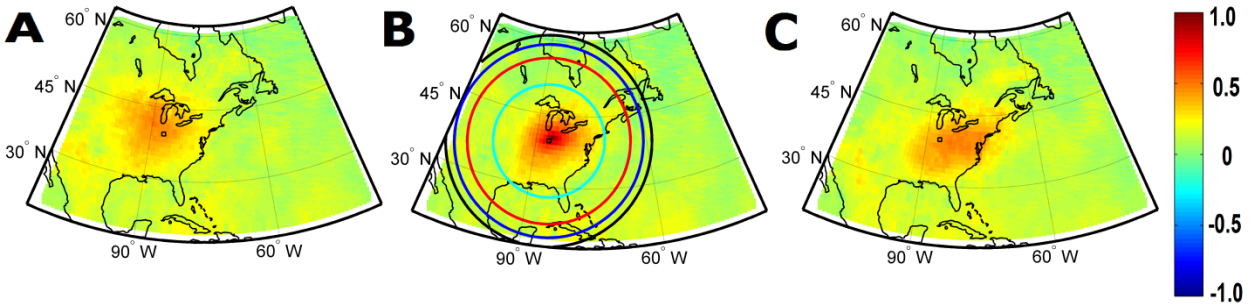

Figure 2.7 Spatial correlation (r) of aerosol optical depth (AOD) at 0.55 μm based on a centroid located at the grid cell containing Morgan-Monroe State Forest (MMSF) computed using daily data from Terra (2000-2013) with A) a minus one-day lag of data from all grid cells relative to MMSF, B) no lag (i.e. measurements from the same calendar date) and C) a plus one-day lag vs. MMSF. The circles shown in frame B) denote the semivariogram ranges for r for winter (Dec – Feb, cyan), spring (Mar – May, red), summer (June – Aug, blue), and fall (Sept – Nov, black).

2.6B), but also capture an additional mode of variability at a ~ 30-day period. The differences in MODIS and AERONET AE power spectra are partly, but not solely, due to spatial averaging in the L3 data product (see Figure SM2.8) and are also partly attributable to the high AE retrieval uncertainty.

The spatial autocorrelation of AOD is consistent with a relatively isotropic spatial field. Semivariograms of AOD derived using r indicate spatial coherence extends to a range of over 1000 km (i.e. the synoptic scale) and is largest during summer (95% of the semivariogram sill is reached at ~ 2200 km) and fall (~2400 km), and smaller during the winter (~1300 km) and spring (~1900 km) (Figure 2.7B). Semivariograms computed using COD indicate smaller scales of coherence, but similar seasonality. The spatial scale at which AOD becomes heterogeneous (as represented by semivariogram range values for COD) is also smallest in the winter (~ 200 km) and largest in the summer (~ 900 km) (Figure 2.8). AE exhibits smaller scales of spatial correlation than AOD, but this result must be viewed with caution due to significant uncertainties in AE retrievals and notable differences in the spatial autocorrelation of AE from the two satellites. Differences in the spatial scales of AOD as manifest in r and COD coherence highlight that although the drivers of particle concentration variability occur on large scales (as manifest in

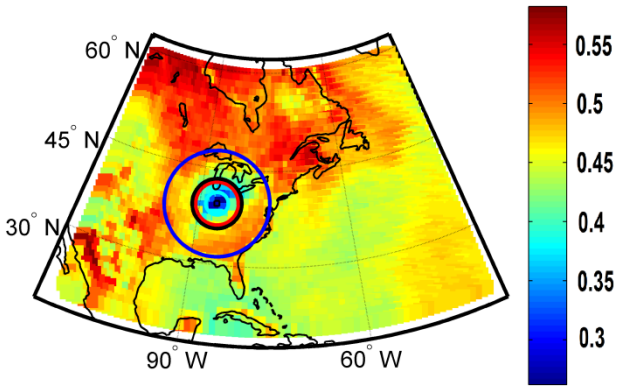

Figure 2.8 Coefficient of divergence (COD) of aerosol optical depth (AOD) at 0.55 μm estimates relative to the MODIS L3 grid cell containing Morgan-Monroe State Forest using daily data from Terra (2000-2013). Also shown (by the solid lines) are semivariograms ranges for COD for winter (Dec – Feb, cyan), spring (Mar – May, red), summer (Jun – Aug, blue), and fall (Sep – Nov, black).

the semivariogram analysis of r), the absolute concentrations (as manifest in the semivariogram analysis of COD) and mean particle diameter (as manifest in the semivariogram analysis of AE) exhibit evidence of a more heterogeneous field. This is physically consistent with the heterogeneity of land use (Figure 2.1B), and thus primary aerosol and precursor emissions across the study area (*Pitchford et al.*, 2009). To test the sensitivity of the scale of coherence of aerosol columnar properties to the centroid location an analysis was conducted in which the centroid location was moved 5° to the north, south, west, and east and the spherical distance at which the correlation coefficient for AOD dropped below an arbitrary threshold of 0.3 was computed. As shown in Figure SM2.9, the results indicate that the resulting scale of coherence is not very sensitive to the precise centroid chosen, and thus confirms the results presented above are somewhat generalizable.

The importance of advection in determining aerosol concentrations implied in the mean AOD spatial fields is also clearly observed using a time lagged AOD correlation (i.e. MMSF at time t vs. all other grid cells at time t ± one day). The highest correlation with AOD measurements from MMSF is observed westward of MMSF in the minus one day lagged

correlations, and extends eastward of MMSF in the plus one day lagged analysis (Figure 2.7A, C).

The occurrence of high AOD has greatest relevance to air quality and climate forcing, thus an analysis of the scales on which such events occur was undertaken using MMSF as the focal node. The mean 90^{th} percentile AOD in the grid cell containing MMSF is 0.45, while the domain average is 0.33, which again emphasizes the Midwest as a region of high AOD. Consistent with the occurrence of highest mean AOD values in summer and spring (Figure 2.4), extreme AOD events occurred more frequently in these seasons (of the top 10% AOD days, 48% and 32% occur in summer and spring, respectively, Figure 2.9B inset). Due to low mean AOD values in winter, a lower percent of extreme AOD events are expected in the season (6%), but it is noted that lower solar angle, increased bright surfaces (e.g. snow), and the resultant lower retrieval frequency of aerosol properties also contributes to a low number of extreme AOD values in winter. The frequency of co-occurrence of extreme AOD (hereafter AOD_{EXT}) at the grid cell containing MMSF and every other grid cell exhibits a marked decrease with spherical distance (Figure 2.9A). AOD_{EXT} decreases to < 50 % at distances beyond ~ 150 km from MMSF. Nevertheless, AOD_{EXT} is above that predicted by random chance (~10%) over most of eastern North America, which implies a large-scale control on the occurrence of high AOD. As in the analysis of all AOD values (Figure 2.7), the distance over which significant AOD_{EXT} is observed is greatest in fall (Figure 2.9B), indicating that both typical and high aerosol loadings are spatially coherent at largest scales during this season.

As described above, both time series and spatial analysis of AOD exhibit high variance at scales consistent with synoptic scale meteorological phenomena. Further, prior research has linked supra-regional air pollution episodes with high temperature and humidity (*Chu*, 2004),

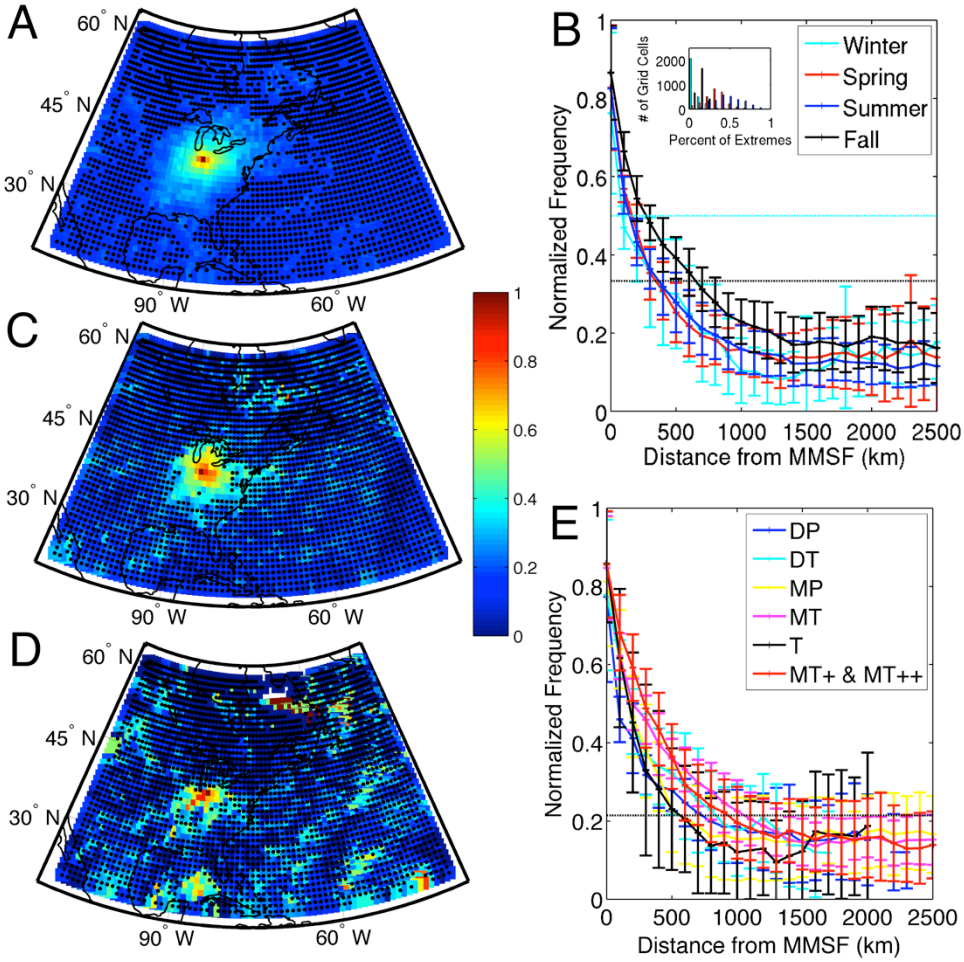

Figure 2.9 A) Frequency of co-occurrence of extreme (> 90th percentile) aerosol optical depth at 0.55 μm (AOD_{EXT}) for the grid cell containing Morgan-Monroe State Forest (MMSF) and all other grid cell normalized by n > 90th percentile at MMSF. Stippling indicates grid cells where AOD_{EXT} is below that expected by random chance, and thus is not statistically significant. B) Mean normalized AOD_{EXT} versus distance from MMSF (binned by 100 km distance classes from MMSF) by season, and error bars (± one standard deviation from mean). Dashed lines represent significance as described in section 2.2. Inset shows histogram of percentage of extremes occurring in each season for all grid cells. C), D): As in A moist tropical plus/plus plus (MT+/MT++) air masses (C) and transitional (D) synoptic-scale meteorological conditions. E): As in B), but by weather code (codes are listed in Section 2.1 (Sheridan, 2002)).

and with atmospheric stagnation (*Horton et al.*, 2014). Thus the spatial coherence of extreme AOD values was conditionally sampled by the prevailing synoptic-scale meteorology (Figure 2.9E). Although MODIS retrievals of aerosol properties are not randomly distributed in time, consistent with *a priori* expectations, highest AOD_{EXT} occurred during Moist Tropical (MT and MT+/MT++) days, and while the average spatial scale of 'simultaneous' occurrence of AOD in

excess of the local 90th percentile value is 150 km, during MT+/MT++ days the region for which AOD_{EXT} > 50% of days extends up to ~ 300 km from MMSF (Figure 2.9C, E). On transitional days (T), the scale of spatial coherence of extremes is smallest (Figure 2.9E) and consistent with interpretations of this synoptic class as representing mid-latitude cyclone and frontal passages, is dependent on relative direction from MMSF (Figure 2.9D).

Discussion and concluding remarks

Satellite-based measurements of AOD and AE offer the potential for significant insights into causes of spatiotemporal variability in aerosol concentrations and aerosol-climate interactions. However, more research is needed to evaluate satellite products in terms of their ability to capture physically consistent features, and to understand and reduce uncertainty. Accordingly, herein we present statistical analyses of the MODerate resolution Imaging Spectroradiometer (MODIS) Level-3 (L3) and Level-2 data products and observations from AErosol RObotic NETwork (AERONET) stations, and use them to characterize spatiotemporal scales of variability and coherence in columnar aerosol burdens over eastern North America.

AOD from the L3 MODIS data product from Terra and Aqua, and AERONET observations exhibit good accord in terms of absolute values, spatial variability, and seasonality. Highest AOD is observed over the lower Midwest and Southeast, and co-occurrence of high AOD and low temporal variability is maximized over the Southeast during the summer. The largest COV in AOD is observed over eastern Canada and off the northeast coast of the USA, which highlights the importance of advection of aerosols and precursors from the Midwest (*Jamieson and Wadleigh,* 2000). It is also consistent with temporally transient aerosol sources in Canada that can enhance particle concentrations on sub-seasonal time scales (e.g. forest fires (*Song et al.,* 2001)). Power spectra of AOD from MODIS and an AERONET site in central

Illinois also exhibit good accord in terms of absolute values and the dominant spatiotemporal scales of variability. Consistent with analyses using a synoptic classification and previous analyses of satellite (*Ford and Heald*, 2013) and surface measurements (*Tai et al.*, 2010), the dominant mode of variability in AOD, as manifest both in spatial and temporal analyses, is the synoptic-scale. AOD and particularly extreme AOD values exhibit large spatial scales of coherence that are maximized during fall, summer, and under stagnant maritime tropical air masses, and are minimized in transitional synoptic patterns (e.g. frontal passages). The larger spatial scale of coherence in fall and summer is consistent with in-situ measurements of large-scale particle pollution episodes associated with blocking anticyclones (and stagnation), warm temperature and high relative humidity, and sufficient insolation for photochemical production of secondary aerosols during these seasons (*Chu*, 2004). Conversely, the high frequency of precipitation, lower boundary layer depths, and localized precursor emissions and favorable thermodynamics for secondary nitrate aerosol formation (*Chu*, 2004; *Pitchford et al.*, 2009) during winter and spring may explain the reduced spatial coherence during those seasons. The inter-annual variability in AOD as manifest in the spectral analysis may reflect the role of internal climate modes such as El Niño-Southern Oscillation (ENSO) in causing year-to-year variability in precipitation frequency (*Barlow et al.*, 2001) and therefore wet scavenging of particles and/or the frequency of synoptic conditions associated with atmospheric stagnation.

Estimates of AE from the MODIS observations are more uncertain (*Levy et al.*, 2013) and AE in the MODIS L3 data product exhibit larger discrepancies that are partly, but not solely, attributable to high uncertainty at low AOD and/or spatial averaging methodology. Although the presence of physically interpretable modes of variance, that are consistent between the two satellites, and MODIS and AERONET, implies the time series are to some degree reflective of

physical processes (e.g. semiannual variability in AE is consistent with changes in primary and precursor emissions associated with the seasonality of electricity consumption and agricultural activities, and seasonality in atmospheric thermodynamic conditions), AE from the L3 data product should be used with care.

Spatiotemporal variability in aerosol populations documented here serve to enhance confidence in AOD from the MODIS L3 data set, help to infer process-level controls on climate relevant aerosol populations, and also provide tools with which to evaluate atmospheric chemistry models (via analysis of amount of variance or coherence expressed at different scales).

Acknowledgements

This work was supported by NASA Headquarters under the NASA Earth and Space Science Fellowship Program - Grant “14-EARTH14F-0207” and a grant to SCP from NSF (1102309, 1517365). The data used in this study were acquired as part of the NASA's Earth-Sun System Division and archived and distributed by the MODIS Level 1 and Atmosphere Archive and Distribution System (LAADS). The authors acknowledge useful conversations with R.J. Barthelmie and G. Filippelli, valuable input from two anonymous reviewers, and B. Holben, C. Lehmann, and M. Tragesser for establishing and maintaining the Bondville and Dayton AERONET sites.

REFERENCES

Alston, E. J., I. N. Sokolik, and O. V. Kalashnikova (2012), Characterization of atmospheric aerosol in the US Southeast from ground-and space-based measurements over the past decade, *Atmospheric Measurement Techniques*, *5*(7), 1667-1682.

Anderson, J. C., J. Wang, J. Zeng, G. Leptoukh, M. Petrenko, C. Ichoku, and C. Hu (2013), Long-term statistical assessment of Aqua-MODIS aerosol optical depth over coastal regions: bias characteristics and uncertainty sources, *Tellus B*, *65*, 20805, http://dx.doi.org/10.3402/tellusb.v65i0.20805.

Anderson, T. L., R. J. Charlson, D. M. Winker, J. A. Ogren, and K. Holmén (2003), Mesoscale Variations of Tropospheric Aerosols*, *Journal of the Atmospheric Sciences*, *60*(1), 119-136.

Barlow, M., S. Nigam, and E. Berbery (2001), ENSO, Pacific decadal variability, and US summertime precipitation, drought, and stream flow, *Journal of Climate*, *14*(9), 2105-2128.

Boucher, O., et al. (2013), *Clouds and aerosols. In: Climate Change 2013: The Physical Science Basis. Contribution of Working Group I to the Fifth Assessment Report of the Intergovernmental Panel on Climate Change [Stocker, T.F., D. Qin, G.-K. Plattner, M. Tignor, S.K. Allen, J. Boschung, A. Nauels, Y. Xia, V. Bex and P.M. Midgley (eds.)]*, Cambridge University Press, Cambridge, United Kingdom and New York, NY, USA.

Brook, R. D., S. Rajagopalan, C. A. Pope III, J. R. Brook, A. Bhatnagar, A. V. Diez-Roux, F. Holguin, Y. Hong, R. V. Luepker, and M. A. Mittleman (2010), Particulate matter air pollution and cardiovascular disease, *Circulation*, *121*(21), 2331-2378.

Chu, S.-H. (2004), $PM_{2.5}$ episodes as observed in the speciation trends network, *Atmospheric Environment*, *38*(31), 5237-5246.

Clark, I. (1979), *Practical Geostatistics*, Applied Science Publishers, London, United Kingdom.

Coleman, J. S. M., and K. Klink (2009), *North American atmospheric circulation effects on Midwestern USA climate, in Understanding Climate Change: Climate variability, predictability and change in the Midwestern United States, [S. C. Pryor (ed.)]*, pp. 156-168, Indiana University Press, Bloomington.

Ford, B., and C. L. Heald (2013), Aerosol loading in the Southeastern United States: reconciling surface and satellite observations, *Atmospheric Chemistry and Physics*, *13*(18), 9269-9283.

Green, M., S. Kondragunta, P. Ciren, and C. Xu (2009), Comparison of GOES and MODIS aerosol optical depth (AOD) to aerosol robotic network (AERONET) AOD and IMPROVE $PM_{2.5}$ mass at Bondville, Illinois, *Journal of the Air & Waste Management Association*, *59*(9), 1082-1091.

Hand, J., B. Schichtel, M. Pitchford, W. Malm, and N. Frank (2012), Seasonal composition of remote and urban fine particulate matter in the United States, *Journal of Geophysical Research: Atmospheres*, *117*(D5), doi:10.1029/2011JD017122.

Holben, B., D. Tanre, A. Smirnov, T. Eck, I. Slutsker, N. Abuhassan, W. Newcomb, J. Schafer, B. Chatenet, and F. Lavenu (2001), An emerging ground-based aerosol climatology: Aerosol optical depth from AERONET, *Journal of Geophysical Research: Atmospheres*, *106*(D11), 12067-12097.

Hollmann, R., C. Merchant, R. Saunders, C. Downy, M. Buchwitz, A. Cazenave, E. Chuvieco, P. Defourny, G. De Leeuw, and R. Forsberg (2013), The ESA climate change initiative: satellite data records for essential climate variables, *Bulletin of the American Meteorological Society*, *94*(10), 1541-1552.

Horton, D. E., C. B. Skinner, D. Singh, and N. S. Diffenbaugh (2014), Occurrence and persistence of future atmospheric stagnation events, *Nature Climate Change*, *4*(8), 698-703.

Hubanks, P. A., M. D. King, S. Platnick, and R. Pincus (2008), MODIS atmosphere L3 gridded product algorithm theoretical basis document, *ATBD Reference Number: ATBD-MOD-30.* , downloaded from: http://modis-atmos.gsfc.nasa.gov/_docs/MOD08MYD08%20ATBD%20C005.pdf.

Ichoku, C., L. A. Remer, and T. F. Eck (2005), Quantitative evaluation and intercomparison of morning and afternoon Moderate Resolution Imaging Spectroradiometer (MODIS) aerosol measurements from Terra and Aqua, *Journal of Geophysical Research: Atmospheres*, *110*(D10), doi:10.1029/2004JD004987.

Jamieson, R., and M. Wadleigh (2000), Tracing sources of precipitation sulfate in eastern Canada using stable isotopes and trace metals, *Journal of Geophysical Research: Atmospheres*, *105*(D16), 20549-20556.

Levy, R., S. Mattoo, L. Munchak, L. Remer, A. Sayer, F. Patadia, and N. Hsu (2013), The Collection 6 MODIS aerosol products over land and ocean, *Atmospheric Measurement Techniques*, *6*(11), 159-259, doi:10.5194/amtd-6-159-2013.

Levy, R. C., G. G. Leptoukh, R. Kahn, V. Zubko, A. Gopalan, and L. A. Remer (2009), A critical look at deriving monthly aerosol optical depth from satellite data, *IEEE Transactions on Geoscience and Remote Sensing*, *47*(8), 2942-2956.

Levy, R. C., L. A. Remer, and O. Dubovik (2007), Global aerosol optical properties and application to Moderate Resolution Imaging Spectroradiometer aerosol retrieval over land, *Journal of Geophysical Research: Atmospheres*, *112*(D13), doi:10.1029/2006JD007815.

Levy, R. C., L. A. Remer, R. G. Kleidman, S. Mattoo, C. Ichoku, R. Kahn, and T. Eck (2010), Global evaluation of the Collection 5 MODIS dark-target aerosol products over land, *Atmospheric Chemistry and Physics*, *10*(21), 10399-10420.

Li, R., C. Wiedinmyer, and M. Hannigan (2013), Contrast and correlations between coarse and fine particulate matter in the United States, *Science of the Total Environment*, *456*, 346-358.

Liebhold, A., and A. Sharov (1998), *Testing for correlation in the presence of spatial autocorrelation in insect count data. In: Population and community ecology for insect management and conservation [Baumgärtner, J., P. Brandmayr, and B. Manly (eds.)]*, Balkema, Rotterdam, Netherlands.

Pitchford, M. L., R. L. Poirot, B. A. Schichtel, and W. C. Malm (2009), Characterization of the winter Midwestern particulate nitrate bulge, *Journal of the Air & Waste Management Association*, *59*(9), 1061-1069.

Pryor, S. C., A. M. Spaulding, and R. J. Barthelmie (2010), New particle formation in the Midwestern USA: Event characteristics, meteorological context and vertical profiles, *Atmospheric Environment*, *44*(35), 4413-4425, doi:10.1016/j.atmosenv.2010.07.045.

Remer, L. A., Y. Kaufman, D. Tanré, S. Mattoo, D. Chu, J. V. Martins, R.-R. Li, C. Ichoku, R. Levy, and R. Kleidman (2005), The MODIS aerosol algorithm, products, and validation, *Journal of the Atmospheric Sciences*, *62*(4), 947-973.

Sheridan, S. C. (2002), The redevelopment of a weather-type classification scheme for North America, *International Journal of Climatology*, *22*(1), 51-68.

Song, X.-H., A. V. Polissar, and P. K. Hopke (2001), Sources of fine particle composition in the northeastern US, *Atmospheric Environment*, *35*(31), 5277-5286.

Sullivan, R. C., and S. C. Pryor (2014), Quantifying spatiotemporal variability of fine particles in an urban environment using combined fixed and mobile measurements, *Atmospheric Environment*, *89*, 664-671.

Tai, A. P., L. J. Mickley, and D. J. Jacob (2010), Correlations between fine particulate matter ($PM_{2.5}$) and meteorological variables in the United States: Implications for the sensitivity of $PM_{2.5}$ to climate change, *Atmospheric Environment*, *44*(32), 3976-3984.

Wade, K. S., J. A. Mulholland, A. Marmur, A. G. Russell, B. Hartsell, E. Edgerton, M. Klein, L. Waller, J. L. Peel, and P. E. Tolbert (2006), Effects of instrument precision and spatial variability on the assessment of the temporal variation of ambient air pollution in Atlanta, Georgia, *Journal of the Air & Waste Management Association*, *56*(6), 876-888.

Wang, J., S. A. Christopher, U. S. Nair, J. S. Reid, E. M. Prins, J. Szykman, and J. L. Hand (2006), Mesoscale modeling of Central American smoke transport to the United States: 1. "Top-down" assessment of emission strength and diurnal variation impacts, *Journal of Geophysical Research: Atmospheres*, *111*(D05S17), doi:*10.1029/2005JD006416*.

Wilks, D. (1997), Resampling hypothesis tests for autocorrelated fields, *Journal of Climate*, *10*(1), 65-82.

Xia, X., T. F. Eck, B. N. Holben, G. Phillippe, and H. Chen (2008), Analysis of the weekly cycle of aerosol optical depth using AERONET and MODIS data, *Journal of Geophysical Research: Atmospheres*, *113*(D14217), doi:10.1029/2007JD009604.

Supplemental Materials: Spatiotemporal coherence of mean and extreme aerosol particle events over eastern North America as observed from satellite

Sullivan, R. C., Levy, R. C., and Pryor, S. C.

The synoptic classification of Sheridan

Herein we employ the synoptic classification of (*Sheridan*, 2002). In this classification each day is defined as: dry polar (DP), dry moderate (DM), dry tropical (DT), moist polar (MP), moist moderate (MM), moist tropical (MT), moist tropical plus (MT+), moist tropical plus plus (MT++), or transitional (T; which reflects substantial time-evolution of conditions during a given day such as those associated with frontal passages). The moist tropical (MT) classes of synoptic conditions are demonstrated herein to be of particular importance to the occurrence of large-scale high AOD events. As shown, this class of synoptic conditions occurs in all months of the year due to the classification requirement that conditions in the seed day for MT are a function both of the specific station and the time of the year, but MT days are more prevalent in summer (Figure SM2.1).

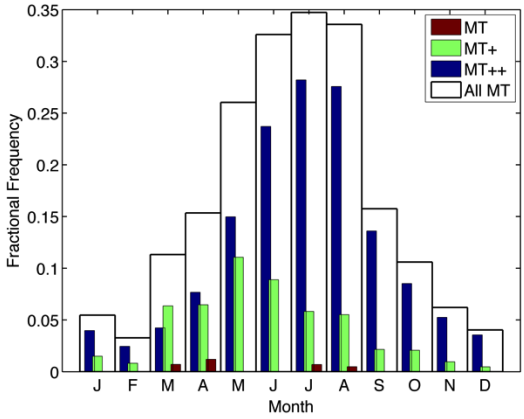

Figure SM2.1 Fractional frequency ($\frac{n: synoptic\ type}{n: days\ in\ month}$) of occurrence of maritime tropical (MT), maritime tropical plus (MT+), and maritime tropical plus plus (MT++) by month.

Quantifying the duration of consecutive days of missing data in the AERONET and MODIS L3 data products

As described in the main text, in order to compute power spectra of the time series of AOD and AE from the MODIS and AERONET data products it is necessary to have an unbroken time series. However, the MODIS L3 and AERONET time series are incomplete. The missing observations are approximately randomly distributed throughout the L3 time series, and as shown in Figure SM2.2, the majority of missing data are for periods of 1 day. Because application of FFT requires a continuous time series, days without good retrievals are filled with average values from closest preceding and succeeding good retrievals, weighted by temporal displacement from the missing day. This inflates the variance in the data set at short-time scales less than 'infilling' with the mean value. It is noted that the frequency of missing data at periods > 1 day is higher in the AERONET time series, and thus this method may mask variability at short time scales.

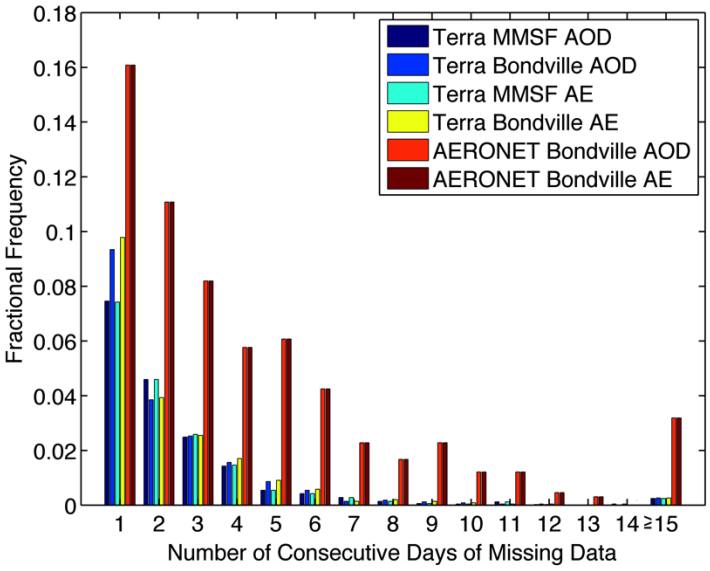

Figure SM2.2 Fractional frequency ($\frac{n}{length\ of\ time\ series}$) of consecutive missing days in Terra MODIS L3 data sets for the grid cells containing Morgan-Monroe State Forest (MMSF) and Bondville, and AERONET in Bondville.

Evaluation of the diurnal variability of AOD and AE using AERONET data

Aerosol populations exhibit diurnal cycles that cannot be represented by once daily observations. Although Terra and Aqua sample different aerosol populations due to differences in overpass timing, it is impossible to differentiate a physical signal from calibration bias. Thus, sub-daily variability is characterized using AERONET measurements. As shown, AOD exhibits consistently higher median and mean values in the early morning and late afternoon, but AE does not exhibit a clear dependence on the hour of the day (Figure SM2.3).

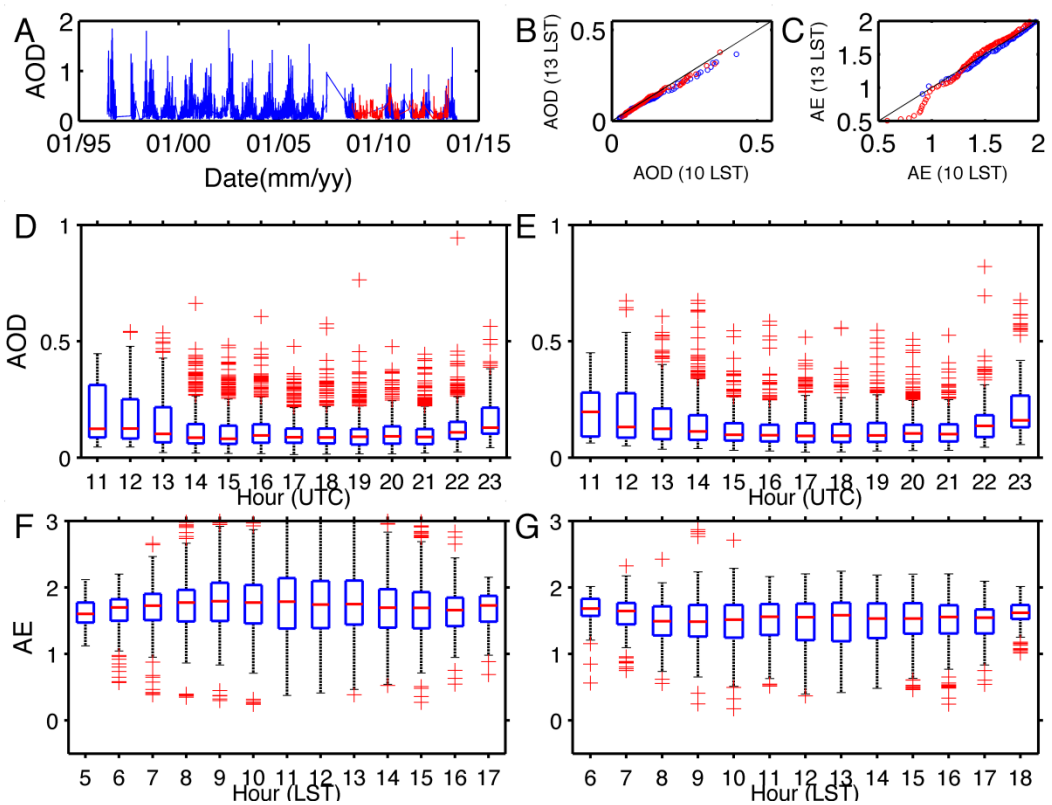

Figure SM2.3 A) Time series and Empirical Quantile-Quantile plots for Bondville (blue) and Dayton (red) AERONET B) aerosol optical depth at 0.5 μm (AOD) and C) Ångström exponent at 0.44 and 0.675 μm (AE) measurements at 10 and 13 LST. D, E) Box plots of AOD and F, G) AE by hour of the day as measured by the AERONET instrumentation at Bondville, IL (D, F) and Dayton, OH (E, G). To ensure equal representation of data from each climatological season, 54 days (i.e. minimum retrieval days at Dayton for any season) were randomly drawn to represent each season within 09/03/2008 – 06/24/2013. Outliers (red +) lie beyond approximately +/- 2.7 σ from the mean.

Comparing average AE in the L3 product with AE derived from average AOD

The L3 AE product used in this study is calculated by averaging all L2 AE values within each 1° × 1° L3 grid cell. A more accurate representation of AE at this scale can be derived from L3 averaged aerosol optical depth (AOD) at 470 and 660 nm:

$$AE = -\frac{\ln\left(\frac{AOD_{470}}{AOD_{660}}\right)}{\ln\left(\frac{470}{660}\right)}$$

We compared the published L3 AE product with AE calculated from L3 AOD_{470} and AOD_{660} using data from MODIS Terra for 2008-2013. A least-squares linear regression fit for the two estimates of AE for the grid cells containing MMSF and Bondville have a variance explanation (r^2) of 0.34 and 0.07, respectively, but the association is improved when constraining the comparison to $0.5 \leq AE \leq 1.8$ (r^2 = 0.70 and 0.43, regression slope = 0.85 and 0.71, and intercept = 0.06 and 0.20, respectively; Figure SM2.4).

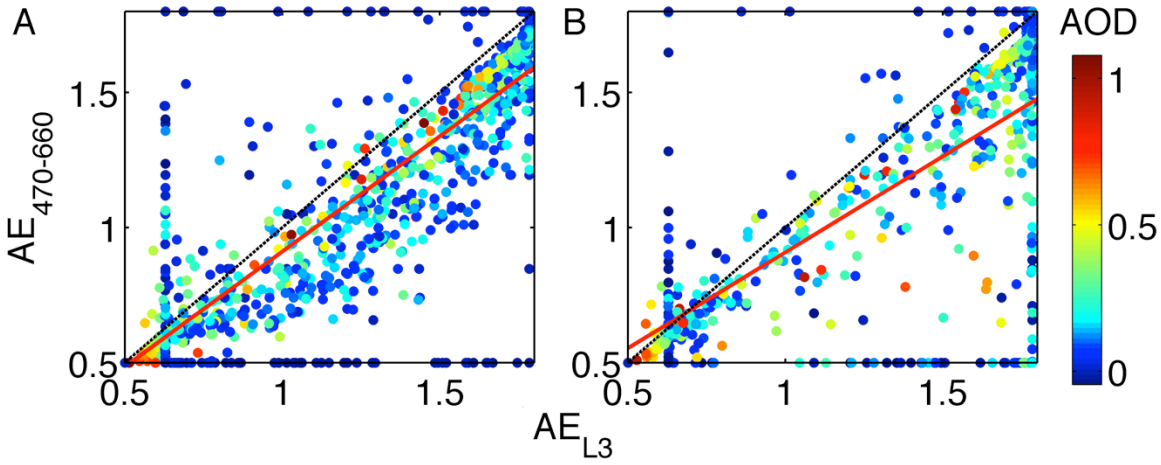

Figure SM2.4 Scatterplot of the L3 Ångström exponent (AE) value vs. AE calculated from the L3 aerosol optical depth at 0.47 μm (AOD_{470}) and 0.66 μm (AOD_{660}), colored by AOD for the grid cell containing (A) Morgan-Monroe State Forest (MMSF) and (B) Bondville. Also shown is a linear regression fit (red) and 1:1 relationship (black).

Seasonality and spatial patterns of AOD and AE from AERONET

The ability of the MODIS L3 product to capture mean and seasonal AOD and AE is assessed by comparison with the AERONET deployments within our study domain. For the study period used here (2000-2013), 111 AERONET stations had some data availability, though the length of operation and data availability varies greatly (Figure SM2.5; see AERONET website (http://aeronet.gsfc.nasa.gov/) for an exhaustive list of stations and deployment periods). Consistent with analyses of data from MODIS (Figure 2.4 and 2.5), the highest annual AOD is measured over the lower Midwest and Southeast US, the highest seasonal AOD is measured in the Southeast during the summer (Figure SM2.6), and high AE is characteristic of the eastern US (Figure SM2.7).

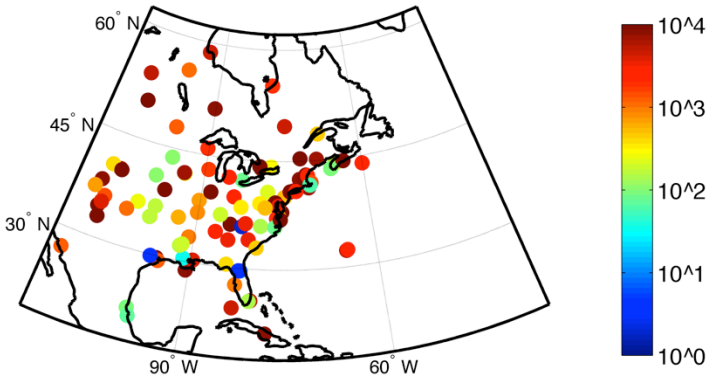

Figure SM2.5 Locations of AERONET deployments in the study domain and number of hours with at least one valid retrieval during the study period (2000-2013).

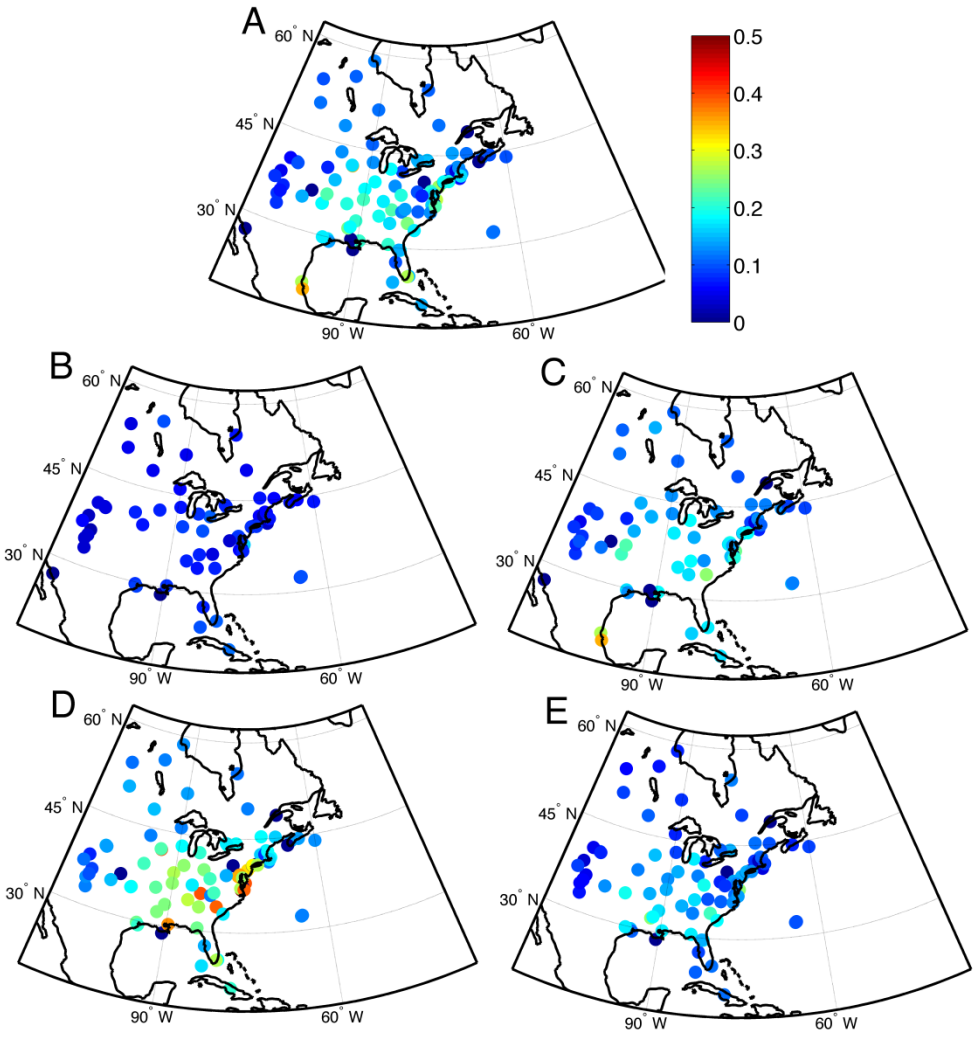

Figure SM2.6 Mean aerosol optical depth (AOD) at 0.50 μm based on observations at AERONET stations during 2000-2013. The panels show the mean AOD computed for A) All data, B) winter, C) spring, D) summer, and E) fall.

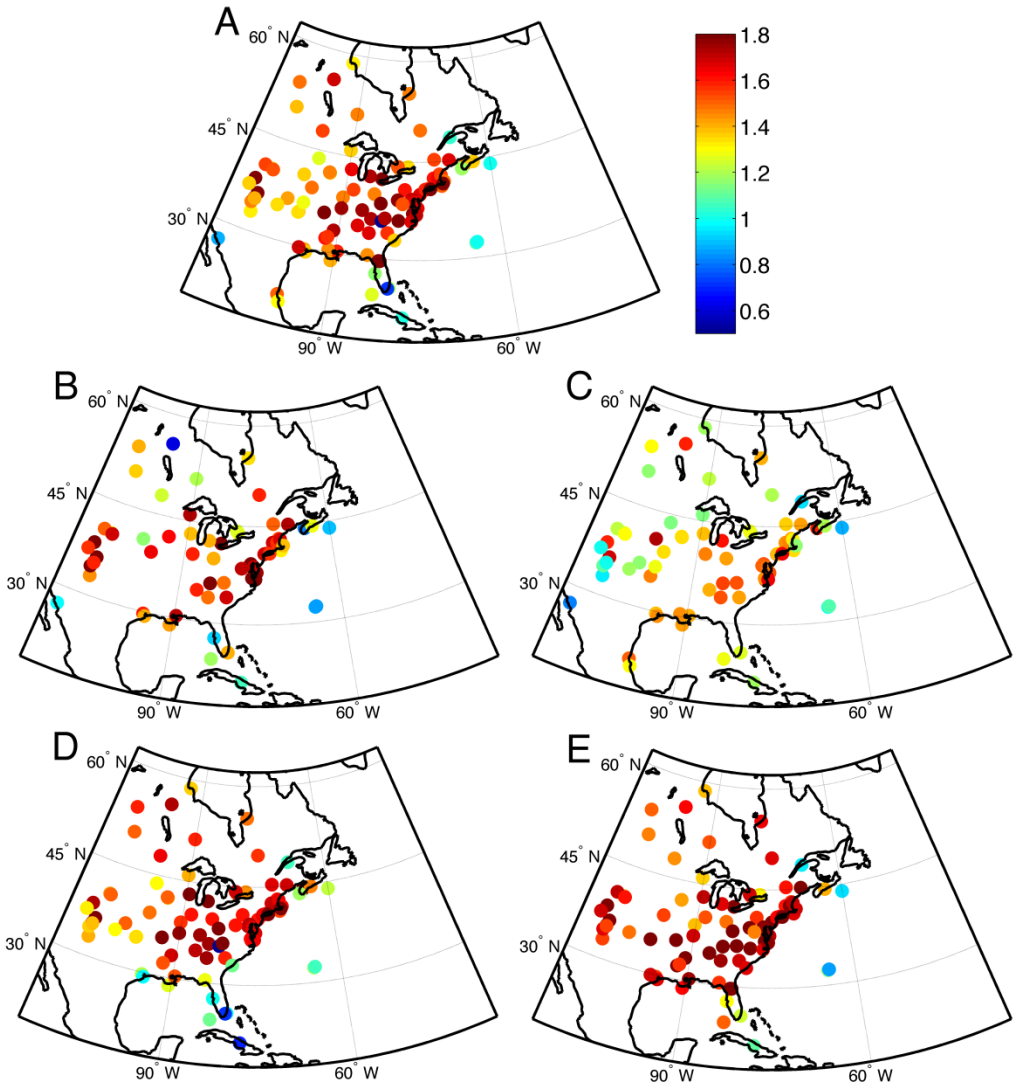

Figure SM2.7 Mean Ångström exponent (AE) at 0.44 μm – 0.675 μm based on observations at AERONET stations during 2000-2013. The panels show the mean AE computed for A) All data, B) winter, C) spring, D) summer, and E) fall.

Power spectra of AE from the L3 product and AE derived from average AOD

Although greater variance on short waveperiods (~days) is observed in the AE time series derived from AOD_{470} and AOD_{660} versus that from published L3 AE values, as with analysis of the L3 product, a variance peak at seasonal and semiannual time scales is more pronounced at Bondville than MMSF (Figure SM2.8). Thus the discrepancies in dominant time scale of variability between these two locations do not appear to be solely the result of spatial averaging of AE in the L3 data product.

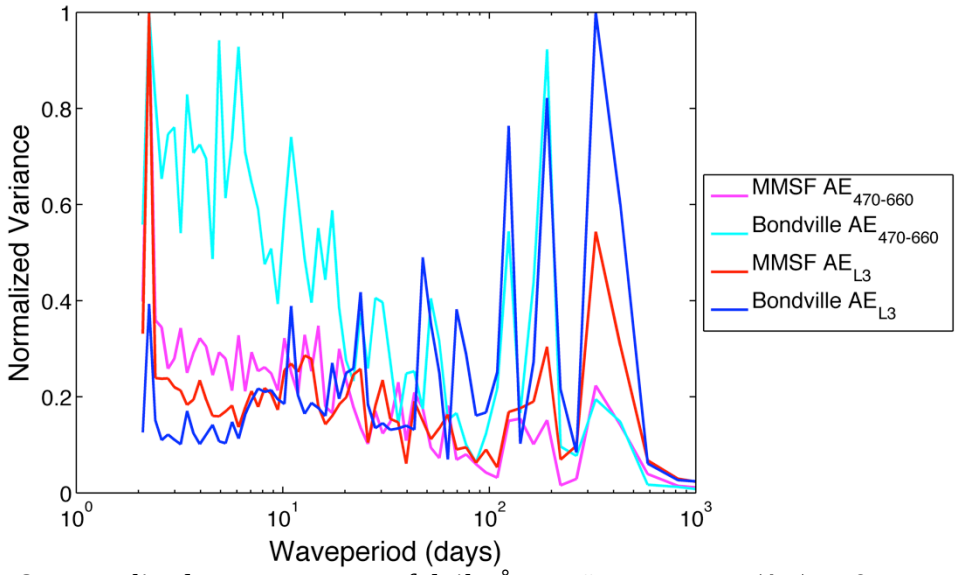

Figure SM2.8 Normalized power spectra of daily Ångström exponent (AE) at 0.47 μm – 0.65 μm calculated from L3 aerosol optical depth at 0.47 μm (AOD_{470}) and 0.66 μm (AOD_{660}) for the grid cells containing Morgan-Monroe State Forest (MMSF) and Bondville from Terra (2008-2013). The power spectra have been normalized by maximum variance at any frequency (wave period). Also shown for reference are the normalized power spectra for daily AE from the L3 product (2008-2013).

Evaluation of centroid location and spatial coherence

MMSF was selected as the reference grid cell in the analyses of spatial coherence because it is near the center of gravity of our domain and is near the center of highest annual mean surface $PM_{2.5}$ in eastern US (1998-2008) (*Tai et al.*, 2010). To test the sensitivity of the scale of coherence of aerosol columnar properties to the centroid location, an analysis was conducted in which the centroid location was moved 5° to the north, south, west, and east and the spherical distance at which the correlation coefficient for AOD dropped below an arbitrary threshold of 0.3 was computed. As shown in Figure SM2.9, the results indicate that the resulting scale of coherence is not very sensitive to the precise centroid chosen. When the reference grid cell is moved 5° from MMSF in each of the cardinal and ordinal directions, the distance where r > 0.3 extends to ~ 750 km on average. When the northern directions (i.e. N, NW, and NE), where data density is low, are ignored, the distance where r > 0.3 extends to ~ 830 km on average.

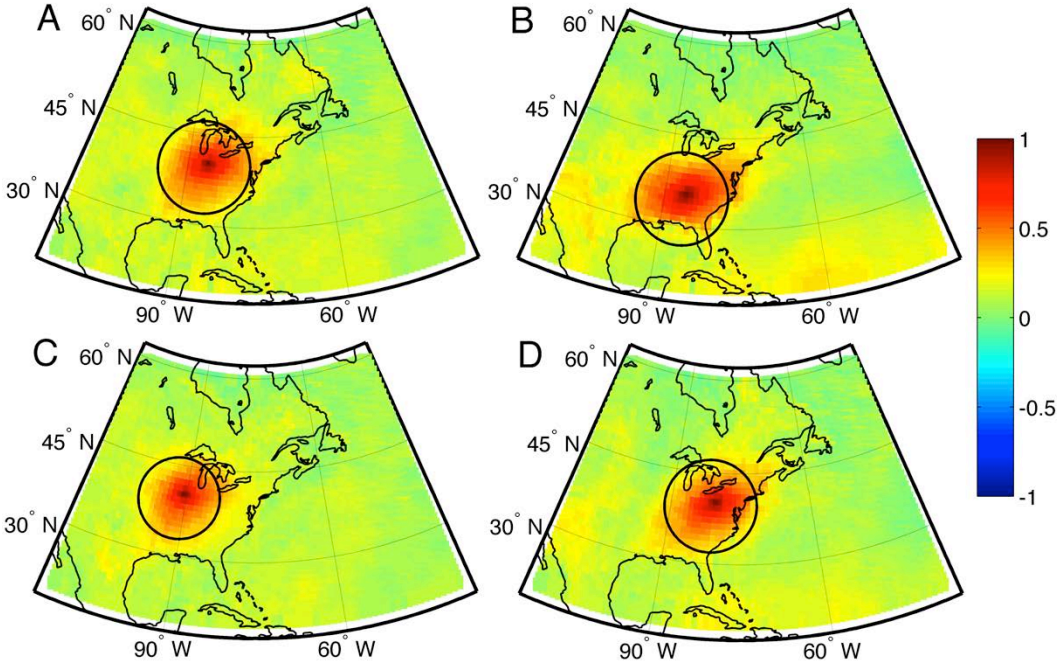

Figure SM2.9 Spatial correlation (r) of aerosol optical depth (AOD) at 0.55 μm based on a centroid located at the grid cell containing A) Morgan-Monroe State Forest (MMSF) and 5° B) south, C) west, and D) east of MMSF computed using daily data from Terra (2000-2013). The black circles represent the mean spherical distance from the centroid where r = 0.3.

CHAPTER 3

DYNAMIC AND CHEMICAL CONTROLS ON NEW PARTICLE FORMATION OCCURRENCE AND CHARACTERISTICS FROM IN SITU AND SATELLITE-BASED MEASUREMENTS

Sullivan, R. C., and S. C. Pryor (2016), Dynamic and chemical controls on new particle formation occurrence and characteristics from in situ and satellite-based measurements, *Atmos. Environ.*, *127*, 316–325, doi:10.1016/j.atmosenv.2015.12.050.

Abstract

We analyze the association between satellite-based measurements of chemical conditions (sulfur dioxide (SO_2), nitrogen dioxide (NO_2), and formaldehyde (HCHO) concentrations), insolation (UV), and aerosol particle properties (aerosol optical depth (AOD) and Ångström exponent (AE)); and the occurrence of new particle formation (NPF), formation rates (J_6), growth rates (GR), and survival probabilities (SP) using particle size distribution measurements taken during two extended field campaigns at a forested location in southern Indiana. When conditionally sampled by event occurrence and non-occurrence the satellite-derived parameters exhibit significant differences and also show some degree of skill in predicting NPF though logistic regression analysis. During leaf-on measurement periods, NPF occurrence exhibits strong seasonality (NPF is more frequent in spring vs. summer) and is associated with a low condensational sink, while leaf-off NPF occurrence is associated with high near-surface UV receipt. Multiple linear regression equations of J_6, GR, and SP using the chemical conditions as predictors exhibit some significant r^2 values ($p < 0.1$), but are relatively unstable and many of the regression coefficients do not differ significantly from zero.

Introduction

New particle formation (NPF) events enhance aerosol particle (hereafter particles) concentrations (Kulmala et al., 2004) and occur on regional scales (Crippa and Pryor, 2013). They thus have the potential to impact regional and possibly global climate (Merikanto et al., 2009). For newly formed particles (~1-3 nm) to become climate relevant, they must survive and grow to sufficient diameters to act as cloud condensation nuclei (~100 nm). NPF events have been estimated to contribute up to 50% of particles > 100 nm on a regional scale over northeastern North America (Pierce et al., 2014), but this contribution is likely to vary regionally (Kulmala et al., 2004; Westervelt et al., 2013) and such estimates are sensitive to the data analysis and model assumptions. The climate impact of NPF events is determined by factors such as the in situ particle population, frequency of NPF events, nucleation rate (i.e. how many new particles form, described here using the formation rate of 6-30 nm particles, J_6), growth rates (GRs), and survival probabilities (SPs, i.e. percentage of new particles that grow to climate relevant size). Herein we use statistical analyses of in situ and remote sensing data to diagnose the dependence of NPF occurrence, J_6, GR, and SP on parameters known, or thought, to play a key role in dictating each of those variables. These conditions are not necessarily mutually inclusive, i.e. conditions conducive to NPF event occurrence may be unfavorable for high formation rates and/or GR. For example, low condensational sink (CS) was found to be conducive to NPF occurrence and high J_6, while high CS was associated with high GR in the Yangtze River Delta in China (Qi et al., 2015). Clean air masses are also conducive to NPF in northeastern North America, but polluted air masses are associated with higher J_{10} (Pierce et al., 2014).

Specific objectives of the analyses herein are to characterize:

1. Chemical and physical regimes associated with NPF occurrence.
2. The association between different chemical regimes and J_6, GR, and SP of NPF events.

We develop a framework that can be uniformly applied to all in situ observational data sets of ultrafine particle size distributions (PSDs). As in situ trace gas measurements are not always available, we draw predictor variables from satellite-borne radiometers. It is acknowledged that these observations are associated with larger uncertainty than in situ measurements, and are typically not continuous through time. However, they provide consistent information about atmospheric composition across a range of spatial scales, and are uniformly available at least at low- and mid-latitudes. Further, they quantify columnar conditions and thus may be more strongly linked to regional-scale NPF than point measurements made at/or near the surface.

Methods

Data sets

PSD measurements used to describe the occurrence and characteristics of NPF events were taken during two extended field campaigns at a forested location in southern Indiana (in the Morgan Monroe State Forest, MMSF; 39.317°N, 86.417°W; Figure 3.1) (Pryor et al., 2014, 2010):

- Data collected during Jan. 2007 – Apr. 2009 using a Scanning Mobility Particle Sizer (SMPS comprised of an Electrostatic Classifier, nano-DMA, and Condensation Particle Counter) (Pryor et al., 2010). The measurements were taken sequentially every ~2.5 min for 10 minutes out of every half hour at 2 m, 34 m, and 46 m for a particle diameter range of 3.22 – 105.5 nm (due to low tubing penetration efficiencies, only the 81 bins > 6 nm are used here).
- Data collected during Mar. 2012 – Dec. 2013 using a TSI Fast Mobility Particle Sizer (FMPS 3091; 32 logarithmically spaced bins 6 – 520 nm) (Pryor et al., 2014). Measurements were

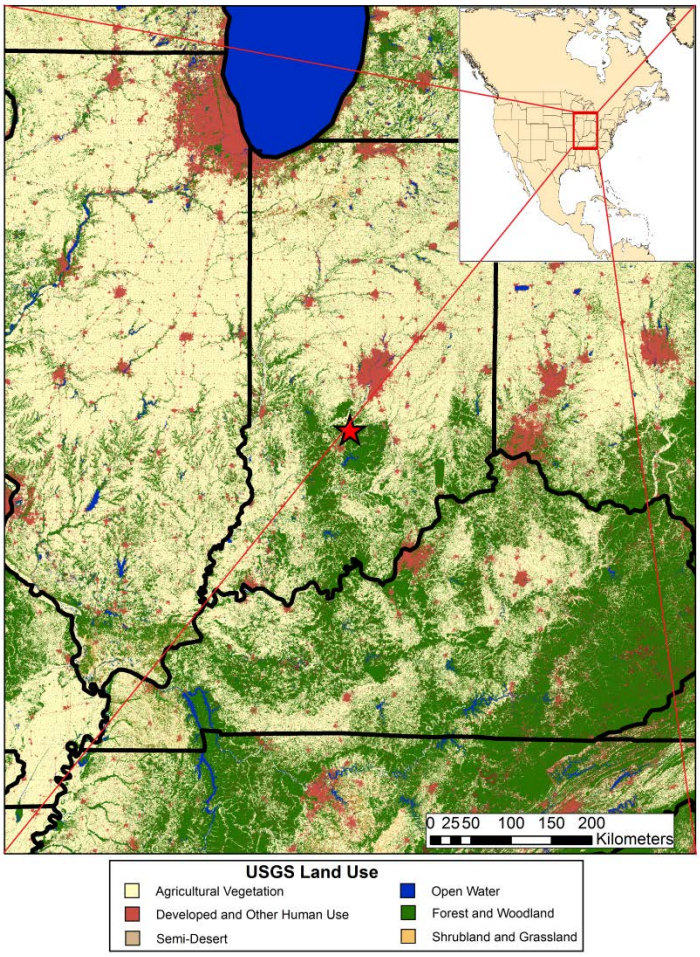

Figure 3.1. USGS land use surrounding the Morgan Monroe State Forest research site in Southern, IN (39.317°N, 86.417°W; red star) (US Geological Survey, 2011).

taken sequentially for 10 minutes out of every half hour at each of three sample heights: 12 m, 20 m, and 28 m. The FMPS reports at 1 Hz, but the data have been averaged to 2 min.

Analyses presented here employ predictands derived using PSD measurements from 34 m for 2007–2009 and 28 m for 2012–2013; both heights are above the canopy, but represent near surface concentrations.

The selection of predictor variables was based on the following reasoning:

- While uncertainty remains regarding the relative importance of different nucleation mechanisms (Boy et al., 2007) (e.g. cluster activation (Kulmala et al., 2006), kinetic (McMurry, 1980), ion mediated (Yu and Turco, 2000), binary (Jaecker-Voirol and Mirabel,

1989), or ternary nucleation (Kulmala et al., 2000)), most studies indicate a key role for sulfuric acid (H_2SO_4) with either ammonia (NH_3) or organic molecules contributing to the critical clusters (Almeida et al., 2013; O'Dowd et al., 2002; Sipilä et al., 2010). Although not uniformly observed, our further expectation is that NPF likelihood and intensity will tend to be reduced under conditions of a high CS, and that near-surface detection of NPF will be enhanced under conditions of high turbulence intensity (since there is some evidence that nucleation is concentrated aloft from the surface (Crippa et al., 2012; Pryor et al., 2011)).

- The relative contribution of different species to particle growth may vary over the course of an event. Prior research at MMSF has indicated initial particle growth is dominated by ammonium and sulfate although later growth exhibited evidence of some contribution from organics (Pryor et al., 2011). In Pittsburg H_2SO_4 also dominated formation and initial growth, followed by growth from ammonium, and organics contributing to particle growth later in the event (Zhang et al., 2004).
- A newly formed particle can grow to climate relevant size, given there are sufficient condensable vapors present and that it does not coagulate with other particles. Thus SP may be increased in conditions favorable for high GR and reduced under high CS or in conditions favorable for high J_6 and thus greater coagulation loss.

Based on the above, statistical models of NPF occurrence and properties (predictands are NPF occurrence, J_6, GR, and SP) are built using the following predictor variables:

- $LAI \times T_{max}$ (where T_{max} is the daily maximum hourly air temperature and LAI is the leaf area index as measured every sixth day at MMSF). LAI and T_{max} used here are from in situ measurements, but proxies of both (e.g. skin temperature and LAI) are available from the Moderate Resolution Imaging Spectroradiometer (MODIS)) (Huete et al., 1999; Wan, 1999).

$LAI \times T_{max}$ is used as a proxy for biogenic volatile organic compound (BVOC) emissions (Guenther et al., 1993), the oxidation products of which may be involved in nucleation and/or growth of freshly nucleated particles (Laaksonen et al., 2008). This variable is thus anticipated to have a positive association with NPF occurrence, J_6, GR, and SP.

- Formaldehyde (HCHO). Although satellite retrievals of HCHO are highly uncertain (Barkley et al., 2013), HCHO is one of very few products of VOC oxidation that is detected by satellite-borne radiometers, and while it is not directly relevant to NPF or ultrafine particle growth, satellite-derived HCHO concentrations are used as an index of the abundance of relatively low-volatility oxidized organics of both anthropogenic and biogenic origin (Chance et al., 2000; Henze and Seinfeld, 2006). Given contradictory evidence that high isoprene concentrations may either suppress (Kiendler-Scharr et al., 2009) or participate in NPF (Surratt et al., 2006) and that yields of HCHO from isoprene oxidation are non-linearly dependent on NO_x (Wolfe et al., 2015), it is difficult to assert an a priori expectation of the relationship between HCHO and NPF occurrence or intensity. Since HCHO is a product of oxidation of a wide array of VOCs and generation of less volatile products it is anticipated to have a positive association with GR and SP.
- Sulfur dioxide (SO_2). SO_2 is used here as a proxy for H_2SO_4, a key NPF precursor (Sipilä et al., 2010) and a key component of condensational growth (Pryor et al., 2011). It is thus anticipated to have a positive association with NPF occurrence, J_6, GR, and SP.
- Nitrogen dioxide (NO_2). NO_2 is used as a proxy for anthropogenic gas and particle emissions (Russell et al., 2012). Given NO_x emissions are associated with both increased CS (due to co-emitted particles) and possible enhancement of condensable vapors (e.g. collocation of NO_2 and SO_2 from major industrial complexes) it is anticipated to have a negative association

with NPF occurrence and positive association with J_6, GR, and SP.

- Ultraviolet radiation (UV). UV is used as an index of oxidant production, and is anticipated to have a positive association with NPF occurrence, J_6, GR, and SP.
- UV×SO_2 is used as a proxy for the production of H_2SO_4 from SO_2.
- Aerosol optical depth (AOD) × Ångström exponent (AE). AE $1/\propto$ particle size, and with AOD (AOD×AE) is used here to represent particle surface area and as an index of CS, and thus the competition for condensable vapors. It is therefore anticipated to have a negative association with NPF occurrence, J_6, GR, and SP.

SO_2 (column density assuming center of mass at 2.5 km), NO_2 (tropospheric column density), HCHO (total column amount), and local solar noon spectral irradiance at 310 nm (UV) are retrieved from the Ozone Monitoring Instrument (OMI) on the AURA satellite (overpass ~1345 local standard time (LST)) (Chance, 2002). All OMI data flagged as impacted by row anomalies are excluded from analyses (OMI Team, 2012) and a cloud screen of 0.3 is used to remove cloud contaminated retrievals. AOD and AE are retrieved using the 'dark-target' algorithm from MODIS on the Terra (~1030 LST) satellite (Levy et al., 2010). We use the Level 2 products at 13 km × 24 km and 10 km × 10 km at nadir for OMI (version 005) and MODIS (collection 051), respectively (see time series of the predictors in Figure 3.2).

Given NPF is frequently observed to occur on regional scales and aerosol particle optical properties are coherent on the mesoscale (Anderson et al., 2003) or regional scale (Sullivan et al., 2015), to increase the data availability all valid satellite retrievals within a 100 km radius of MMSF are averaged for each day to generate a value for each predictor. On average, ~60 and ~30 (~50) pixels within this radius are averaged for MODIS and OMI trace gases (UV), respectively. This averaging masks only moderate variability of AOD and AE as indicated by the

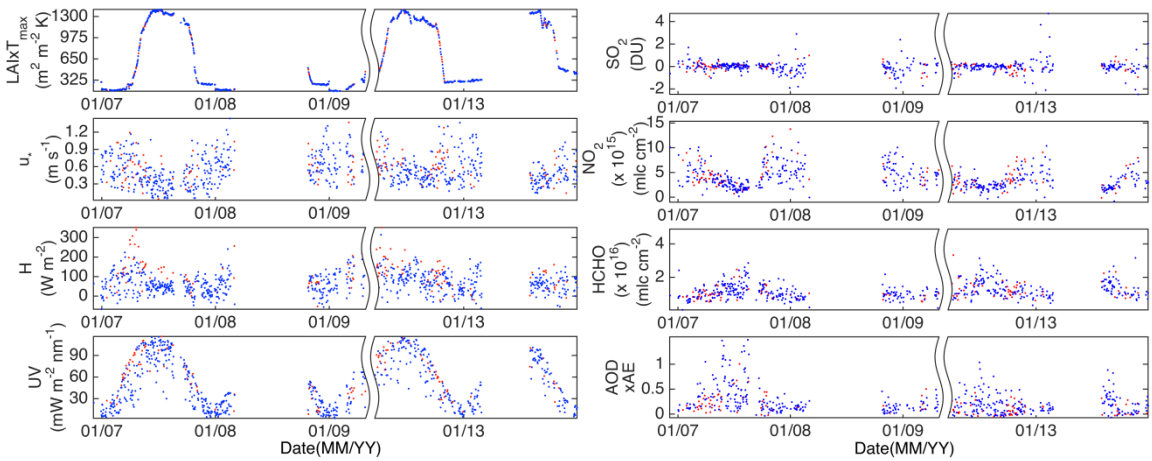

Figure 3.2. Daily biological, dynamic, radiative, chemical, and aerosol properties on days with PSD measurements (2007–2009 and 2012–2013). LAI×T_{max}, u_*, and H are from in situ measurements and UV, SO_2, NO_2, HCHO, and AOD×AE are satellite measurements from OMI and MODIS averaged over a 100 km radius around the Morgan Monroe State Forest research site (Figure 3.1). Event days are shown in red and non-event days are in blue.

mean and average standard deviation of both: <AOD> = 0.19 (σ = 0.06) and <AE> = 1.27 (σ = 0.28). UV measurements also did not vary greatly within the averaging radius (mean and average σ of 56.2 mW m^{-2} nm^{-1} and 5.9 mW m^{-2} nm^{-1}). The trace gas measurements exhibit higher heterogeneity within the averaging radius with mean (average σ) SO_2, NO_2, and HCHO of -0.03 DU (0.51 DU), 3.72×10^{15} mlc cm^{-2} (1.42×10^{15} mlc cm^{-2}), and 1.21×10^{16} mlc cm^{-2} (6.43×10^{15} mlc cm^{-2}). Negative SO_2 values are considered valid within retrieval uncertainty and highlight the challenge in observing SO_2 from satellites (e.g. due to high ozone absorption of UV) (Veefkind et al., 2011).

Although some controls of NPF vary at the synoptic scale (e.g. high near-surface UV receipt), the meteorological context for nucleation detection in the near-surface layer is likely manifest at smaller scales (Crippa et al., 2012). Thus, while dynamical conditions are also compared for event and non-events days (Table 3.1), they are not included in the regression or principal component analyses due to lack of physical interpretability of components with high weighting on variables with a large scale discrepancy (i.e. in situ turbulence measurements

Table 3.1. Median dynamic and chemical conditions measured during NPF event and non-event days (2007–2009 and 2012–2013) at MMSF. LAI×T_{max}, u_*, and H are from in situ measurements and UV, SO_2, NO_2, HCHO, and AOD×AE are satellite measurements from OMI and MODIS averaged over a 100 km radius around the research site (Figure 3.1). As events are not distributed evenly across seasons, and the mechanisms of and controls on NPF may differ across seasons (Yu et al., 2015) (Figure 3.2), leaf-on and leaf-off periods are treated independently. ***Bold*** *(Italic) values indicate rejection of the null hypothesis that event and non-event days are from the same population (Wilcoxon rank sum test α =* ***0.05*** *(0.10)). Also shown are variables with high (|loading|≥0.5) loadings on the first (single underline), second (double underline), and third (dashed underline) principal components of the PCA of the seven data-sets (negative loadings are indicated by the shading).*

			n	LAI×T_{max} ($m^2\ m^{-2}$ K)	u_* ($m\ s^{-1}$)	H ($W\ m^{-2}$)	UV ($mW\ m^{-2}\ nm^{-1}$)	SO_2 (DU)	NO_2 × 10^{15} ($mlc\ cm^{-2}$)	HCHO × 10^{16} ($mlc\ cm^{-2}$)	AOD ×AE	UV×SO_2 ($DU\ mW\ m^{-2}\ nm^{-1}$)
Leaf-on	2007 – 2009	Non-event	129	**1300**	**0.33**	**45**	88	0.047	**2.77**	1.3	*0.37*	4.8
		Event	27	**1100**	**0.48**	**120**	87	0.020	**3.64**	1.2	*0.33*	1.3
	2012 – 2013	Non-event	205	**1200**	**0.44**	**76**	83	-0.008	2.34	**1.4**	**0.19**	-0.2
		Event	53	**1100**	**0.59**	**130**	78	0.022	2.89	**1.2**	**0.06**	1.8
Leaf-off	2007 – 2009	Non-event	257	**230**	0.62	**66**	**22**	-0.115	5.10	8.9	0.13	-2.8
		Event	47	**250**	0.58	**100**	**41**	0.008	4.55	8.5	0.16	0.5
	2012 – 2013	Non-event	97	**310**	0.53	60	**22**	-0.049	3.75	*1.0*	0.11	-1.2
		Event	20	**370**	0.58	72	**35**	-0.245	5.52	*1.1*	0.14	-6.3

versus satellite derived concentrations averaged over a 100 km footprint). The physical parameters included in the analysis derive from measurements at 46 m and are:

- Friction velocity (u_*) is used as a metric of turbulent mixing, which can both initiate nucleation (Wehner et al., 2010), and is associated with eroding of the nocturnal boundary layer and entrainment of freshly nucleated particles and/or precursors (e.g. SO_2/H_2SO_4) into the near surface layer (Crippa et al., 2012; Pryor et al., 2011). It is thus anticipated to be higher on NPF event days.
- Sensible heat flux (H) is used as an index of buoyancy-driven turbulent mixing and BVOC emissions being flushed upward from the canopy. It is thus anticipated to be higher on NPF event days.

Mean u_* and H are calculated for the duration of each NPF event (defined in Sec 2.2; mean event start – end for non-event days).

Event classification, growth rates, formation rates, and survival probabilities

We use the following automated methodology to identify the occurrence of clear NPF events followed by sustained growth, and to compute the event variables (J_6, GR, and SP):

- Only measurement days with > 95% (~23 hours) of data available are included.
- The geometric mean diameter for particles < 100 nm (D_g) and for nucleation mode particles (< 30 nm; D_{gNuc}) is used to define the start of NPF when D_g-D_{gNuc} is first ≤ 10 nm within 2 hours of the maximum nucleation mode concentration, and ends when D_g-D_{gNuc} > 10 nm (Crippa and Pryor, 2013).
- J_6 is calculated as the rate change in nucleation mode particle concentration (N_{nuc}; 6 – 30 nm), corrected for particle loss to coagulation (F_{coag}) and growth (F_{growth}) (Westervelt et al., 2013):

$$J_6 = \frac{dN_{nuc}}{dt} + F_{coag} + F_{growth} \ldots (1)$$

$$\text{where } F_{coag} = \sum_{i=6\ nm}^{i=30\ nm} \left[\frac{1}{2} K(T)_{ii} N_i + \sum_{j=i+\Delta D_p}^{j=\max(D_p)} \left(K(T)_{ij} N_j\right)\right] \ldots (2),$$

$$F_{growth} = \sum_{i=6\ nm}^{i=30\ nm} \left[\frac{N_i}{30\ nm - D_{pi}} * GR\right] \ldots (3),$$

K(T) is the Fuch's form Brownian coagulation coefficient calculated using the ambient T, N_i and D_{pi} are the number concentration and median diameter of bin *i*, and ΔD_p is the bin width.

- GR is calculated using linear regression fits to the time series of D_{gNuc} for 0 – 3 hours after the event start (Pryor et al., 2014, 2010).
- All events with negative GR or J_6 were removed, as were those with duration of ≤ 1 hour.
- SP estimates are derived from the timescale for particle growth (τ^{growth}) from one bin into the next relative to the timescale for coagulation loss (τ^{coag}) to larger particles (Westervelt et al., 2013):

$$SP = \prod_{i=6\ nm}^{i=100\ nm - \Delta D_p} \exp\left(-\frac{\tau^{growth}_{D_{pi}, D_{pi+\Delta D_p}}}{\tau^{coag}_{dp_i}}\right) \ldots (4)$$

$$\tau^{growth}_{D_{pi}, D_{pi+\Delta D_p}} = \frac{(D_{pi+\Delta D_p} - D_{pi})}{GR} \ldots (5)$$

$$\tau^{coag}_{dp_i} = \frac{1}{\frac{1}{2} K(T)_{ii} N_i + \sum_{j=i+\Delta D_p}^{\max(D_p)} K(T)_{ij} N_j} \ldots (6)$$

NPF events are not distributed evenly across seasons (Figure 3.2), and the mechanisms of and controls on NPF may differ across seasons (Yu et al., 2015), thus analyses are conducted independently for leaf-on ($LAI \times T_{max} \geq 50^{th}$ percentile; ~460 $m^2\ m^{-2}\ K$) and leaf-off periods ($LAI \times T_{max} < 50^{th}$ percentile).

Although there is no significant difference in GR, estimated J_6 is significantly higher in 2007–2009 than in 2012–2013 (Figure 3.3). This difference may derive from differing

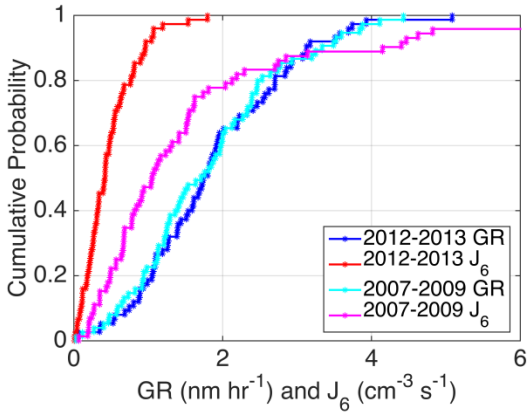

Figure 3.3. Cumulative probability plot of GR (blue/cyan) and J_6 (red/magenta) as derived from measurements with the SMPS in 2007–2009 and FMPS in 2012–2013. Systematically higher nucleation mode number concentration measured by the SMPS relative to the FMPS (Pryor et al., 2010) may explain the ~2 times higher J_6 measured in 2007–2009 relative to 2012–2013.

instrumentation, sampling protocols (e.g. tubing length and loss correction; Pryor et al., 2014, 2010), or physical causes (e.g. from the drought of 2012 (Pryor et al., 2014)). For example, although inter-comparison of the FMPS and SMPS data indicate Pearson correlation of hourly average total particle number concentration > 0.9, N_{nuc} from the SMPS was systematically higher (Pryor et al., 2010), potentially leading to higher estimated J_6. Lab inter-comparison of these instruments also indicate that, to a degree that is a function of composition, the SMPS exhibits higher modal peak concentrations and lower modal diameter than the FMPS (Hornsby and Pryor, 2014). Thus, the data sets from the two experimental campaigns are treated separately.

Statistical Methods

None of the predictor variables pass an Anderson-Darling test for normality ($\alpha = 0.05$), so the concentrations are standardized prior to regression analyses and a Wilcoxon rank sum test (Wilks, 2011) is used to test the null hypothesis that event and non-event conditions are from the

same populations and thus address Objective 1.

Event occurrence is a categorical variable, so logistic regression is employed to predict the logit (natural logarithm of the odds) of NPF event occurrence (Peng et al., 2002):

$$\ln\left(\frac{p}{1-p}\right) = \alpha + \beta_1 x_1 + \cdots + \beta_i x_i \ \ldots(7)$$

$$\text{and thus } p = \frac{e^{\alpha+\beta_1 x_1+\cdots+\beta_i x_i}}{1+e^{\alpha+\beta_1 x_1+\cdots+\beta_i x_i}} \ldots(8)$$

where p is the probability of event occurrence, α is the regression constant, and β_i is the regression coefficient for predictor variable x_i. As residual variance cannot be quantified for a binary variable, a generalized coefficient of determination (pseudo-r^2, $r_p{}^2$) is used to assess model fit (Nagelkerke, 1991):

$$r_p{}^2 = \frac{1-\left(\frac{L_I}{L_M}\right)^{\frac{2}{n}}}{1-L_I^{\frac{2}{n}}} \ldots(9)$$

where L_I is the likelihood of the null model (intercept only), L_M is the likelihood of the logistic regression model, and n is the number of observations. Goodness of fit is quantified using a likelihood ratio χ^2 test, with degrees of freedom = number of predictor variables:

$$\chi^2 = -2\ln\left[\frac{L_I}{L_M}\right] \ldots(10)$$

Multiple linear regression (MLR) analysis is used to determine the association between different chemical regimes and J_6, GR, and SP of NPF events.

Prior to conducting the regression analyses, principal component analysis (PCA) is applied to the predictor variable correlation matrices to evaluate the co-variability of the predictor variables. Since application of PCA requires a complete data set, missing observations are filled with the mean of all available measurement days (~30-35%, 15%, and 35% of days (~20-25%, 15%, and 25% of event days) are missing data from OMI (SO_2, NO_2, and HCHO),

OMI (UV), and MODIS (AOD×AE), respectively).

All predictor variables are mean centered and standardized prior to application of the PCA and regression analyses. Although not a strict requirement for use of PCA, the results are generally more robust under the condition of multivariate normality (Kim and Kim, 2012), thus HCHO and NO_2 concentrations were also log-transformed. Principal components with eigenvalues greater than one are retained (Kaiser, 1960) (i.e. the first three components) and rotated using a Varimax (orthogonal) rotation (Richman, 1986).

Results

Principal component analysis

Some degree of multicollinearity is expected amongst the predictor variables, and was diagnosed using PCA to provide context for interpretation of the regression analyses. The first three principal components explain 84% and 77% (69% and 64%), and 76% and 78% (85% and 63%) of the variability in the predictor variables in 2007–2009 events and non-events, and 2012–2013 events and non-events during leaf-on (leaf-off).

The three orthogonal modes (Table 3.1) for all data sub-sets exhibit high loadings on:

- SO_2 and UV×SO_2. This mode represents variability in the availability of SO_2 (and by association H_2SO_4), and (at least for orthogonal components) indicates this variability is decoupled from the other predictors.
- LAI×T_{max}, UV, and NO_2(-). Although it was postulated that LAI×T_{max}, UV, and NO_2 could be proxies for BVOC emissions, photochemical production of oxidants, and primary emissions, respectively, the co-variability of these predictors likely indicate their temporal variability is dominated by seasonality (with higher NO_2 in the cooler months, hence the negative weighting).

- HCHO and AOD×AE. This mode indicates co-variability of the proxy of VOC oxidation and CS, and may reflect the impact of stagnation in causing a build up of both HCHO and CS or the contribution of BVOC oxidation products to secondary organic aerosol formation (and thus increased AOD).

The three primary modes of variability (as manifest in the PCs) are very consistent between the two experimental periods, during leaf-on and leaf-off, and during NPF event and non-event days (Table 3.1). This implies that it may be possible to build more parsimonious models (using only a few of the predictors) but also that the chemical environments on event vs. non-event days are not readily differentiated.

Event versus non-event conditions

The automated event detection scheme indicates sustained NPF with clear evidence of growth (equivalent to A-class event days as defined by (Dal Maso et al., 2005)) on 16% and 20% of days with valid PSD measurements in 2007–2009 and 2012–2013, respectively. These frequencies are slightly lower than those derived using a subjective classification scheme (18% and 27%, respectively) (Pryor et al., 2014, 2010), likely due to stringent requirements for data completeness applied here to ensure the validity of calculated statistical metrics (J_6, GR, and SP).

Differences in dynamical and chemical conditions during event and non-event days are largely consistent with a priori expectations, indicate some consistency across the two experimental periods, and exhibit a clear dependence on season (leaf-on vs. leaf-off) (Figure 3.4; Table 3.1). During leaf-on periods, u_*, H, and NO_2 are significantly ($\alpha = 0.05$) (NO_2 not significant in 2012–2013) higher on NPF event days. Higher u_* and H on event days may reflect turbulent initiation of NPF, or entrainment of nucleated particles or SO_2/H_2SO_4 into the near-surface layer during destabilization of the nocturnal boundary layer (Crippa et al., 2012; Pryor et

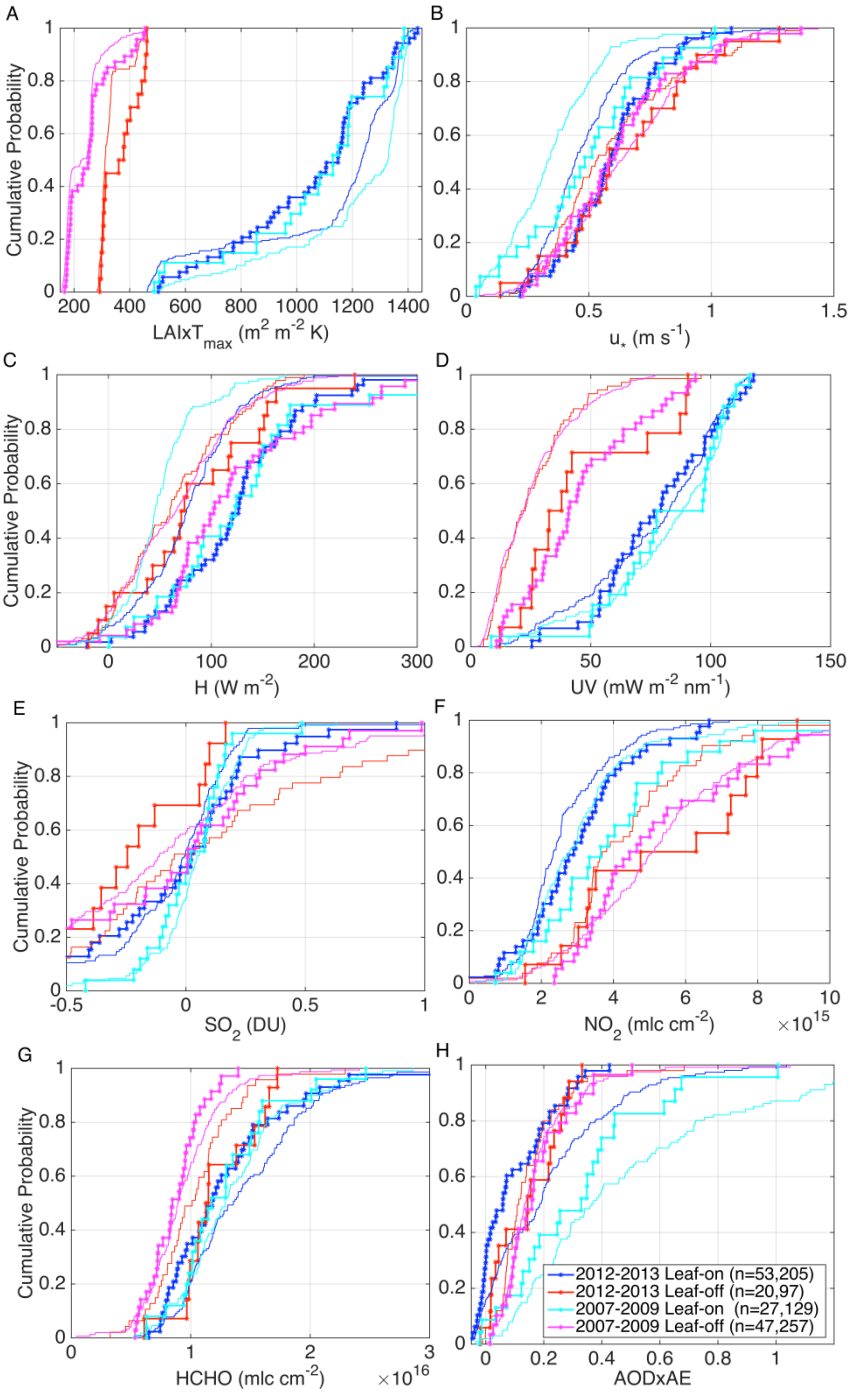

Figure 3.4. Cumulative probability plots of the predictor variables during events (starred, thick lines) and non-events (thin lines) (2007–2009 and 2012–2013). Statistical differences in event versus non-event distributions are quantified using a Wilcoxon rank sum test and presented in Table 3.1.

al., 2011; Wehner et al., 2010). Higher NO_2 on NPF event days may indicate that anthropogenic precursor emissions are more important to NPF than the associated increase in CS due to primary

particle emissions, or may be indicative of co-variability of NO_2 and the hydroxyl radical (OH). Also during the leaf-on period, LAI×T_{max}, HCHO, and AOD×AE (HCHO not significant and α = 0.1 for AOD×AE in 2007 – 2009) are significantly lower on event days. Lower LAI×T_{max} on event days is likely reflective of the higher NPF event frequency in spring than summer, while lower HCHO may reflect the role of high isoprene concentrations in reducing oxidant availability (and thus suppressing NPF) (Kiendler-Scharr et al., 2009) or the co-variability of HCHO and AOD×AE (see discussion in section 3.1). Lower AOD×AE is also observed on event days consistent with high CS inhibiting NPF. Contrary to a priori expectations, neither UV nor SO_2 differed significantly during event and non-event days in the leaf-on seasons. We postulate that the lack of difference in SO_2 concentrations may reflect the relatively high uncertainty in remotely-sensed SO_2 concentrations (or higher sensitivity to high-elevation SO_2) (OMI Team, 2012; Veefkind et al., 2011) and/or that although H_2SO_4 plays a key role in NPF (Crippa et al., 2013; Pryor et al., 2011) due to continuing very high regional emissions of SO_2 (Pryor et al., 2010) it may not be a limiting factor in southern Indiana. The lack of apparent dependence on UV receipt during the leaf-on season suggests sufficient UV may be present during this period and other predictors become more significant, or may simply reflect the confounding influence of season (with highest NPF frequency in spring, when UV receipt is comparatively low).

During leaf-off periods, significantly higher LAI×T_{max}, H, and UV occurred on event days (H not significant in 2012–2013), which may be linked to photochemical production of H_2SO_4 driving cold-season nucleation and/or the coming of spring. There were no significant differences in u_*, SO_2, NO_2, HCHO, or AOD×AE on event versus non-event days during leaf-off in both measurement periods.

Thus apart from SO_2, all of the proposed predictor variables of NPF occurrence, J_6, GR,

and SP exhibited significant differences in magnitude on event and non-event days. Hence all were included in the regression analyses.

Logistic regression equations with NPF occurrence as the predictand have a r_p^2 of 0.19 (0.19) and 0.13 (0.28) for 2007–2009 and 2012–2013 leaf-on (leaf-off), and all 4 models had χ^2 p-values < 0.01 indicating skill in predicting event occurrence over climatology (Table 3.2). Consistent with the above discussion, during leaf-on, AOD×AE has a significant (p-value < 0.1) negative regression coefficient for event occurrence, indicating increased CS suppresses NPF. LAI×T_{max} also has a negative regression coefficient, consistent with the higher event occurrence in spring than summer. The negative coefficient on SO_2, but positive coefficient on UV×SO_2 in the logistic regression models of NPF occurrence may reflect the key importance of H_2SO_4 production during transport into the region, although these variables only have significant coefficients in MLR of data from 2007-2009. During leaf-off, there is a significant positive regression coefficient on UV, supporting the postulate that production of H_2SO_4 drives cold-season nucleation occurrence.

Influence of ambient conditions on growth rates, formation rates, and survival probabilities

MLR equations for GR exhibited the lowest r^2 values (0.13 to 0.65) and also the smallest number of significant regression coefficients – with only UV exhibiting a non-zero coefficient for leaf-on during 2007-2009 (Table 3.2). MLR equations for J_6 are associated with higher r^2 values during leaf-on, but still relatively few predictors are associated with significant regression coefficients (Table 3.2). For example, the regression equation for J_6 in the leaf-on period of 2007-2009 has a significant negative weighting on HCHO and the intercept only (positive), but is associated with an r^2 of 0.52, while there are no significant regression coefficients for J_6 during leaf-on in 2012-2013. For the same experimental period, the coefficient in the equation for SP is

Table 3.2. Regression coefficients (c) and p-values for predictor variables used in the logistic (event occurrence) and multiple linear (J_6, GR, and SP) regression models. Also shown is the generalized coefficients of determination (Nagelkerke, 1991) and likelihood ratio χ^2 test p-values for the logistic regressions, and variance explained (r^2) and F-test p-values for the multiple linear regression models. ***Bold*** *indicates significant (p-value < 0.1) regression coefficients. Sample size is shown in the second column (event, non-event).*

			Event Occurrence		GR (nm h^{-1})		J_6 (cm^{-3} s-1)		SP	
Leaf-on	2007-2009 n=27, 130		c	p-value	c	p-value	c	p-value	c	p-value
		Intercept	**-1.88**	**0.00**	**2.13**	**0.00**	**4.10**	**0.00**	**0.06**	**0.00**
		$LAI \times T_{max}$ (m^2 m^{-2} K)	**-0.51**	**0.05**	-0.02	0.92	0.61	0.34	0.01	0.50
		SO_2 (DU)	**-2.76**	**0.02**	-0.38	0.63	2.53	0.31	**-0.19**	**0.01**
		NO_2 (mlc cm^{-2})	0.34	0.25	0.21	0.35	-0.68	0.32	0.01	0.74
		HCHO (mlc cm^{-2})	0.36	0.25	0.40	0.15	**-2.07**	**0.02**	**0.04**	**0.09**
		UV (mW m^{-2} nm^{-1})	0.39	0.19	**0.41**	**0.08**	-0.07	0.92	0.02	0.35
		AOD×AE	**-0.73**	**0.05**	-0.21	0.41	-0.30	0.71	-0.01	0.52
		$UV \times SO_2$ (DU mW m^{-2} nm^{-1})	**2.64**	**0.02**	0.09	0.91	-2.93	0.24	**0.14**	**0.04**
		r_p^2, r^2 (p-value)	0.19 (0.008)		0.25 (0.51)		0.52 (0.03)		0.49 (0.05)	
	2012-2013 n=55, 206		c	p-value	c	p-value	c	p-value	c	p-value
		Intercept	**-1.54**	**0.00**	**2.01**	**0.00**	**1.47**	**0.00**	**0.06**	**0.00**
		$LAI \times T_{max}$ (m^2 m^{-2} K)	**-0.35**	**0.08**	0.08	0.65	-0.06	0.72	-0.01	0.70
		SO_2 (DU)	-0.13	0.69	0.63	0.13	-0.34	0.39	**0.07**	**0.03**
		NO_2 (mlc cm^{-2})	0.16	0.40	0.06	0.73	-0.24	0.20	0.00	0.94
		HCHO (mlc cm^{-2})	0.11	0.59	0.26	0.16	0.18	0.31	0.00	0.79
		UV (mW m^{-2} nm^{-1})	0.28	0.18	0.04	0.80	-0.03	0.86	0.01	0.62
		AOD×AE	**-0.83**	**0.00**	-0.13	0.42	0.23	0.14	**-0.03**	**0.06**
		$UV \times SO_2$ (DU mW m^{-2} nm^{-1})	0.29	0.38	-0.46	0.25	0.45	0.24	**-0.07**	**0.04**
		r_p^2, r^2 (p-value)	0.13 (0.002)		0.13 (0.41)		0.23 (0.07)		0.15 (0.31)	

			Event Occurrence		GR (nm h^{-1})		J_6 (cm^{-3} s-1)		SP	
			c	p-value	c	p-value	c	p-value	c	p-value
Leaf-off	2007-2009 n=47, 256	Intercept	**-1.96**	**0.00**	**1.59**	**0.00**	**3.90**	**0.00**	**0.12**	**0.00**
		LAI×T_{max} (m^2 m^{-2} K)	-0.06	0.71	0.24	0.16	-0.88	0.22	**0.08**	**0.00**
		SO_2 (DU)	0.14	0.71	0.11	0.80	-0.12	0.95	0.06	0.29
		NO_2 (mlc cm^{-2})	0.09	0.59	-0.13	0.43	-0.76	0.29	-0.02	0.32
		HCHO (mlc cm^{-2})	-0.08	0.62	0.00	1.00	0.20	0.80	0.03	0.15
		UV (mW m^{-2} nm^{-1})	**0.93**	**0.00**	-0.26	0.15	0.93	0.21	**-0.07**	**0.00**
		AOD×AE	-0.12	0.46	0.26	0.14	-0.52	0.47	-0.01	0.66
		UV×SO_2 (DU mW m^{-2} nm^{-1})	-0.16	0.62	-0.03	0.94	0.61	0.74	-0.05	0.37
		r_p^2, r^2 (p-value)	0.19 (<0.001)		0.13 (0.55)		0.13 (0.59)		0.35 (0.01)	
	2012-2013 n=18, 96		c	p-value	c	p-value	c	p-value	c	p-value
		Intercept	**-2.08**	**0.00**	**1.47**	**0.00**	**1.03**	**0.00**	**0.05**	**0.00**
		LAI×T_{max} (m^2 m^{-2} K)	**0.54**	**0.06**	-0.03	0.87	-0.46	0.17	**0.09**	**0.00**
		SO_2 (DU)	-0.41	0.48	0.34	0.39	**1.13**	**0.10**	**-0.09**	**0.06**
		NO_2 (mlc cm^{-2})	0.55	0.14	-0.11	0.61	-0.10	0.78	-0.01	0.53
		HCHO (mlc cm^{-2})	0.37	0.29	0.13	0.50	-0.26	0.40	0.03	0.18
		UV (mW m^{-2} nm^{-1})	**0.84**	**0.01**	0.13	0.61	**0.83**	**0.07**	**-0.07**	**0.02**
		AOD×AE	-0.29	0.35	0.35	0.13	-0.15	0.67	**0.06**	**0.02**
		UV×SO_2 (DU mW m^{-2} nm^{-1})	0.01	0.98	-0.33	0.35	**-1.55**	**0.02**	**0.10**	**0.02**
		r_p^2, r^2 (p-value)	0.28 (0.005)		0.65 (0.08)		0.67 (0.07)		0.75 (0.02)	

significant and positive on HCHO which may reflect the covariation of HCHO and AOD×AE manifest in the PCA, and thus that HCHO is reflecting increased CS and suppression of J_6 due to competition for the low volatility vapors, and that the particles that do form have higher SP due to lower Aitken mode number concentrations (e.g. less self coagulation and/or competition for condensable vapors with other newly formed particles). SO_2 and UV×SO_2 have significant

regression coefficients for equations for SP during both leaf-on experiments and leaf-off in 2012-2013, but the signs are not consistent (positive (negative) for SO_2 ($UV \times SO_2$) for 2007-2009 leaf-on and 2012-2013 leaf-off, but negative (positive) for 2012-2013 leaf-on) making interpretation challenging.

Discussion and concluding remarks

PSD measurements made in a deciduous forest in the Midwestern USA in 2007–2009 and 2012–2013 are used to detect NPF and characterize those events (J_6, GR, and SP). The resulting data sets are then used to determine the degree to which those variables can be 'predicted' using in situ measurements of atmospheric dynamics and satellite-based measurements of atmospheric composition. Previous work has indicated some potential for using of satellite-driven proxy algorithms for daily nucleation mode particle concentrations (Kulmala et al., 2011) and/or ultrafine particle concentrations (Crippa et al., 2013). Results presented herein indicate that many of the proposed predictor variables: $LAI \times T_{max}$, NO_2, HCHO, UV, AOD×AE, and $UV \times SO_2$ exhibit different median values when conditionally sampled by event versus non-event days (Table 3.1), and exhibit some skill (as measured by r^2 values of regression equations, Table 3.2) in predicting event occurrence (by logistic regression) and the magnitudes of J_6, GR, and SP. However, the regression coefficients are relatively unstable (i.e. some differ in sign between the two experimental periods) and generally do not differ significantly from zero, indicating only modest explanation of the variability of NPF characteristics. The generalizability of these findings merits further investigation, as do possible causes of these results which include: (i) decoupling of columnar gas concentrations from those at the surface where the PSD measurements are made, (ii) the relatively large uncertainty in the satellite measurements, (iii) the spatial averaging used (approx. 100 km, necessitated by the relatively low numbers of

satellite retrievals in the pixel containing the measurement site), (iv) selection of inappropriate or inadequate predictor variables (e.g. NH_3 is key to NPF, but only measured ~weekly from the Tropospheric Emission Spectrometer (TES), and key gases (e.g. H_2SO_4) are present at low concentrations and/or characterized by absorption bands that are not unique), (v) relatively small sample size of event days, and/or (vi) although NPF occurs on regional scales, event metrics (J_6, GR, and SP) may exhibit heterogeneity on finer scales.

Acknowledgements

This work was supported under the NASA Earth and Space Science Fellowship Program - Grant "14-EARTH14F-0207" and a grant to SCP from NSF (1102309, 1517365). The satellite data used in this study were acquired as part of the NASA Earth-Sun System Division and Science Mission Directorate, and archived and distributed by the MODIS Level 1 and Atmosphere Archive and Distribution System and by the Goddard Earth Sciences Data and Information Services Center. The authors acknowledge K. Novick for maintaining the MMSF AmeriFlux site.

REFERENCES

Almeida, J., Schobesberger, S., Kürten, A., Ortega, I.K., Kupiainen-Määttä, O., Praplan, A.P., Adamov, A., Amorim, A., Bianchi, F., Breitenlechner, M., 2013. Molecular understanding of sulphuric acid-amine particle nucleation in the atmosphere. Nature 502, 359–363.

Anderson, T.L., Charlson, R.J., Winker, D.M., Ogren, J.A., Holmén, K., 2003. Mesoscale Variations of Tropospheric Aerosols*. J. Atmos. Sci. 60, 119–136.

Barkley, M.P., Smedt, I. De, Van Roozendael, M., Kurosu, T.P., Chance, K., Arneth, A., Hagberg, D., Guenther, A., Paulot, F., Marais, E., 2013. Top-down isoprene emissions over tropical South America inferred from SCIAMACHY and OMI formaldehyde columns. J. Geophys. Res. Atmos. 118, 6849–6868.

Boy, M., Bonn, B., Kazil, J., Lovejoy, N., Turnipseed, A., Greenberg, J., Karl, T., Mauldin, L., Kusciuch, E., Smith, J., 2007. Relevance of several nucleation theories in different environments, in: Nucleation and Atmospheric Aerosols. Springer, pp. 87–91.

Chance, K., 2002. OMI algorithm theoretical basis document, volume IV: OMI trace gas algorithms. Available at http://eospso.gsfc.nasa.gov/sites/default/files/atbd/ATBD-OMI-04.pdf.

Chance, K., Palmer, P.I., Spurr, R.J.D., Martin, R. V, Kurosu, T.P., Jacob, D.J., 2000. Satellite observations of formaldehyde over North America from GOME. Geophys. Res. Lett. 27, 3461–3464.

Crippa, P., Petäjä, T., Korhonen, H., Afandi, Gse., Pryor, S.C., 2012. Evidence of an elevated source of nucleation based on model simulations and data from the NIFTy experiment. Atmos. Chem. Phys. 12, 8021–8036. doi:10.5194/acp-12-8021-2012

Crippa, P., Pryor, S.C., 2013. Spatial and temporal scales of new particle formation events in eastern North America. Atmos. Environ. 75, 257–264. doi:10.1016/j.atmosenv.2013.04.051

Crippa, P., Spracklen, D., Pryor, S.C., 2013. Satellite-derived estimates of ultrafine particle concentrations over eastern North America. J. Geophys. Res. Atmos. 118, 9968–9981. doi:10.1002/jgrd.50707

Dal Maso, M., Kulmala, M., Riipinen, I., Wagner, R., Hussein, T., Aalto, P.P., Lehtinen, K.E.J., 2005. Formation and growth of fresh atmospheric aerosols: eight years of aerosol size distribution data from SMEAR II, Hyytiala, Finland. Boreal Environ. Res. 10, 323–336.

Guenther, A.B., Zimmerman, P.R., Harley, P.C., Monson, R.K., Fall, R., 1993. Isoprene and monoterpene emission rate variability: model evaluations and sensitivity analyses. J. Geophys. Res. Atmos. 98, 12609–12617.

Henze, D.K., Seinfeld, J.H., 2006. Global secondary organic aerosol from isoprene oxidation. Geophys. Res. Lett. 33. doi:10.1029/2006GL025976

Hornsby, K.E., Pryor, S.C., 2014. A laboratory comparison of real-time measurement methods for 10–100-nm particle size distributions. Aerosol Sci. Technol. 48, 571–582.

Huete, A., Justice, C., Van Leeuwen, W., 1999. MODIS vegetation index (MOD13). Algorithm Theor. basis Doc. Available http//modis.gsfc.nasa.gov/data/atbd/atbd_mod13.pdf.

Jaecker-Voirol, A., Mirabel, P., 1989. Heteromolecular nucleation in the sulfuric acid-water system. Atmos. Environ. 23, 2053–2057.

Kaiser, H.F., 1960. The application of electronic computers to factor analysis. Educ. Psychol. Meas. 141–151.

Kiendler-Scharr, A., Wildt, J., Dal Maso, M., Hohaus, T., Kleist, E., Mentel, T.F., Tillmann, R., Uerlings, R., Schurr, U., Wahner, A., 2009. New particle formation in forests inhibited by isoprene emissions. Nature 461, 381–384.

Kim, D., Kim, S.-K., 2012. Comparing patterns of component loadings: Principal Component Analysis (PCA) versus Independent Component Analysis (ICA) in analyzing multivariate non-normal data. Behav. Res. Methods 44, 1239–1243.

Kulmala, M., Arola, A., Nieminen, T., Riuttanen, L., Sogacheva, L., Leeuw, G. de, Kerminen, V.-M., Lehtinen, K.E.J., 2011. The first estimates of global nucleation mode aerosol concentrations based on satellite measurements. Atmos. Chem. Phys. 11, 10791–10801.

Kulmala, M., Lehtinen, K.E.J., Laaksonen, A., 2006. Cluster activation theory as an explanation of the linear dependence between formation rate of 3nm particles and sulphuric acid concentration. Atmos. Chem. Phys. 6, 787–793.

Kulmala, M., Pirjola, L., Mäkelä, J.M., 2000. Stable sulphate clusters as a source of new atmospheric particles. Nature 404, 66–69.

Kulmala, M., Vehkamäki, H., Petäjä, T., Dal Maso, M., Lauri, A., Kerminen, V.-M., Birmili, W., McMurry, P.H., 2004. Formation and growth rates of ultrafine atmospheric particles: a review of observations. J. Aerosol Sci. 35, 143–176.

Laaksonen, A., Kulmala, M., O'Dowd, C.D., Joutsensaari, J., Vaattovaara, P., Mikkonen, S., Lehtinen, K.E.J., Sogacheva, L., Maso, M.D., Aalto, P., 2008. The role of VOC oxidation products in continental new particle formation. Atmos. Chem. Phys. 8, 2657–2665.

Levy, R.C., Remer, L.A., Kleidman, R.G., Mattoo, S., Ichoku, C., Kahn, R., Eck, T.F., 2010. Global evaluation of the Collection 5 MODIS dark-target aerosol products over land. Atmos. Chem. Phys. 10, 10399–10420.

McMurry, P.H., 1980. Photochemical aerosol formation from SO_2: A theoretical analysis of smog chamber data. J. Colloid Interface Sci. 78, 513–527.

Merikanto, J., Spracklen, D. V, Mann, G.W., Pickering, S.J., Carslaw, K.S., 2009. Impact of nucleation on global CCN. Atmos. Chem. Phys. 9, 8601–8616.

Metzger, A., Verheggen, B., Dommen, J., Duplissy, J., Prevot, A.S.H., Weingartner, E., Riipinen, I., Kulmala, M., Spracklen, D. V, Carslaw, K.S., 2010. Evidence for the role of organics in aerosol particle formation under atmospheric conditions. Proc. Natl. Acad. Sci. 107, 6646–6651.

Nagelkerke, N.J.D., 1991. A note on a general definition of the coefficient of determination. Biometrika 78, 691–692.

O'Dowd, C.D., Aalto, P., Hmeri, K., Kulmala, M., Hoffmann, T., 2002. Aerosol formation: Atmospheric particles from organic vapours. Nature 416, 497–498.

OMI Team, 2012. Ozone monitoring instrument (OMI) data user's guide. OMI-DUG-5.0. Available at: http://disc.sci.gsfc.nasa.gov/Aura/data-holdings/additional/documentation/README.OMI_DUG.pdf.

Peng, C.-Y.J., Lee, K.L., Ingersoll, G.M., 2002. An introduction to logistic regression analysis and reporting. J. Educ. Res. 96, 3–14.

Pierce, J.R., Westervelt, D.M., Atwood, S.A., Barnes, E.A., Leaitch, W.R., 2014. New-particle formation, growth and climate-relevant particle production in Egbert, Canada: analysis from 1 year of size-distribution observations. Atmos. Chem. Phys. 14, 8647–8663.

Pryor, S.C., Barthelmie, R.J., Sørensen, L.L., McGrath, J.G., Hopke, P., Petäjä, T., 2011. Spatial and vertical extent of nucleation events in the Midwestern USA: insights from the

Nucleation In ForesTs (NIFTy) experiment. Atmos. Chem. Phys. 11, 1641–1657. doi:10.5194/acp-11-1641-2011
Pryor, S.C., Hornsby, K.E., Novick, K.A., 2014. Forest canopy interactions with nucleation mode particles. Atmos. Chem. Phys. 14, 11985–11996. doi:10.5194/acp-14-11985-2014
Pryor, S.C., Spaulding, A.M., Barthelmie, R.J., 2010. New particle formation in the Midwestern USA: Event characteristics, meteorological context and vertical profiles. Atmos. Environ. 44, 4413–4425. doi:10.1016/j.atmosenv.2010.07.045
Qi, X.M., Ding, A.J., Nie, W., Petäjä, T., Kerminen, V.-M., Herrmann, E., Xie, Y.N., Zheng, L.F., Manninen, H., Aalto, P., 2015. Aerosol size distribution and new particle formation in the western Yangtze River Delta of China: 2 years of measurements at the SORPES station. Atmos. Chem. Phys. 15, 12445-12464.
Richman, M., 1986. Rotation of principal components. J. Climatol. 6, 293–335.
Russell, A.R., Valin, L.C., Cohen, R.C., 2012. Trends in OMI NO_2 observations over the United States: effects of emission control technology and the economic recession. Atmos. Chem. Phys. 12, 12197–12209.
Sipilä, M., Berndt, T., Petäjä, T., Brus, D., Vanhanen, J., Stratmann, F., Patokoski, J., Mauldin, R.L., Hyvärinen, A.-P., Lihavainen, H., 2010. The role of sulfuric acid in atmospheric nucleation. Science 327, 1243–1246.
Sullivan, R.C., Levy, R.C., Pryor, S.C., 2015. Spatiotemporal coherence of mean and extreme aerosol particle events over eastern North America as observed from satellite. Atmos. Environ. 112, 126–135. doi:10.1016/j.atmosenv.2015.04.026
Surratt, J.D., Murphy, S.M., Kroll, J.H., Ng, N.L., Hildebrandt, L., Sorooshian, A., Szmigielski, R., Vermeylen, R., Maenhaut, W., Claeys, M., 2006. Chemical composition of secondary organic aerosol formed from the photooxidation of isoprene. J. Phys. Chem. A 110, 9665–9690.
US Geological Survey, 2011. Gap Analysis Program (GAP) National Land Cover, Version 2.
Veefkind, J.P., Boersma, K.F., Wang, J., Kurosu, T.P., Krotkov, N., Chance, K., Levelt, P.F., 2011. Global satellite analysis of the relation between aerosols and short-lived trace gases. Atmos. Chem. Phys. 11, 1255–1267.
Wan, Z., 1999. MODIS land-surface temperature algorithm theoretical basis document. MODIS Land-surface Temp. Algorithm Theor. Basis Doc. (LST ATBD). Available http//modis.gsfc.nasa.gov/data/atbd/atbd_mod11.pdf.
Wehner, B., Siebert, H., Ansmann, A., Ditas, F., Seifert, P., Stratmann, F., Wiedensohler, A., Apituley, A., Shaw, R.A., Manninen, H.E., 2010. Observations of turbulence-induced new particle formation in the residual layer. Atmos. Chem. Phys. 10, 4319–4330.
Westervelt, D.M., Pierce, J.R., Riipinen, I., Trivitayanurak, W., Hamed, A., Kulmala, M., Laaksonen, A., Decesari, S., Adams, P.J., 2013. Formation and growth of nucleated particles into cloud condensation nuclei: model–measurement comparison. Atmos. Chem. Phys. 13, 7645–7663.
Wilks, D.S., 2011. Statistical methods in the atmospheric sciences. Academic press.
Wolfe, G.M., Kaiser, J., Hanisco, T.F., Keutsch, F.N., de Gouw, J.A., Gilman, J.B., Graus, M., Hatch, C.D., Holloway, J., Horowitz, L.W., 2015. Formaldehyde production from isoprene oxidation across NO_x regimes. Atmos. Chem. Phys. Discuss. 15, 31587–31620.
Yu, F., Luo, G., Pryor, S.C., Pillai, P.R., Lee, S.H., Ortega, J., Schwab, J.J., Hallar, A.G., Leaitch, W.R., Aneja, V.P., Smith, J.N., Walker, J.T., Hogrefe, O., Demerjian, K.L., 2015. Spring and summer contrast in new particle formation over nine forest areas in North

America. Atmos. Chem. Phys. Discuss. 15, 21271–21298. doi:10.5194/acpd-15-21271-2015
Yu, F., Turco, R.P., 2000. Ultrafine aerosol formation via ion-mediated nucleation. Geophys. Res. Lett. 27, 883–886.
Zhang, Q.I., Stanier, C.O., Canagaratna, M.R., Jayne, J.T., Worsnop, D.R., Pandis, S.N., Jimenez, J.L., 2004. Insights into the chemistry of new particle formation and growth events in Pittsburgh based on aerosol mass spectrometry. Environ. Sci. Technol. 38, 4797–4809.

CHAPTER 4

USING SATELLITE-BASED MEASUREMENTS TO EXPLORE SPATIOTEMPORAL SCALES AND VARIABILITY OF DRIVERS OF NEW PARTICLE FORMATION

Sullivan, R. C., P. Crippa, A. G. Hallar, L. Clarisse, S. Whitburn, M. Van Damme, W. R. Leaitch, J. T. Walker, A. Khlystov, and S. C. Pryor (2016), Using satellite-based measurements to explore spatiotemporal scales and variability of drivers of new particle formation, *J. Geophys. Res. Atmos.*, *121*(12), 12217–12235.

Abstract

New particle formation (NPF) can potentially alter regional climate by increasing aerosol particle (hereafter particle) number concentrations and ultimately cloud condensation nuclei. The large scales on which NPF is manifest indicate potential to use satellite-based (inherently spatially averaged) measurements of atmospheric conditions to diagnose the occurrence of NPF and NPF characteristics. We demonstrate the potential for using satellite-based measurements of insolation (UV), trace gas concentrations (sulfur dioxide (SO_2), nitrogen dioxide (NO_2), ammonia (NH_3), formaldehyde (HCHO), ozone (O_3)), aerosol optical properties (aerosol optical depth (AOD), Ångström exponent (AE)), and a proxy of biogenic volatile organic compound emissions (leaf area index (LAI), temperature (T)) as predictors for NPF characteristics: formation rates, growth rates, survival probabilities, and ultrafine particle (UFP) concentrations at five locations across North America. NPF at all sites is most frequent in spring, exhibits a one-day autocorrelation, and is associated with low condensational sink (AOD×AE) and HCHO concentrations, and high UV. However, there are important site-to-site variations in NPF frequency and characteristics, and in which of the predictor variables (particularly gas concentrations) significantly contribute to the explanatory power of regression models built to predict those characteristics. This finding may provide a partial explanation for the reported

spatial variability in skill of simple generalized nucleation schemes in reproducing observed NPF. In contrast to more simple proxies developed in prior studies (e.g. based on AOD, AE, SO_2, UV), use of additional predictors (NO_2, NH_3, HCHO, LAI, T, O_3) increases the explained temporal variance of UFP concentrations at all sites.

Introduction and motivation

New particle formation (NPF) events generate large concentrations of ultrafine particles (UFP; particle diameter (Dp) < 100 nm), often occur on regional scales, and exhibit high temporal autocorrelation (multi-day persistence) [*Hussein et al.*, 2009; *Jeong et al.*, 2010; *Crippa and Pryor*, 2013]. Therefore NPF may substantially increase the concentration of particles with Dp ≥ 100 nm and cloud condensation nuclei (CCN) [*Spracklen et al.*, 2008b; *Merikanto et al.*, 2009; *Yu and Luo*, 2009; *Pierce et al.*, 2012, 2014], and thus impact regional climates [*Spracklen et al.*, 2008a; *Paasonen et al.*, 2013]. However, the magnitude of this effect remains uncertain [*Carslaw et al.*, 2013].

Although the precise atmospheric conditions conducive to NPF are not fully understood [*Boy et al.*, 2007] and may vary in space and time [*Kulmala et al.*, 2004; *Yu and Luo*, 2009; *Westervelt et al.*, 2013; *Yu and Hallar*, 2014; *Yu et al.*, 2015], most observational studies are consistent with ternary nucleation involving sulfuric acid (H_2SO_4), water vapor, and some other low-volatility and/or stabilizing condensable species (e.g. oxidation products of biogenic volatile organic compounds (BVOCs) or ammonia (NH_3)) [*Kulmala et al.*, 2000; *Metzger et al.*, 2010; *Sipilä et al.*, 2010; *Zhang et al.*, 2010; *Kirkby et al.*, 2011; *Pryor et al.*, 2011; *Riccobono et al.*, 2014]. Further, the intensity and probability of NPF appears to be positively associated with high insolation and a reduction of the condensational sink (CS) (and thus competition for semi-volatile species) [*O'Dowd et al.*, 2002; *Zhang et al.*, 2004a; *Sipilä et al.*, 2010; *Pryor et al.*,

2011; *Almeida et al.*, 2013; *Pierce et al.*, 2014]. In situ studies indicate that although initial growth of the recently nucleated particles is largely due to coagulation and condensation of the nucleating gases, growth beyond diameters of 10's nm may exhibit an increased contribution from condensation of semi-volatile, low-volatility, and extremely low volatility organic gases [*Zhang et al.*, 2004a; *Smith et al.*, 2005, 2008; *Knol et al.*, 2009; *Pryor et al.*, 2011; *Pierce et al.*, 2012; *Yu and Hallar*, 2014; *Jokinen et al.*, 2015]. These commonalities coupled with the occurrence of NPF on regional scales has led to suggestions that nucleation mode and UFP concentrations can be predicted using satellite-based, and thus spatially averaged, atmospheric properties such as: accumulation mode particle properties (aerosol optical depth (AOD) and Ångström exponent (AE)), trace gas concentrations (sulfur dioxide (SO_2) and nitrogen dioxide (NO_2)), and ultra-violet irradiance (UV) [*Kulmala et al.*, 2011; *Crippa et al.*, 2013; *Sundström et al.*, 2015]. More recent work at a single site in the Midwestern USA indicated potential to diagnose not only the total UFP concentrations from remote sensing observations, but also the probability of NPF and descriptors of NPF events: particle formation rates (J_n, where 'n' is determined by the minimum detectable particle diameter for each instrument), growth rates (GR), and survival probabilities (SP) [*Sullivan and Pryor*, 2016].

Based on this prior research, we postulate that satellite-derived observations of key properties known, or theorized, to determine the frequency and temporal persistence of NPF, J_n, GR, SP, and UFP concentrations ($N_{n\text{-}100nm}$), may also be used diagnostically to explain some of the observed spatial variability in these characteristics of NPF [*Pierce et al.*, 2014; *Qi et al.*, 2015; *Rose et al.*, 2015], and reported variations in the closure between models based on simplified nucleation schemes (with fixed nucleation rate coefficients) and observations [*Spracklen et al.*, 2008b; *Zhang et al.*, 2010; *Lee et al.*, 2013]. Given the likely impact of NPF on

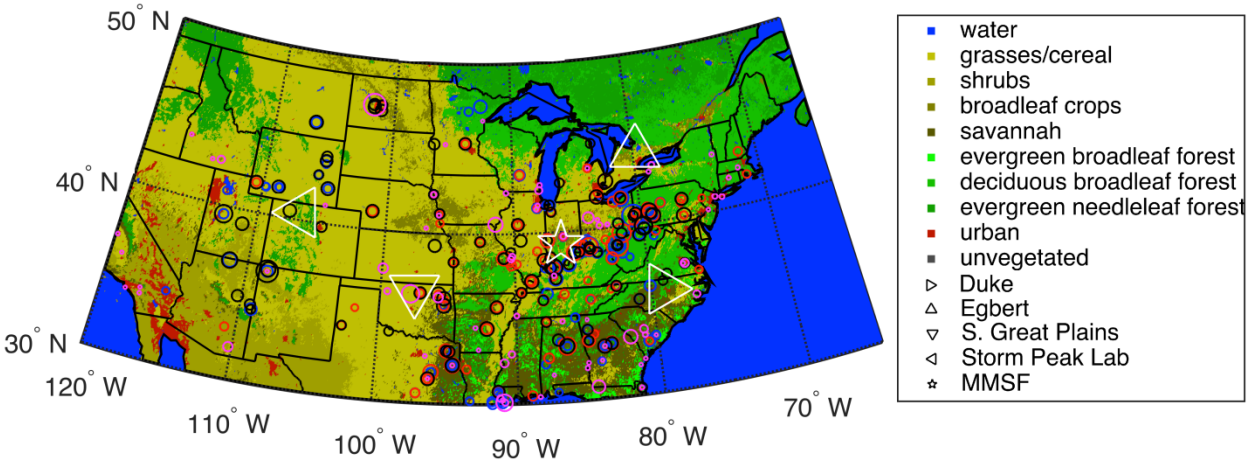

Figure 4.1. Locations at which the particle size distribution measurements analyzed herein were taken (see Table 4.1 for details). Background denotes the land cover classification from the MODIS combined Terra and Aqua dataset using the LAI/FPAR scheme (type 3) for 2012 [Land Processes Distributed Active Archive Center (LP DAAC), 2014]. Overlaid circles are the 100 largest point source emissions for $PM_{2.5}$ (blue), SO_2 (red), NO_x (black), and NH_3 (magenta) from the EPA 2011 National Emissions Inventory [US Environmental Protection Agency, 2011], arbitrarily scaled as a fraction of the largest single emission source for each pollutant. Note, point sources do not clearly reflect the spatial patterns of NH_3 emissions from animal and fertilizer sources. Annual mean particle and trace gas concentrations from the satellite measurements used here are shown in Figure S4.1.

climate, and substantial uncertainty and model-to-model variability in simulating NPF, improved treatment of NPF in global models is critical for improved understanding of aerosol-climate impacts. Herein we use in situ particle size distribution (PSD) measurements from five sites distributed across North America (Figure 4.1; Table 4.1) to address the following research questions:

1) Can satellite-based measurements of parameters known to be important to NPF and subsequent growth (or proxies for those variables) be used to explain site-to-site variations in NPF frequency and one-day autocorrelation? For example, is there a relationship between the inherent spatial scales of coherence of the satellite-based measurements of the drivers of NPF and the one-day autocorrelation in NPF occurrence, and if so which one of the drivers appears to limit the persistence of NPF?

2) Do satellite-based observations offer insights into the causes of variability in NPF

Table 4.1. Description of particle size distribution measurement sites and instrumentation. Locations of the sites relative to land use and point source emissions are given in Figure 4.1.

Site	Location	Elevation (m)	Dates	Instrument[a]	Dp range	Bins	Reference
Duke Forest, NC	35.98 N 79.09 W	179	11/2005 - 09/2007	SMPS	7 - 289 nm	103	[*Pillai et al.*, 2013]
Egbert, ON, CAN	44.23 N 79.78 W	251	05/2007 - 05/2008	SMPS	11 - 398 nm	26	[*Pierce et al.*, 2014]
Southern Great Plains, OK (SGP)	36.61 N 97.49 W	312	01/2010 - 11/2014	TDMA	12 nm – 15 μm	207	[*Ackerman and Stokes*, 2003][b]
Storm Peak Laboratory, CO (SPL)	40.46 N 106.74 W	3210	03/2012 - 07/2014	SMPS	9 – 346 nm	104	[*Hallar et al.*, 2011, 2016]
Morgan Monroe State Forest, IN (MMSFa)	39.32 N 86.42 W	275	01/2007 - 03/2009	SMPS	6 - 100 nm	81	[*Pryor et al.*, 2010]
Morgan Monroe State Forest, IN (MMSFb)	39.32 N 86.42 W	275	03/2012 - 12/2013	FMPS	6 - 523 nm	32	[*Pryor et al.*, 2014]

[a]*SMPS: Scanning Mobility Particle Sizer, FMPS: Fast Mobility Particle Sizer, TDMA: Tandem Differential Mobility Analyzer.*
[b]*These data are acquired as part of the US Department of Energy's Atmospheric Radiation Measurement program, and to our knowledge have not been published elsewhere; the program and the site are described in this reference.*

characteristics (probability of NPF, J_n, GR, SP, and $N_{n\text{-}100nm}$) at the five sites?

3) Do proxy algorithms wherein the predictands are the NPF characteristics at the five sites and the predictors are drawn from the suite of remote sensing parameters exhibit commonalities in terms of the most important predictors and the variance explained?

4) Does a proxy model of UFP concentrations using a larger suite of predictors exhibit more explanatory power than the prior satellite-based proxies, which have employed AOD and AE, SO_2 (or NO_2), and UV?

Additionally, given in situ PSD measurements are time consuming and expensive, and thus are typically made for limited time periods, we perform a statistical analysis to quantify how using a limited sample of environmental conditions impacts the generalizability of inferences drawn from data collected during time-limited campaigns.

Methods

Particle size distribution data

The PSD measurements used herein all have durations of a year or more, and derive from locations distributed across North America with different land use and proximity to major point source emissions (Table 4.1; Figure 4.1). While all PSD measurements are taken at/near the surface, the high elevation of Storm Peak Laboratory (SPL) renders it representative of free tropospheric air on a near daily basis [*Yu and Hallar*, 2014]. Prior to presenting the derived NPF descriptors it is important to note that the individual sites used different instrumentation (and thus have different minimum Dp detection limits, Table 4.1) and sampling protocols that may confound inter-comparison across the five sites. For example, archiving of data from Southern Great Plains (SGP) at 30-minute resolution reduces the confidence in the calculated NPF metrics for that site. However, these are the longest records of UFP PSD measurements currently

available for North America. Further, analysis of data collected using two different instruments (an FMPS and SMPS) at Morgan Monroe State Forest (MMSF) can be used to partly evaluate the impact of instrumentation versus spatial variability in determining NPF characteristics and drivers.

Remote sensing measurements

Once daily satellite-based observations used herein as predictors of NPF and their associated uncertainties are summarized in Table 4.2. The justification for the selection of these variables is as follows:

1. The cross product of aerosol optical depth (AOD) and Ångström exponent (AE) is used as a proxy for CS following *Crippa et al.* [2013], and is anticipated to be negatively associated with NPF occurrence, J_n, GR, and SP.
2. SO_2 is used as a proxy for H_2SO_4 following *Crippa et al.* [2013], *Kulmala et al.* [2011], and *Sundström et al.* [2015], although it must be noted that the retrievals exhibit a low signal to noise ratio, except near large emissions [*Krotkov et al.*, 2008; *Fioletov et al.*, 2011], and many negative concentrations are reported in the OMI SO_2 product. Although nucleation rates may be $\propto [SO_2]^n$ [*Kuang et al.*, 2008] or dependent on H_2SO_4 production ($\propto SO_2 \times UV$), we do not include exponential or compound predictor variables due to the low sensitivity of satellite-based measurements of SO_2 and to avoid overfitting the regression models. Sensitivity analyses indicate that inclusion of previously used compound variables (e.g. $SO_2 \times UV/CS$ [*Kulmala et al.*, 2011; *Sundström et al.*, 2015]) does not increase the variance explanation of nearly all of the regression models (mean improvement across sites and metrics < 1%). SO_2 is anticipated to be positively associated with NPF occurrence, J_n, GR, and SP.

Table 4.2. Description of daily (1 in 8 days for LAI) satellite-based measurements used herein.

Predictor	Satellite/ Instrument	Overpass (LST)	Available beginning (% missing [b]: total, ≤ 2 days)	Version	Resolution (at nadir)	Uncertainty/ Accuracy[c]	Proxy for	Citation
"Dark target" Aerosol optical depth at 550nm (AOD)	Terra/ MODIS	1030	2000 (49 %, 71 %)	Collection 6	10 km	± 0.05 ± 0.15 × AOD	AOD×AE ∝ Condensational sink	[*Levy et al.*, 2013]
Ångström exponent 470-660 nm (AE)	Terra/ MODIS	1030	2000 (49 %, 71 %)	Collection 6	10 km	±0.4[d]		[*Levy et al.*, 2013]
Sulfur Dioxide (SO_2; DU)	Aura/OMI	1345	2004 (49 %, 75 %)	Version 3	13 km × 24 km	Greatest of 1.1 DU, 50%	H_2SO_4 production	[*Chance*, 2002; *Brinksma et al.*, 2003]
Local solar noon spectral irradiance at 310 nm (UV; mW m^{-2} nm^{-1})	Aura/OMI	1345	2004 (20 %, 99 %)	Version 3	13 km × 24 km	10%	Production of oxidants	[*Chance*, 2002; *Brinksma et al.*, 2003]
Nitrogen Dioxide (NO_2; molec. cm^{-2})	Aura/OMI	1345	2004 (43 %, 79 %)	Version 3	13 km × 24 km	2×10^{14} molec. cm^{-2} (30%) background (polluted)[e]	Anthropogenic emissions	[*Chance*, 2002; *Brinksma et al.*, 2003]
Ammonia (NH_3; molec. cm^{-2})	MetOp/IASI	930[a]	2008 (58 %, 63 %)	NN Version 1	12 km	< 100% or $< 5 \times 10^{15}$ molec. cm^{-2}	Ternary nucleation	[*Whitburn et al.*, 2016]
Formaldehyde (HCHO; molec. cm^{-2})	Aura/OMI	1345	2004 (44 %, 78 %)	Version 3	13 km × 24 km	35%	Production of low-volatility vapors from BVOC	[*Chance*, 2002; *Brinksma et al.*, 2003]
Leaf area index (LAI; m^2 m^{-2})	Terra&Aqua /MODIS	1030& 1330	2002	Version 5	1 km	1 m^2 m^{-2}	LAI×T ∝ BVOC emissions	[*Fang et al.*, 2012]
Daytime land surface temperature (T; K)	Terra&Aqua /MODIS	1030& 1330	2002	Version 5	1 °	1 K		[*Wan*, 2008]
Ozone (O_3; DU)	Aura/OMI	1345	2004 (43 %, 79%)	Version 3	13 km × 24 km	Greatest of 10 DU, 5%	Oxidant and stagnation	[*Chance*, 2002; *Brinksma et al.*, 2003]

[a] *9:30 is the overpass time at the equator. Only AM retrievals are used.*

[b]*Percentage of missing days (averaged across the five sites and entire satellite observation period), and percentage of missing days with a duration of less than or equal to two consecutive days. MODIS LAI is an 8 day composite product, and thus missing days are not shown for LAI or T.*
[c]*OMI Accuracy: "root sum of the square of all errors, including forward model, inverse model, and instrument errors" [Brinksma et al., 2003].*
[d]*MODIS AE is typically bimodal in nature and thus uncertainty is ambiguous [Levy et al., 2010].*
[e]*When averaged to 26 km × 48 km [Brinksma et al., 2003].*

3. UV is used as a proxy for photochemical production of oxidants (e.g. the hydroxyl radical (OH)) and thus oxidation of SO_2 to H_2SO_4 and BVOCs to low-volatility products following *Crippa et al.* [2013], *Kulmala et al.* [2011], and *Sundström et al.* [2015], and is anticipated to be positively associated with NPF occurrence, J_n, GR, and SP.
4. NO_2 is used as a proxy for air masses influenced by anthropogenic emissions (including primary emitted particles and condensable vapors) [*Russell et al.*, 2012], following *Kulmala et al.* [2011] and *Sundström et al.* [2015]. Additionally, satellite-based measurements of NO_2 have been observed to correlate better with in situ SO_2 measurements than satellite-based retrievals of SO_2 [*Sundström et al.*, 2015]. NO_2 is anticipated to be negatively associated with NPF occurrence and SP due to its association with primary particle emissions and thus increased CS, but positively associated with J_n and GR due to increased precursor concentrations.
5. NH_3 may play a role in enhancing NPF by acting as a stabilizing base for nucleating clusters, and is used here following *Crippa et al.* [2013] (daily NH_3 estimates are used herein, versus seasonal averages in *Crippa et al.* [2013]), and is anticipated to be positively associated with NPF occurrence, J_n, GR, and SP.
6. Formaldehyde (HCHO) is a product of oxidation of VOCs and one of the few organic species retrievable from satellite-based measurements. It is used as a proxy for the abundance of low-volatility VOCs [*Chance et al.*, 2000; *Henze and Seinfeld*, 2006]. The dominant source of HCHO estimated from satellite-based measurements appears to be the oxidation of isoprene because of the short lifetime of isoprene and production of HCHO in the initial oxidation steps, while most anthropogenic VOC emissions require more oxidation steps prior to HCHO formation and thus are diluted prior to HCHO production [*Millet et al.*, 2008].

Organics play a role in NPF and/or growth of newly formed particles at least in some environments [*O'Dowd et al.*, 2002; *Zhang et al.*, 2004a, 2004b; *Henze and Seinfeld*, 2006; *Metzger et al.*, 2010; *Paasonen et al.*, 2010; *Pryor et al.*, 2011; *Pierce et al.*, 2012; *Riipinen et al.*, 2012; *Kulmala et al.*, 2013], but uncertainty remains regarding whether isoprene products contribute to, or suppress NPF [*Surratt et al.*, 2006; *Kiendler-Scharr et al.*, 2009]. Thus the expected association between HCHO and NPF occurrence is uncertain, but it is anticipated to be positively associated with J_n, GR, and SP.

7. The cross product of leaf area index (LAI) and skin temperature (T) is used as an additional proxy of BVOC emissions [*Guenther et al.*, 1993], and is anticipated to be positively associated with NPF occurrence, J_n, GR, and SP.
8. Ozone (O_3) is both a key atmospheric oxidant [*Helmig*, 1997; *Seinfeld and Pandis*, 2006] and a proxy for atmospheric stagnation [*Valente et al.*, 1998]. Total column O_3 as retrieved from the Ozone Monitoring Instrument (OMI) is naturally dominated by stratospheric concentrations, but the presence of a temporal mode of variance at synoptic time scales (see below) indicates that these measurements are also responsive to tropospheric variability. O_3 is anticipated to be positively associated with NPF occurrence, J_n, GR, and SP.

Prior research has demonstrated the potential for using satellite-based measurements as proxies for daily ultrafine or nucleation mode particle concentrations [*Kulmala et al.*, 2011; *Crippa et al.*, 2013; *Sundström et al.*, 2015] using AOD and AE, SO_2, and UV as predictors. We use a proxy based solely on variables 1-3 ('simple model') as a benchmark against which to evaluate whether a model including additional predictor variables: NO_2, NH_3, HCHO, LAI×T, and O_3 ('full model') exhibits improved performance.

All observations as obtained from the respective retrieval teams are subject to the following post-processing:

1. For the spectral and spatial correlation analyses, spatially consistent time series are required. Thus, the remotely sensed measurements are spatially averaged to a 0.5° × 0.5° grid. This resolution was selected to remove some noise through spatial averaging, without removing important mesoscale variability [*Anderson et al.*, 2003]. Due to the lower temporal resolution of the Moderate Resolution Imaging Spectroradiometer (MODIS) LAI measurements (1 in 8 days), LAI×T is excluded from these analyses. For all remaining analyses (Wilcoxon rank sum test, regression trees, and multiple linear regression), all valid retrievals within 100 km of each PSD measurement site are averaged for each observation day to reduce noise, particularly in the trace gas measurements [*Krotkov et al.*, 2008; *Fioletov et al.*, 2011] and to enhance data availability for these predictands.
2. For all variables, days without valid measurements are filled using a weighted mean of the nearest preceding and succeeding measurement days, which will likely reduce the explanatory power of the regression models built herein. The percentages of missing data are given in Table 4.2.
3. AE is calculated from AOD at 470 and 660 nm after spatial averaging using the Ångström power law [*Ångström*, 1964].
4. NH_3 measurement availability begins in 2008 (Table 4.2) and thus they are only available for the full duration of PSD measurements at SGP, SPL, and MMSFb, and for a portion of the PSD measurements at Egbert and MMSFa (Table 4.1), but many days do not have coincident measurements (e.g. all of 2007) and are filled with a mean NH_3 value. There are no coincident NH_3 and PSD measurements at Duke, and thus NH_3 is excluded from the

regression analysis at this site. Satellite-based measurements of NH_3 can have a high associated uncertainty related to unfavorable atmospheric conditions and/or low NH_3 abundances [*Whitburn et al.*, 2016]. Thus, only NH_3 pixels with relative uncertainty < 100 % of the retrieved concentration or an absolute error < 5×10^{15} molecules cm^{-2} are used.

5. All OMI pixels impacted by the row anomalies [*OMI Team*, 2012] are treated as missing data.
6. All OMI and Infrared Atmospheric Sounding Interferometer (IASI) retrievals are filtered using a cloud screen to remove retrieval with cloud fractions > 0.3 [*Fioletov et al.*, 2011; *McLinden et al.*, 2014; *Vinken et al.*, 2014]. The MODIS aerosol retrieval algorithm filters out cloud contaminated pixels prior to averaging spectral reflectances and deriving spectral AOD [*Levy et al.*, 2013], and therefore, no additional cloud screening is applied here.
7. Prior to regression analyses, NO_2 and HCHO are log transformed to more closely approximate Gaussian distributions and all predictors are converted to standard normal scores. Therefore any systematic bias in satellite retrievals should not impact the analyses as only relative concentrations are considered. Random errors in the retrievals will propagate through the analyses and are expected to reduce the association between the regression predictors and predictands, but not sign or slope of the relationship.

NPF at the measurement sites typically begin in the morning hours (~ 9:00 – 11:00 LST; Figure 4.2c), and event metrics are calculated for the subsequent 3 hours, thus are typically centered on the satellite overpass times (9:30 – 13:45 LST; Table 4.2). It is noted that the once daily measurements cannot characterize diurnal variability of the predictor variables and may thus reduce the predictive skill of the models built from them, particularly when events do not occur near the satellite overpass (e.g. at SGP). Further, satellite-based measurements are

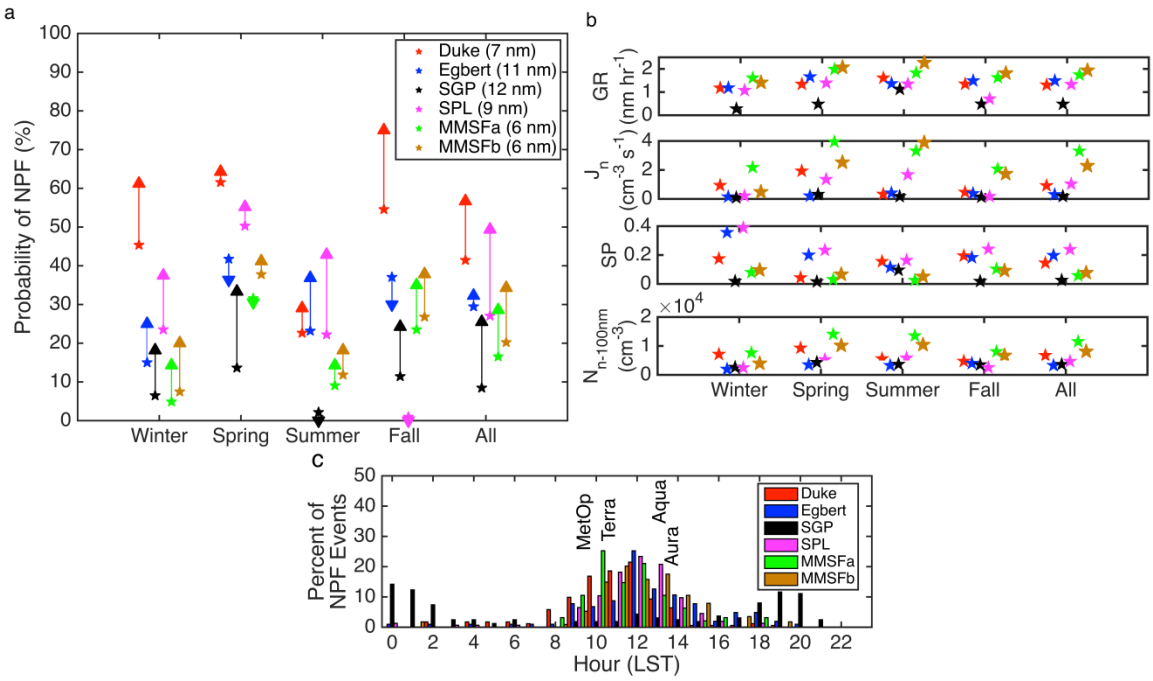

Figure 4.2. a) Probability of a NPF event occurring (p(1); stars) and the probability of an event occurring given that an event occurred on the prior day (p(1|1); terminal point of arrows) by season. The instrument's minimum particle Dp measured at each site is given in parenthesis in the legend. b) Event metrics (growth rates (GR), formation rate (J_n, where 'n' is determined by the minimum detectable particle diameter for each instrument), and survival probabilities (SP)) and daily mean ultrafine particle concentration (Dp < 100 nm; $N_{n—100nm}$,) by season and location. c) Percentage of NPF event days that begin in each hour of the day by measurement site. Also shown are the approximate overpass times for the MetOp (930; NH_3), Terra (1030; AOD×AE, LAI×T), Aqua (1330; LAI×T), and Aura (1345; SO_2, UV, NO_2, HCHO) satellites (ordinate position selected for visibility). Calculations of the event metrics values are described in section 2.3.

columnar measurements and may not fully characterize near-surface conditions [e.g. *van Donkelaar et al.*, 2006, 2013; *Lamsal et al.*, 2008; *Sundström et al.*, 2015], and may reduce the explanatory power of the regression models built herein.

Event classification and characteristics, and statistical methods

To quantify similarities and differences in NPF frequency, persistence, and seasonality across North America, an automated methodology is applied to each of the PSD data sets to identify event occurrence and estimate J_n, GR, and SP (an earlier version of the approach was described in *Sullivan and Pryor* [2016]). In brief, a NPF event is reported, and included in the analysis, if:

1. The minimum nucleation mode geometric mean diameter (< 30 nm; D_{gNuc}) occurs within 10 hours of the peak nucleation mode number concentration and while the difference in the geometric mean diameter for Dp < 100 nm (D_g) and D_{gNuc} is less than or equal to 10 nm,
2. The r^2 of the regression fit for the GR calculation (tracking D_{gNuc} from event start to + 3 hrs.) is ≥ 0.5,
3. And the event metrics can be reasonably calculated (e.g. GR and $J_n > 0$; eq. 1-6):

$$J_n = \frac{dN_{nuc}}{dt} + F_{coag} + F_{growth} \ldots (1)$$

$$\text{where } F_{coag} = \sum_{i=\min(D_p)}^{i=30\ nm} \left[\frac{1}{2} K_{ii} N_i + \sum_{j=i+\Delta D_p}^{j=\max(D_p)} \left(K_{ij} N_j\right)\right] \ldots (2)$$

$$\text{and } F_{growth} = \sum_{i=\min(D_p)}^{i=30\ nm} \left[\frac{N_i}{30\ nm - D_{pi}} * GR\right] \ldots (3)$$

$$SP = \prod_{i=\min(D_p)}^{i=100\ nm-\Delta D_p} \exp\left(-\frac{\tau_{D_{pi},D_{pi+\Delta D_p}}^{growth}}{\tau_{Dp_i}^{coag}}\right) \ldots (4)$$

$$\text{where } \tau_{D_{pi},D_{pi+\Delta D_p}}^{growth} = \frac{(D_{pi+\Delta D_p} - D_{pi})}{GR} \ldots (5)$$

$$\text{and } \tau_{D_{pi}}^{coag} = \frac{1}{\frac{1}{2} K_{ii} N_i + \sum_{j=i+\Delta D_p}^{\max(D_p)} K_{ij} N_j} \ldots (6)$$

where K is the Fuch's form Brownian coagulation coefficient, N_{nuc} is the number concentration of particles ≤ 30 nm, N_i and D_{pi} are the number concentration and median diameter of bin *i*, ΔD_p is the bin width, and J_n is averaged from event start to + 3 hrs.

The classification algorithm is thus designed to capture unambiguous 'A' type (appearance of nucleation mode particles, followed by clear, sustained growth) NPF events and will classify all days not meeting all of the above criteria as a 'non-event' day even though new particles may be forming (e.g. 'B' or 'C' type events (no appearance of particles in the smallest diameters measured or lack of clear, sustained growth) [*Pryor et al.*, 2010]), thereby reducing NPF

frequencies relative to a subjective approach.

Prior research indicates that the dominant NPF mechanism may vary seasonally [*Yu and Hallar*, 2014; *Yu et al.*, 2015]. Thus, the analyses described below are conducted by climatological season, or for leaf-active (defined here as LAI×T ≥ 50th percentile) and leaf-dormant (LAI×T < 50th percentile) periods.

The persistence of NPF events is characterized using the conditional probability of events with a lag of one day (i.e. p(1|1)) relative to the probability of an event on any day (p(1)), thus:

1. p(1) ≈ p(1|1): No autocorrelation
2. p(1) < p(1|1): Positive autocorrelation
3. p(1) > p(1|1): Negative autocorrelation

Once the sites have been characterized in terms of the NPF occurrence, intensity, and persistence, we then seek to determine if inherent scales in the NPF predictors (satellite observations) around each site can be used to diagnose and explain the observed consistencies and site-to-site differences in NPF frequency and event characteristics. To identify the dominant temporal scales of variability in the satellite-based predictors of NPF and the spatial scale on which they exhibit coherence, the time series of remotely sensed parameters at each measurement site were subject to a fast Fourier transformation and used to compute power spectra. The spatial coherence is defined as the distance from the PSD measurement site at which the mean correlation coefficient (Pearson's r) between the time series of the predictors at that site and each surrounding grid cell drops below an arbitrary threshold of 0.3.

Finally we focus on assessing the potential to extend satellite-based proxies of UFP concentrations by expanding both the number of predictor variables used (i.e. the suite of satellite observations included) and the range of characteristics of NPF events considered. We

begin by applying the non-parametric Wilcoxon rank sum test to quantify whether the remote sensing predictors exhibit different values on NPF event vs. non-event days at each site. This tests the null hypothesis that it is equally probable that a given observation from one sample is either greater than or less than a given observation from a second sample (different populations across the range of observations, not solely mean or median). We then build regression trees [*Hyvönen et al.*, 2005] to recursively partition the predictors based on the occurrence (or not) of NPF. In this way we can determine which predictors (and predictor interactions) are most important in terms of predicting whether an individual day as described using the remote sensing variables will be characterized by NPF or not. The predictors that are most important lie closer to the root node and can be used to interpret how the dependence of NPF on a given predictor variable is conditional on other predictor variables. Finally, multiple linear regression models (eq. 7) are fit in which the predictands are J_n, GR, SP, and $N_{n\text{-}100nm}$ and the predictors are all of the remote sensing variables, and the variance explanation are compared with those from a smaller suite of previously used predictors (i.e. AOD×AE, SO_2, and UV [*Kulmala et al.*, 2011; *Crippa et al.*, 2013; *Sundström et al.*, 2015]):

$$y_j = \beta_1 x_{1,j} + \cdots + \beta_i x_{i,j} + constant \ldots (7)$$

where y_j is the predictand, β_i is the coefficient weighting, and $x_{i,j}$ is the standard normal score of the predictor variable, 'i', on day, 'j'.

The predictor variable coefficient weights (β_i) are used to diagnose which predictors control each event characteristic, and the degree to which they differ among the measurement sites. The results of this analysis are interpreted cautiously because multiple linear regression assumes a linear relationship between the predictors and predictands, multivariate normality, and no multicollinearity amongst the predictors. To investigate the impact of using finite temporal

sample, the multiple linear regression is conducted as a Monte Carlo experiment (1000 iterations) in which we sub-sample the PSD datasets to train the regression models using a k-fold (k = 5 folds) cross-validation with 20% of the data withheld from the training model. This is designed to quantify how model skill and coefficient weightings depend on precise time period of field measurements.

Results

NPF characteristics at the five sites

NPF is frequently observed at all five sites with highest NPF frequency, total sub-100 nm particle concentrations ($N_{n\text{-}100nm}$), and highest GR in spring, with a secondary peak in NPF frequency in fall (except at SPL, where prior analyses have indicated a secondary fall peak [*Hallar et al.*, 2016]) (Figure 4.2). The discrepancy with prior research at SPL may be due to the lower data availability in fall (due to limited site access) and that while nucleation mode particle formation is observed it is not frequently followed by clear, sustained growth to larger particle sizes (requisite for classification of an event day). Similarly, the low NPF frequency in summer at SGP may be due to missing data in the summer of 2011 and/or the lower temporal frequency (30 min^{-1}) of the PSD measurements at the site resulting in fewer days meeting the strict criteria for an event day.

All sites exhibit an overall positive one-day autocorrelation of NPF ($p(1) < p(1|1)$) indicating a higher probability of an event if one occurred on the prior day, although this is not observed for all seasons (Figure 4.2a). Despite these commonalities, there are also differences in NPF characteristics among the five sites. For example, NPF event frequency is substantially higher at Duke than the other sites (Figure 4.2a). Also, seasonally averaged GR, particle formation rates (J_n), and $N_{n\text{-}100nm}$ are highest at MMSF in both periods (MMSFa and MMSFb)

suggesting that the impact of differences in instrumentation during the two sampling periods on NPF metrics is modest compared to the spatial variability. The observation that GR, J_n, and $N_{n\text{-}100nm}$ concentrations are highest at MMSF may be due, at least in part, to the lowest min(Dp) at this site, but given the min(Dp) at Duke differed from that at MMSF by only 1 nm, some of the site-to-site variability in these metrics may also reflect spatial variability in NPF events.

Spatiotemporal scales of the predictors

The proposed satellite predictors of NPF exhibit similar dominant scales of temporal variability at all sites (Figure 4.3). SO_2 exhibits highest variance at synoptic timescales (3-10 days) at all sites except SPL, where the variance is focused on the annual mode. The dominance of the annual mode at SPL may reflect reduced upwind power plant emissions [*Mast et al.*, 2005] or the fact that this site is frequently in the free troposphere, while the SO_2 product is designed to represent SO_2 in the planetary boundary layer (Figure 4.3b) [*Krotkov et al.*, 2006; *Fioletov et al.*, 2011]. Despite large spatial gradients in isoprene emissions and HCHO concentrations across the study area [*Millet et al.*, 2006, 2008], HCHO variability is dominated by the synoptic scale at all sites (Figure 4.3f), while NO_2 concentrations exhibit high variance on both synoptic and seasonal timescales (Figure 4.3d). O_3 concentrations and UV are naturally dominated by the annual cycle (Figure 4.3c and g) and exhibit the highest spatial scales of coherence (Figure 4.4), but O_3 concentrations also exhibit a variance peak at synoptic time scales (though it is smallest at SPL). The short atmospheric lifetime of NH_3 [*Clarisse et al.*, 2009], and seasonality in NH_3 fertilizer application and emissions from other agricultural activities [*Aneja et al.*, 2003; *Goebes et al.*, 2003], is reflected in NH_3 variability being characterized by the synoptic and seasonal modes (Figure 4.3e), and that seasonality may be in part responsible for the observed seasonality in GR and J_n (Figure 4.2). AOD×AE varies on the annual time scale at all sites and strongly at the

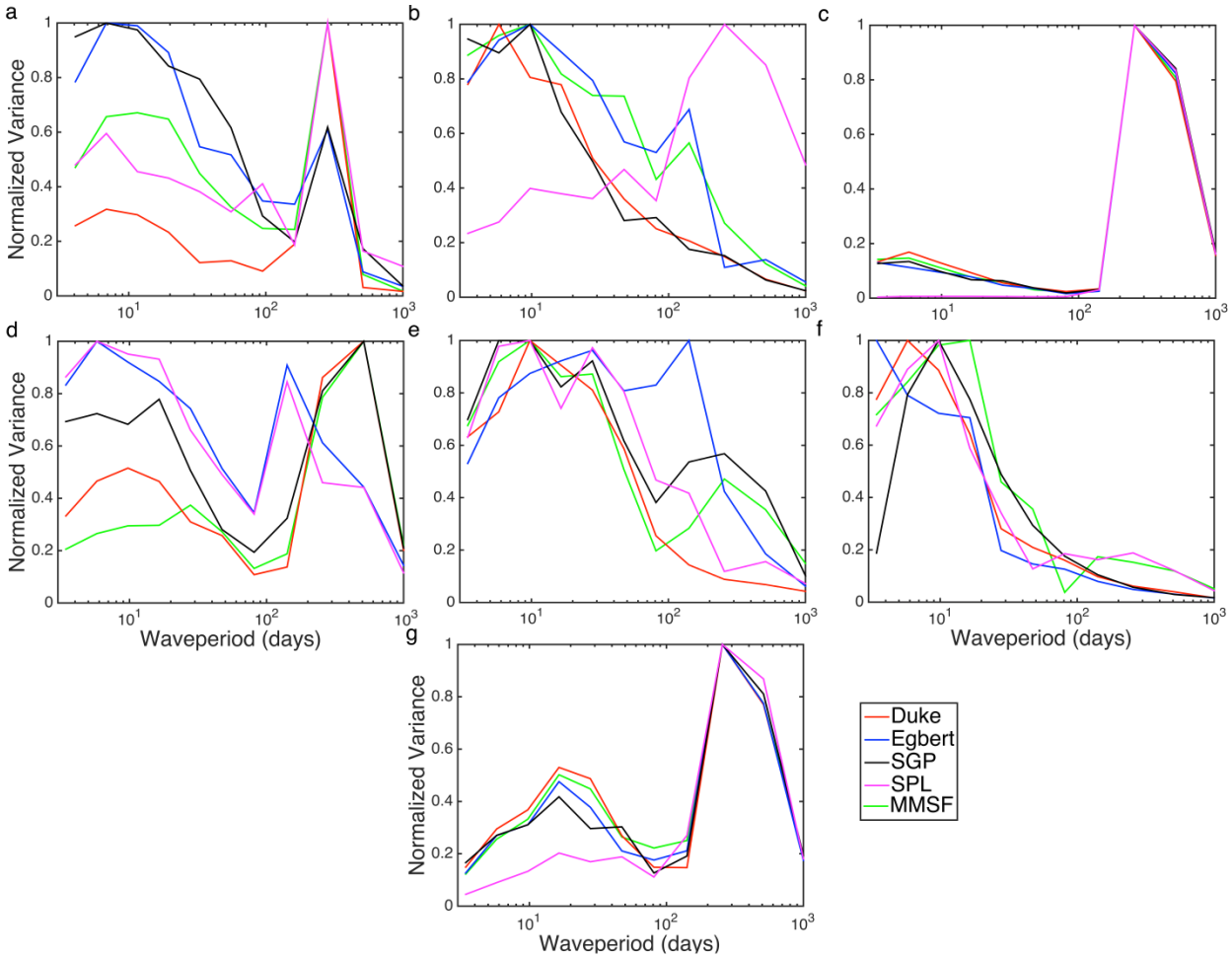

Figure 4.3. Normalized variance of once daily a) AOD×AE, b) SO_2, c) UV, d) NO_2, e) NH_3, f) HCHO, and g) O_3 for the grid cells containing each PSD measurement site (indicated by different colors). The variance at each waveperiod is normalized by the maximum variance at any frequency (waveperiod) and the power spectra have been smoothed to emphasize the primary modes of variability. For this analysis the entire satellite measurement period is used. The OMI measurements (SO_2, UV, NO_2, HCHO, O_3) are from 2004 – 2014, MODIS measurements (AOD×AE) are from 2000 – 2014, and IASI measurements (NH_3) are from 2008 – 2014. Due to low temporal resolution of MODIS LAI (1 in 8 days), LAI×T is omitted.

synoptic time scale at Egbert and SGP, moderately at SPL and MMSF, and weakly at that time scale at Duke. Many of the variables show a minimum in variance at the ~180 day period, supporting separation of the data into leaf-active and leaf-dormant periods for the regression analysis below.

In accord with previous analyses that suggest NPF occurs at the regional scale and exhibits temporal autocorrelation, at least for lags of one day, the predictors also exhibit

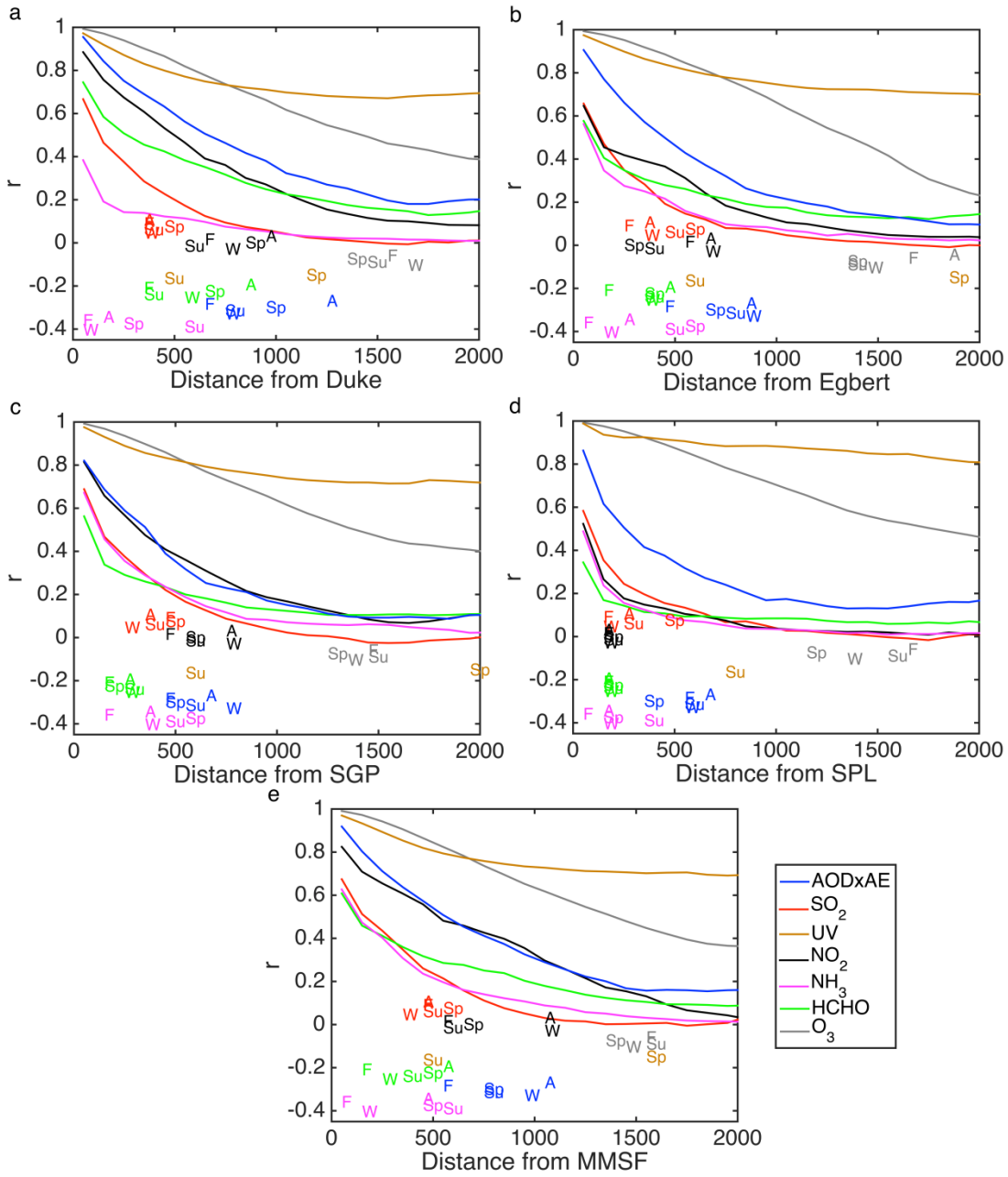

Figure 4.4. Mean correlation (r; binned in 100 km distances) between the time series of each of the predictors for the grid cell containing each PSD measurement site and all other grid cells expressed as a function of separation distance. The mean correlation is thus computed over all azimuth directions. The PSD measurement sites are a) Duke Forest, b) Egbert, c) Southern Great Plains, d) Storm Peak Laboratory, and e) Morgan Monroe State Forest. The distance at which r < 0.3 by season is indicated by the abscissa location of 'W' = winter, 'Sp' = spring, 'Su' = summer, 'F' = fall, and 'A' = all measurements, with the ordinate location selected solely for visibility. For this analysis the entire satellite measurement period is used. The OMI measurements (SO_2, UV, NO_2, HCHO, O_3) are from 2004 – 2014, MODIS measurements (AOD×AE) are from 2000 – 2014, and IASI measurements (NH_3) are from 2008 – 2014. Due to low temporal resolution of MODIS LAI (1 in 8 days), LAI×T is omitted.

relatively large scales of spatial coherence around all PSD measurement sites (Figure 4.4). Further, consistent with the highest overall probability of NPF and p(1|1) at Duke, all predictors (except NH_3) exhibit comparatively large scales of spatial coherence there (Figure 4.4a). At all sites the gas-phase concentrations (particularly SO_2, NH_3, and HCHO) exhibit smaller scales of coherence than AOD×AE and UV (Figure 4.4), potentially indicating that they may play a greater role in determining the likelihood of NPF events. NH_3 concentrations exhibit greater spatial coherence in the spring and summer, particularly at Egbert, SPL, and MMSF (Figure 4.4 b, c, and e). This finding is consistent with the higher NH_3 concentrations on event days during the leaf-active period (Table 4.3), and may contribute to the spring peak in NPF frequency and high observed GR at these sites during these seasons [*Zhang et al.*, 2010; *Pryor et al.*, 2011]. NO_2 and AOD×AE exhibit similar (and large) spatial scales at MMSF and SGP implying anthropogenic primary particle emissions may dominate accumulation mode concentrations and thus the CS (Figure 4.4c and e). HCHO exhibits much larger scales of coherence than SO_2 and NH_3 at Duke due to the large regional isoprene emissions in the southeastern US [*Millet et al.*, 2008] as reflected in the high leaf-active HCHO concentrations at this site (Table 4.3). These local differences in the temporal variability and spatial coherence of the predictor variables may thus offer partial explanations for the site-to-site variations in NPF occurrence and characteristics.

Association between satellite-based measurements and NPF occurrence and event characteristics at the five sites

Consistent with prior research [*Yu et al.*, 2015; *Sullivan and Pryor*, 2016], NPF frequency and characteristics exhibit marked seasonality (Figure 4.2) as does the dependence on the satellite-based predictors. For example, NPF is more frequent when LAI×T is lower during leaf-

Table 4.3. Median [p25-p75] conditions from satellite-based measurements on event and non-event days (n) during leaf-active and leaf-dormant measurements. ***Bold*** *indicate rejection of the null hypothesis that the samples are from the same population (α=0.1, Wilcoxon rank sum test). Note NH_3 measurements are available beginning in 2008 and are thus available for only a portion of the PSD measurements at Egbert and MMSFa (no coincident measurements at Duke), and days without coincident measurements (e.g. all of 2007) and are filled with a mean NH_3 value. Thus the distributions of NH_3 on event versus non-event days can be significantly different, despite the median values being strongly driven by missing data.*

		Duke		Egbert		Southern Great Plains		Storm Peak Laboratory		Morgan Monroe State Forest a		Morgan Monroe State Forest b	
		Event	Non-event	Event	Non-event	Event	Non-event	Event	Non-event	Event	Non-event	Event	Non-event
leaf-active	n	64	144	55	122	83	655	68	219	66	183	54	152
	AODxAE	**0.47 [0.14-0.73]**	**0.68 [0.43-0.92]**	**0.26 [0.14-0.37]**	**0.32 [0.22-0.55]**	**0.10 [0.03-0.18]**	**0.15 [0.07-0.25]**	**0.14 [0.09-0.22]**	**0.21 [0.13-0.29]**	**0.19 [0.11-0.35]**	**0.32 [0.16-0.59]**	**0.05 [-0.02-0.26]**	**0.22 [0.08-0.35]**
	SO_2 (DU)	0.06 [-0.19-0.02]	-0.05 [-0.21-0.06]	**0.08 [-0.06-0.21]**	**-0.05 [-0.22-0.11]**	-0.02 [-0.20-0.14]	-0.01 [-0.15-0.11]	0.02 [-0.10-0.18]	0.09 [-0.05-0.20]	**-0.03 [-0.19-0.12]**	**0.04 [-0.07-0.18]**	0.01 [-0.16-0.16]	0.00 [-0.13-0.09]
	UV (mW m^2 nm^{-1})	96 [74-106]	97 [86-105]	**82 [69-90]**	**75 [50-91]**	**84 [67-109]**	**96 [75-111]**	**129 [124-134]**	**125 [115-134]**	68 [54-98]	72 [44-97]	**91 [76-100]**	**86 [68-99]**
	NO_2 ($\times 10^{15}$ molec. cm^{-2})	2.91 [2.13-3.94]	2.64 [2.22-3.14]	2.53 [1.37-3.93]	2.11 [1.33-3.53]	1.72 [1.30-2.11]	1.65 [1.28-2.05]	0.75 [0.52-0.95]	0.69 [0.48-0.87]	**3.93 [3.10-5.13]**	**3.41 [2.21-4.73]**	**2.54 [1.92-3.30]**	**2.11 [1.69-2.68]**
	NH_3 ($\times 10^{15}$ molec. cm-2)	N/A	N/A	2.32 [2.32-2.32]	2.32 [2.32-2.32]	**8.06 [4.21-13.4]**	**6.41 [2.68-10.9]**	1.20 [0.65-2.30]	1.63 [0.45-3.21]	0.18 [0.18-0.18]	0.18 [0.18-0.18]	6.16 [3.17-10.9]	6.37 [2.82-10.4]
	HCHO ($\times 10^{16}$ molec. cm^{-2})	**1.53 [1.17-1.87]**	**1.79 [1.49-2.25]**	1.00 [0.82-1.26]	1.11 [0.86-1.35]	**1.05 [0.89-1.32]**	**1.16 [0.94-1.43]**	**1.15 [0.84-1.64]**	**1.40 [1.08-1.82]**	**1.06 [0.91-1.20]**	**1.25 [0.96-1.56]**	**1.19 [0.98-1.72]**	**1.51 [1.20-1.80]**
	LAIxT (m^2 m^{-2} K)	**1053 [665-1197]**	**1140 [1035-1207]**	594 [401-769]	682 [394-784]	**322 [248-405]**	**351 [268-423]**	332 [271-415]	359 [277-390]	**188 [130-462]**	**512 [182-855]**	**546 [486-673]**	**658 [508-689]**
	O_3 (DU)	315 [301-328]	311 [303-326]	311 [294-336]	316 [294-337]	**313 [298-331]**	**305 [295-322]**	**314 [299-323]**	**291 [283-297]**	**315 [295-337]**	**305 [284-325]**	**311 [302-329]**	**304 [296-314]**

leaf-dormant	n	108	99	48	130	79	657	86	197	29	203	60	146
	AODxAE	0.11 [0.06-0.23]	0.10 [0.05-0.19]	0.20 [0.10-0.27]	0.20 [0.14-0.25]	0.07 [0.03-0.16]	0.09 [0.04-0.17]	0.23 [0.21-0.26]	0.23 [0.17-0.27]	0.14 [0.09-0.20]	0.14 [0.11-0.17]	0.08 [0.02-0.15]	0.10 [0.05-0.17]
	SO_2 (DU)	**0.08 [-0.10-0.26]**	**-0.03 [-0.23-0.19]**	**-0.09 [-0.53-0.12]**	**0.02 [-0.36-0.29]**	0.02 [-0.21-0.21]	-0.02 [-0.24-0.17]	**-0.03 [-0.27-0.18]**	**-0.15 [-0.38-0.05]**	-0.13 [-0.43-0.23]	-0.13 [-0.46-0.18]	**-0.20 [-0.40-0.07]**	**-0.05 [-0.36-0.20]**
	UV (mW m^2 nm^{-1})	**47 [36-64]**	**29 [21-42]**	**19 [10-35]**	**12 [7-22]**	**37 [31-57]**	**35 [25-51]**	**78 [47-104]**	**50 [28-74]**	**29 [26-41]**	**15 [10-23]**	**43 [27-63]**	**27 [18-38]**
	NO_2 ($\times 10^{15}$ molec. cm^{-2})	5.23 [4.15-6.71]	5.46 [4.32-6.85]	**3.36 [1.49-5.25]**	**3.95 [2.25-6.65]**	2.53 [2.01-3.31]	2.49 [1.93-3.14]	**0.39 [0.28-0.57]**	**0.56 [0.35-1.00]**	5.01 [3.32-7.04]	4.79 [3.06-5.89]	3.86 [3.14-5.39]	4.17 [3.25-5.31]
	NH_3 ($\times 10^{15}$ molec. cm-2)	N/A	N/A	2.32 [1.85-2.32]	2.32 [-0.31-2.41]	3.89 [1.92-9.00]	4.17 [1.49-8.71]	1.23 [-0.06-3.35]	1.62 [-0.05-3.91]	0.18 [0.18-0.76]	0.18 [-2.92-0.70]	**4.26 [0.87-9.77]**	**1.75 [-0.51-6.68]**
	HCHO ($\times 10^{16}$ molec. cm^{-2})	0.96 [0.82-1.12]	0.96 [0.83-1.12]	0.84 [0.64-1.17]	0.84 [0.63-0.97]	1.12 [0.92-1.26]	1.04 [0.90-1.20]	1.03 [0.93-1.31]	1.04 [0.91-1.27]	0.88 [0.70-1.11]	0.86 [0.72-1.01]	1.06 [0.91-1.17]	1.00 [0.84-1.18]
	LAIxT (m^2 m^{-2} K)	**288 [223-312]**	**245 [236-298]**	23 [13-165]	19 [15-64]	**149 [139-170]**	**141 [110-160]**	49 [36-97]	61 [40-118]	**86 [62-95]**	**74 [54-85]**	**163 [115-287]**	**100 [83-141]**
	O_3 (DU)	299 [280-324]	299 [264-326]	319 [289-365]	336 [300-366]	**281 [266-302]**	**294 [274-318]**	**308 [287-336]**	**295 [275-332]**	315 [297-336]	310 [286-339]	292 [275-305]	296 [278-314]

active and higher during leaf-dormant measurement days (Table 4.3), due to the higher frequency of events during spring and fall (Figure 4.2). The dominant difference in the satellite-based predictors on NPF event versus non-event days during leaf-dormant periods is insolation receipt (UV) and the resultant production of atmospheric oxidants, while the differences in the predictors during the leaf-active periods are more complex. Consistent with the expectation that a higher CS will tend to suppress NPF, non-event days are characterized by higher AOD×AE at all sites during the leaf-active period (Table 4.3). However, this is not the case during the leaf-dormant season when particle loading is generally lower (except SPL; Table 4.3) [*Sullivan et al.*, 2015], indicating that another parameter(s) (e.g. availability and/or oxidation of NPF precursors) may limit NPF during leaf-dormant periods. Despite the large uncertainty in NH_3 retrievals, consistent with *a priori* expectations of ternary nucleation, higher concentrations are observed on NPF event days at the two sites located near high NH_3 emissions, SGP (significant difference leaf-active; $\alpha = 0.1$) and MMSFb (higher p25 and p75 leaf-active; significantly difference leaf-dormant) [*Goebes et al.*, 2003; *US Environmental Protection Agency*, 2011]. Higher HCHO concentrations are observed on leaf-active non-event days at all sites (not significant at Egbert, p-value = 0.11), supportive of the postulate that isoprene (likely the major source of remotely sensed HCHO) tends to quench available oxidants, reduce H_2SO_4 production, and suppress NPF. There was no significant difference in HCHO on event and non-event days during leaf-dormant periods, supporting the assertion that satellite-based measurements of HCHO are primarily indicative of BVOC emissions. Significantly higher O_3 concentrations are observed on NPF days during the leaf-active season (though not at Duke or Egbert) possibly indicating that high non-isoprene VOC concentrations are associated with both high O_3 production and an increased likelihood of NPF.

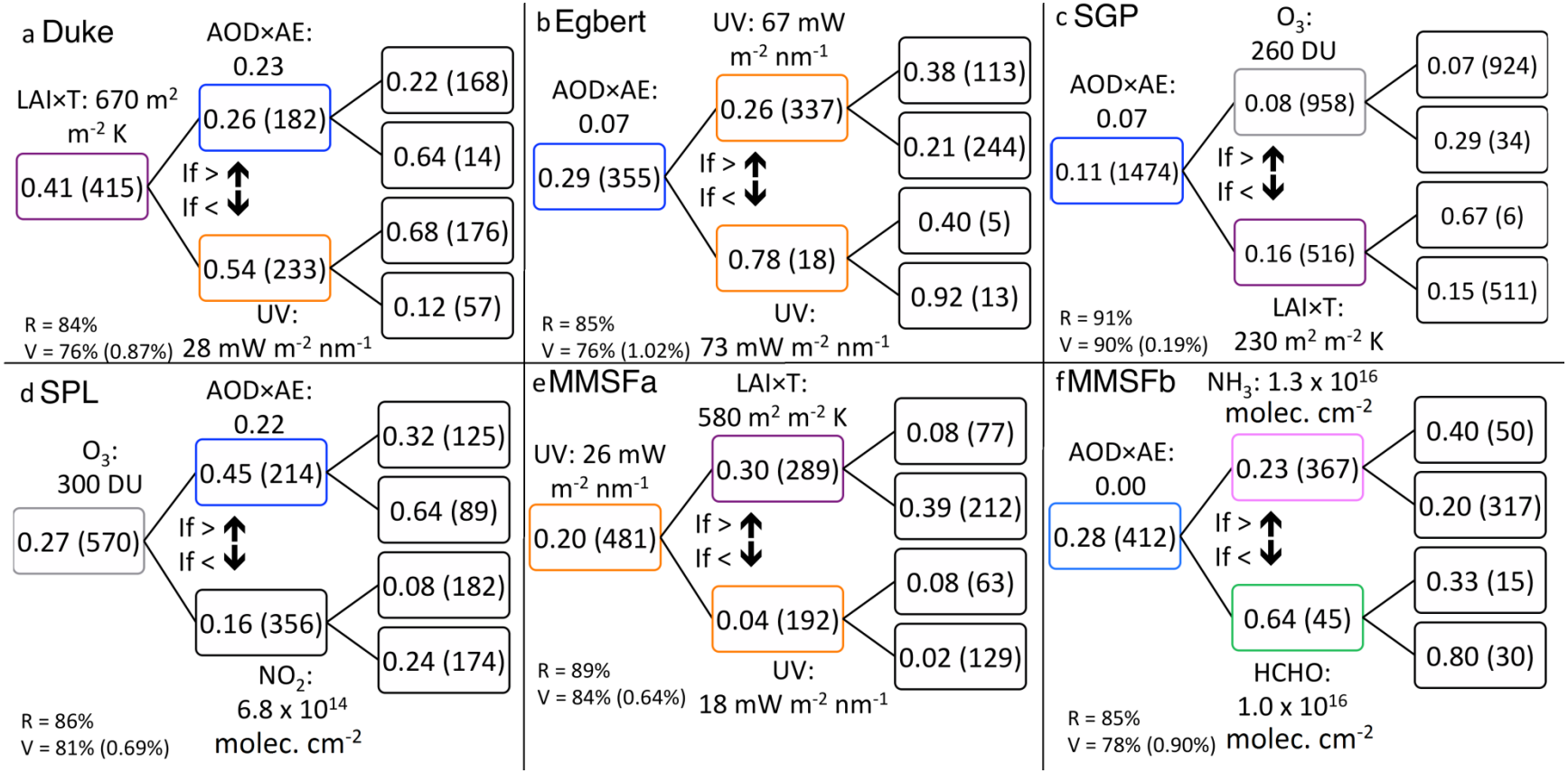

Figure 4.5. Regression trees for predicting NPF event occurrence at a) Duke, b) Egbert, c) SGP, d) SPL, e) MMSFa, and f) MMSFb. The branches upward and downward are for all days above and below the variable threshold given at the node, respectively. The colors of the boxes correspond to the variable colors from Figure 4.4, with the addition that purple is used for LAI×T. The probability of an event is given at each node and the sample size is given in the parenthesis (note the far left nodes are the entire dataset at each site). Also given is the resubstitution accuracy (R) and mean (standard deviation) cross-validation accuracy (V) after withholding 20% of measurements days, over 1000 iterations. The trees are built using a maximum of 10 nodes and minimum leaf size of 5, but have been truncated here for legibility.

Regression trees constructed to 'predict' event occurrence illustrate the importance of predictor interactions (Figure 4.5). For example, in the MMSFa data set the overall NPF frequency is 20%, but increases to 30% when UV > 26 mW m^{-2} nm^{-1} and to 39% when UV > 26 mW m^{-2} nm^{-1} and LAI×T < 580 m^2 m^{-2} K (Figure 4.5e). At Duke, the first node is LAI×T ≈ median (Table 4.3), with an increase in NPF frequency from 26% to 64% conditional on AOD×AE < 0.23 if LAI×T > 670 m^2 m^{-2} K and from 54% to 68% when UV > 28 mW m^{-2} nm^{-1} if LAI×T < 670 m^2 m^{-2} K (cf. 41% for all days; Figure 4.5a). This is consistent with the event versus non-event day conditions described above, where AOD×AE and UV are important discriminators between event and non-event days during leaf-active and leaf-dormant period, respectively (Table 4.3). AOD×AE is the 1st or 2nd level node variable at all sites except MMSFa, and in all cases low AOD×AE is associated with increased probability of NPF (Figure 4.5a-d, and f). LAI×T and UV are also important discriminators of event and non-event days, each being the 1st or 2nd level node at three of the six sites. Higher UV is typically associated with increased probability of NPF, while the relationship with LAI×T is less clear because, as discussed above, NPF frequency is highest at moderate LAI×T (i.e. in spring and fall). O_3 is the 1st node and NO_2 is a 2nd level node at SPL, where higher O_3 and lower NO_2 favors NPF, indicating that the presence of high concentrations of stabilizing organics coinciding with low anthropogenic emissions is favorable for NPF (Figure 4.5d). MMSF is in a location of high BVOC and NH_3 emissions. Accordingly, NH_3 and HCHO are the 2nd level nodes with higher NH_3 and lower HCHO being associated with increased probability of NPF at MMSFb (NH_3 measurements are not available for most of MMSFa), again emphasizing the role of a stabilizing base (such as NH_3) in promoting NPF and supporting the postulate that high isoprene emissions can suppress NPF (Figure 4.5f).

In general, multiple linear regression models constructed using the satellite-derived variables as predictors and NPF characteristics as predictands explain more of the variability in GR, J_n, SP, and $N_{n\text{-}100nm}$ at each site than a random model with equal sample size and number of predictors, indicating that the satellite-based predictors exhibit some explanatory skill in characterizing NPF events over North America (Figure 4.6). The multiple linear regression models exhibit higher explanatory power for J_n, SP, and $N_{n\text{-}100nm}$ than for GR, indicating that the proxy variables are better able to capture the intensity of NPF events than the growth rates (Figure 4.6), potentially because the species that participate in nucleation and subsequent growth may differ [*Kulmala et al.*, 2004]. Further, although there is some site-to-site consistency in terms of which predictor variables have significant coefficients in the models, the absolute form of the regression models is variable from site-to-site, and generally the r^2 of the regression models is higher in the leaf-dormant periods (Figure 4.6 and 4.7).

At all sites UV has a positive β_i for regression equations of J_n (and $N_{n\text{-}100nm}$) particularly in leaf-dormant periods. Consistent with higher UV on leaf-dormant NPF event days (Table 4.3), this indicates that UV not only controls whether NPF occurs, but also the intensity (J_n). Conversely, increased UV is associated with decreased SP, consistent with higher formation rates increasing particle loss through self-coagulation and reducing survival probability of individual particles. In general, β_i for AOD×AE are negative in equations for J_n and $N_{n\text{-}100nm}$, particularly during the leaf-active period. AOD×AE has a significant positive β_i for SP during leaf-active events at MMSFa, but a negative β_i for SP at SGP and MMSFb, indicating the controls on survival probabilities may vary both in space and time. Higher AOD×AE is expected to reduce SP by increasing coagulation loss, but as discussed above AOD×AE appears to be driven by anthropogenic emissions at MMSF and SGP (Figure 4.4c and e), and thus may also

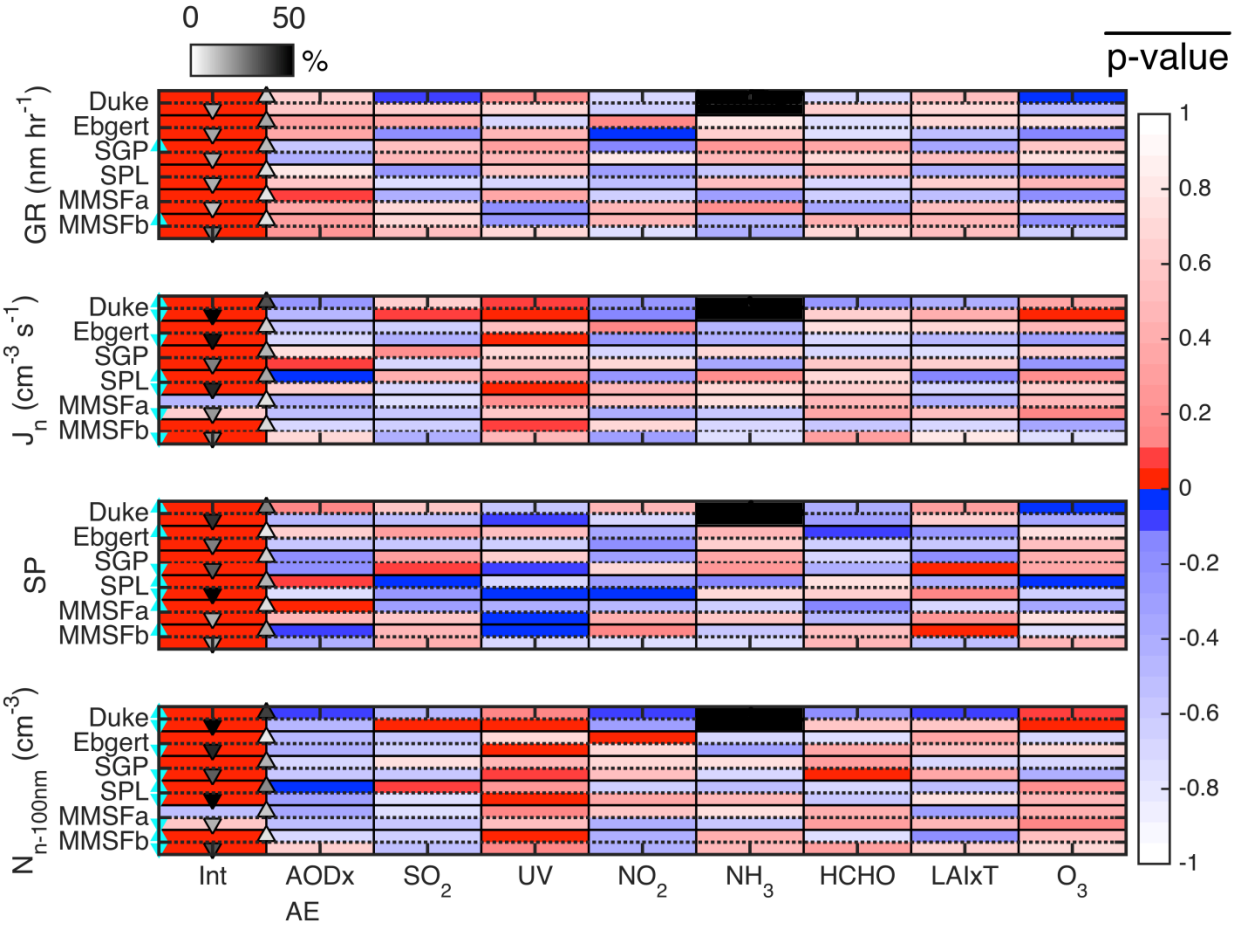

Figure 4.6. P-value of the regression coefficients on each of the predictor variables averaged across the 5 training/validation cross-validation data sub-sets and across the 1000 iterations of sub-sampling, used in the multiple linear regression (eq. 7) to predict event metrics (growth rate, formation rate, and survival probability) and daily mean ultrafine particle (Dp < 100 nm; $N_{n-100nm}$, where n is the instrument minimum Dp detection limit) concentrations. Satellite-based measurements of NH_3 are not available prior to 2008, and thus are not available for Duke (black fill) and portions of the Egbert and MMSFa PSD measurement days. For each site, the first and second rows are leaf-active and leaf-dormant periods, respectively. Red and blue indicate a positive and negative coefficient weighting, respectively, with the opacity indicating the significance (mean p-value) of the weighing. A cyan triangle on the ordinate indicates a significant p-value ($\alpha = 0.1$) for the regression model trained on the complete dataset, and full model coefficients are given in Tables S1 and S2. The shading of the second (black) triangles (upward = leaf-active, downward = leaf-dormant; abscissa offset solely for visibility) are the percentage of data sub-sets that show significantly ($\alpha = 0.1$) higher r^2 in predicting the NPF characteristics than expected by random chance (F-statistic for the sample size and number of predictors).

indicate the presence of high precursor concentrations. Increased precursor concentrations can increase GR (e.g. AOD×AE exhibits positive β_i for GR at MMSFa) and therefore increase SP, which may explain the positive association between AOD×AE and SP at MMSFa and the lack of

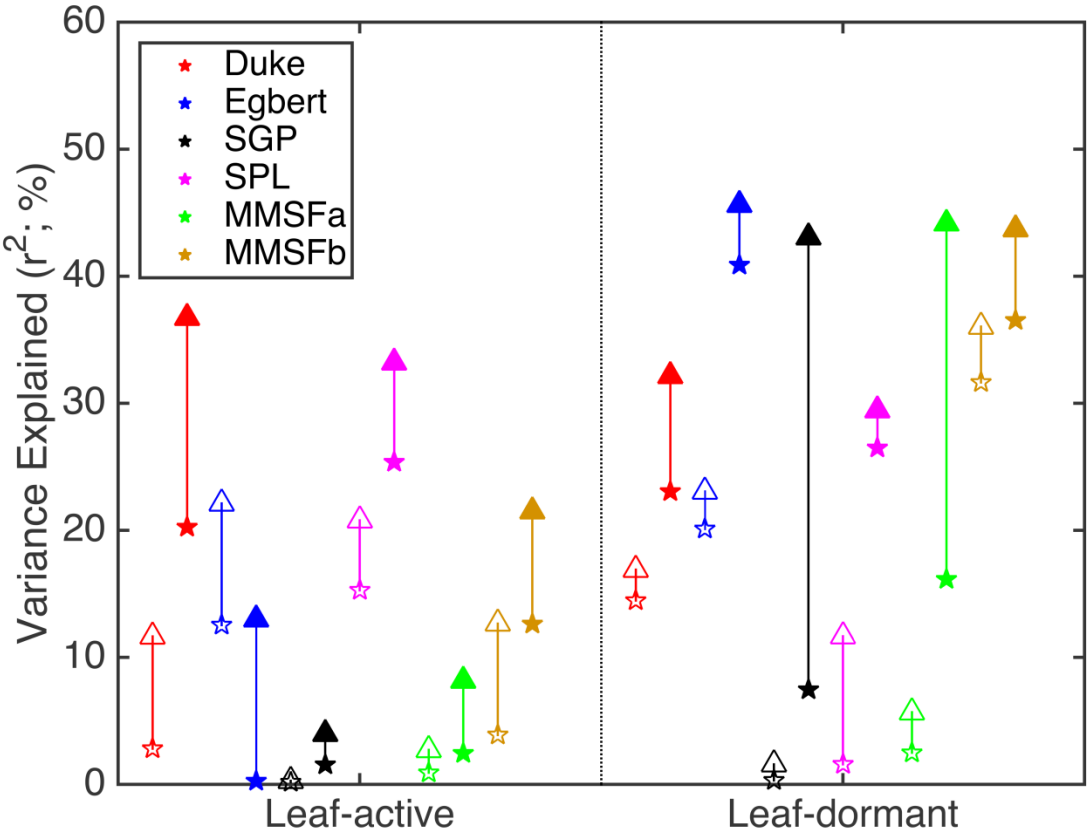

Figure 4.7. Variance of daily mean UFP particle concentration ($N_{n\text{-}100nm}$) explained (r^2) for each data set using a simple model (stars; where in the predictors are: AOD×AE, SO_2, and UV [Kulmala et al., 2011; Crippa et al., 2013; Sundström et al., 2015]) and the full model developed herein (triangles; wherein the predictors are: AOD×AE, SO_2, UV, NO_2, NH_3, HCHO, LAI×T, and O_3), during all measurement days (open symbols) and during only event days (filled symbols).

AOD×AE dependence in the MMSFa regression tree (Figure 4.5). The sign and significance of the β_i weights on SO_2, NO_2, NH_3, HCHO, and O_3 are highly variable by site and leaf activity (Tables S1 and S2), which may reflect differential NPF mechanisms in space and time, and thus explain the site-to-site differences in NPF frequency and characteristics. For example: SO_2 has a positive, significant β_i for $N_{n\text{-}100nm}$ at SPL (leaf-active) and Duke (leaf-dormant), but generally negative β_i elsewhere; NO_2 has a negative, significant β_i for $N_{n\text{-}100nm}$ at Duke (leaf-active), but positive, significant β_i at Egbert (leaf-active), and variable sign elsewhere; and NH_3, HCHO, and O_3 are generally split between positive and negative β_i across the sites for all NPF metrics. As

each of the predictor variables are significant at at least one site, we retain them all, but site-to-site variability in which predictor variable(s) are most important suggests a key challenge in building a generalizable model.

Impact of sub-sampling on stability of analyses

The regression trees described in Section 3.3 were built using all measurement days, but were also built after withholding 20% of the data, for cross-validation analysis. The full model regression trees had re-substitution accuracies of 85-91%. When the testing data is withheld from the training models, the cross-validation accuracies averaged 76-90% (mean standard deviation of accuracies ~< 1%) across 1000 iterations of cross-validation (Figure 4.5). Thus, sub-sampling only moderately reduces the models' accuracy, and the results are relatively stable independent of the specific sub-sampled days.

Running the multiple linear regressions as Monte Carlo experiments, and iterating the cross-validation analysis, provides insights into the models' stability. Without cross-validation, multiple linear regression models explain a significant amount of the observed variability in the NPF characteristics (see cyan triangles in Figure 4.6). However, when the cross-validation is performed, it is not uncommon that the training datasets show poor performance in predicting characteristics (particularly for GR; Figure 4.6) when some of the validation data were withheld from training the models. This implies the models are not generalizable. Conversely, the models for J_n and $N_{n\text{-}100nm}$ at Duke, Egbert (leaf-dormant), and SPL (leaf-dormant), and SP at Duke (leaf-dormant) and SPL (leaf-dormant) seem robust, independent of the data set sub-sampling, indicating the precise measurement dates may not significantly impact the inferences drawn herein.

Improved satellite-based proxy for ultrafine particle concentrations

Both the simple proxy model, where UFP total number concentrations ($N_{n\text{-}100nm}$) are predicted using only AOD×AE, SO_2, and UV as predictors, and the full models, which include additional predictor variables: NO_2, NH_3, HCHO, LAI×T, and O_3, have much higher explanatory skill when only NPF event days are considered (Figure 4.7). The full model improves explanatory skill over the simpler model at all sites during both leaf-active and leaf-dormant periods (Figure 4.7), and is associated with variance explanation (r^2) on NPF event days of 29-46% during the leaf-dormant period and 4-37% during leaf-active periods (Figure 4.7). The increase in variance explanation with the addition of extra predictors is particularly large at Duke, SGP, and MMSF. These are locations influenced by high organic emissions (quantified using HCHO, LAI×T, and O_3), anthropogenic emissions (quantified using NO_2), and ternary nucleation precursor emissions (e.g. NH_3) (Figure 4.1) [*Goebes et al.*, 2003], and may be indicative of an enhanced role of these species in dictating UFP concentrations at these sites.

Discussion and conclusions

We examine the frequency, persistence, and characteristics of NPF events at five locations across North America, and employ statistical analysis of satellite-based measurements of atmospheric composition to explain spatial similarities and variability in NPF frequency, autocorrelation, formation rates, growth rates, survival probabilities, and daily mean ultrafine particle concentrations. Despite large geographic separation, and vastly different local land use and point source pollution emissions between the sites, NPF is observed at all sites with peak frequencies in spring and fall, and exhibits positive one-day autocorrelation. Accordingly, the temporal modes of variability and spatial scales of coherence of the remotely sensed variables thought to control NPF also show considerable site-to-site consistency, and are typically

coherent on larger scales at sites with larger one-day autocorrelation in NPF occurrence. There is also broad agreement in terms of the conditions associated with NPF events between the sites: NPF is more frequent during moderate LAI×T, low AOD×AE and low HCHO during leaf-active periods, and high UV in leaf-dormant periods. The spatial consistencies in the primary drivers of NPF may explain why simplified nucleation schemes can be used with some skill in global models to characterize the impact of NPF on particle size distributions and CCN concentrations [*Spracklen et al.*, 2008b]. However, event characteristics (J_n, GR, SP, and $N_{n\text{-}100nm}$) exhibit greater site-to-site variability in terms of their dependence on the remote-sensing predictors. Site-to-site variability in NPF characteristics and the corresponding variability in satellite-based measurements of the drivers of GR, J_n, SP, and $N_{n\text{-}100nm}$ may explain the spatial variability in the performance of simplified NPF schemes [*Lee et al.*, 2013]. Generalized schemes with a single NPF mechanism and set of coefficients may not be able to capture the variability in precise nucleation mechanisms [*Yu et al.*, 2015] and/or importance of specific precursor species at the different sites. Proxy models of total UFP concentrations that expand the suite of remote sensing predictors exhibit improved variance explanation relative to simpler models that have been previously proposed [*Kulmala et al.*, 2011; *Crippa et al.*, 2013; *Sundström et al.*, 2015] (Figure 4.7). However, the model coefficients and hence the magnitude and even sign of the dependencies of $N_{n\text{-}100nm}$ on the suite of predictors considered (AOD×AE, SO_2, UV, NO_2, NH_3, HCHO, LAI×T, O_3) (Figure 4.6) implies great challenges to generating a single generalizable proxy. We recommend future NPF schemes try to reproduce the (spatially variable) relationships between NPF and its drivers presented here, and connect existing theory with ground and satellite observations to evaluate new model treatments of NPF before accepting them, and ultimately improve understanding of regional to global scale impacts of NPF on climate.

Future research is necessary to examine how satellite-based measurement error impacts the explanatory skill (and variability) of the proxies and to further examine the feasibility of developing global proxies for NPF occurrence and characteristics. Further, it may be appropriate to develop the proxies using non-linear techniques or additional (or compound) variables. Given the high uncertainty in direct satellite measurements, the proxies may benefit from use of variables from reanalysis products such as MERRA-2 [*Bosilovich et al.*, 2016] or output from satellite-constrained chemical transport models (CTM) since a number of CTM now exhibit skill for many of the predictor variables used here [*Westervelt et al.*, 2013]. If such a proxy could be found it may provide computationally efficient first order estimates of the impact of NPF on particle size distributions, CCN concentrations, and ultimately the potential impact of NPF on climate.

Acknowledgments

Funding was supplied by: NASA Earth and Space Science Fellowship Program - Grant "14-EARTH14F-0207" (RCS), L'Oréal-UNESCO UK and Ireland Fellowship For Women In Science (PC), Belgian F.R.S-FNRS (LC), Boursier FRIA (SW), NSF (1102309, 1517365) and NASA (NNX16AG31G) (SCP). We also gratefully acknowledge computational resources provided by the Lilly Endowment, Inc. to the Indiana University Pervasive Technology Institute and the Indiana METACyt Initiative. The MODIS and OMI satellite data were collected under the NASA Earth-Sun System Division and Science Mission Directorate, SGP PSD data were acquired under the DoE Atmospheric Radiation Measurement Program. SPL is a permittee of the Medicine-Bow Routt National Forests, and we acknowledge assistance from Randolph Borys and Ian McCubbin. The views expressed in this article are those of the author(s) and do not necessarily represent the views or policies of the U.S. Environmental Protection Agency.

Data are available from: MODIS and OMI satellite data (NASA, http://reverb.echo.nasa.gov/reverb), IASA NH_3 (L. Clarisse, lclariss@ulb.ac.be), PSD from Duke (J. T. Walker,Walker.Johnt@epa.gov), Egbert (W. R. Leaitch, richard.leaitch@canada.ca), SGP (US DoE, http://www.archive.arm.gov/), SPL (A. G. Hallar, gannet.hallar@dri.edu), and MMSF (S. C. Pryor, sp2279@cornell.edu).

REFERENCES

Ackerman, T. P., and G. M. Stokes (2003), The atmospheric radiation measurement program, *Phys. Today*, *56*(PNNL-SA-37894), 38–44.

Almeida, J., S. Schobesberger, A. Kürten, I. K. Ortega, O. Kupiainen-Määttä, A. P. Praplan, A. Adamov, A. Amorim, F. Bianchi, and M. Breitenlechner (2013), Molecular understanding of sulphuric acid-amine particle nucleation in the atmosphere, *Nature*, *502*(7471), 359–363.

Anderson, T. L., R. J. Charlson, D. M. Winker, J. A. Ogren, and K. Holmén (2003), Mesoscale variations of tropospheric aerosols*, *J. Atmos. Sci.*, *60*(1), 119–136.

Aneja, V. P., D. R. Nelson, P. A. Roelle, J. T. Walker, and W. Battye (2003), Agricultural ammonia emissions and ammonium concentrations associated with aerosols and precipitation in the southeast United States, *J. Geophys. Res. Atmos.*, *108*(D4), doi:10.1029/2002JD002271.

Ångström, A. (1964), The parameters of atmospheric turbidity, *Tellus*, *16*(1), 64–75.

Bosilovich, M. G., R. Lucchesi, and M. Suarez (2016), MERRA-2: File Specification. GMAO Office Note No. 9 (Version 1.1), 73 pp, available from http://gmao.gsfc.nasa.gov/pubs/office_notes,

Boy, M., B. Bonn, J. Kazil, N. Lovejoy, A. Turnipseed, J. Greenberg, T. Karl, L. Mauldin, E. Kusciuch, and J. Smith (2007), Relevance of several nucleation theories in different environments, in *Nucleation and Atmospheric Aerosols*, pp. 87–91, Springer.

Brinksma, E. J., K. F. Boersma, P. F. Levelt, and R. D. McPeters (2003), OMI validation requirements document, Version 1, *Rep. RS-OMIE-KNMI-345. Available http//projects.knmi.nl/omi/documents/validation/RS-OMIE-KNMI-345_i1.pdf*, 66 pages.

Carslaw, K. S., L. A. Lee, C. L. Reddington, K. J. Pringle, A. Rap, P. M. Forster, G. W. Mann, D. V Spracklen, M. T. Woodhouse, and L. A. Regayre (2013), Large contribution of natural aerosols to uncertainty in indirect forcing, *Nature*, *503*(7474), 67–71.

Chance, K. (2002), OMI algorithm theoretical basis document, volume IV: OMI trace gas algorithms, *Available at http://eospso.gsfc.nasa.gov/sites/default/files/atbd/ATBD-OMI-04.pdf*.

Chance, K., P. I. Palmer, R. J. D. Spurr, R. V Martin, T. P. Kurosu, and D. J. Jacob (2000), Satellite observations of formaldehyde over North America from GOME, *Geophys. Res. Lett.*, *27*(21), 3461–3464.

Clarisse, L., C. Clerbaux, F. Dentener, D. Hurtmans, and P.-F. Coheur (2009), Global ammonia distribution derived from infrared satellite observations, *Nat. Geosci.*, *2*(7), 479–483.

Crippa, P., and S. C. Pryor (2013), Spatial and temporal scales of new particle formation events in eastern North America, *Atmos. Environ.*, *75*, 257–264, doi:10.1016/j.atmosenv.2013.04.051.

Crippa, P., D. Spracklen, and S. C. Pryor (2013), Satellite-derived estimates of ultrafine particle concentrations over eastern North America, *J. Geophys. Res. Atmos.*, *118*(17), 9968–9981, doi:10.1002/jgrd.50707.

Fang, H., S. Wei, and S. Liang (2012), Validation of MODIS and CYCLOPES LAI products using global field measurement data, *Remote Sens. Environ.*, *119*, 43–54.

Fioletov, V. E., C. A. McLinden, N. Krotkov, M. D. Moran, and K. Yang (2011), Estimation of SO_2 emissions using OMI retrievals, *Geophys. Res. Lett.*, *38*(21), doi:10.1029/2011GL049402.

Goebes, M. D., R. Strader, and C. Davidson (2003), An ammonia emission inventory for

fertilizer application in the United States, *Atmos. Environ.*, *37*(18), 2539–2550.
Guenther, A. B., P. R. Zimmerman, P. C. Harley, R. K. Monson, and R. Fall (1993), Isoprene and monoterpene emission rate variability: model evaluations and sensitivity analyses, *J. Geophys. Res. Atmos.*, *98*(D7), 12609–12617.
Hallar, A. G., D. H. Lowenthal, G. Chirokova, R. D. Borys, and C. Wiedinmyer (2011), Persistent daily new particle formation at a mountain-top location, *Atmos. Environ.*, *45*(24), 4111–4115.
Hallar, A. G., R. Petersen, I. B. McCubbin, D. Lowenthal, S. Lee, E. Andrews, and F. Yu (2016), Climatology of new particle formation and corresponding precursors at Storm Peak Laboratory, *Aerosol Air Qual. Res.*, *16*(3), 816–826.
Helmig, D. (1997), Ozone removal techniques in the sampling of atmospheric volatile organic trace gases, *Atmos. Environ.*, *31*(21), 3635–3651.
Henze, D. K., and J. H. Seinfeld (2006), Global secondary organic aerosol from isoprene oxidation, *Geophys. Res. Lett.*, *33*(9), doi:10.1029/2006GL025976.
Hussein, T., H. Junninen, P. Tunved, A. Kristensson, M. Dal Maso, I. Riipinen, P. P. Aalto, H.-C. Hansson, E. Swietlicki, and M. Kulmala (2009), Time span and spatial scale of regional new particle formation events over Finland and Southern Sweden, *Atmos. Chem. Phys*, *9*(14), 4699–4716.
Hyvönen, S., H. Junninen, L. Laakso, M. D. Maso, T. Grönholm, B. Bonn, P. Keronen, P. Aalto, V. Hiltunen, and T. Pohja (2005), A look at aerosol formation using data mining techniques, *Atmos. Chem. Phys.*, *5*(12), 3345–3356.
Jeong, C.-H., G. J. Evans, M. L. McGuire, R.-W. Chang, J. P. D. Abbatt, K. Zeromskiene, M. Mozurkewich, S.-M. Li, and W. R. Leaitch (2010), Particle formation and growth at five rural and urban sites, *Atmos. Chem. Phys.*, *10*(16), 7979–7995.
Jokinen, T., T. Berndt, R. Makkonen, V.-M. Kerminen, H. Junninen, P. Paasonen, F. Stratmann, H. Herrmann, A. B. Guenther, and D. R. Worsnop (2015), Production of extremely low volatile organic compounds from biogenic emissions: Measured yields and atmospheric implications, *Proc. Natl. Acad. Sci.*, *112*(23), 7123–7128.
Kiendler-Scharr, A., J. Wildt, M. Dal Maso, T. Hohaus, E. Kleist, T. F. Mentel, R. Tillmann, R. Uerlings, U. Schurr, and A. Wahner (2009), New particle formation in forests inhibited by isoprene emissions, *Nature*, *461*(7262), 381–384.
Kirkby, J., J. Curtius, J. Almeida, E. Dunne, J. Duplissy, S. Ehrhart, A. Franchin, S. Gagné, L. Ickes, and A. Kürten (2011), Role of sulphuric acid, ammonia and galactic cosmic rays in atmospheric aerosol nucleation, *Nature*, *476*(7361), 429–433.
Knol, A. B., J. J. de Hartog, H. Boogaard, P. Slottje, J. P. van der Sluijs, E. Lebret, F. R. Cassee, J. A. Wardekker, J. G. Ayres, and P. J. Borm (2009), Expert elicitation on ultrafine particles: likelihood of health effects and causal pathways, *Part. Fibre Toxicol.*, *6*(1), 19, doi:10.1186/1743-8977-6-19.
Krotkov, N. A., S. A. Carn, A. J. Krueger, P. K. Bhartia, and K. Yang (2006), Band residual difference algorithm for retrieval of SO_2 from the Aura Ozone Monitoring Instrument (OMI), *Geosci. Remote Sensing, IEEE Trans.*, *44*(5), 1259–1266.
Krotkov, N. A., B. McClure, R. R. Dickerson, S. A. Carn, C. Li, P. K. Bhartia, K. Yang, A. J. Krueger, Z. Li, and P. F. Levelt (2008), Validation of SO_2 retrievals from the Ozone Monitoring Instrument over NE China, *J. Geophys. Res. Atmos.*, *113*(D16), doi:10.1029/2007JD008818.
Kuang, C., P. H. McMurry, A. V McCormick, and F. L. Eisele (2008), Dependence of nucleation

rates on sulfuric acid vapor concentration in diverse atmospheric locations, *J. Geophys. Res. Atmos.*, *113*(D10), doi:10.1029/2007JD009253.
Kulmala, M., L. Pirjola, and J. M. Mäkelä (2000), Stable sulphate clusters as a source of new atmospheric particles, *Nature*, *404*(6773), 66–69.
Kulmala, M., H. Vehkamäki, T. Petäjä, M. Dal Maso, A. Lauri, V.-M. Kerminen, W. Birmili, and P. H. McMurry (2004), Formation and growth rates of ultrafine atmospheric particles: a review of observations, *J. Aerosol Sci.*, *35*(2), 143–176.
Kulmala, M., A. Arola, T. Nieminen, L. Riuttanen, L. Sogacheva, G. de Leeuw, V.-M. Kerminen, and K. E. J. Lehtinen (2011), The first estimates of global nucleation mode aerosol concentrations based on satellite measurements, *Atmos. Chem. Phys.*, *11*(21), 10791–10801.
Kulmala, M., J. Kontkanen, H. Junninen, K. Lehtipalo, H. E. Manninen, T. Nieminen, T. Petäjä, M. Sipilä, S. Schobesberger, and P. Rantala (2013), Direct observations of atmospheric aerosol nucleation, *Science*, *339*(6122), 943–946.
Lamsal, L. N., R. V Martin, A. Van Donkelaar, M. Steinbacher, E. A. Celarier, E. Bucsela, E. J. Dunlea, and J. P. Pinto (2008), Ground-level nitrogen dioxide concentrations inferred from the satellite-borne Ozone Monitoring Instrument, *J. Geophys. Res. Atmos.*, *113*(D16), doi:10.1029/2007JD009235.
Land Processes Distributed Active Archive Center (LP DAAC) (2014), Land Cover Type Yearly L3 Global 0.05Deg CMG, V051. NASA EOSDIS LP DAAC, USGS Earth Resources Observation and Science (EROS) Center, Sioux Falls, South Dakota (https://lpdaac.usgs.gov), accessed 11/13/2015, at http://dx.doi.org/10.5067/MODIS/MCD12C1.006,
Lee, L. A., K. J. Pringle, C. L. Reddington, G. W. Mann, P. Stier, D. V Spracklen, J. R. Pierce, and K. S. Carslaw (2013), The magnitude and causes of uncertainty in global model simulations of cloud condensation nuclei, *Atmos. Chem. Phys*, *13*(17), 8879–8914.
Levy, R. C., L. A. Remer, R. G. Kleidman, S. Mattoo, C. Ichoku, R. Kahn, and T. F. Eck (2010), Global evaluation of the Collection 5 MODIS dark-target aerosol products over land, *Atmos. Chem. Phys.*, *10*(21), 10399–10420.
Levy, R. C., S. Mattoo, L. A. Munchak, L. A. Remer, A. M. Sayer, F. Patadia, and N. C. Hsu (2013), The Collection 6 MODIS aerosol products over land and ocean, *Atmos. Meas. Tech.*, *6*, 2989–3034.
Mast, M. A., D. H. Campbell, and G. P. Ingersoll (2005), *Effects of emission reductions at the Hayden powerplant on precipitation, snowpack, and surface-water chemistry in the Mount Zirkel Wilderness Area, Colorado, 1995-2003*, U.S. Geological Survey Scientific Investigations Report 2005–5167, 32 p. Available at: https://store.usgs.gov/yimages/PDF/2.
McLinden, C. A., V. Fioletov, K. F. Boersma, S. K. Kharol, N. Krotkov, L. Lamsal, P. A. Makar, R. V Martin, J. P. Veefkind, and K. Yang (2014), Improved satellite retrievals of NO_2 and SO_2 over the Canadian oil sands and comparisons with surface measurements, *Atmos. Chem. Phys.*, *17*(7), 3637–3656.
Merikanto, J., D. V Spracklen, G. W. Mann, S. J. Pickering, and K. S. Carslaw (2009), Impact of nucleation on global CCN, *Atmos. Chem. Phys.*, *9*(21), 8601–8616.
Metzger, A., B. Verheggen, J. Dommen, J. Duplissy, A. S. H. Prevot, E. Weingartner, I. Riipinen, M. Kulmala, D. V Spracklen, and K. S. Carslaw (2010), Evidence for the role of organics in aerosol particle formation under atmospheric conditions, *Proc. Natl. Acad. Sci.*, *107*(15), 6646–6651.

Millet, D. B., D. J. Jacob, S. Turquety, R. C. Hudman, S. Wu, A. Fried, J. Walega, B. G. Heikes, D. R. Blake, and H. B. Singh (2006), Formaldehyde distribution over North America: Implications for satellite retrievals of formaldehyde columns and isoprene emission, *J. Geophys. Res. Atmos.*, *111*(D24), doi:10.1029/2005JD006853.

Millet, D. B., D. J. Jacob, K. F. Boersma, T. Fu, T. P. Kurosu, K. Chance, C. L. Heald, and A. Guenther (2008), Spatial distribution of isoprene emissions from North America derived from formaldehyde column measurements by the OMI satellite sensor, *J. Geophys. Res. Atmos.*, *113*(D2), doi:10.1029/2007JD008950.

O'Dowd, C. D., P. Aalto, K. Hmeri, M. Kulmala, and T. Hoffmann (2002), Aerosol formation: Atmospheric particles from organic vapours, *Nature*, *416*(6880), 497–498.

OMI Team (2012), *Ozone monitoring instrument (OMI) data user's guide*, OMI-DUG-5.0. Available at: http://disc.sci.gsfc.nasa.gov/Aura/data-holdings/additional/documentation/README.OMI_DUG.pdf.

Paasonen, P., T. Nieminen, E. Asmi, H. E. Manninen, T. Petäjä, C. Plass-Dülmer, H. Flentje, W. Birmili, A. Wiedensohler, and U. Horrak (2010), On the roles of sulphuric acid and low-volatility organic vapours in the initial steps of atmospheric new particle formation, *Atmos. Chem. Phys.*, *10*(22), 11223–11242.

Paasonen, P., A. Asmi, T. Petäjä, M. K. Kajos, M. Äijälä, H. Junninen, T. Holst, J. P. D. Abbatt, A. Arneth, and W. Birmili (2013), Warming-induced increase in aerosol number concentration likely to moderate climate change, *Nat. Geosci.*, *6*(6), 438–442.

Pierce, J. R., W. R. Leaitch, J. Liggio, D. M. Westervelt, C. D. Wainwright, J. P. D. Abbatt, L. Ahlm, W. Al-Basheer, D. J. Cziczo, and K. L. Hayden (2012), Nucleation and condensational growth to CCN sizes during a sustained pristine biogenic SOA event in a forested mountain valley, *Atmos. Chem. Phys.*, *12*(7), 3147–3163.

Pierce, J. R., D. M. Westervelt, S. A. Atwood, E. A. Barnes, and W. R. Leaitch (2014), New-particle formation, growth and climate-relevant particle production in Egbert, Canada: analysis from 1 year of size-distribution observations, *Atmos. Chem. Phys.*, *14*(16), 8647–8663.

Pillai, P., A. Khlystov, J. Walker, and V. Aneja (2013), Observation and analysis of particle nucleation at a forest site in southeastern US, *Atmosphere*, *4*(2), 72–93.

Pryor, S. C., A. M. Spaulding, and R. J. Barthelmie (2010), New particle formation in the Midwestern USA: Event characteristics, meteorological context and vertical profiles, *Atmos. Environ.*, *44*(35), 4413–4425, doi:10.1016/j.atmosenv.2010.07.045.

Pryor, S. C., R. J. Barthelmie, L. L. Sørensen, J. G. McGrath, P. Hopke, and T. Petäjä (2011), Spatial and vertical extent of nucleation events in the Midwestern USA: insights from the Nucleation In ForesTs (NIFTy) experiment, *Atmos. Chem. Phys.*, *11*(4), 1641–1657, doi:10.5194/acp-11-1641-2011.

Pryor, S. C., K. E. Hornsby, and K. A. Novick (2014), Forest canopy interactions with nucleation mode particles, *Atmos. Chem. Phys.*, *14*(21), 11985–11996, doi:10.5194/acp-14-11985-2014.

Qi, X. M., A. J. Ding, W. Nie, T. Petäjä, V.-M. Kerminen, E. Herrmann, Y. N. Xie, L. F. Zheng, H. Manninen, and P. Aalto (2015), Aerosol size distribution and new particle formation in the western Yangtze River Delta of China: 2 years of measurements at the SORPES station, *Atmos. Chem. Phys.*, *15*, 12445–12464.

Riccobono, F., S. Schobesberger, C. E. Scott, J. Dommen, I. K. Ortega, L. Rondo, J. Almeida, A. Amorim, F. Bianchi, and M. Breitenlechner (2014), Oxidation products of biogenic

emissions contribute to nucleation of atmospheric particles, *Science*, *344*(6185), 717–721.
Riipinen, I., T. Yli-Juuti, J. R. Pierce, T. Petäjä, D. R. Worsnop, M. Kulmala, and N. M. Donahue (2012), The contribution of organics to atmospheric nanoparticle growth, *Nat. Geosci.*, *5*(7), 453–458.
Rose, C., K. Sellegri, E. Freney, R. Dupuy, A. Colomb, J.-M. Pichon, M. Ribeiro, T. Bourianne, F. Burnet, and A. Schwarzenboeck (2015), Airborne measurements of new particle formation in the free troposphere above the Mediterranean Sea during the HYMEX campaign, *Atmos. Chem. Phys.*, *15*(17), 10203–10218.
Russell, A. R., L. C. Valin, and R. C. Cohen (2012), Trends in OMI NO_2 observations over the United States: effects of emission control technology and the economic recession, *Atmos. Chem. Phys.*, *12*(24), 12197–12209.
Seinfeld, J. H., and S. N. Pandis (2006), *Atmospheric chemistry and physics: from air pollution to climate change*, Hoboken, NJ: Wiley.
Sipilä, M., T. Berndt, T. Petäjä, D. Brus, J. Vanhanen, F. Stratmann, J. Patokoski, R. L. Mauldin, A.-P. Hyvärinen, and H. Lihavainen (2010), The role of sulfuric acid in atmospheric nucleation, *Science*, *327*(5970), 1243–1246.
Smith, J. N., K. F. Moore, F. L. Eisele, D. Voisin, A. K. Ghimire, H. Sakurai, and P. H. McMurry (2005), Chemical composition of atmospheric nanoparticles during nucleation events in Atlanta, *J. Geophys. Res. Atmos.*, *110*(D22), doi:10.1029/2005JD005912.
Smith, J. N., M. J. Dunn, T. M. VanReken, K. Iida, M. R. Stolzenburg, P. H. McMurry, and L. G. Huey (2008), Chemical composition of atmospheric nanoparticles formed from nucleation in Tecamac, Mexico: Evidence for an important role for organic species in nanoparticle growth, *Geophys. Res. Lett.*, *35*(4), doi:10.1029/2007GL032523.
Spracklen, D. V, B. Bonn, and K. S. Carslaw (2008a), Boreal forests, aerosols and the impacts on clouds and climate, *Philos. Trans. R. Soc. London A Math. Phys. Eng. Sci.*, *366*(1885), 4613–4626.
Spracklen, D. V, K. S. Carslaw, M. Kulmala, V. Kerminen, S. Sihto, I. Riipinen, J. Merikanto, G. W. Mann, M. P. Chipperfield, and A. Wiedensohler (2008b), Contribution of particle formation to global cloud condensation nuclei concentrations, *Geophys. Res. Lett.*, *35*(6), doi:10.1029/2007GL033038.
Sullivan, R. C., and S. C. Pryor (2016), Dynamic and chemical controls on new particle formation occurrence and characteristics from in situ and satellite-based measurements, *Atmos. Environ.*, *127*, 316–325, doi:10.1016/j.atmosenv.2015.12.050.
Sullivan, R. C., R. C. Levy, and S. C. Pryor (2015), Spatiotemporal coherence of mean and extreme aerosol particle events over eastern North America as observed from satellite, *Atmos. Environ.*, *112*, 126–135, doi:10.1016/j.atmosenv.2015.04.026.
Sundström, A.-M., A. Nikandrova, K. Atlaskina, T. Nieminen, V. Vakkari, L. Laakso, J. P. Beukes, A. Arola, P. G. van Zyl, and M. Josipovic (2015), Characterization of satellite-based proxies for estimating nucleation mode particles over South Africa, *Atmos. Chem. Phys.*, *15*(9), 4983–4996.
Surratt, J. D., S. M. Murphy, J. H. Kroll, N. L. Ng, L. Hildebrandt, A. Sorooshian, R. Szmigielski, R. Vermeylen, W. Maenhaut, and M. Claeys (2006), Chemical composition of secondary organic aerosol formed from the photooxidation of isoprene, *J. Phys. Chem. A*, *110*(31), 9665–9690.
US Environmental Protection Agency (2011), 2011 National Emissions Inventory, , Downloaded from https://www3.epa.gov/ttnchie1/net/.

Valente, R. J., R. E. Imhoff, R. L. Tanner, J. F. Meagher, P. H. Daum, R. M. Hardesty, R. M. Banta, R. J. Alvarez, R. T. McNider, and N. V Gillani (1998), Ozone production during an urban air stagnation episode over Nashville, Tennessee, *J. Geophys. Res. Atmos.*, *103*(D17), 22555–22568.

van Donkelaar, A., R. V Martin, and R. J. Park (2006), Estimating ground-level $PM_{2.5}$ using aerosol optical depth determined from satellite remote sensing, *J. Geophys. Res. Atmos.*, *111*(D21), doi:10.1029/2005JD006996.

van Donkelaar, A., R. V Martin, R. J. D. Spurr, E. Drury, L. A. Remer, R. C. Levy, and J. Wang (2013), Optimal estimation for global ground-level fine particulate matter concentrations, *J. Geophys. Res. Atmos.*, *118*(11), 5621–5636.

Vinken, G. C. M., K. F. Boersma, A. van Donkelaar, and L. Zhang (2014), Constraints on ship NO_x emissions in Europe using GEOS-Chem and OMI satellite NO_2 observations, *Atmos. Chem. Phys.*, *14*(3), 1353–1369.

Wan, Z. (2008), New refinements and validation of the MODIS land-surface temperature/emissivity products, *Remote Sens. Environ.*, *112*(1), 59–74.

Westervelt, D. M., J. R. Pierce, I. Riipinen, W. Trivitayanurak, A. Hamed, M. Kulmala, A. Laaksonen, S. Decesari, and P. J. Adams (2013), Formation and growth of nucleated particles into cloud condensation nuclei: model–measurement comparison, *Atmos. Chem. Phys.*, *13*(15), 7645–7663.

Whitburn, S., M. Van Damme, L. Clarisse, S. Bauduin, C. Heald, J. Hadji-Lazaro, D. Hurtmans, M. A. Zondlo, C. Clerbaux, and P.-F. Coheur (2016), A flexible and robust neural network IASI-NH3 retrieval algorithm, *J. Geophys. Res. Atmos.*, *121*, doi:10.1002/2016JD024828.

Yu, F., and A. Hallar (2014), Difference in particle formation at a mountaintop location during spring and summer: Implications for the role of sulfuric acid and organics in nucleation, *J. Geophys. Res. Atmos.*, *119*(21), 12246–12255, doi:10.1002/2014JD022136.

Yu, F., and G. Luo (2009), Simulation of particle size distribution with a global aerosol model: contribution of nucleation to aerosol and CCN number concentrations, *Atmos. Chem. Phys.*, *9*(20), 7691–7710.

Yu, F. et al. (2015), Spring and summer contrast in new particle formation over nine forest areas in North America, *Atmos. Chem. Phys.*, *15*(24), 13993–14003, doi:10.5194/acpd-15-21271-2015.

Zhang, Q. I., C. O. Stanier, M. R. Canagaratna, J. T. Jayne, D. R. Worsnop, S. N. Pandis, and J. L. Jimenez (2004a), Insights into the chemistry of new particle formation and growth events in Pittsburgh based on aerosol mass spectrometry, *Environ. Sci. Technol.*, *38*(18), 4797–4809.

Zhang, R., I. Suh, J. Zhao, D. Zhang, E. C. Fortner, X. Tie, L. T. Molina, and M. J. Molina (2004b), Atmospheric new particle formation enhanced by organic acids, *Science*, *304*(5676), 1487–1490.

Zhang, Y., P. H. McMurry, F. Yu, and M. Z. Jacobson (2010), A comparative study of nucleation parameterizations: 1. Examination and evaluation of the formulations, *J. Geophys. Res. Atmos.*, *115*(D20), doi:10.1029/2010JD014150

Journal of Geophysical Research: Atmospheres

Supporting Information for

Using satellite-based measurements to explore spatiotemporal scales and variability of drivers of new particle formation

Sullivan, R. C.[1*], Crippa, P.[2], Hallar A. G.[3], Clarisse, L.[4], Whitburn, S.[4], Van Damme, M.[4], Leaitch, W. R.[5], Walker, J. T.[6], Khlystov, A.[7], and Pryor S.C.[1,8]

[1]Department of Earth and Atmospheric Sciences, Cornell University, Ithaca, NY, USA
[2]COMET, School of Civil Engineering and Geosciences, Newcastle University, Newcastle upon Tyne, UK
[3]Storm Peak Laboratory, Desert Research Institute, Steamboat Springs, CO, USA and Atmospheric Science Department, University of Utah, Salt Lake City, UT, USA
[4]Spectroscopie de l'Atmosphère, Service de Chimie Quantique et Photophysique, Université Libre de Bruxelles (ULB), Bruxelles, Belgium
[5]Environment Canada, Toronto, Ontario, Canada
[6]U.S. Environmental Protection Agency, Office of Research and Development, National Risk Management Research Laboratory, Durham, NC, USA
[7]Desert Research Institute, Reno, NV, USA
[8]Pervasive Technology Institute, Indiana University, Bloomington, IN, USA
*Corresponding author (rcs365@cornell.edu)

Contents of this file

Introduction

This supporting information provides a figure illustrating the spatial distribution of the predictor variables and tables containing the full model regression coefficients.

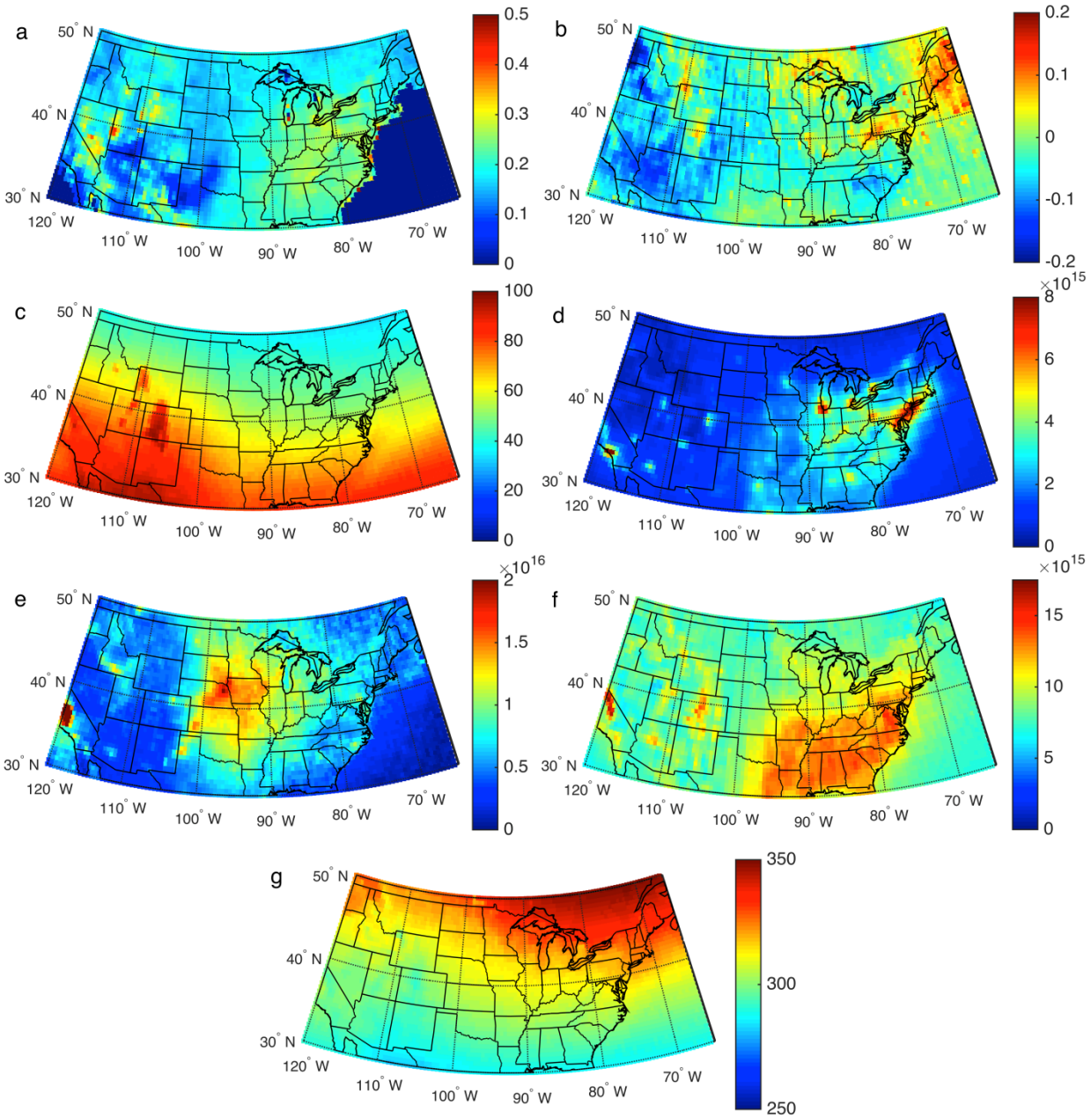

Figure S4.1. *Annual mean values for the predictor variables computed from the time series of all available measurements within each 0.5° × 0.5° grid cell: a) AOD×AE, b) SO_2 (DU), c) UV ($mW\ m^2\ nm^{-1}$), d) NO_2 ($molec.\ cm^{-2}$), e) NH_3 ($molec.\ cm^{-2}$), f) HCHO ($molec.\ cm^{-2}$), and g) O_3 (DU). The OMI measurements (SO_2, UV, NO_2, HCHO, O_3) are from 2004 – 2014, MODIS measurements (AOD×AE) are from 2000 – 2014, and IASI measurements (NH_3) are from 2008 – 2014. Due to the strong annual cycle in LAI, LAI×T is not shown.*

Table S4.1. *Multiple linear regression coefficient weights (eq. 7) for the models built using all measurements on leaf-active event days. Significant weights (α = 0.1) are in* ***bold****. Models with significant p-values are shown as cyan triangles in Figure 4.6.*

			Int.	AOD ×AE	SO_2 (DU)	UV (mW m^2 nm^{-1})	NO_2 ($\times10^{15}$ molec. cm^{-2})	NH_3 ($\times10^{15}$ molec. cm^{-2})	HCHO ($\times10^{16}$ molec. cm^{-2})	LAI×T (m^2 m^{-2} K)	O_3 (DU)
Leaf-active	Duke	GR (nm hr^{-1})	**1.83**	0.06	**-0.31**	0.20	-0.02	NaN	-0.05	0.10	**-0.30**
		J_n (cm^{-3} s^{-1})	**1.57**	-0.88	0.16	**1.15**	-0.81	NaN	-0.88	-0.61	0.60
		SP	**0.23**	**0.06**	0.02	-0.01	0.02	NaN	-0.03	0.04	**-0.06**
		N (cm^{-3})	**6156**	**-1630**	-571	**1267**	**-1502**	NaN	**-1160**	**-1449**	**1315**
	Egbert	GR (nm hr^{-1})	**1.82**	0.20	0.18	-0.05	**0.32**	-0.01	-0.03	0.03	0.00
		J_n (cm^{-3} s^{-1})	**0.70**	-0.09	-0.07	0.14	**0.32**	-0.10	0.04	0.09	0.16
		SP	**0.18**	0.01	0.04	0.03	-0.04	-0.01	**-0.08**	**-0.07**	0.00
		N (cm^{-3})	**4377**	-355	-205	33	**1089**	15	-24	621	-41
	SGP	GR (nm hr^{-1})	**0.72**	-0.03	0.04	0.08	**-0.11**	0.08	0.09	-0.07	0.04
		J_n (cm^{-3} s^{-1})	**0.39**	0.01	0.09	0.03	-0.01	0.02	-0.02	-0.02	0.03
		SP	**0.09**	-0.03	0.02	0.01	-0.02	0.02	-0.01	-0.03	0.02
		N (cm^{-3})	**4552**	-20	29	273	103	77	523	-81	-95
	SPL	GR (nm hr^{-1})	**1.64**	0.01	-0.11	0.13	-0.15	-0.15	0.06	-0.10	**-0.18**
		J_n (cm^{-3} s^{-1})	**1.30**	**-0.97**	0.16	0.93	-0.42	**1.08**	0.03	**-0.42**	0.43
		SP	**0.27**	**0.05**	**-0.06**	-0.02	-0.03	**-0.08**	0.00	-0.02	**-0.06**
		N (cm^{-3})	**4347**	**-1726**	**686**	1425	-88	-458	-99	-276	**790**
	MMSFa	GR (nm hr^{-1})	**2.22**	**0.51**	-0.10	0.12	-0.14	-0.13	-0.11	-0.11	**-0.26**
		J_n (cm^{-3} s^{-1})	**5.22**	-2.27	0.98	-1.27	-1.17	-0.88	1.20	-2.10	**3.07**
		SP	**0.09**	**0.06**	-0.01	-0.02	-0.02	0.00	**-0.04**	-0.01	-0.01
		N (cm^{-3})	**11625**	**-3346**	806	2121	-1105	-620	2137	**-4467**	**3203**
	MMSFb	GR (nm hr^{-1})	**2.50**	0.21	0.04	-0.24	0.12	-0.12	0.14	0.16	-0.20
		J_n (cm^{-3} s^{-1})	**2.20**	-0.31	-0.37	**1.65**	0.09	-0.32	-0.45	-0.29	-0.67
		SP	**0.08**	**-0.04**	0.01	**-0.05**	**0.03**	-0.01	0.01	**0.08**	0.00
		N (cm^{-3})	**8277**	-264	-295	**2619**	-701	797	-116	**-1871**	530

Table S4.2. *Multiple linear regression coefficient weights (eq. 7) for the models built using all measurements on leaf-dormant event days. Significant weights (α = 0.1) are in* ***bold****. Models with significant p-values are shown as cyan triangles in Figure 4.6.*

			Int.	AOD ×AE	SO_2 (DU)	UV (mW m^2 nm^{-1})	NO_2 ($\times 10^{15}$ molec. cm^{-2})	NH_3 ($\times 10^{15}$ molec. cm^{-2})	HCHO ($\times 10^{16}$ molec. cm^{-2})	LAI×T (m^2 m^{-2} K)	O_3 (DU)
Leaf-dormant	Duke	GR (nm hr^{-1})	**1.42**	0.07	0.06	0.05	-0.04	NaN	0.06	0.05	-0.11
		J_n (cm^{-3} s^{-1})	**1.55**	-0.25	**0.81**	**1.09**	**-0.54**	NaN	0.04	0.37	**0.75**
		SP	**0.18**	-0.02	-0.02	**-0.05**	-0.01	NaN	-0.02	0.01	-0.02
		N (cm^{-3})	**6987**	-448	**1534**	**2835**	-594	NaN	92	199	**1510**
	Egbert	GR (nm hr^{-1})	**1.17**	0.14	**-0.22**	0.12	**-0.46**	0.00	0.00	-0.12	**-0.30**
		J_n (cm^{-3} s^{-1})	**0.27**	-0.02	-0.05	**0.31**	-0.12	-0.08	-0.02	-0.06	-0.12
		SP	**0.30**	-0.03	-0.02	-0.02	-0.08	0.01	-0.01	-0.03	0.04
		N (cm^{-3})	**2628**	-221	-32	**940**	49	-359	279	175	47
	SGP	GR (nm hr^{-1})	**0.46**	-0.07	0.06	0.05	0.01	0.04	0.01	0.05	0.01
		J_n (cm^{-3} s^{-1})	**0.32**	**0.51**	-0.05	0.08	0.04	-0.10	0.02	0.05	-0.14
		SP	**0.09**	-0.04	**0.05**	**-0.05**	0.00	0.02	-0.02	**0.06**	0.02
		N (cm^{-3})	**3067**	-173	-187	**855**	154	-60	**1330**	402	-237
	SPL	GR (nm hr^{-1})	**1.30**	0.06	-0.01	-0.01	-0.06	0.08	-0.03	0.06	0.07
		J_n (cm^{-3} s^{-1})	**0.96**	0.03	-0.05	**0.63**	0.11	0.09	0.00	-0.03	0.06
		SP	**0.35**	0.00	-0.02	**-0.13**	**-0.05**	0.00	0.01	**0.06**	-0.01
		N (cm^{-3})	**4276**	-435	-87	**1284**	300	334	-172	25	240
	MMSFa	GR (nm hr^{-1})	**1.89**	0.19	0.10	-0.32	0.11	0.96	-0.27	0.16	0.10
		J_n (cm^{-3} s^{-1})	6.03	-1.34	-4.58	**8.78**	-3.85	-11.88	4.17	**-7.47**	2.06
		SP	**0.33**	0.03	0.05	**-0.15**	0.04	0.03	-0.04	0.09	0.03
		N (cm^{-3})	**8043**	-1602	-1648	**7774**	-3042	-7484	4642	**-6506**	-1329
	MMSFb	GR (nm hr^{-1})	**1.68**	0.24	0.18	0.04	0.00	-0.13	-0.01	0.15	-0.11
		J_n (cm^{-3} s^{-1})	**1.37**	0.08	-0.50	0.40	-0.42	-0.02	0.49	0.05	-0.05
		SP	**0.11**	-0.03	0.04	0.00	-0.01	-0.01	0.02	-0.02	0.03
		N (cm^{-3})	**5683**	234	-561	**1328**	-516	339	778	325	100

CHAPTER 5

DEVELOPING AND DIAGNOSING CLIMATE CHANGE INDICATORS OF REGIONAL AEROSOL OPTICAL PROPERTIES

Ryan C. Sullivan, Robert C. Levy, Arlindo M. da Silva, and Sara C. Pryor, *submitted*.

Abstract

Climate indicators (CIs) are increasingly being used to track changes in physical, chemical, biological, and societal components of the climate system. Given the importance of aerosol particles to radiative transfer, new aerosol-CIs are proposed, and their use in tracking and diagnosing causes of temporal changes in regional-scale aerosol populations is illustrated. The aerosol-CIs are computed using daily output from a satellite-constrained global reanalysis, but are sufficiently flexible that they could be derived from any gridded dataset, including numerical models. These CIs represent the total columnar burden (aerosol optical depth, AOD), dominant size mode (Ångström exponent, AE), and relative magnitude of radiation scattering versus absorption (single scattering albedo, SSA), along with metrics of the spatial coherence of these properties. When applied to U.S. National Climate Assessment regions, the aerosol-CIs indicate negative trends in mean and extreme AOD and SSA over the central and eastern U.S. These are consistent with lower aerosol burdens and a transition towards a relatively absorbing aerosol, driven primarily by declining sulfur dioxide emissions. Conversely, the northwest is characterized by increasing mean and extreme AOD that is attributed to increased wildfire emissions and long-range (transcontinental) transport. Regional and national reductions in precursor emissions are leading to declining spatial autocorrelation of aerosol-CIs in all regions and an increased importance of local emissions in dictating aerosol burdens. However, an increase in the intensity of synoptic scale circulation patterns associated with high aerosol

burdens is causing an increase in the distance at which the properties of aerosol populations become independent.

Introduction

Climate indicators (CIs) describe key properties of the climate system and are playing an increasing role in quantifying, diagnosing, and attributing changes through time[1,2]. Many agencies that contribute to the U.S. Global Change Research Program (USGCRP) have developed and applied CIs to document and track changes in the physical, chemical, and anthropogenic (socio-economic) components of the climate system. The spatial or temporal resolutions of CIs vary widely: Some are global in scale while others are regional, and while some focus on the drivers of global change, others are more strongly focused on response variables. Existing USGCRP CIs thus include: regional and global air temperature, precipitation, sea level, sea and land ice, and atmospheric concentrations of carbon dioxide, methane, nitrogen oxides, and fluorinated gases[1].

Atmospheric aerosol particles (aerosols) impact global and regional climate (via both direct and indirect radiative forcing), biogeochemical cycles, and human health. According to some estimates aerosol particles may have offset 0.8 Wm^{-2} (25%)[3] of the historical globally-averaged warming due to increased greenhouse gas concentrations. They have also been implicated as a major source of regional and sub-regional variations in trends in near-surface temperature (e.g. in the 'warming hole' of the central Great Plains)[4,5]. Despite this, CIs of climate-relevant aerosol properties have yet to be developed[2]. Herein we propose a suite of aerosol-CIs, and illustrate how they are derived and applied using regions of the U.S. National Climate Assessment (NCA) program (Figure 5.1). We demonstrate how these aerosol-CIs can be used to quantify variability and temporal trends in aerosol populations, and attribute changes

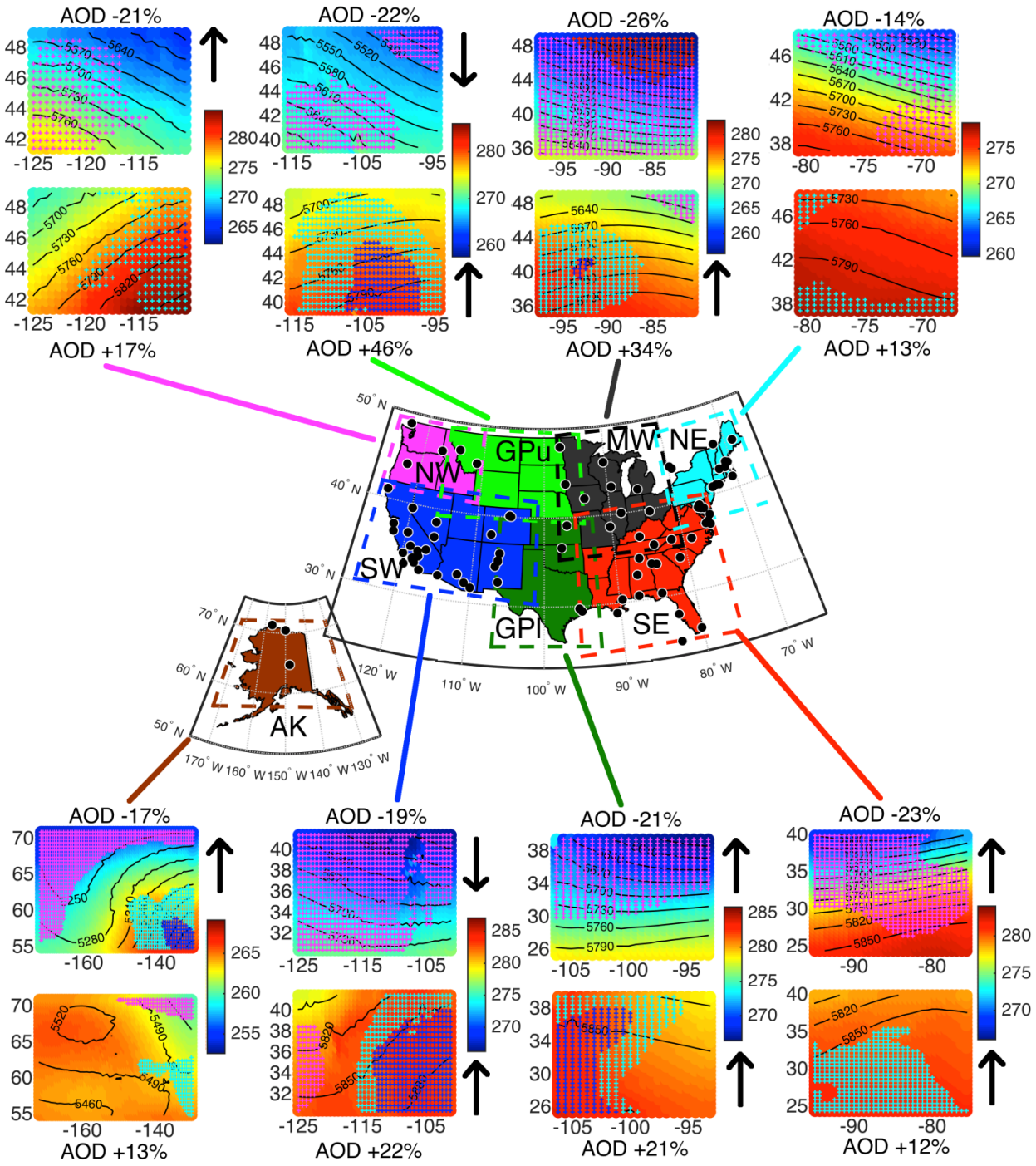

Figure 5.1. The eight U.S. National Climate Assessment (NCA) regions in which the aerosol-CIs are computed. The CIs are computed using MERRA-2 daily output from all grid cells within the dashed lines enclosing each region. Note the Great Plains region has been divided into two regions to ease interpretation of the analyses. Abbreviations: AK = Alaska, NW = Northwest, SW = Southwest, GPu = Upper Great Plains, GPl = Lower Great Plains, MW = Midwest, SE = Southeast, and NE = Northeast. Also shown within the map are the locations of AERONET sites from which data are presented in Figure 5.2. The panels above and below this map depict the mean synoptic conditions for synoptic types associated with anomalously low and high AOD. The mean temperature at 700 hPa (in K) are shown by the background colors, the solid black

lines depict the 500 hPa geopotential isoheights (in m), and the red, magenta, cyan, and blue stippling represent water vapor mixing ratio anomalies -2, -1, +1, and +2 standard deviations from the mean for all days. The arrows beside the panels indicate the presence and direction of significant trends in the PC scores associated with these synoptic types.

through time to specific drivers of aerosol variability: Gaseous precursor and primary aerosol emissions, and meteorological conditions at the synoptic scale.

CIs must be predicated on high- and uniform-quality, publically available data with well-defined provenance and an expectation that the variables on which they are based will continue to be measured into the future. Therefore direct observations, such as those from satellite or ground based remote sensing, are not suitable for deriving aerosol-CIs due to spatiotemporal discontinuities and a bias towards sampling cloud-free conditions[6]. Thus, herein we apply the aerosol-CIs to output from the first homogeneous, gridded, aerosol and meteorologically satellite-constrained reanalysis product: Modern-Era Retrospective Analysis for Research and Application, Version 2 (MERRA-2)[7,8]. However, the proposed aerosol-CIs are designed to be sufficiently flexible to be applied to any gridded dataset including output from next-generation reanalyses and/or numerical models.

Aerosols impact regional and global climate by directly scattering and absorbing radiation, acting as cloud condensation nuclei and altering cloud lifetimes and albedo, and changing the atmospheric thermal structure and thus atmospheric stability (ref. 9 and references therein). Aerosol radiative forcing and climate impact is a function of the aerosol number concentration, size distribution, and chemical composition, and remains a major source of uncertainty in quantifying anthropogenic forcing of Earth's climate[3]. Due to their short atmospheric lifetimes (cf. major greenhouse gases) aerosol radiative forcing exhibits high spatiotemporal variability, and local primary aerosol and precursor gas emissions have a major impact on regional aerosol populations and thus climate impacts. For example, during 1980 –

2009, the global mean annual aerosol optical depth (AOD), a measure of the extinction of insolation by atmospheric aerosols and thus the reduction of radiation that reaches Earth's surface, was unchanged (i.e. remained within ± 0.01 of an estimated global average of ~ 0.15)[10]. However, mean annual AOD decreased by up to 27% over parts of the U.S. and Europe due in part to regulation of precursor and primary aerosol emissions, while mean annual AOD increased by up to 22% over countries undergoing large economic development[10–12]. Following emission reductions associated with the U.S. Clean Air Act[13], near-surface fine aerosol concentrations ($PM_{2.5}$, i.e. the mass concentration of aerosols with diameters less than 2.5 μm) decreased by 40% across the continental U.S. during this period[10], consistent with a 38% decrease in modeled AOD from 1980 – 2006[14], and ~3% yr^{-1} decrease in summer AOD over the eastern U.S. from 2001 – 2013 measured using satellite-based remote sensing (the Multi-angle Imaging SpectroRadiometer (MISR))[15]. For these reasons, we advocate that aerosol-CIs are urgently needed to track a key aspect of the radiation balance of Earth, air quality, and biogeochemical cycles, and that aerosol-CIs should be generated and interpreted at the regional scale.

Specific objectives of this research are:

1. Motivate and develop CIs of key climate-relevant aspects of aerosol populations at the regional scale.
2. Apply the aerosol-CIs to each NCA region (Figure 5.1) to provide an illustrative example of how they can be used to quantify, characterize, and diagnose causes of historical trends in climate-relevant aerosol properties.

To the first order, three key properties of the aerosol population determine the magnitude of the aerosol radiative forcing and thus the climate impact: total columnar burden, size of the aerosols, and their composition[16]. Thus the aerosol-CIs we propose are based on: AOD which is

proportional to aerosol mass concentration and is a direct measure of the extinction of radiation, Ångström exponent (AE) which is inversely proportional to particle size, and single scattering albedo (SSA) which is the ratio of scattering to total extinction, and describes the relative efficiency of radiation scattering (leading to an increase in the global albedo and cooling) by aerosols to radiation absorption (leading to atmospheric warming)[3]. The proposed aerosol-CIs are designed to characterize and track changes in regionally averaged mean conditions of these variables and their extreme values, in addition to the spatial scales of aerosol features (both spatial autocorrelation and scales of coherence) (see Methods).

Results

Evaluation of MERRA-2

We present a demonstration of the proposed aerosol-CIs using a unique and recently releases reanalysis product, MERRA-2. The release of this dataset constitutes the first real opportunity to develop and apply aerosol-CIs for the U.S. NCA regions, or any other part of the globe. Aerosol properties in the MERRA-2 reanalysis product are derived in part based on assimilation of AOD at 550 nm derived from remotely sensed properties such as spectral reflectances, solar and instrument geometry, cloud cover, and surface features[8]. MERRA-2 has been subject to extensive evaluation relative to independent observations (see methods), thus only limited additional evaluation was undertaken as part of this study and is focused on evaluation of the joint probabilities of AOD, and AE and SSA relative to those from ground-based measurements of columnar aerosol properties from AErosol RObotic NETwork (AERONET) stations[17]. The results indicate good agreement between MERRA-2 and AERONET AOD, but that MERRA-2 underestimates the dynamic range of observed AE and SSA (Figure 5.2). Such underestimation is common when comparing gridded aerosol datasets

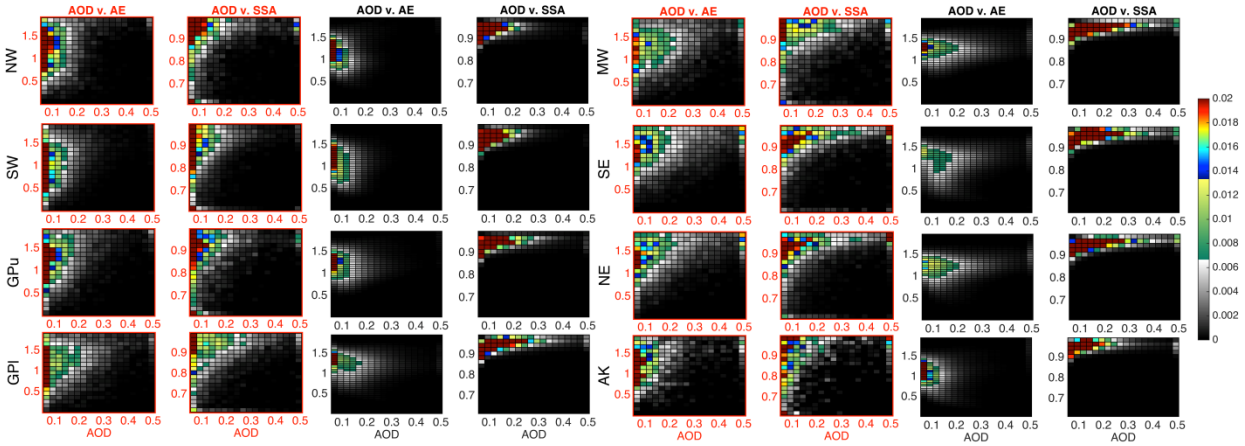

Figure 5.2. Joint probability distributions (jpd) for the daily mean aerosol optical properties in all grid cells in each region from MERRA-2 (black) and all stations in each region from AERONET (red). The jpd for AERONET include only stations with > 1 year of data and data from all months (except for in Alaska where no data are available in winter). Locations of AERONET stations are shown in Figure 5.1. In all panels AOD is shown on the abscissa axis, while the AE and SSA are shown in the ordinate axis. AOD and SSA are at 550 and 440 nm, and AE is at 470 – 870 nm and 440 – 675 nm, respectively for MERRA-2 and AERONET.

that represent area means (~2,500 m^2 for MERRA-2) versus in situ observations such as the pseudo-point measurements from AERONET. MERRA-2 reproduces the observed region-to-region variability in aerosol radiative properties and the MERRA-2 versus AERONET differences tend to be smaller than region-to-region differences (Figure 5.2).

Development of aerosol-CIs

As discussed above, AOD, AE, and SSA describe key aspects of aerosol particle populations that have greatest climate relevance. Accordingly our proposed aerosol-CIs include daily (and seasonally averaged) values derived from regionally-averaged estimates of the mean AOD, AE, and SSA and extreme (90^{th} percentile (P90 AOD)) AOD, along with two key metrics of the spatial patterns of these variables: the daily global spatial autocorrelation value (characterized using Moran's-I[18]; AOD-I, AE-I, SSA-I) and the range of spatial coherence as derived using semivariograms[19] of daily AOD, AE, and SSA fields within each region (AOD-SC, AE-SC, SSA-SC) (Figure 5.3). These ten aerosol-CIs are designed to track evolution of regional aerosol populations in terms of the overall aerosol columnar burden, relative abundance

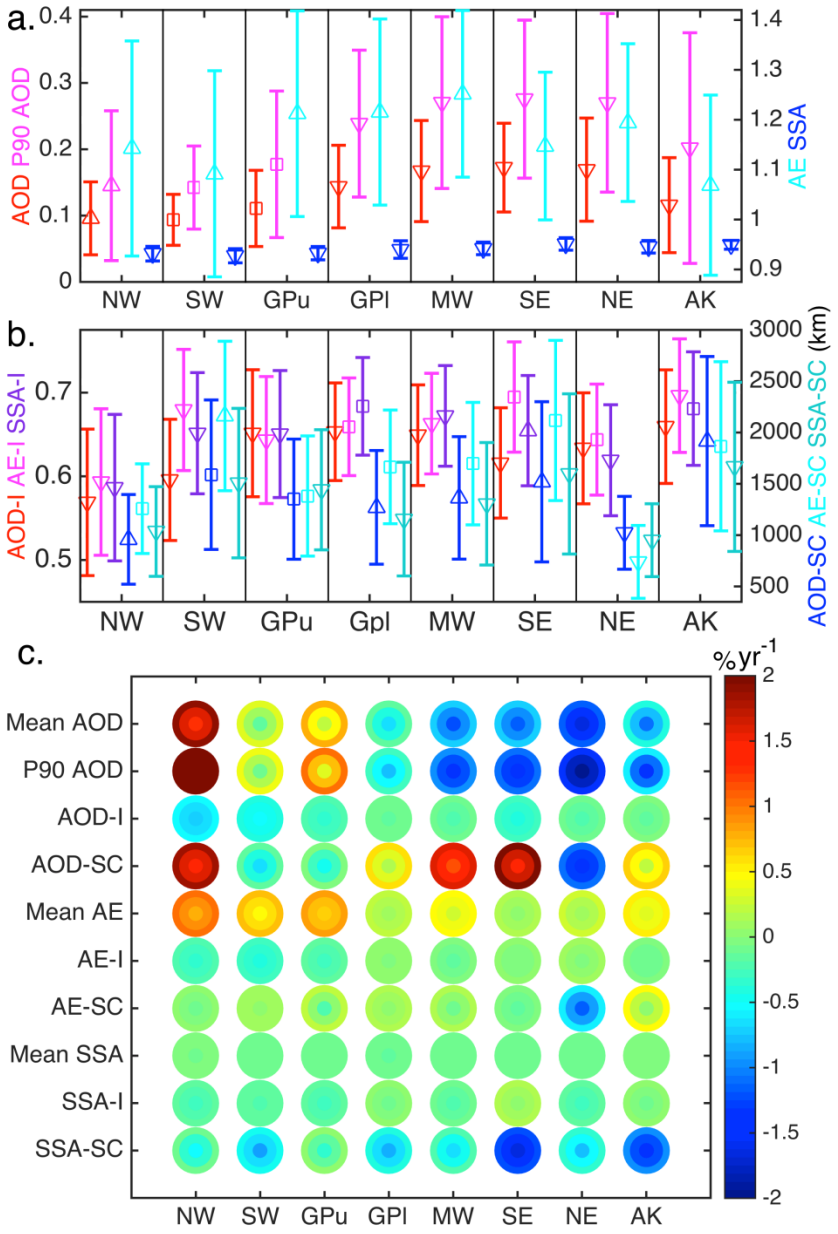

Figure 5.3. a and b) Mean (marker) and ±1 standard deviation (whiskers) values of the aerosol-CIs during the study period (2000 – 2015). Upward and downward facing triangles indicate significant positive and negative trends as determined using Kendall's tau, while square markers indicate no significant trend (at α=0.05). c) Percentage change per year in the CIs estimated using a linear regression fit (shown in Figure S5.1 and S5.2). The middle circles denote the normalized regression slopes (i.e. trends), and the inner and outer circles are the lower and upper bounds, respectively, of the 95% confidence intervals of these slopes.

of fine versus coarse mode aerosols, relative proportions of absorbing versus scattering aerosols, and the regional consistency of the spatial patterns of those properties.

Each aerosol-CI contains unique information about regional aerosol properties that have different implications for direct and indirect radiative forcing, in addition to air quality and thus human health. These CIs also exhibit intra-annual and inter-annual variability and trends that are not consistent across indicators indicating the utility of all of the proposed aerosol-CIs to trend diagnostic and attribution analyses (Figure 5.3). The spatial indices are particularly important both in terms of interpreting trends in the other aerosol-CIs and because for a true climate impact to be realized, aerosol radiative forcing must be expressed over a large area. Thus, there is a need to understand and quantify the degree to which climate-relevant aspects of aerosol populations are regionally coherent.

Application of the aerosol-CIs to regions of the U.S. NCA

Consistent with previous research, mean and extreme (P90) AOD declined in virtually all of the NCA regions over the period 2000 – 2015 (Figure 5.3). Significant (hereafter $\alpha = 0.05$, unless otherwise indicated) decreases are observed in five regions: the lower Great Plains (GPl), Midwest (MW), Southeast (SE), Northeast (NE), and Alaska (AK), but increased mean and extreme AOD is observed for the Northwest (NW), and there was no change in the Southwest (SW) and upper Great Plains (GPu). The direction of change and the presence of significant trends are consistent for mean and extreme (P90) AOD in all regions, but the magnitude of the change is larger for extreme AOD, indicating a narrowing of the probability distributions. The magnitude of significant regional AOD trends are ~ 1 % year^{-1}, while the magnitude of the extreme AOD trends are 1.2 – 1.4 % year^{-1} in regions of decreasing AOD and 1.9 % year^{-1} for the NW (Figure 5.3, 5.4, and S5.1). The key utility of including two indices of spatial coherence is illustrated by the divergent trends in these two aerosol-CIs. All regions exhibit decreased AOD spatial autocorrelation (AOD-I), but increased AOD spatial coherence (AOD-SC) is observed

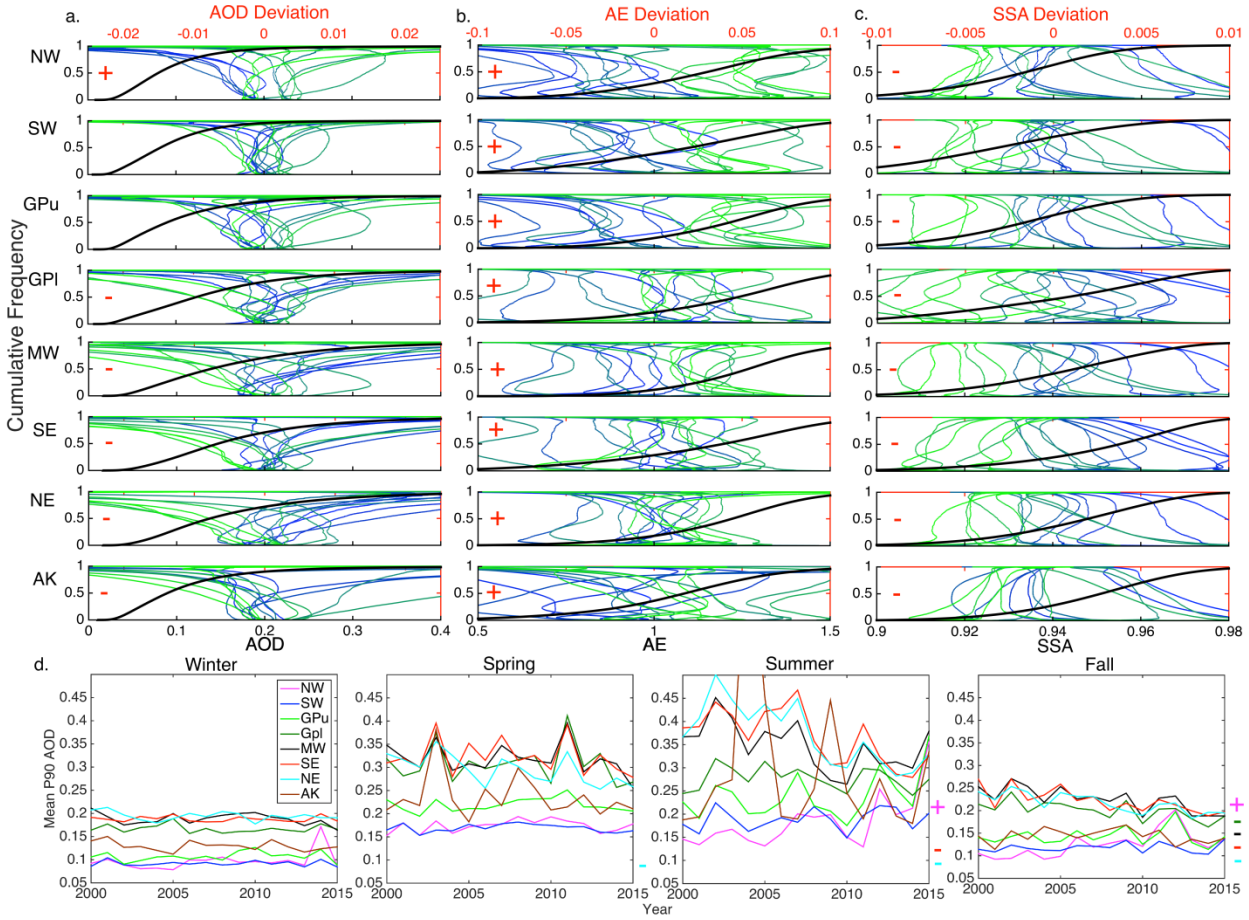

Figure 5.4. Cumulative distribution functions (cdf) of data from 2000-2015 for a) AOD, b) AE, and c) SSA in each region (black). The deviation from the annual mean is shown with the color scheme transitioning from blue (2000) to green (2015). d) Time series of the yearly seasonal mean extreme AOD for each region. Significant trends in the daily mean values are indicated by a red '+' or '-' in each panel (a-c) for positive and negative trends, respectively, and to the right of each panel in (d).

over the NW, GPl, MW, SE, and AK, and decreased AOD-SC is observed in the SW (p-value = 0.07), GPu (p-value = 0.15), and NE (Figure 5.3 and S5.2). Causes of these differences and the inter-annual variability in the aerosol-CI trends are examined below. Extreme AOD decreased in spring, summer, and fall in NE; summer and fall in SE and MW (p-value = 0.06 for MW summer); fall in GPl; and increased in summer and fall in NW (Figure 5.4).

Mean AE significantly increased across all eight regions, indicating a relative increase in fine mode particles (Figure 5.3, 5.4, and S5.1). However, trends in the spatial metrics of AE are not uniform across the regions. Significant negative trends in AE-I are observed in NW, SW,

GPu, MW, and AK (Figure 5.3 and S5.2), but only two regions exhibited significant changes in AE-SC and they showed different signs (increased in SW and decreased in NE). Thus, there is evidence that as the aerosol populations are becoming increasingly dominated by the fine mode at the regional scale, but there remain sub-regions within many of the NCA regions with high coarse mode concentrations, possibly due to wind-blown dust events[20].

Mean SSA and SSA-SC decreases are observed in all eight regions (Figure 5.3). There are also decreases in SSA-I for all regions except SE where there were significant increases in SSA-I, although the significance of the trend is lower in GPl (p-value = 0.06) and AK (p-value = 0.16). It is noted that SSA is determined by the aerosol composition and the dynamic range of SSA in MERRA-2 is lower than observations[7,21] (Figure 5.2), therefore the aerosol-CIs that relate to SSA must be viewed with caution in the current reanalysis product. However, these trends are consistent with a tendency towards a relatively more absorbing aerosol thus reducing the net cooling from aerosols. Further, aerosol populations are becoming more spatially heterogeneous in terms of the relative contribution of absorption to total radiative extinction.

When applied to the U.S. NCA regions, the aerosol-CIs thus indicate substantial evolution of aerosol populations through time in ways that are relevant to regional climate forcing and human health. Overall aerosol burdens have declined (2000-2015) and the aerosol populations have changed to become more dominated by smaller diameter and more absorbing aerosols. They are also evolving in a way that causes a decrease in spatial autocorrelation, but increases in spatial coherence.

Attribution of temporal trends in the aerosol-CIs

Attribution of observed trends in the aerosol-CIs, particularly deconvoluting changes resulting from changing anthropogenic emissions, natural emissions, and atmospheric conditions

is critical to demonstrating the effectiveness of emission reduction policies, exploring and prioritizing potential climate change mitigation strategies, and making projections of possible future values of the aerosol-CIs. Thus, the aerosol-CIs for the NCA regions are examined below in the context of these key drivers of aerosol populations.

Aerosol-climate interactions are reciprocal. Aerosols are a major driver of climate variability and change, but equally changes in climate alter aerosol concentrations and composition[22–24]. Further, previous research has illustrated a key role of synoptic scale meteorological conditions in determining regional aerosol concentrations under the current[25,26,4,27] and possible future climate[28,29]. Consistent with that research, in each of the NCA regions, a number of synoptic types derived in a principal component analysis (PCA) of MERRA-2 meteorological output are associated with 10 – 20 % AOD anomalies (positive and negative) (Figure 5.1). The link to meteorological conditions at the synoptic scale is less pronounced for AE (the anomalies are <10 %) and it appears SSA is relatively insensitive of the prevailing meteorological conditions (no synoptic type had a regionally average SSA anomaly of > 2%). This finding re-emphasizes the complexity of aerosol populations and their related climate forcing, and highlights the importance of having multiple aerosol-CIs in order to fully characterize changes in climate-relevant aerosol properties.

Over all regions, synoptic types characterized by cooler (or milder) and drier conditions are associated with lower AOD. Conversely, anomalously high AOD is associated with warm and/or humid synoptic types, consistent with enhanced AOD under stagnant flow[25] and aerosol growth by water uptake[30]. Over the northern and western regions (NW, SW, GPu, MW) southwesterly and northwesterly geostrophic flow is typically associated with both mean and extreme high and low AOD anomalies, respectively (Figure 5.1). Anomalously low AE in

virtually all regions is often associated with cool, dry synoptic conditions, consistent with an increase in dust loading during dry conditions[20]. Conversely, high AE is associated with warm, humid conditions at the synoptic scale consistent with predominance of hygroscopic secondary aerosols.

Consistent with prior research that has indicated changes in global and regional temperature and humidity are likely to result in changing characteristics of the synoptic types[25,31], although the frequency of individual synoptic types over each region did not exhibit temporal trends during the study period, the majority of synoptic types associated with large positive AOD anomalies in each region exhibit a significant positive trend in PC scores, while the types associated with negative AOD anomalies exhibited trends that are divided between increasing and decreasing trends (Figure 5.1). While there is evidence that some cool, dry days are also becoming cooler and drier, the dominant signal in this analysis is that synoptic types associated with elevated, regionally averaged AOD are evolving to become more intense, i.e. warm, moist days becoming warmer and moister. These changes in the synoptic-scale climate may thus partially offset emissions reductions[22,24].

The reduction in mean and extreme AOD in all regions except the NW is consistent with policy enacted under the U.S. Clean Air Act that has resulted in declining anthropogenic pollutant emissions over the study period (2000 – 2015). Emissions of key aerosol precursor species, sulfur dioxide (SO_2) and nitrogen oxides (NO_x), exhibit a significant negative trend for all eight NCA regions; ammonia (NH_3) exhibits a negative trend in all regions except the MW and NE; and volatile organic compounds (VOC) exhibit a negative trend in all regions except the NW and SE. Consistent with this, mean and extreme AOD significantly decreased in GPl, MW, SE, and NE; seasonal extreme AOD decreased in the fall in GPl; summer and fall in MW and

SE; and spring, summer, and fall in NE. Seasonal extreme AOD in these four regions are positively correlated with annual SO_2 and NO_x emissions (Pearson's r range = 0.51 – 0.80). These overall tendencies in aerosol-CIs for GPl, MW, SE, and NE are thus consistent with a decrease in sulfate aerosol abundance due to the reduction in SO_2 emissions, which causes a decrease in AOD. Further, because sulfate has a high SSA, this would also contribute to the observed decline in regionally-averaged SSA. Secondary organic aerosols are also a substantial component of aerosol mass and AOD over much of the eastern USA[32]. Thus an additional contributory factor to declining AOD in these regions is the reduction in anthropogenic VOC emissions. The correlation between annual VOC emissions and extreme summer and fall AOD in the NE and MW is 0.61 – 0.77. Thus, consistent with prior research, historical temporal trends of AOD across much of the contiguous U.S. are strongly responsive to emission reductions due to the Clean Air Act.

Despite reductions in anthropogenic aerosol precursor gas emissions, it is worthy of note that primary aerosol emissions exhibit a significant trend only in the NW, GPu, and MW (Figure 5.5), and that both biogenic VOC and wildfire emissions exert a substantial impact on aerosol burdens and optical properties[33,34]. For example, there is a clear peak in extreme AOD in the spring of 2011 in the GPl, MW, and SE when wildfire burned area in the GPl was approximately four times greater than any other year (Figure 5.4 and 5.5). In the GPl, the lack of association between anthropogenic emissions and extreme AOD in three of four seasons, coupled with decreased SSA, may be in part due to increased abundance of absorbing aerosols, consistent with remote sensing measurements that indicate increased aerosol absorption optical depth (AAOD) over the central U.S. from increased dust emissions[20]. The declining trend in aerosol-CIs in AK

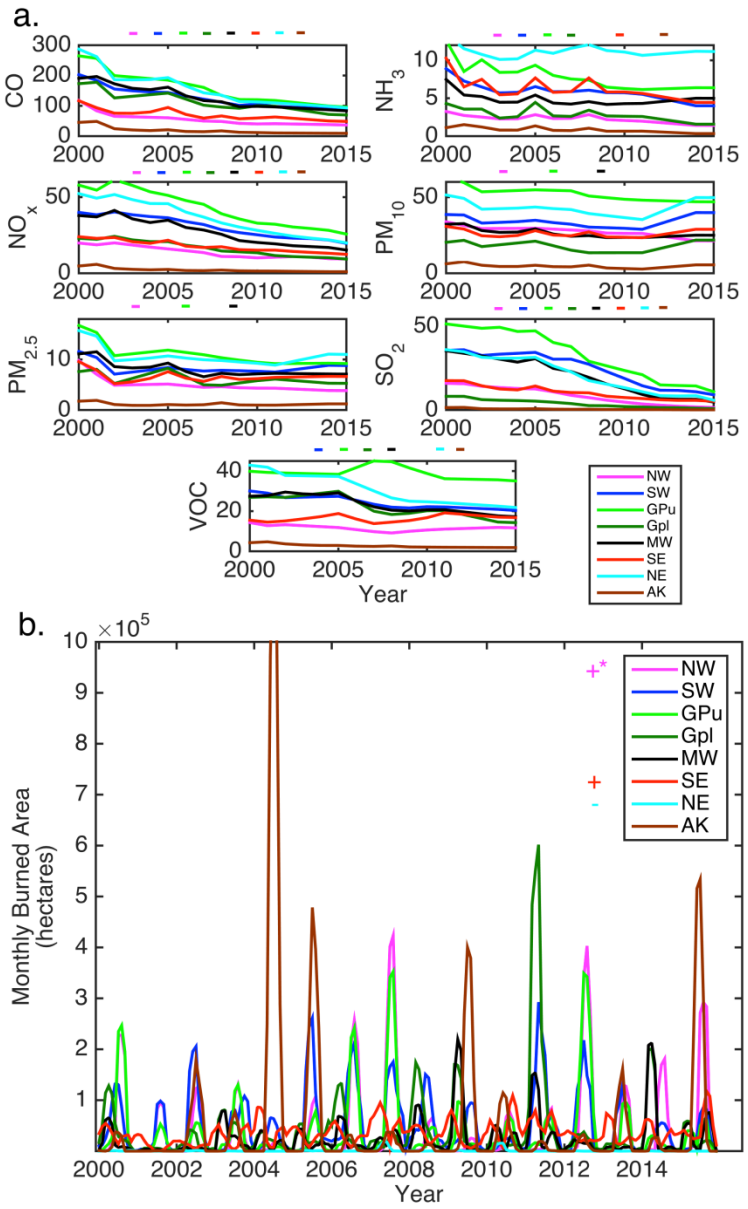

*Figure 5.5. a) Time series of annual anthropogenic emissions as reported in the U.S. EPA National Emissions Inventory of carbon monoxide (CO), ammonia (NH_3), nitrogen oxides (NO_x), particulate matter < 10 μm (PM_{10}), fine particulate matter < 2.5 μm ($PM_{2.5}$), sulfur dioxide (SO_2), and volatile organic compounds (VOC) by region, in thousands of tons per year[41]. b) Time series of wildfire occurrence expressed as monthly burned area for each region, derived from MODIS measurements[40]. The sign of significant trends are shown above each panel in a) and next to the legend in b) (*positive trend in NW monthly burned area p-value = 0.13).*

is also not very strongly linked to changes in anthropogenic emissions, but there is a significant positive association between extreme summer AOD and wildfire burned area (r = 0.98). This is clearly evident in 2004, 2009, and 2015, when positive excursions in monthly burned area (Figure 5.5) coincide with spikes in summer extreme AOD (Figure 5.3).

Only the NW region exhibits a significant positive trend in annual mean AOD, with extreme AOD increasing in the summer and fall. This is despite declines in regional anthropogenic emissions, and may reflect confounding influences from increased wildfires (seasonal burned area and extreme AOD in summer and fall exhibit co-variability with r = 0.53 and 0.75, respectively) and long-range transport. For example, Siberian fires in the summer of 2012 impacted air quality in the Pacific NW[34], and are evident in high P90 AOD during the 2012 summer and fall (Figure 5.3).

Consistent with decreased anthropogenic aerosol precursor emissions in each region (Figure 5.5), decreased spatial autocorrelation in the aerosol-CIs (Figure 5.3 and S5.2) indicates an increasing influence of local sources on sub-regional aerosol concentrations and thus increased grid cell–to–grid cell variability in aerosol populations. Conversely, scales of spatial coherence are increasing, which may be linked to changes in synoptic scale conditions (Figure 5.1). High and low AOD are generally associated with warm, humid and cool, dry conditions, respectively, and the PC scores for the majority of synoptic types are significantly increasing. It follows that the more intense extreme synoptic conditions may be resulting in an increasing scale of aerosol events. As climate conditions continue to evolve, this highlights the critical need to better understand the feedbacks between climate and aerosol populations.

Discussion

The motivation for climate indicators is that they must represent key components of the climate system. This is certainly the case for the aerosol-CIs. The guidance for developing CIs is that they should be relatively straightforward to compute and readily evaluated in both the contemporary and possible future climate. Thus, the aerosol-CIs we propose can be readily

derived for any gridded data set and therefore can be applied to any region using current and future generation reanalysis products and/or output from regional and climate models.

The aerosol-CIs presented herein are designed to be useful in tracking changes in climate relevant aspects of the aerosol population and to assist in diagnosing the causes of changes in aerosol populations at the regional scale. Their utility in the former regard is illustrated by application to the NCA regions, and specifically the finding that mean and extreme AOD and SSA is declining and AE is increasing in virtually all regions consistent with a tendency towards lower aerosol burdens that are increasingly dominated by fine mode (small diameter) and more absorbing aerosols. This implies a decline in the degree to which aerosols have offset greenhouse gas related warming of the climate over much of the contiguous U.S.

The aerosol-CIs are also defined using two geospatial metrics: Spatial correlation and spatial coherence. The former (Moran's I) characterizes normalized co-variability and is a measure of the degree to which daily fields of AOD, AE, and SSA exhibit spatial clustering. The latter is a measure of the distance (range in the semivariogram) at which spatial fields become independent. The utility of these two spatial metrics in terms of diagnosing causes of changes in aerosol populations at the regional level is also indicated by the presence of divergent trends in AOD-I and AOD-SC in the NCA regions. These findings imply a tendency towards more grid cell–to–grid cell variability in aerosol populations (due to declining regional precursor and aerosol emissions leading to an increase in the relative importance of local emissions) within larger areas of increased spatial coherence (i.e. large range values from the semivariograms) possibly due to an increase in the intensity of the predominant modes of synoptic scale meteorology.

Methods

MERRA-2

The aerosol-CIs proposed herein use a recently released model data product, Modern-Era Retrospective Analysis for Research and Application, Version 2 (MERRA-2). This product is the first data-constrained, gridded reanalysis of aerosol properties and its release affords the first real opportunity to develop and apply aerosol-CIs for the U.S. NCA (or any global region). MERRA-2 is derived using assimilation of both meteorological and aerosol observations every 6 and 3 hours, respectively, into the Goddard Earth Observing System, version 5 (GEOS-5) model[8]. It provides hourly, global gridded output of meteorological variables and aerosol optical properties including AOD, AE, and aerosol scattering extinction at 0.625° by 0.5° resolution. The aerosol characteristics are constrained using a wide suite of remote sensing products. For example, AOD at 550 nm is derived from Moderate Resolution Imaging Spectroradiometer (MODIS) measurements on both the Terra and Aqua satellites (Collection 5)[35] of reflectances, solar and instrument geometry, cloud cover, and surface features[8] using a neural network retrieval (NNR) trained using AERONET measurements. It is noted that an artificial trend exists in Terra data assimilated into MERRA-2, which may confound the trend analysis; thus trends identified here should be further validated with future MERRA releases in which this trend is corrected. A similar approach is used to assimilate Advanced Very High Resolution Radiometer (AVHRR)[36] measurements of radiances, total precipitable water, wind speed, and solar and instrument geometry trained to the MODIS NNR. MISR AOD is assimilated only over bright surfaces[37], and ground-based AOD measurements from the AERONET[17] are assimilated after 1999. As the density of assimilated aerosol optical properties and meteorological measurements increases greatly after 2000[8,38], the analysis presented here is limited to 2000 – 2015.

MERRA-2 aerosol properties that are not directly assimilated have been compared to, and found to be in reasonable agreement with, satellite-based measurements and near-surface measurements of $PM_{2.5}$, although there is an underestimation of winter $PM_{2.5}$ concentrations over the northwest and northeast, potentially due to lack of nitrate aerosols in MERRA-2[7].

Physical variable from MERRA-2 used here within the synoptic-scale meteorological classification have also been extensively evaluated in the previous MERRA release[39].

Wildfire and anthropogenic emissions

Estimates of wildfire occurrence and spatial extent used herein to diagnose trends in the aerosol-CIs derive from the Global Fire Emissions Database (GFED4) monthly burned area product. GFED4 provides monthly estimates of hectares of burned area on a 0.25° grid derived from the MODIS (Collection 5.1) monthly burned area product[40].

Annual estimates of anthropogenic emissions of carbon monoxide (CO), NH_3, NO_x, PM_{10}, $PM_{2.5}$, SO_2, and VOCs are also used in attribution of changes in the aerosol-CIs. These estimates are accumulated for all states within each of the NCA regions and derive from the EPA's state level National Emissions Inventory (NEI)[41]. It is noted that there is inherent uncertainty in emissions estimates due to spatiotemporal variability in emission sources, measurement and sampling errors, and the simplification of modeled emissions processes. For example, SO_2 emissions rely on the sulfur content of the combustible material, biogenic emissions vary with environmental conditions, and NH_3 emissions lack wide-spread regulatory restrictions and ambient NH_3 measurements are scarce[42,43]. Additionally, MERRA-2 aerosol speciation depends, in part, on the magnitude of prescribed emissions, which do not evolve (i.e. persistency is assumed) during the later years of the study period[8]. Despite these uncertainties,

measurements of species important for secondary aerosol formation, e.g. SO_2, suggest that trends in emissions are robust[15,44].

Statistical methods used to derive and interpret the aerosol-CIs

The aerosol-CIs we propose quantify the regionally-averaged mean AOD, AE, and SSA; extreme (90th percentile) AOD; and two geostatistical metrics of spatial autocorrelation and spatial coherence of AOD, AE, and SSA.

The global spatial autocorrelation for each region and aerosol parameter is computed at the daily timescale and quantified using Moran's I[18]:

$$I = \frac{N}{\sum_{i=1}^{N}\sum_{j=1}^{N,i\neq j} w_{ij}} \frac{\sum_{i=1}^{N}\sum_{j=1}^{N,i\neq j} w_{ij}(X_i - \bar{X})(X_j - \bar{X})}{\sum_{i=1}^{N}(X_i - \bar{X})} \dots (1)$$

$$w_{ij} = \frac{1}{{D_{ij}}^2} \frac{1}{\sum_{i=1}^{N}\sum_{j=1}^{N,i\neq j} \frac{1}{{D_{ij}}^2}} \dots (2)$$

where N is the number of grid cells, w_{ij} is the weight for grid cells i and j, X_i is the daily mean value (AOD, AE, or SSA) at grid cell i, $\overline{X}$ is the mean of the daily means for all grid cells, and D_{ij} is the great circle distance between the centroid of grid cell i and j. Values approaching 1 and -1 indicate positive and negative spatial autocorrelation, respectively, while 0 indicates a random spatial field. Significance for rejecting the null hypothesis of no spatial autocorrelation is determined by calculating a z-score for each I:

$$Z = \frac{I - E(I)}{Var(I)} \dots (3)$$

$$E(I) = -\frac{1}{N-1} \dots (4)$$

$$Var(I) = \frac{NS_4 - S_3S_4}{(N-1)(N-2)(N-3)\sum_{i=1}^{N}\sum_{j=1}^{N,i\neq j} w_{ij}} - E(I)^2 \dots (5)$$

$$S_1 = \frac{1}{2}\sum_{i=1}^{N}\sum_{j=1}^{N,i\neq j}(2w_{ij})^2 \ldots (6)$$

$$S_2 = \sum_{i=1}^{N}\left(2\sum_{j=1}^{N,i\neq j} w_{ij}\right)^2 \ldots (7)$$

$$S_3 = \frac{\frac{1}{N}\sum_{i=1}^{N}(X_i - \bar{X})^4}{\left(\frac{1}{N}\sum_{i=1}^{N}(X_i - \bar{X})^2\right)^2} \ldots (8)$$

$$S_4 = (N^2 - 3N + 3)S_1 - NS_2 + 3\left(\sum_{i=1}^{N}\sum_{j=1}^{N,i\neq j} w_{ij}\right)^2 \ldots (9)$$

$$S_5 = (N^2 - N)S_1 - 2NS_2 + 6\left(\sum_{i=1}^{N}\sum_{j=1}^{N,i\neq j} w_{ij}\right)^2 \ldots (10)$$

The spatial coherence of each variable in each region is computed using semivariograms which describe the semivariance as a function of separation distance between all grid cell pairs[19]:

$$\gamma(h) = \frac{\sum_{i=1}^{N,i\in Q}\sum_{j=1}^{N,D_{ij}\in\Delta h}[X_i - X_j]^2}{N(\Delta h)\times|Q|} \ldots (11)$$

Where N(h) is the number of grid cell pairs that are separated by a great circle distance of h, X_i and X_j are the daily mean values (AOD, AE, or SSA) at grid cells i and j, respectively, Δh is a bin range of separation distances, and Q is the set of all grid cells not within three grid cells of the domain border. The empirical semivariogram fit, $\gamma(h)$, is binned in 100 km increments (i.e. $\gamma(1-100\text{ km})$ includes all grid cell pairs separated by 1 – 100 km). An exponential fit is used to model $\gamma(h)$ assuming an exponential decay in correlation with distance and for physical interpretability of the model[45,46].

$$\gamma'(h) = C_n + C_p\left(1 - e^{-\frac{3h}{\alpha}}\right) \ldots (12)$$

Where $\gamma'(\mathrm{h})$ is the exponential model fit; C_n is the nugget describing the semivariance at zero spatial lag, resulting from variability at scales below data resolution[45]; C_p is the partial sill, where

the sill, $C_n + C_p$, is the semivariance as $h \to \infty$; and a is the range or distance at which 95% of the sill is reached, indicating the distance at which two locations are no longer correlated. $\gamma(h)$ is calculated for each day, and $\gamma'(h)$ is fit to the mean $\gamma(h)$ for all days in each season[46]. For the CIs to be tracked through time, a single daily quantity is required. Thus, the daily "scale of spatial coherence", SC, is herein defined as the minimum h where $\gamma(h) > 0.75a_s$, where a_s is the range for that season. AE semivariance tends to increase linearly with distance leading to high uncertainty in a range determined using the exponential semivariogram model.

Temporal trends in the aerosol-CIs are quantified and the significance determined using Kendall's tau-b (τ_b) rank coefficient[47]. τ_b is calculated by comparing all pairs of observations, $\{(t_i, X_i), (t_j, X_j)\}$ where X_i and X_j are the variable (AOD, AE, SSA) at time t_i and t_j, respectively:

$$\tau_b = \frac{C - D}{\sqrt{\left[\frac{N(N-1)}{2} - \sum_{i=1}^{N} \frac{tx_i(tx_i - 1)}{2}\right]\left[\frac{N(N-1)}{2} - \sum_{i=1}^{N} \frac{tt_i(tt_i - 1)}{2}\right]}} \ldots (13)$$

$$C - D = \sum_{i=1}^{N} \sum_{j=i+1}^{N, j \neq i} \begin{Bmatrix} if\ \left[sign\left((X_i - X_j)(t_i - t_j)\right) > 0\right] = 1 \\ if\ \left[sign\left((X_i - X_j)(t_i - t_j)\right) < 0\right] = -1 \\ else = 0 \end{Bmatrix} \ldots (14)$$

$$tx_i = |X :\ X = X_i| \ldots (15)$$

$$tt_i = |t :\ t = t_i| \ldots (16)$$

where N is the number of observations. $\tau_b > 0$ indicates a positive trend and $\tau_b < 0$ indicates a negative trend. The significance of the trend is quantified using z-scores[48]:

$$Z = \frac{C - D}{\sqrt{\frac{v_o - v_x - v_t}{18} + v_1 + v_2}} \ldots (17)$$

$$v_0 = N(N-1)(2N+5) \ldots (18)$$

$$v_x = \sum_{i=1}^{N} tx_i(tx_i - 1)(2tx_i + 5) \ldots (19)$$

$$v_t = \sum_{i=1}^{N} tt_i(tt_i - 1)(2tt_i + 5) \dots (20)$$

$$v_1 = \frac{\sum_{i=1}^{N} tx_i(tx_i - 1) \sum_{j=1}^{N} tt_j\left(tt_j - 1\right)}{2N(N-1)} \dots (21)$$

$$v_2 = \frac{\sum_{i=1}^{N} tx_i(tx_i - 1)(tx_i - 2) \sum_{j=1}^{N} tt_j\left(tt_j - 1\right)\left(tt_j - 2\right)}{9N(N-1)(N-2)} (22)$$

The slope of the trends, in terms of percentage change per year, is estimated to be the slope of a linear regression fit to the CIs' time series.

It is hypothesized that changes in anthropogenic and natural precursor and primary aerosol emissions will be associated with changes in the aerosol populations. The significance of this association is quantified using the Pearson's r correlation coefficient.

Prior research indicates that synoptic meteorological conditions are also a key control of aerosol concentrations[25,26]. Thus, PCA is used to derive a daily synoptic classification and investigate the interaction between synoptic conditions and aerosol properties, and to determine the impact of meteorology on the CIs trends. Predictors used in the PCA are air temperature and water vapor at 700 hPa plus 500 hPa geopotential heights from MERRA-2. The number of PCs to retain for each region was determined using a scree test[49] and the retained factors are rotated using a Varimax rotation[50]. Between six and nine components (i.e. unique synoptic types) were retained for each of the eight NCA regions. The PC scores for each day (i.e. similarity to the major modes of variability as characterized by the PCs) are used to track changes in the frequency of each synoptic type (i.e. counts of days with highest similarity to each of the modes) and the intensity of the types (i.e. the magnitude of the scores for each PC). The mean anomaly of each aerosol-CI on all days classified by each synoptic type, calculated relative to the mean aerosol-CI computed for all days, is used to illustrate the importance of meteorological conditions at the synoptic (regional) scale in determining aerosol properties.

Data availability

MERRA-2 data is available from the Goddard Earth Science Data and Information Services Center (https://disc.sci.gsfc.nasa.gov/), GFED4 is available from http://www.globalfiredata.org/, and NEI is available from https://www.epa.gov/sites/production/files/2016-12/state_tier1_90-16.xls.

Acknowledgements

We acknowledge computational resources provided by the Lilly Endowment, Inc. to the Indiana University Pervasive Technology Institute and the Indiana METACyt Initiative, and thank the AERONET PIs for establishing and maintaining the sites used herein.

Competing interests

The authors declare no competing interests.

Contributions

RCS and SCP jointly identified the research objectives and designed the research methodology, RCS conducted the majority of the analyses, SCP analyzed the AERONET observations, and SCP and RCS jointly wrote the manuscript. RCL and AMS provided expertise on the MERRA-2 dataset, and discussed and commented on the manuscript.

Funding

Funding was supplied by: NASA Earth and Space Science Fellowship Program - Grant “14-EARTH14F-0207” (RCS) and NASA (NNX16AG31G) (SCP and RCL).

REFERENCES

1. Melillo, J. M., Richmond, T. T. & Yohe, G. *Climate change impacts in the United States: Third National Climate Assessment*. *U.S. Global Change Research Program* (2014). doi:10.7930/J0Z31WJ2
2. Karl, T. R., Knight, R. W., Easterling, D. R. & Quayle, R. G. Indices of climate change for the United States. *Bull. Am. Meteorol. Soc.* **77,** 279–292 (1996).
3. Myhre, G. *et al. Anthropogenic and natural radiative forcing*. *Climate Change 2013: The Physical Science Basis. Contribution of Working Group I to the Fifth Assessment Report of the Intergovernmental Panel on Climate Change* (Cambridge University Press, 2013).
4. Meehl, G. A., Arblaster, J. M. & Branstator, G. Mechanisms contributing to the warming hole and the consequent US east–west differential of heat extremes. *J. Clim.* **25,** 6394–6408 (2012).
5. Yu, S. *et al.* Attribution of the United States 'warming hole': Aerosol indirect effect and precipitable water vapor. *Sci. Rep.* **4,** doi: 10.1038/srep06929 (2014).
6. Zhang, J. & Reid, J. S. An analysis of clear sky and contextual biases using an operational over ocean MODIS aerosol product. *Geophys. Res. Lett.* **36,** doi: 10.1029/2009GL038723 (2009).
7. Buchard, V. *et al.* The MERRA-2 aerosol reanalysis, 1980 – onward, part II: Evaluation and case studies. *J. Clim.* (in review)
8. Randles, C. *et al.* The MERRA-2 aerosol reanalysis, 1980 - onward, part I: system description and data assimilation evaluation. *J. Clim.* (in review)
9. Yu, H. *et al.* A review of measurement-based assessments of the aerosol direct radiative effect and forcing. *Atmos. Chem. Phys.* **6,** 613–666 (2006).
10. Chin, M. *et al.* Multi-decadal aerosol variations from 1980 to 2009: a perspective from observations and a global model. *Atmos. Chem. Phys.* **14,** 3657–3690 (2014).
11. Hsu, N. C. *et al.* Global and regional trends of aerosol optical depth over land and ocean using SeaWiFS measurements from 1997 to 2010. *Atmos. Chem. Phys.* **12,** 8037–8053 (2012).
12. Cherian, R., Quaas, J., Salzmann, M. & Wild, M. Pollution trends over Europe constrain global aerosol forcing as simulated by climate models. *Geophys. Res. Lett.* **41,** 2176–2181 (2014).
13. Streets, D. G., Wu, Y. & Chin, M. Two-decadal aerosol trends as a likely explanation of the global dimming/brightening transition. *Geophys. Res. Lett.* **33,** doi: 10.1029/2006GL026471 (2006).
14. Streets, D. G. *et al.* Anthropogenic and natural contributions to regional trends in aerosol optical depth, 1980–2006. *J. Geophys. Res. Atmos.* **114,** doi: 10.1029/2008JD011624 (2009).
15. Keppel-Aleks, G. & Washenfelder, R. A. The effect of atmospheric sulfate reductions on diffuse radiation and photosynthesis in the United States during 1995–2013. *Geophys. Res. Lett.* **43,** 9984–9993 (2016).
16. Seinfeld, J. H. & Pandis, S. N. *Atmospheric chemistry and physics: from air pollution to climate change*. (John Wiley & Sons, 2006).
17. Holben, B. N. *et al.* AERONET—A federated instrument network and data archive for aerosol characterization. *Remote Sens. Environ.* **66,** 1–16 (1998).
18. Moran, P. A. P. Notes on continuous stochastic phenomena. *Biometrika* **37,** 17–23 (1950).

19. Curran, P. J. The semivariogram in remote sensing: an introduction. *Remote Sens. Environ.* **24,** 493–507 (1988).
20. Zhang, L. *et al.* What factors control the trend of increasing AAOD over the United States in the last decade? *J. Geophys. Res. Atmos.* **122,** 1797–1810 (2017).
21. Buchard, V. *et al.* Using the OMI aerosol index and absorption aerosol optical depth to evaluate the NASA MERRA Aerosol Reanalysis. *Atmos. Chem. Phys.* **15,** 5743–5760 (2015).
22. Dawson, J. P., Adams, P. J. & Pandis, S. N. Sensitivity of $PM_{2.5}$ to climate in the Eastern US: a modeling case study. *Atmos. Chem. Phys.* **7,** 4295–4309 (2007).
23. Paasonen, P. *et al.* Warming-induced increase in aerosol number concentration likely to moderate climate change. *Nat. Geosci.* **6,** 438–442 (2013).
24. Megaritis, A. G., Fountoukis, C., Charalampidis, P. E., Pilinis, C. & Pandis, S. N. Response of fine particulate matter concentrations to changes of emissions and temperature in Europe. *Atmos. Chem. Phys.* **13,** 3423–3443 (2013).
25. Horton, D. E., Skinner, C. B., Singh, D. & Diffenbaugh, N. S. Occurrence and persistence of future atmospheric stagnation events. *Nat. Clim. Chang.* **4,** 698–703 (2014).
26. Gkikas, A., Houssos, E. E., Hatzianastassiou, N., Papadimas, C. D. & Bartzokas, A. Synoptic conditions favouring the occurrence of aerosol episodes over the broader Mediterranean basin. *Q. J. R. Meteorol. Soc.* **138,** 932–949 (2012).
27. Tai, A. P. K. *et al.* Meteorological modes of variability for fine particulate matter ($PM_{2.5}$) air quality in the United States: implications for $PM_{2.5}$ sensitivity to climate change. *Atmos. Chem. Phys.* **12,** 3131–3145 (2012).
28. Pye, H. O. T. *et al.* Effect of changes in climate and emissions on future sulfate-nitrate-ammonium aerosol levels in the United States. *J. Geophys. Res. Atmos.* **114,** doi: 10.1029/2008JD010701 (2009).
29. Dawson, J. P., Bloomer, B. J., Winner, D. A. & Weaver, C. P. Understanding the meteorological drivers of US particulate matter concentrations in a changing climate. *Bull. Am. Meteorol. Soc.* **95,** 521–532 (2014).
30. Brock, C. A. *et al.* Aerosol optical properties in the southeastern United States in summer–Part 2: Sensitivity of aerosol optical depth to relative humidity and aerosol parameters. *Atmos. Chem. Phys.* **16,** 5009–5019 (2016).
31. Hansen, J., Sato, M. & Ruedy, R. Perception of climate change. *Proc. Natl. Acad. Sci.* **109,** E2415–E2423 (2012).
32. Hand, J. L., Schichtel, B. A., Pitchford, M., Malm, W. C. & Frank, N. H. Seasonal composition of remote and urban fine particulate matter in the United States. *J. Geophys. Res. Atmos.* **117,** doi: 10.1029/2011JD017122 (2012).
33. Ehn, M. *et al.* A large source of low-volatility secondary organic aerosol. *Nature* **506,** 476–479 (2014).
34. Teakles, A. D. *et al.* Impacts of the July 2012 Siberian fire plume on air quality in the Pacific Northwest. *Atmos. Chem. Phys.* **17,** 2593–2611 (2017).
35. Levy, R. C. *et al.* Global evaluation of the Collection 5 MODIS dark-target aerosol products over land. *Atmos. Chem. Phys.* **10,** 10399–10420 (2010).
36. Heidinger, A. K., Foster, M. J., Walther, A. & Zhao, X. The pathfinder atmospheres–extended AVHRR climate dataset. *Bull. Am. Meteorol. Soc.* **95,** 909–922 (2014).
37. Kahn, R. A. *et al.* Multiangle Imaging Spectroradiometer (MISR) global aerosol optical depth validation based on 2 years of coincident Aerosol Robotic Network (AERONET)

observations. *J. Geophys. Res. Atmos.* **110,** doi: 10.1029/2004JD004706 (2005).
38. McCarty, W. *et al.* in *Technical Report Series on Global Modeling and Data Assimilation, Volume 46* (ed. Koster, R. D.) (2016). doi:20160014544
39. Rienecker, M. M. *et al.* MERRA: NASA's modern-era retrospective analysis for research and applications. *J. Clim.* **24,** 3624–3648 (2011).
40. Giglio, L., Randerson, J. T. & Werf, G. R. e. *J. Geophys. Res. Biogeosciences* **118,** 317–328 (2013).
41. US Environmental Protection Agency. Air Pollutant Emissions Trends Data: State Average Annual Emissions Trend. (2016). Available at: https://www.epa.gov/sites/production/files/2016-12/state_tier1_90-16.xls. (Accessed: 7th February 2017)
42. Aneja, V. P., Nelson, D. R., Roelle, P. A., Walker, J. T. & Battye, W. Agricultural ammonia emissions and ammonium concentrations associated with aerosols and precipitation in the southeast United States. *J. Geophys. Res. Atmos.* **108,** (2003).
43. U.S. Environmental Protection Agency. in *Emission Inventory Improvement Program* (Available at: https://www.epa.gov/sites/production/files/2015-08/documents/vi04.pdf, 1996).
44. Fioletov, V. E., McLinden, C. A., Krotkov, N., Moran, M. D. & Yang, K. Estimation of SO_2 emissions using OMI retrievals. *Geophys. Res. Lett.* **38,** doi: 10.1029/2011GL049402 (2011).
45. Liebhold, A. M. & Sharov, A. A. in *Population and community ecology for insect management and conservation* (ed. Baumgärtner, J., P. Brandmayr, and B. M.) 111–117 (Balkema, 1998).
46. Sullivan, R. C., Levy, R. C. & Pryor, S. C. Spatiotemporal coherence of mean and extreme aerosol particle events over eastern North America as observed from satellite. *Atmos. Environ.* **112,** 126–135 (2015).
47. Agresti, A. *Analysis of ordinal categorical data*. (John Wiley & Sons, 2010).
48. Wilks, D. S. *Statistical methods in the atmospheric sciences*. **100,** (Academic press, 2011).
49. Cattell, R. B. The scree test for the number of factors. *Multivariate Behav. Res.* **1,** 245–276 (1966).
50. Richman, M. Rotation of principal components. *J. Climatol.* **6,** 293–335 (1986).

Supporting Information for

Developing and diagnosing climate change indictors of regional aerosol optical properties

Short title: Aerosol climate indicators

Ryan C. Sullivan[a*], Robert C. Levy[b], Arlindo M. da Silva[b], and Sara C. Pryor[a,c]

a. Department of Earth and Atmospheric Sciences, Cornell University, Ithaca, NY

b. NASA Goddard Space Flight Center, Greenbelt, MD

c. Pervasive Technology Institute, Indiana University, Bloomington, IN

**Corresponding author:*

1126 Bradfield Hall, Ithaca, NY 14853

rcs365@cornell.edu

Contents of this file

Figure S5.1 and S5.2

Introduction

This supporting information provides figures illustrating the trends in the aerosol climate indicators.

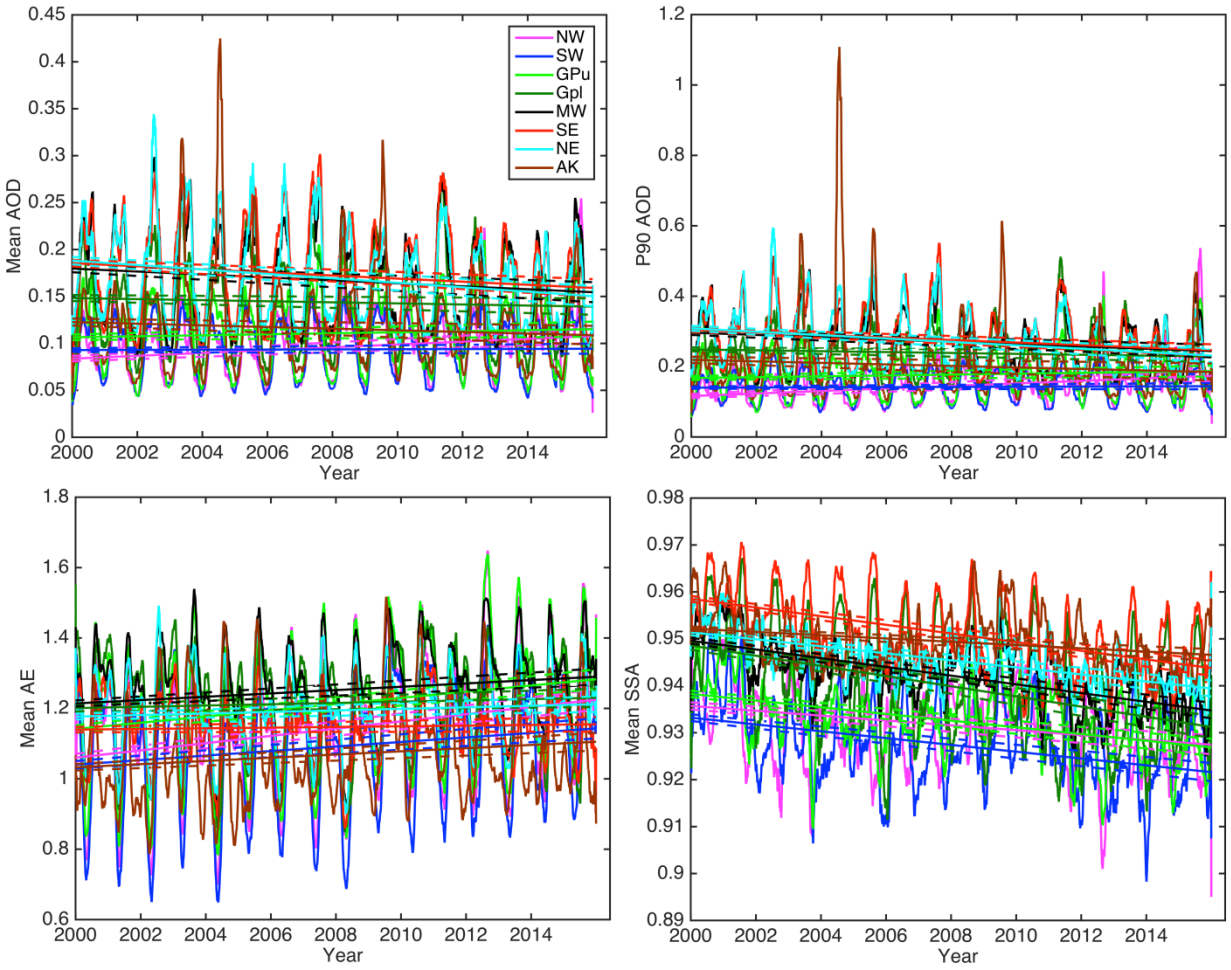

Figure S5.1. Trends in mean AOD, AE, and SSA, and extreme AOD. The time series has been smoothed in the plot using a 50-day running mean for legibility. The solid and dashed lines are the linear regression fit and 95 % confidence interval for the regression slope, respectively. No smoothing was applied for the regression fit.

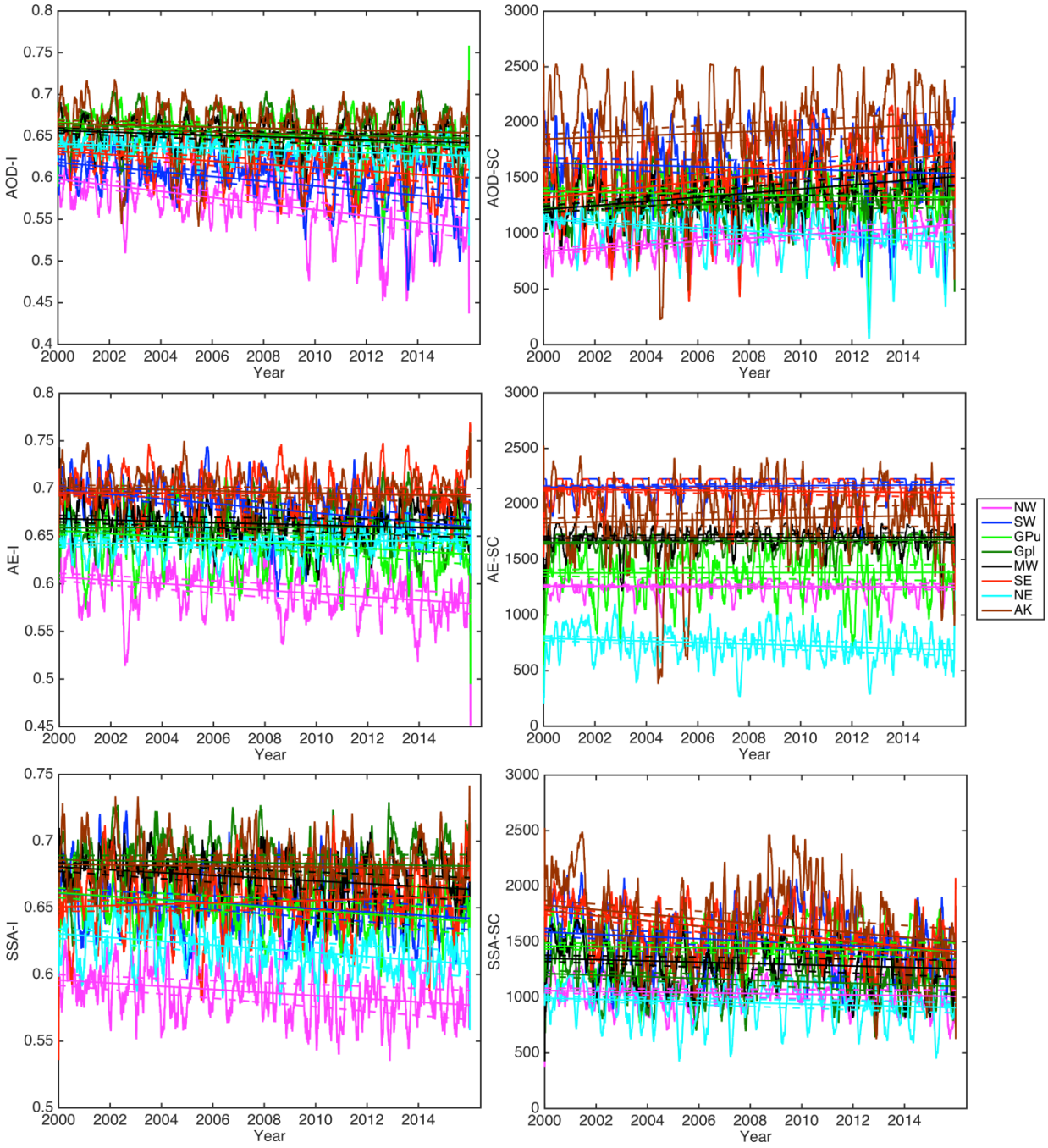

Figure S5.2. As in Figure S5.1 for trends in Moran's I (I) and scales of spatial coherence (SC) of AOD, AE, and SSA.

CHAPTER 6

NEW PARTICLE FORMATION LEADS TO CLOUD DIMMING

Ryan C. Sullivan, Paola Crippa, Hitoshi Matsui, L. Ruby Leung, Chun Zhao, Abhinav Thota, and Sara C. Pryor, *submitted.*

New particle formation (NPF), nucleation of condensable vapors to the solid or liquid phase, is a significant source of atmospheric aerosol particle number concentrations. With sufficient growth, these nucleated particles may be a significant source of cloud condensation nuclei (CCN), thus altering cloud albedo, structure, and lifetimes, and insolation reaching the Earth's surface. Herein we present one of the first numerical experiments to quantify the impact of NPF on cloud radiative properties that is conducted at a convection permitting resolution and that explicitly simulates cloud droplet number concentrations. Consistent with observations, these simulations suggest that in spring over the Midwestern U.S.A., NPF occurs frequently and on regional scales. However, the simulations suggest that NPF is not associated with enhancement of regional cloud albedos as would be expected from an increase of CCN. These simulations indicate that NPF reduces ambient sulfuric acid concentrations sufficiently to inhibit growth of preexisting particles to CCN sizes. This reduction in CCN-sized particles reduces cloud albedo, resulting in a domain average positive top of atmosphere cloud radiative forcing of 10 W m^{-2} and up to ~ 50 W m^{-2} in individual grid cells relative to a simulation in which NPF is excluded.

Atmospheric aerosol particles (hereafter aerosols) have the potential to offset some fraction of the climate change associated with increased greenhouse gas concentrations[1]. In addition to directly scattering and absorbing insolation, aerosols impact cloud properties, further

perturbing surface insolation and climate[2,3]. New particle formation (NPF) has been observed to occur in numerous environmental conditions across the Earth and contributes significantly to aerosol number concentrations[4–6]. However, the degree to which freshly nucleated aerosols can grow sufficiently to act as cloud condensation nuclei (CCN), increase cloud albedo, and result in negative radiative forcing, remains uncertain[7,8], and a full understanding of the complex cloud-aerosol interactions is lacking[9,10].

A number of challenges confront attempts to quantify the impact of NPF on CCN number concentrations and cloud properties at the local/regional/global scale. These include: (1) Uncertainties in the precise nucleation mechanism responsible for NPF and appropriate scaling parameters within NPF schemes. While previous numerical modeling and in situ measurement studies have suggested that a significant portion of global CCN originates from NPF[11–14], the impact is regionally variable, scale dependent, and dependent on the assumed nucleation pathway[15,16]. (2) Uncertainties in, or challenges to, representation of the impact of NPF on gas phase concentrations, aerosol particle size distributions (PSD), and aerosol-cloud interactions including the supersaturation necessary for CCN activation[17].

NPF is not inevitably associated with increased CCN concentrations, at least at the regional scale. For example, NPF can alter the condensational sink (CS) sufficiently to inhibit growth of pre-existing particles to CCN sizes[18], which is consistent with observations of increased contribution of NPF to CCN concentrations during less polluted conditions[19]. Some experimental studies have sought to estimate the contribution of NPF to CCN concentrations by comparing concentrations before and after NPF events, but are subject to large uncertainties due to violations of the stationarity assumption. Further, the actual activation of particles is dependent on the supersaturation. Some analyses have sought to derive CCN estimates

theoretically from aerosol number concentrations and assumed supersaturations that may not realistically represent true in-cloud conditions[20,21]. The high degree of sensitivity to assumed water vapor supersaturation is illustrated by previous simulations over the Beijing region of China, which found that while NPF increased CCN at high supersaturations, it reduced CCN at lower supersaturations[22].

Recent increases in computing resources and complexity of available aerosol-cloud microphysics schemes[23,24] enable simulation of the impact of NPF on aerosol PSD, while explicitly resolving convective clouds at high resolution and cloud droplet number distributions (i.e. double-moment microphysics), and thus permit evaluation of the resultant aerosol-cloud impacts.

Herein, we use the Weather Research and Forecasting model coupled with Chemistry (WRF-Chem v3.6.1) with the NPF mechanism of Matsui et al. 2011 (ref. 22) to simulate and quantify the impact of NPF on cloud radiative properties during May 2008. WRF-Chem is applied to a domain of 800 × 800 km at 4 km resolution, for the period 9 – 27 May 2008 (9 – 11 May are used as spin-up) using the Morrison double-moment microphysics scheme and without any cumulus parameterization to explicitly resolve convection and cloud droplet number concentrations (See Table S6.1 for full simulation settings). The high spatial-resolution used herein is generally believed to be sufficient to resolve convection[25]. May was chosen as the simulation period because it is the month of highest observed NPF frequency over the Midwestern U.S.A.[26], and during this specific month (May 2008) an intensive field experiment was conducted in southern Indiana permitting detailed evaluation of simulated aerosol PSD along an 80 km transect across the middle of the domain extending from a small town, to an expansive forest, and to the major urban area of Indianapolis[27] (Figure 6.1a). Near-surface

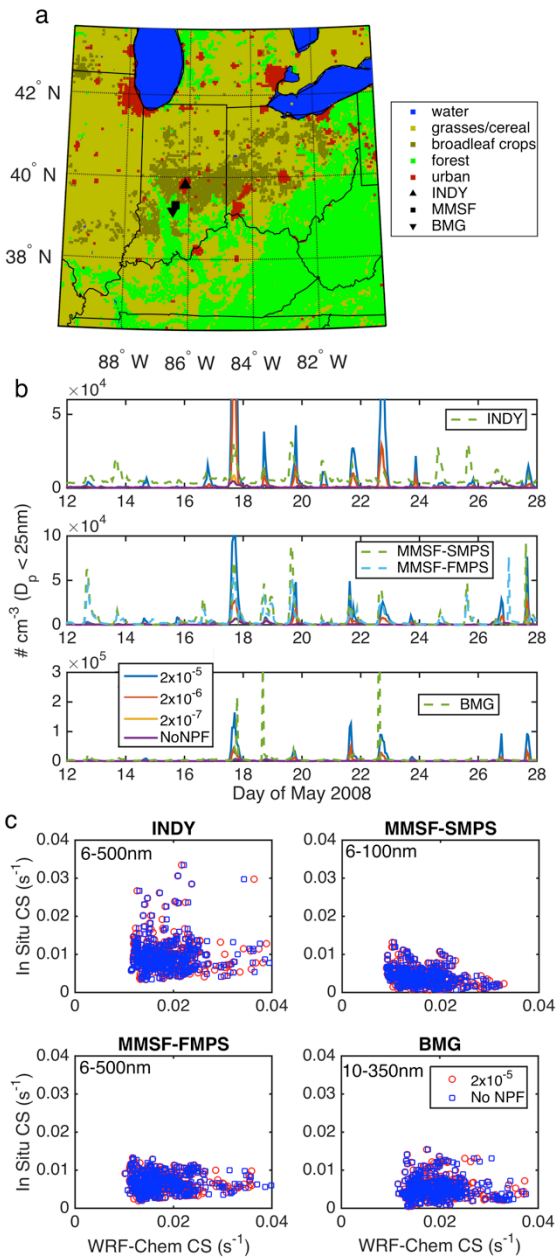

Figure 6.1. a) Land use within the simulation domain from MODIS for 2012. Also shown are locations of the three in situ particle size distribution measurement sites (BMG, MMSF, and INDY). b) Time series of hourly nucleation mode number concentrations from WRF-Chem (solid-lines; see legend in bottom panel) with various prefactors and NPF turned off, and from in situ measurements (dashed-lines). Note two instruments (an SMPS and an FMPS) were operated simultaneously at MMSF. c) Comparison of the hourly average condensational sink (CS) from WRF-Chem (abscissa axis) and in situ measurements (ordinate axis). As CS did not vary greatly across the simulations, only the highest prefactor and no NPF are shown. Approximate D_p range used to compute the CS is shown in the upper left of each panel.

aerosol and gas phase concentrations are also evaluated using data from EPA's Air Quality

System (AQS) (see details in SI). Cloud properties are evaluated using satellite-based remote

sensing measurements from the MOderate Resolution Imaging Spectroradiometer on the Aqua satellite (MODIS-Aqua) at 5 km nadir resolution.

Four sets of WRF-Chem simulations are conducted. They vary in terms of whether NPF is enabled and the prefactor used to quantify the number of particles formed as a function of the sulfuric acid concentration. The precise nucleation mechanism (e.g., activation, binary, ternary, ion-induced, organic[28]) for NPF likely varies in space and time[29,30]. Within the boundary layer most studies indicate that the production of ~1 nm diameter particles during NPF events scales with sulfuric acid vapor concentrations raised to a power n ($[H_2SO_4]^n$), multiplied by a prefactor[31–34]. Further, in situ measurements within the domain indicate ultrafine particle number concentrations are strongly associated with $[H_2SO_4]$[27]. Thus, herein we implement an activation type nucleation mechanism[22,35,36] with n = 1 and prefactors of 2×10^{-7}, 2×10^{-6}, and $2\times10^{-5} \times [H_2SO_4]$; and compare those with a simulation in which NPF is excluded. This suite of simulations is inclusive of nucleation prefactors used in prior studies (and is evaluated in terms of the degree of agreement with PSD measured at three sites during the study period), and permit both an analysis of the sensitivity of our results to the nucleation prefactor and clear quantification of the impact of NPF on CCN concentrations and cloud properties. Simulations such as those presented herein are highly computationally demanding (the four simulations of the 19 day period presented herein required ~350,000 core hours on a Cray supercomputer), thus previous studies have either chosen to simulate relatively short periods[35], to simulate at comparatively low resolution, requiring use of cumulous parameterizations[37], to employ a single prefactor[30], or to simplify the gas-particle chemical schemes (most frequently neglecting production of secondary organic aerosol mass)[38]. Herein, we selected to simulate a long period, to evaluate the sensitivity to NPF prefactors, and to conduct the simulations at convective

permitting scales with a high precision cloud microphysics scheme. Due to evidence from in situ measurements that partitioning of semi-volatile products of oxidation of volatile organic compounds makes only a small contribution to the growth of nano-scale particles in this environment[27,1], production of organic aerosol mass is excluded from the simulations.

Evaluation of the simulations

Prior to use of the WRF-Chem output to quantify the impact of NPF on cloud properties, the simulations were subject to a detailed model performance evaluation (see SI). In brief, the results of this evaluation indicate that for all three observing sites, the activation scheme replicates the day-to-day variability in occurrence and intensity of NPF (Figure 6.1b, Figures S6.1 and S6.2). The highest correlation between hourly measured and simulated nucleation mode concentrations (particle diameter (D_p) < 25 nm) occurred with a prefactor of 2×10^{-5} (r = 0.20 – 0.48), and the lowest root mean squared error resulted from a prefactor of 2×10^{-6} (RMSE = 8.7×10^{3} – 3.9×10^{4} cm^{-3}). The RMSE is the same magnitude as instrument uncertainty (e.g., RMSE = 7.8×10^{3} cm^{-3} for two co-located instruments at the central measurement location (Morgan Monroe State Forest, MMSF) that operate with different PSD discretization and measurement principle: Scanning Mobility Particle Sizer (MMSF-SMPS) and Fast Mobility Particle Sizer (MMSF-FMPS)). Although the model exhibits similar values of the CS to near-surface observations, the range is higher in the model except at the site in Indianapolis (INDY), due to the higher background aerosol concentration in the urban area (Figure 6.1c). This is consistent with a positive bias in simulated near-surface aerosol mass ($PM_{2.5}$ and PM_{10}) relative to EPA measurements across the study domain (Figure S6.3)[39]. Conversely, the simulations are negatively biased for near-surface sulfur dioxide (SO_2) and nitrogen dioxide (NO_2) concentrations (Figures S6.3 and S6.4). This is likely associated with a negative bias in [H_2SO_4],

and thus may explain our observation that the highest correlation between in situ nucleation mode particle concentrations and the simulation occurs for the largest NPF prefactor. For brevity, the remainder of the study focuses primarily on output from the $2\times10^{-5} \times [H_2SO_4]$ and control (no NPF) simulations.

Cloud fraction is a dominant modulator of radiative fluxes, but capturing cloud presence at the correct location, at the correct time is one of the greatest challenges to atmospheric models[40,41]. Both the no NPF and $2\times10^{-5} \times [H_2SO_4]$ prefactor simulations exhibit relatively high skill in identifying cloud presence and cloud-top height. When compared with MODIS-Aqua retrievals on a pixel-to-pixel and hour-to-hour basis, 50 % of cloud impacted pixels (i.e., grid cells with clouds in any vertical layer) are correctly simulated across the entire domain (Figure 6.2b) and cloud top heights exhibit $r > 0.6$ over 20 % of grid cells (and positive over almost all of the grid cells within the domain). For all grid cells mean (standard deviation across grid cells) $r = 0.38$ (0.30) and root mean square error (RMSE) = 369 hPa (64 hPa) between the NPF simulation and MODIS, relative to a mean (standard deviation) cloud top height of 390 hPa (± 230 hPa) and 529 hPa (248 hPa) from WRF-Chem and MODIS-Aqua, respectively (Figure 6.2c). Thus, we conclude the simulations reproduce the observed cloud fields sufficiently well that they are adequate for evaluating differences in cloud properties between the control and NPF simulations.

Spatial scales of NPF and impact on top of atmosphere radiative forcing

For an appreciable climate impact, aerosol forcing must occur on relatively large (e.g. regional) scales. In situ measurements taken at spatially distributed sites have indicated that NPF is indeed a regional phenomenon, but exhibits important sub-regional heterogeneity due to local emissions and/or sulfur-rich plumes[42–45]. Herein we examine the spatial scales of NPF to determine whether the model reproduces these features. Using the definition that a NPF event

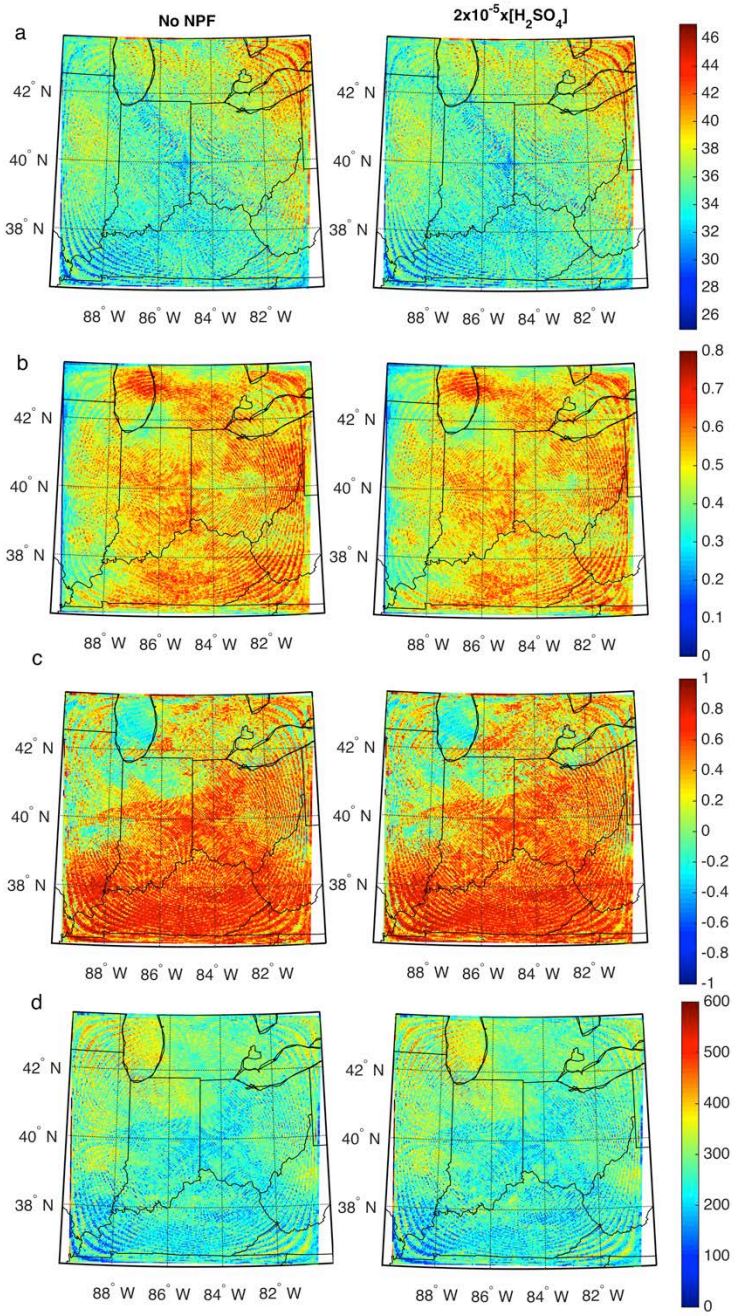

Figure 6.2. a) Number of MODIS retrievals in each grid cell when a cloud was present in MODIS or WRF-Chem. b) Fraction of retrievals for which WRF-Chem correctly simulated the presence of clouds (see Eq. 5 in Methods). c) Pearson's correlation coefficient and d) root mean squared error for cloud top heights (hPa) between MODIS and WRF-Chem. The first column shows results for no NPF simulations; the second column is with NPF turned on with a prefactor of $2\times10^{-5} \times [H_2SO_4]$.

day is one in which nucleation mode (D_p < 25 nm) number concentrations during one or more

hours exceed the grid cell mean value by 0.5 standard deviations, 9 of 16 simulation days were

classed as exhibiting nucleation events at Indianapolis (INDY) and Bloomington (BMG), and 11 of 16 days at MMSF. Using this definition, NPF is simulated, on average across all grid cells, on 76 – 78 % of days on which a NPF event day is identified at each of the three in situ measurement sites (Figure 6.3a). When isolating only particularly strong NPF days (i.e. days when nucleation mode particle number concentrations were one standard deviation above the mean), the spatial scale of coherence is smaller, but averaged across the entire domain, strong NPF still occurs on 62 – 66 % of days on which NPF is simulated at each of the three in situ measurement sites (Figure 6.3b). This implies that NPF is being observed and simulated on sufficiently large scales to potentially have an impact on regional cloud properties and thus regional climate.

The impact of NPF on cloud albedo and radiative forcing is quantified by comparing the top of atmosphere outgoing shortwave (TOA-SW) radiation from the NPF simulations and the control simulation without NPF for all grid cells and hours with clouds in both simulations. For most days on which no NPF was observed in the NPF-enabled simulations, the output from all simulations is virtually identical with respect to all cloud radiative properties indicating only modest day-to-day impact from NPF within the simulation domain. On days when NPF was observed, for all prefactors, the NPF simulations have lower TOA-SW for grid cells with simulated clouds than the control simulation, indicating a decrease in cloud albedo, which is of greatest magnitude for the simulations with the highest NPF prefactor (Figure 6.4a-c). Averaged over the entire simulation period (12 – 27 May 2008; including nighttime hours), this forcing is > 14 W m^{-2} (10 W m^{-2}, when including cloud free hours and grid cells) over the majority (50 %) of grid cells and > 30 W m^{-2} over 8 % of the domain, indicating a substantial perturbation in the regional radiative budget (Figure 6.4a and Figure S6.5). NPF does not drastically change

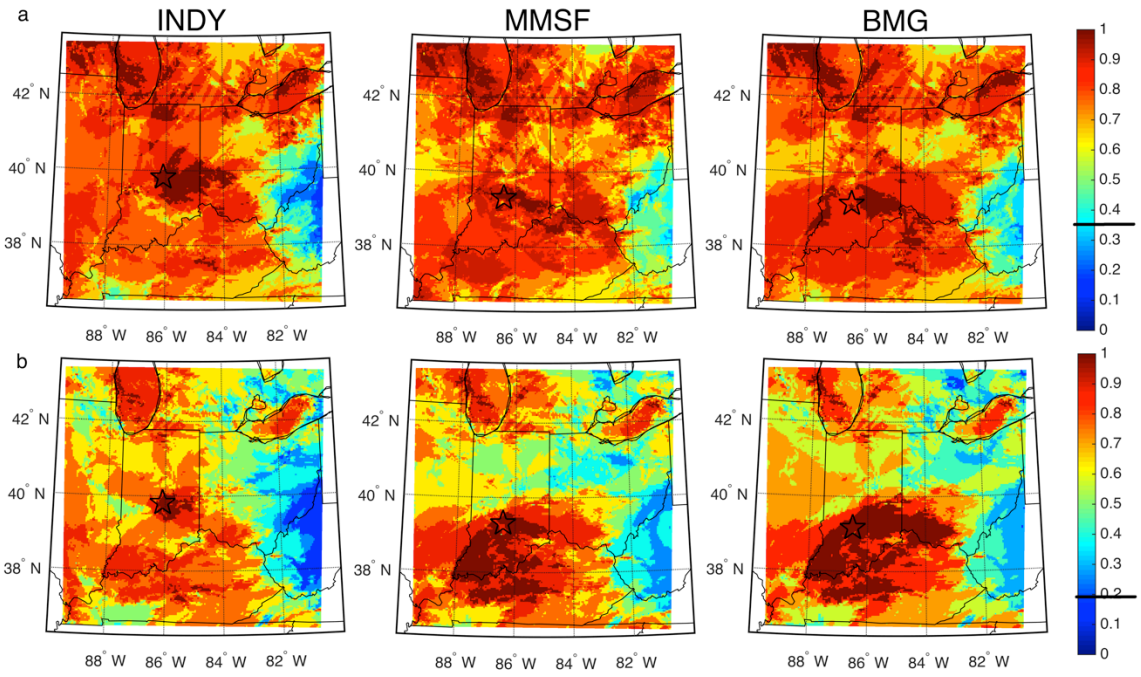

Figure 6.3. Fraction of modeled days on which NPF events were simultaneously predicted in the grid cell and those containing the three observational sites (INDY, MMSF, and BMG). An event day is declared if any hourly nucleation mode concentration is a) > one-half of a standard deviation above the local mean or b) a standard deviation above the local mean. The classification of a) most closely agrees with a subjective classification, while b) identifies only intense NPF event days. The black bars on the color bars represent the coincident NPF days expected for a random field (1000 Monte-Carlo iterations).

simulated cloud top heights. Ninety-percent of all grid cells and simulation hours exhibit a difference in cloud top heights of less than 30 hPa between the NPF simulation and the simulation without NPF. While NPF decreases TOA-SW of simulated clouds, there is also only a modest change in simulated cloud fraction. Ninety-percent of grid cells exhibit little or no difference (between –6 % and +2 %) in the number of hours with cloud present in the simulations with and without NPF. TOA-SW is generally lower when NPF is turned on. This indicates lower cloud albedo and hence reduced reflection of solar radiation on days when NPF is simulated. However, when examining individual days this is not uniform in space or time. For example, the TOA-SW is lower in the NPF simulation for 12 May, but higher on 26 May than in the no NPF simulation (Figure 6.4d).

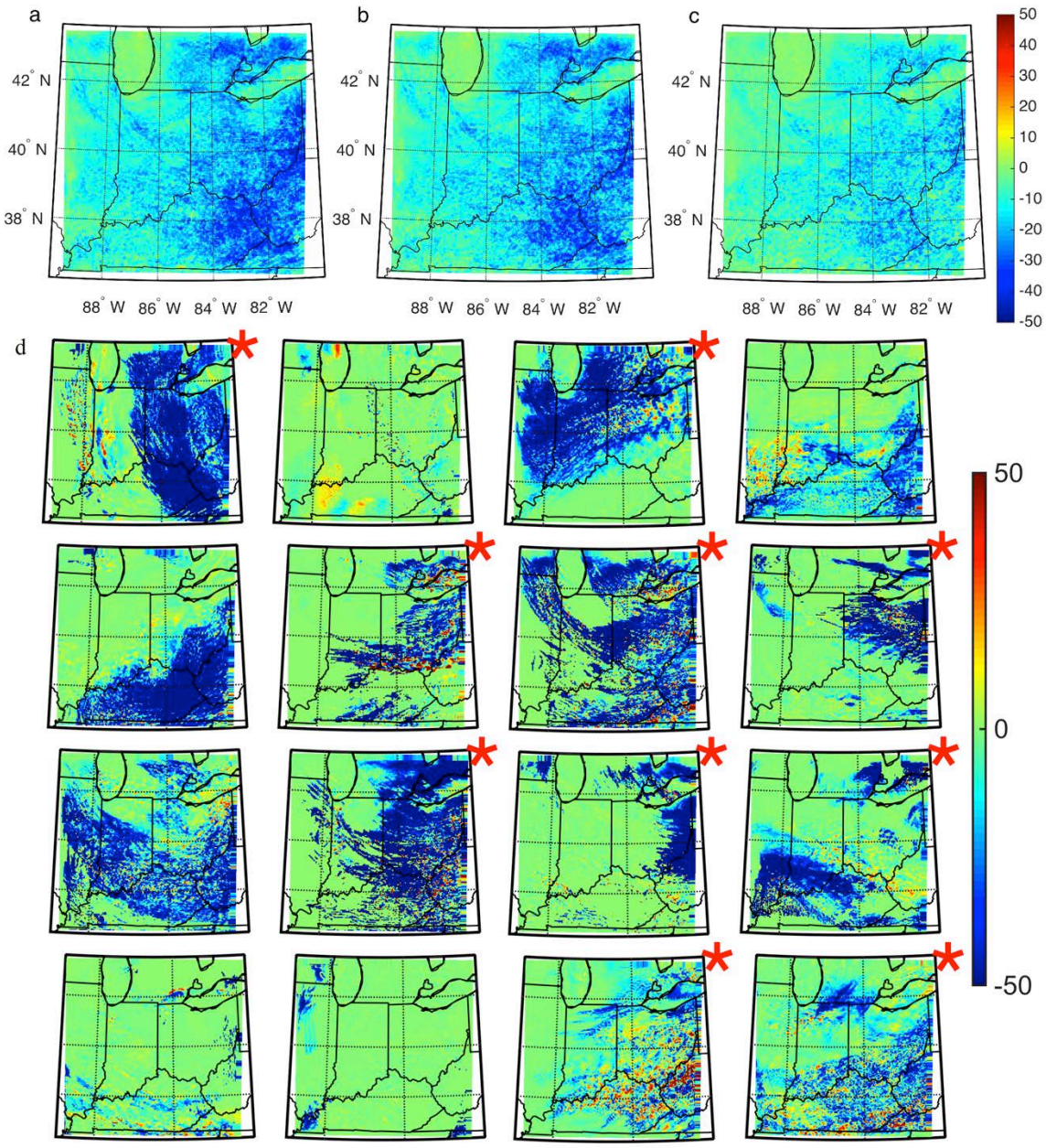

Figure 6.4. Difference in top of atmosphere shortwave radiative flux (W m^{-2}) between the simulations with NPF on and the simulation with NPF off. a-c) Mean difference across the entire study period with a prefactor of a) 2×10^{-5}, b) 2×10^{-6}, c) 2×10^{-7} × $[H_2SO_4]$. d) Daily mean differences for the 2×10^{-5} × $[H_2SO_4]$ simulation. Dates are ordered sequentially in row-major order (i.e. upper left is 12 May, while the lower right shows 27 May) and NPF events days as simulated at MMSF are indicated by red stars in the upper right corner of each panel.

Discussion

New particle formation increases aerosol particle number concentrations, and with sufficient ambient condensable vapor concentrations, those new particles can grow sufficiently to

increase CCN concentrations, and ultimately increase cloud albedo, resulting in a negative radiative forcing (i.e. cooling of the surface and troposphere). Prior research found that at supersaturations of 1% and 0.4%, approximately half of ~ 50 and 80 nm aerosols can act as CCN, respectively[20]. However, the importance of NPF to CCN is very sensitive to the assumed supersaturation, and supersaturations rarely exceed 1% in nature[21]. Consistent with prior studies, our simulations also indicate there is frequently an increase in 50 nm (occasionally 80 nm) diameter aerosols following NPF; however, the increase is often accompanied by a decrease in the concentrations of larger diameter aerosol particles (Figure 6.5a). Therefore, while the number of aerosol particles that are potentially large enough to act as CCN increases, it is typically accompanied by a downward shift in aerosol diameter and thus a requirement for higher water vapor supersaturation. Further consistent with prior studies, the simulations presented herein indicate that the concentration of aerosol particles with diameters > 100 nm are up to two standard deviation above the mean on NPF event days (Figure 6.5b). However, the enhancement of CCN concentrations occurs on those days even in the control simulation without NPF, indicating a non-NPF CCN source that coincides with conditions favorable for NPF (Figure 6.5b). Additionally, on NPF days, this CCN enhancement is reduced and a shift to smaller particle diameters is simulated, potentially due to NPF reducing available semi-volatile species (such as H_2SO_4, Figure 6.5c) and thus inhibiting condensational growth of pre-existing aerosols.

To our knowledge, this is the first study to explicitly resolve changes in cloud droplet number concentrations and cloud albedo due to NPF. Contrary to our *a priori* expectation, in the limited study area and period presented here, NPF reduces cloud albedo and thus cloud forcing, on average, by 10 W m^{-2} and by up to 50 W m^{-2} on individual days in a substantial number of grid cells. It is worthy of note that for all of the NPF prefactor values sampled herein, the TOA-

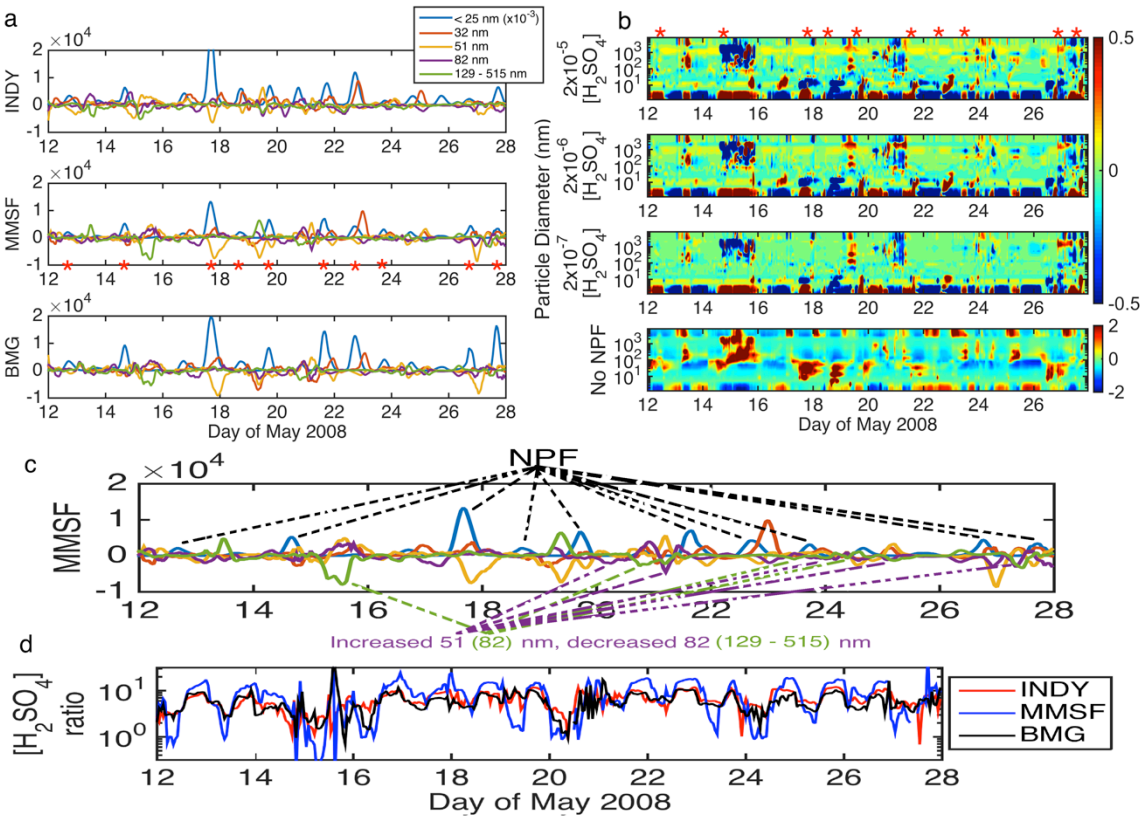

Figure 6.5. a) Difference in particle number concentration ($dN/dlogD_p$; cm^{-3}) by particle diameter (colors) between output from the NPF on and NPF off simulations at the locations of the three in situ measurements sites (location of sites shown in Figure 6.1). b) Differences in anomalies (standard deviations from mean) of the particle number concentrations calculated by diameter across the study period relative to the no NPF simulation at the MMSF grid cell for the various prefactor (top three panels) and anomalies for the no NPF simulation (bottom panel). NPF event days are indicated by red asterisks on the MMSF panel in a) and above the top panel in b). c) As in a) for MMSF, but enlarged and annotated to highlight NPF events and increases in 51 nm (and 82 nm) particles at the expense of larger particles. d) Ratio of sulfuric acid concentrations in the no NPF simulation relative to the simulation with NPF.

SW forcing is, on average, positive (Figure 6.4a-c), though it is of smallest magnitude for the lowest prefactor. It is important to re-emphasize that May is the month with greatest frequency of NPF events in the Midwest and thus the indirect radiative forcing from NPF reported herein cannot be scaled to give an estimate of the annual net radiative forcing. However, for comparison, this radiative forcing is of the opposite sign to the mean annual aerosol indirect forcing of ~ -2 W m^{-2} for the eastern USA derived from coarse-resolution global simulations[46], which in turn is comparable to the annual mean net radiative forcing (of approximately -1 W

m^{-2}) associated with the observed transition of cropland to forests over the eastern US during 1920-1996 (ref. 47). The discrepancy between our results and the global simulations is likely due to our focus on the calendar month of highest NPF frequency and the importance of direct versus parameterized convection and the microphysical scheme in dictating the cloud response to NPF.

It appears that NPF can potentially have a significant positive or negative impact on regional aerosol indirect radiative forcing with the magnitude and even sign of the effect (warming or cooling) varying in space and time even within a region. This has significant implications for making robust regional climate projections, and highlights the importance of explicitly resolving complex cloud-aerosol processes in order to better understand and characterize the indirect radiative forcing due to NPF. The computational demand imposed by the complexity of resolving these processes necessarily limited the spatial domain and temporal duration of the simulations presented herein and led to a decision to use a comparatively simple chemical scheme. Future work will include testing the generalizability of our findings to time of year and geographic location, and the sensitivity of our results to the NPF pathway scheme used and/or inclusion of the partitioning of semi-volatile organic species, and both future emissions and climate scenarios.

Methods

Model description and settings

Simulations were run from 9 – 27 May 2008 (9 – 11 May are used as model spin-up) on a 200×200×45 grid cell domain (the outer 5 grid cells were treated as a buffer zone and excluded from the analysis) centered on 40°N, 85°W using WRF-Chem version 3.6.1 with the activation NPF scheme of Matsui et al, 2011[22]. The simulations were run on a Cray XE6/XK7 supercomputer (Big Red II) for 28 days on 128 cores per simulation. To decrease overall

runtime, the cores were distributed across 16, 16-core Opteron/NVIDIA nodes using only 8/16 cores per node. In total, the simulations presented herein required ~350,000 core hours.

The simulations were run with the following settings (see comprehensive overview of simulation settings in SI):

- A time-step of 20 s (physics, chemistry, and photolysis) was used and output was saved once every hour.
- Anthropogenic emissions were from the 2011 National Emissions Inventory (NEI); biogenic emissions are from the Model of Emissions of Gases and Aerosols from Nature (MEGAN); chemical initial and boundary conditions are from the Model for OZone and Related chemical Tracers (MOZART); and meteorological initial and boundary conditions are from the North American Mesoscale Forecast System (NAM).
- No cumulus parameterization was enabled and the Morrison double-moment microphysics scheme was used with prognostic cloud droplet number.
- The Rapid Radiative Transfer Model for GCMs (RRTMG) was used for both long- and shortwave radiation at 10 min time-steps.
- The Monin-Obukhov Similarity scheme was used for the surface-layer parameterization, the Yonsei University (YSU) scheme was used for the planetary boundary layer physics, and the Noah Land Surface Model was applied.
- Chemistry and aerosols were simulated with the Carbon-Bond Mechanism version Z (CBMZ) and the Model for Simulating Aerosol Interactions and Chemistry (MOSAIC) using 20 sectional aerosol bins from 1 nm – 10 μm with aqueous reactions, and aerosol optical properties were calculated using a volume approximation.

Evaluation methods

The appropriate prefactor for the activation nucleation mechanism used herein is subject to considerable uncertainty and may be spatially and temporally variable[22,36]. Thus simulations were run using 2×10^{-7}, 2×10^{-6}, and $2\times10^{-5} \times [H_2SO_4]$ (Equation 1), and the aerosol number concentrations were compared to in situ measurements from either Scanning Mobility Particle Sizers (SMPS) or Fast Mobility Particle Sizers (FMPS) at three locations near the center of the study domain: Indianapolis, IN (INDY; FMPS $D_p = 6 – 523$ nm), Morgan Monroe State Forest, IN (MMSF; SMPS $D_p = 6 – 110$ nm and FMPS $D_p = 6 – 523$ nm), and Bloomington, IN (BMG; SMPS $D_p = 10 – 414$ nm). The comparisons of nucleation mode particle number concentrations and CS only include simulated aerosol number concentrations in the size bins matching the respective instrument's size bins. The CS is calculated using Equations 2-4 (ref. 48).

$$J = A \times [H_2SO_4] \ldots (1)$$

where J is the nucleation rate of 1 nm particles, A is the prefactor, and $[H_2SO_4]$ is the sulfuric acid vapor concentration.

$$CS = 2\pi D \sum_i \beta_i D_{pi} N_i \ldots (2)$$

$$\beta_i = \frac{1 + Kn}{1 + \left(\frac{4}{3\alpha_i} + 0.337\right) Kn + \frac{4}{3\alpha_i} Kn^2} \ldots (3)$$

$$Kn = \frac{2\lambda}{D_p} \ldots (4)$$

where D is diffusion coefficient (0.06 $cm^2\ s^{-1}$ herein; ref. 49), β_i is the transition regime correction factor and N_i is the aerosol number concentration for aerosols size *i*, Kn is the Knudsen number, α is the sticking coefficient (unity herein), λ is the mean free path of air (68 nm herein).

In situ surface trace gas and aerosol mass measurements used in the model performance assessment are from all available U.S. Environmental Protection Agency monitoring sites within the study domain. Trace gas measurements are daily mean and max values calculated from hourly average measurements for SO_2, NO_2, and carbon monoxide (CO), and 8-hour running average measurements for ozone (O_3); daily mean particulate matter with diameters < 2.5 and 10 μm ($PM_{2.5}$ and PM_{10}) mass measurements are on a one-in-three or one-in-six day schedule depending on the site. The mean error (ME) is calculated for the nearest WRF-Chem grid cell centroid to each site.

Cloud properties used in the model evaluation are from the MODIS instrument on the Aqua satellite (equatorial overpass ~ 1330 local standard time) and have a spatial resolution of 5 × 5 km at nadir. For all retrievals over the domain, comparison is made to the nearest WRF-Chem output hour for the nearest grid cell within 10 km of the retrieval centroid. As no cumulus parameterization is used, grid cells are defined as either cloud or no cloud, and a location is defined as cloudy if clouds are present anywhere in the vertical column; MODIS pixels with a cloud fraction > 0 are defined as cloudy. The percentage of correctly simulated cloudy pixels is quantified as the normalized number of correct forecasts (cloud in both MODIS and WRF-Chem) by the number of missed forecasts (cloud in MODIS, but not WRF-Chem) and false alarms (cloud in WRF-Chem, but not MODIS) (Equation 5). The simulation cloud top height is defined as the highest model level with clouds present and is also evaluated relative to observational estimates from MODIS using the Pearson correlation. It is noted that cloud top heights are not Gaussian; thus Pearson's correlation coefficients should be interpreted cautiously.

$$Percent\ Correct = \frac{h}{m + f + h} \ldots (5)$$

where h is the number of correct forecasts, m is the number of missed forecasts, and f is the number of false alarms.

As there are 190×190 grid cells in the horizontal dimension, an automated method is used to classify each day as either a NPF event or non-event day. A day is defined as a NPF event day if the nucleation mode (D_p < 25 nm) number concentration during any hour was greater than 0.5 standard deviations (σ) above the mean value for that grid cell over the entire simulation period. This threshold is selected to replicate the NPF frequency derived using a subjective classification of the PSD time series at MMSF. Additionally, a NPF event day was considered 'intense' if the nucleation mode number concentration was greater than 1 σ above the local mean. The scale of spatial coherence in NPF occurrence is quantified by calculating the fraction of days on which NPF occurred at each grid cell for all days on which NPF was simulated in the grid cells containing three in situ measurement sites. The frequency of co-occurrence of NPF event days between each site and a random field is computed using a 1000-iteration Monte Carlo simulation. For each iteration a random value is given to each day, and if this value is 0.5 (1) σ above the mean for all days it is classified as an NPF event (intense event) day.

Radiative forcing is quantified using top of atmosphere (TOA) upward shortwave (SW) radiation as a proxy for cloud albedo. The difference between the NPF and control simulations is calculated using all simulation hours in all grid cells with clouds simulated in both the NPF and no NPF simulations. Thus, the difference includes nighttime hours, and therefore the radiative forcing estimates presented here should be viewed as conservative estimates.

Additional model validation is provided in the supplemental information, including: The time series of the particle size distributions at the three in situ measurements sites, the corresponding time series from the simulations, and the time series for each of the NPF

prefactors at MMSF; and the domain mean and variability, as well as spatial distribution in surface trace gas and $PM_{2.5}$ and PM_{10} errors relative to the EPA measurements.

Data availability

The observational datasets and simulation output presented herein are available on request. EPA data are available from: https://www.epa.gov/outdoor-air-quality-data; MODIS data are available from: https://disc.sci.gsfc.nasa.gov/; WRF-Chem is available from: http://www2.mmm.ucar.edu/wrf/users/.

Acknowledgements

Funding was supplied by: NASA Earth and Space Science Fellowship Program - Grant "14-EARTH14F-0207" (RCS) and NASA (NNX16AG31G) (SCP). We acknowledge computational resources provided by the Lilly Endowment, Inc. to the Indiana University Pervasive Technology Institute and the Indiana METACyt Initiative.

Author contributions

RCS and SCP jointly identified the research objectives and designed the research methodology; RCS implemented the NPF scheme into WRF-Chem, ran the simulations, and conducted the analyses; and SCP and RCS jointly wrote the manuscript. SCP collected the in situ PSD used herein. PC contributed to interpreting and contextualizing the results. PC, HM, LRL, and CZ provided guidance on modifying and running the simulations. AT provided guidance on running the simulations in a high performance computing environment. All authors read and commented on the manuscript.

Competing financial interests

The authors declare no competing financial interests.

REFERENCES

1. Paasonen, P. *et al.* Warming-induced increase in aerosol number concentration likely to moderate climate change. *Nat. Geosci.* **6,** 438–442 (2013).
2. Rosenfeld, D., Sherwood, S., Wood, R. & Donner, L. Climate effects of aerosol-cloud interactions. *Science* **343,** 379–380 (2014).
3. Seinfeld, J. H. *et al.* Improving our fundamental understanding of the role of aerosol-cloud interactions in the climate system. *Proc. Natl. Acad. Sci.* **113,** 5781–5790 (2016).
4. Kulmala, M. *et al.* Formation and growth rates of ultrafine atmospheric particles: a review of observations. *J. Aerosol Sci.* **35,** 143–176 (2004).
5. Dunne, E. M. *et al.* Global atmospheric particle formation from CERN CLOUD measurements. *Science* **354,** 1119–1124 (2016).
6. Kulmala, M. *et al.* Direct observations of atmospheric aerosol nucleation. *Science* **339,** 943–946 (2013).
7. Ehn, M. *et al.* A large source of low-volatility secondary organic aerosol. *Nature* **506,** 476–479 (2014).
8. Kerminen, V.-M. *et al.* Cloud condensation nuclei production associated with atmospheric nucleation: a synthesis based on existing literature and new results. *Atmos. Chem. Phys.* **12,** 12037–12059 (2012).
9. Petäjä, T. *et al.* BAECC: A field campaign to elucidate the impact of biogenic aerosols on clouds and climate. *Bull. Am. Meteorol. Soc.* **97,** 1909–1928 (2016).
10. Wendisch, M. *et al.* ACRIDICON–CHUVA Campaign: Studying Tropical Deep Convective Clouds and Precipitation over Amazonia Using the New German Research

Aircraft HALO. *Bull. Am. Meteorol. Soc.* **97,** 1885–1908 (2016).

11. Leng, C. *et al.* Impacts of new particle formation on aerosol cloud condensation nuclei (CCN) activity in Shanghai: case study. *Atmos. Chem. Phys.* **14,** 11353–11365 (2014).
12. Kalivitis, N. *et al.* Atmospheric new particle formation as a source of CCN in the eastern Mediterranean marine boundary layer. *Atmos. Chem. Phys.* **15,** 9203–9215 (2015).
13. Kuang, C., McMurry, P. H. & McCormick, A. V. Determination of cloud condensation nuclei production from measured new particle formation events. *Geophys. Res. Lett.* **36,** doi: 10.1029/2007JD009253 (2009).
14. Merikanto, J., Spracklen, D. V, Mann, G. W., Pickering, S. J. & Carslaw, K. S. Impact of nucleation on global CCN. *Atmos. Chem. Phys.* **9,** 8601–8616 (2009).
15. Kazil, J. *et al.* Aerosol nucleation and its role for clouds and Earth's radiative forcing in the aerosol-climate model ECHAM5-HAM. *Atmos. Chem. Phys.* **10,** 10733–10752 (2010).
16. Ma, N. *et al.* Variation of CCN activity during new particle formation events in the North China Plain. *Atmos. Chem. Phys.* **16,** 8593–8607 (2016).
17. Feingold, G. *et al.* New approaches to quantifying aerosol influence on the cloud radiative effect. *Proc. Natl. Acad. Sci.* **113,** 5812–5819 (2016).
18. Spracklen, D. V *et al.* Contribution of particle formation to global cloud condensation nuclei concentrations. *Geophys. Res. Lett.* **35,** doi: 10.1029/2007GL033038 (2008).
19. Rose, C. *et al.* CCN production by new particle formation in the free troposphere. *Atmos. Chem. Phys.* **17,** 1529–1541 (2017).
20. Dusek, U. *et al.* Size matters more than chemistry for cloud-nucleating ability of aerosol particles. *Science* **312,** 1375–1378 (2006).

21. Seinfeld, J. H. & Pandis, S. N. *Atmospheric chemistry and physics: from air pollution to climate change*. (John Wiley & Sons, 2006).

22. Matsui, H. *et al.* Impact of new particle formation on the concentrations of aerosols and cloud condensation nuclei around Beijing. *J. Geophys. Res. Atmos.* **116,** doi: 10.1029/2011JD016025 (2011).

23. Dipu, S. *et al.* Implementation of aerosol–cloud interactions in the regional atmosphere–aerosol model COSMO-MUSCAT(5.0) and evaluation using satellite data. *Geosci. Model Dev.* **10,** 2231–2246 (2017).

24. Lim, K.-S. S. & Hong, S.-Y. Development of an effective double-moment cloud microphysics scheme with prognostic cloud condensation nuclei (CCN) for weather and climate models. *Mon. Weather Rev.* **138,** 1587–1612 (2010).

25. Yu, X. & Lee, T. Role of convective parameterization in simulations of a convection band at grey-zone resolutions. *Tellus A* **62,** 617–632 (2010).

26. Pryor, S. C., Spaulding, A. M. & Barthelmie, R. J. New particle formation in the Midwestern USA: Event characteristics, meteorological context and vertical profiles. *Atmos. Environ.* **44,** 4413–4425 (2010).

27. Pryor, S. C. *et al.* Spatial and vertical extent of nucleation events in the Midwestern USA: insights from the Nucleation In ForesTs (NIFTy) experiment. *Atmos. Chem. Phys.* **11,** 1641–1657 (2011).

28. Boy, M. *et al.* in *Nucleation and Atmospheric Aerosols* 87–91 (Springer, 2007).

29. Sullivan, R. C. *et al.* Using satellite-based measurements to explore spatiotemporal scales and variability of drivers of new particle formation. *J. Geophys. Res. Atmos.* **121,** 12217–12235 (2016).

30. Yu, F. *et al.* Spring and summer contrast in new particle formation over nine forest areas in North America. *Atmos. Chem. Phys.* **15,** 13993–14003 (2015).

31. Chen, M. *et al.* Acid–base chemical reaction model for nucleation rates in the polluted atmospheric boundary layer. *Proc. Natl. Acad. Sci.* **109,** 18713–18718 (2012).

32. Almeida, J. *et al.* Molecular understanding of sulphuric acid-amine particle nucleation in the atmosphere. *Nature* **502,** 359–363 (2013).

33. Kirkby, J. *et al.* Role of sulphuric acid, ammonia and galactic cosmic rays in atmospheric aerosol nucleation. *Nature* **476,** 429–433 (2011).

34. Sipilä, M. *et al.* The role of sulfuric acid in atmospheric nucleation. *Science* **327,** 1243–1246 (2010).

35. Lupascu, A. *et al.* Modeling particle nucleation and growth over northern California during the 2010 CARES campaign. *Atmos. Chem. Phys.* **15,** 12283–12313 (2015).

36. Sihto, S.-L. *et al.* Atmospheric sulphuric acid and aerosol formation: implications from atmospheric measurements for nucleation and early growth mechanisms. *Atmos. Chem. Phys.* **6,** 4079–4091 (2006).

37. Berg, L. K. *et al.* A new WRF-Chem treatment for studying regional-scale impacts of cloud processes on aerosol and trace gases in parameterized cumuli. *Geosci. Model Dev.* **8,** 409–429 (2015).

38. Matsui, H. *et al.* Spatial and temporal variations of new particle formation in East Asia using an NPF-explicit WRF-chem model: North-south contrast in new particle formation frequency. *J. Geophys. Res. Atmos.* **118,** doi 10.1002/jgrd.50821 (2013).

39. Crippa, P., Sullivan, R. C., Thota, A. & Pryor, S. C. Evaluating the skill of high-resolution WRF-Chem simulations in describing drivers of aerosol direct climate forcing on the

regional scale. *Atmos. Chem. Phys.* **16,** 397–416 (2016).

40. Brisson, E. *et al.* How well can a convection-permitting climate model reproduce decadal statistics of precipitation, temperature and cloud characteristics? *Clim. Dyn.* **47,** 3043–3061 (2016).

41. Bony, S. *et al.* Clouds, circulation and climate sensitivity. *Nat. Geosci.* **8,** 261–268 (2015).

42. Crippa, P. & Pryor, S. C. Spatial and temporal scales of new particle formation events in eastern North America. *Atmos. Environ.* **75,** 257–264 (2013).

43. Hussein, T. *et al.* Time span and spatial scale of regional new particle formation events over Finland and Southern Sweden. *Atmos. Chem. Phys* **9,** 4699–4716 (2009).

44. Jeong, C.-H. *et al.* Particle formation and growth at five rural and urban sites. *Atmos. Chem. Phys.* **10,** 7979–7995 (2010).

45. Vana, M. *et al.* Characteristics of new-particle formation at three SMEAR stations. *Boreal Environ. Res.* 345–362 (2016).

46. Leibensperger, E. M. *et al.* Climatic effects of 1950–2050 changes in US anthropogenic aerosols–Part 1: Aerosol trends and radiative forcing. *Atmos. Chem. Phys.* **12,** 3333–3348 (2012).

47. Ellenburg, W. L., McNider, R. T., Cruise, J. F. & Christy, J. R. Towards an understanding of the twentieth-century cooling trend in the southeastern United States: Biogeophysical impacts of land-use change. *Earth Interact.* **20,** doi: 10.1175/EI-D-15-0038.1 (2016).

48. Dal Maso, M. *et al.* Condensation and coagulation sinks and formation of nucleation mode particles in coastal and boreal forest boundary layers. *J. Geophys. Res. Atmos.* **107,** doi: 10.1029/2001JD001053 (2002).

49. Herrmann, E. *et al.* A computational fluid dynamics approach to nucleation in the water−

sulfuric acid system. *J. Phys. Chem. A* **114,** 8033–8042 (2010).

Supporting Information for

New particle formation leads to cloud dimming

Ryan C. Sullivan[a*], Paola Crippa[b], Hitoshi Matsui[c], L. Ruby Leung[d], Chun Zhao[e], Abhinav Thota[f], and Sara C. Pryor[a,f]

a. Department of Earth and Atmospheric Sciences, Cornell University, Ithaca, NY, USA
b. Department of Civil and Environmental Engineering and Earth Sciences, University of Notre Dame, Notre Dame, IN, USA
c. Graduate School of Environmental Studies, Nagoya University, Nagoya, JPN
d. Pacific Northwest National Laboratory, Richland, WA, USA
e. University of Science and Technology of China, Hefei, China
f. Pervasive Technology Institute, Indiana University, Bloomington, IN, USA
**Corresponding author email: rcs365@cornell.edu*

Contents of this file

Table S6.1 and Figures S6.1-S6.4

Introduction

Settings used for the WRF-Chem simulations presented herein, including domain size and resolution, parameterizations, and emissions inventories used are shown in Table S6.1. A key aspect of the simulations presented herein is inclusion of the NPF parameterization of Matsui et al. 2011 (ref. 1). In brief this parameterization includes a source term for 1 nm particles at a rate proportional to a prefactor and the gas-phase sulfuric acid concentration.

May 2008 was chosen as the simulation period because May is typically characterized by the highest observed NPF frequency over the Midwestern U.S.A.[2], and during this specific month (May 2008) an intensive field experiment was conducted in southern Indiana[3].

The simulations are evaluated using three primary observational data sets: PSD as measured at three near-surface sites in southern Indiana (BMG, MMSF, and INDY, see Figure 6.1 in the main text for locations, and Figures S6.1 and S6.2 herein), near-surface measurements of criteria air pollutants from all available EPA sites within the simulation domain (Figures S6.3

and S6.4), and cloud properties from the MODIS instrumentation on the Aqua satellite (see Figure 6.2 in the main text).

As shown in Figures S6.1 and S6.2 the WRF-Chem simulations using a prefactor of 2×10^{-5} exhibit relatively close accord with the in situ measurements in terms of the frequency, intensity, and growth rates for NPF events at all three measurement locations. Use of a lower prefactor tends to result in much weaker growth into the Aitken mode (Figure S6.2). Thus, discussion in the main text focuses on results from the simulation using a new particle formation rate proportional to $2\times10^{-5} \times [H_2SO_4]$.

The mean and variance in the mean errors (ME) between the concentrations of air pollutants as measured by the EPA and simulated using WRF-Chem, are shown in Figures S6.3 and S6.4. The simulations exhibit a positive bias in simulated near-surface aerosol mass ($PM_{2.5}$ and PM_{10}) relative to virtually all EPA measurements across the study domain (Figures S6.3 and S6.4). Conversely, the simulations are generally negatively biased for near-surface concentrations of gas-phase pollutants such as sulfur dioxide (SO_2) and nitrogen dioxide (NO_2) (Figures S6.3 and S6.4). The magnitude and sign of these biases is consistent with prior (lower resolution) simulations using WRF-Chem over the eastern half of North America[4], and may reflect factors such as inaccuracies in the emission inventory or biases in modeled boundary layer heights/precipitation regimes. The primary impact of these model biases on the NPF simulations presented herein is that they are associated with an overestimation of the in situ condensational sink (Figure 6.1c) and potentially an underestimation of the availability of sulfuric acid for NPF, leading to the greatest agreement between simulations of NPF and in situ measurements for the simulation that uses the highest prefactor relating new particle production to $[H_2SO_4]$. Consistent with expectations, as shown in Figure S6.3 and S4, inclusion of NPF in

the simulation has only a very modest impact on the parameters that are regulated under the Clean Air Act.

The indirect radiative forcing impact of NPF is assessed herein by comparing the top-of-atmosphere (TOA) SW flux difference between simulations including NPF and without NPF. As shown in Figure S6.5 the cumulative probability of the difference in TOA-SW from the simulation with NPF on and a prefactor of 2×10^{-5} versus without NPF exhibits a median value of 10 W m^{-2} when all grid cells within the domain are considered and a median value of 14 W m^{-2} for cloudy pixels. Although these estimates are of smaller magnitude than estimates of episodic direct aerosol forcing over Houston, TX (-30 to -80 W m^{-2}), and modeled aerosol radiative forcing of 10 – 35 W m^{-2} due to wildfires in Europe during the 2003 summer[5,6], this radiative forcing is substantial and worthy of further research.

References

1. Matsui, H. *et al*. Impact of new particle formation on the concentrations of aerosols and cloud condensation nuclei around Beijing. *J. Geophys. Res. Atmos*. **116**, doi: 10.1029/2011JD016025 (2011).
2. Sullivan, R. C. *et al*. Using satellite-based measurements to explore spatiotemporal scales and variability of drivers of new particle formation. *J. Geophys. Res. Atmos.* **121**, 12217–12235 (2016).
3. Pryor, S. C. *et al*. Spatial and vertical extent of nucleation events in the Midwestern USA: insights from the Nucleation In ForesTs (NIFTy) experiment. *Atmos. Chem. Phys*. **11**, 1641–1657 (2011).

4. Crippa, P., Sullivan, R. C., Thota, A. & Pryor, S. C. Evaluating the skill of high-resolution WRF-Chem simulations in describing drivers of aerosol direct climate forcing on the regional scale. *Atmos. Chem. Phys*. **16**, 397–416 (2016).

5. Fast, J. D. *et al*. Evolution of ozone, particulates, and aerosol direct radiative forcing in the vicinity of Houston using a fully coupled meteorology‐chemistry‐aerosol model. *J. Geophys. Res. Atmos*. **111**, doi: 10.1029/2005JD006721 (2006).

6. Hodzic, A. *et al*. Wildfire particulate matter in Europe during summer 2003: meso-scale modeling of smoke emissions, transport and radiative effects. *Atmos. Chem. Phys*. **7**, 4043–4064 (2007).

Domain size	200 x 200
Vertical resolution	45 levels up to 50 hPa
Horizontal resolution	4 km x 4 km
Physics, chemistry, photolysis time-step	20 sec
Radiation time-step	10 min
Cumulus parameterization	None
Microphysics	Morrison double-moment with prognostic cloud droplet number
Long- and shortwave radiation	The Rapid Radiative Transfer Model for GCMs (RRTMG)
Surface-layer physics	Monin-Obukhov Similarity
Planetary boundary layer physics	Yonsei University (YSU)
Land surface	Noah Land Surface Model
Gas-phase chemistry	Carbon-Bond Mechanism version Z (CBMZ)
Aerosols	Model for Simulating Aerosol Interactions and Chemistry (MOSAIC)
Aerosol size bins	20 from 1 nm to 10 μm
Aerosol optical properties	Volume approximation
Anthropogenic emissions	2011 National Emissions Inventory (NEI)
Biogenic emissions	Model of Emissions of Gases and Aerosols from Nature (MEGAN)
Chemical initial and boundary conditions	Model for OZone and Related chemical Tracers (MOZART)
Meteorological initial and boundary conditions	North American Mesoscale Forecast System (NAM)
References	ARW Version 3 Modeling System User's Guide (http://www2.mmm.ucar.edu/wrf/users/docs/user_guide_V3.6/ARWUsersGuideV3.6.1.pdf)
	WRF-Chem version 3.8.1 Users Guide (https://ruc.noaa.gov/wrf/wrf-chem/Users_guide.pdf)

Table S6.1. WRF-Chem v. 3.6.1 simulation settings used herein.

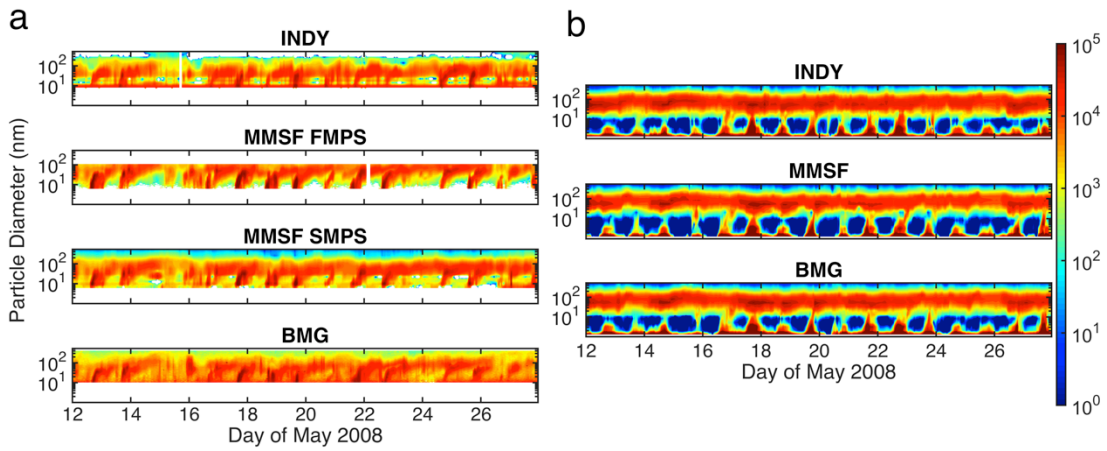

Figure S6.1. Time series of the particle size distributions ($dN/dlogD_p$; cm^{-3}) from a) in situ measurement at INDY, MMSF (note two instruments were operated at MMSF: an SMPS and an FMPS), and BMG (see Figure 6.1 for the locations of these measurement stations), and b) as modeled in the $2\times10^{-5} \times [H_2SO_4]$ NPF simulation. The diameter range shown is consistent across all of the panels; the areas shown in white in (a) denote sizes not measured by the aerosol instrumentation deployed at each site.

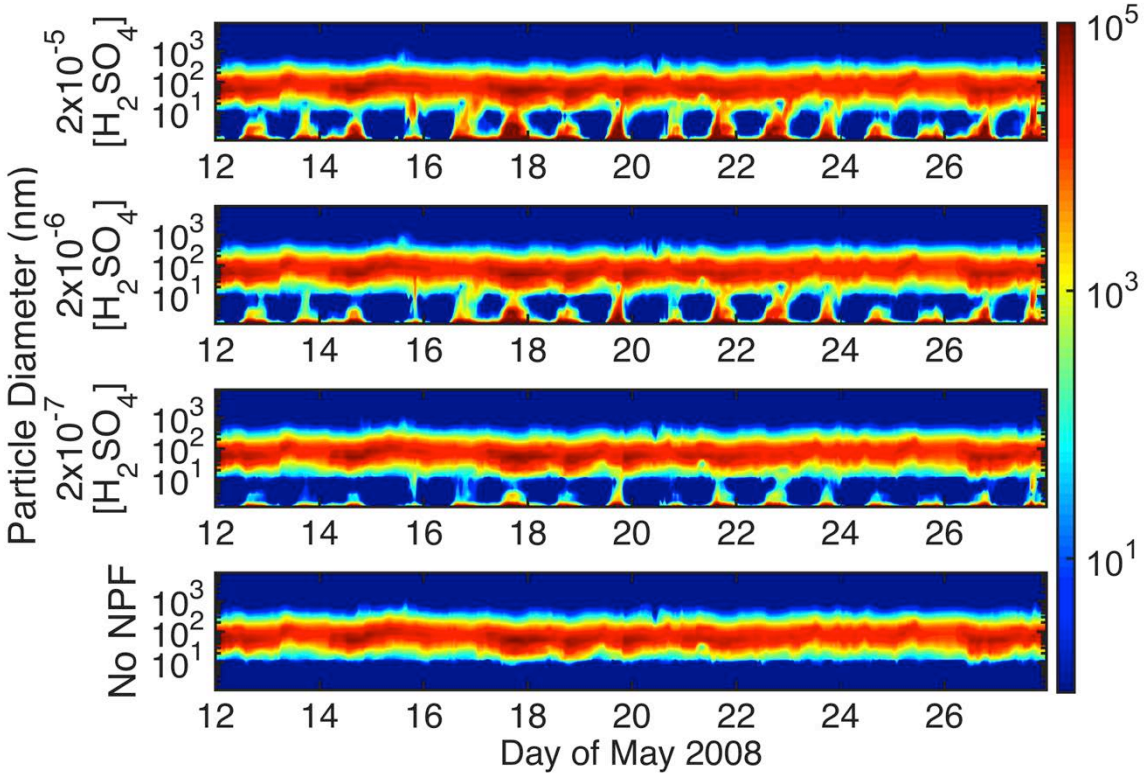

Figure S6.2. Time series of simulated particle size distributions ($dN/dlogD_p$; cm^{-3}) for the grid cell containing MMSF for the variety of NPF prefactors and the control simulation with no NPF.

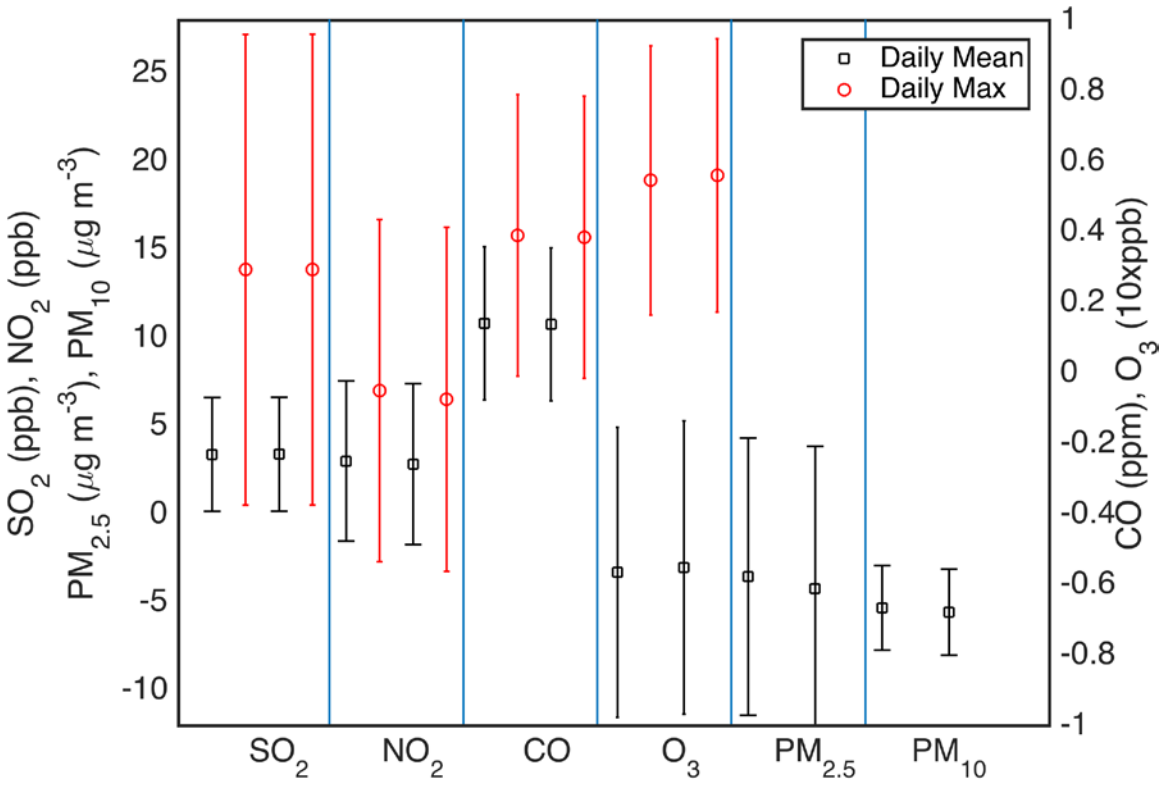

Figure S6.3. Mean (marker) ± 1 standard deviation (whiskers) of the mean error in simulated daily mean and maximum values of near-surface pollutants in WRF-Chem relative to EPA measured concentrations (EPA – WRF-Chem, thus a positive value indicates the model is negatively biased). SO_2, NO_2, and CO are measured hourly, O_3 is an 8-hour running mean, and $PM_{2.5}$ and PM_{10} are measured as a daily average once every three or six days depending on location. The first pair of results is from the $2\times10^{-5} \times [H_2SO_4]$ simulation and the second pair is the control simulation with no NPF.

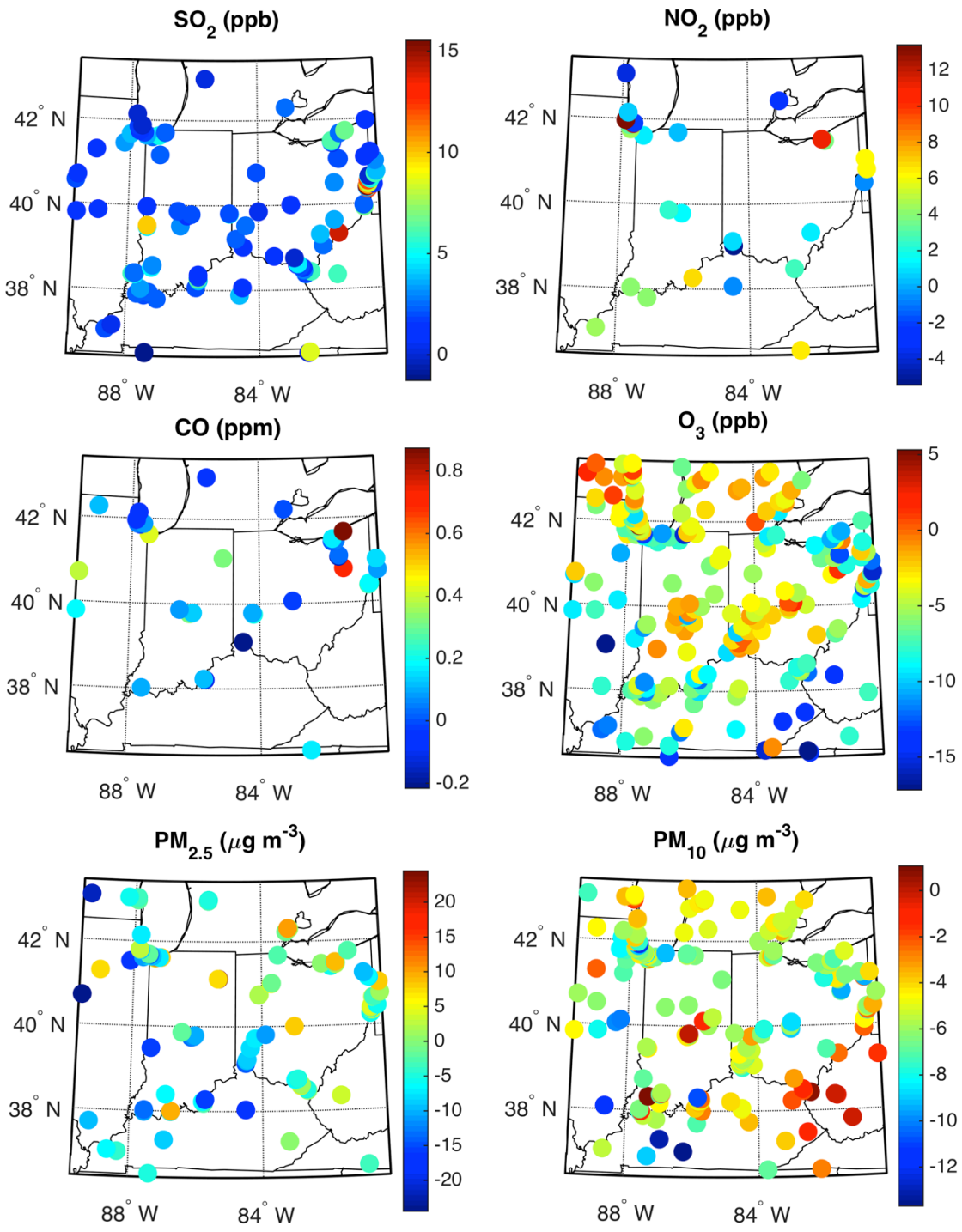

Figure S6.4. Spatial distribution of the mean error in simulated daily mean surface pollutants in WRF-Chem relative to EPA measurements (EPA – WRF-Chem) for the 2×10^{-5} × $[H_2SO_4]$ simulation.

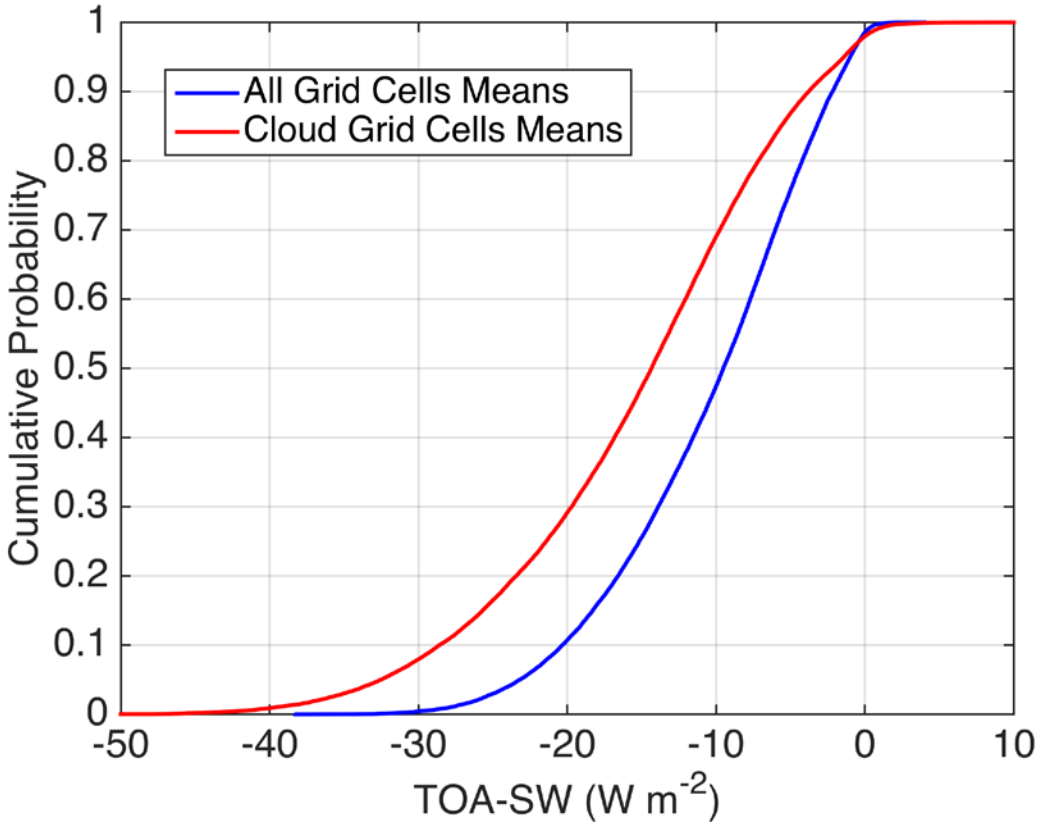

Figure S6.5. Cumulative probability density functions of the grid cell mean difference in TOA-SW from the simulation with NPF on and a prefactor of 2×10^{-5} versus the simulation without NPF. Shown are the grid cell mean changes in TOA-SW when all hours are included (blue), and when only hours with clouds are included (red).

CHAPTER 7

CONCLUSION

The research presented herein integrates in situ and remote sensing measurements with high-resolution numerical simulations to improve understanding of the spatiotemporal scales and drivers of atmospheric aerosol particle concentrations, the drivers and spatiotemporal scales and variability in a key component of aerosol particle dynamics and primary driver of total particle number concentrations: New particle formation (NPF), and the impact of NPF on cloud radiative properties. As described in Chapter 1 my primary research objectives were to:

Research objective 1: Improved quantification of the spatial scales of the columnar burden of optically-active (i.e. accumulation mode) aerosol particles.

Research objective 2: Improved quantification of the spatial scales of new particle formation and their potential impact on cloud properties, and thus indirect climate forcing using in situ, satellite-based observations, and numerical modeling.

A précis of my primary research findings within these research themes follows:

- Research objective 1:
    - My research using remote sensing measurements from the MODIS instrument suite on the Terra and Aqua satellites, AERONET ground-based observations, and the newly released MERRA-2 reanalysis product indicate aerosol optical depth (AOD) (the primary driver of direct aerosol particle climate forcing) exhibits large scales of coherence and that variability in AOD is dominated by the synoptic timescale (i.e. a few days) over eastern North America. The frequency of co-occurrence of extreme AOD values (> local 90^{th} percentile) decreases to below 50% at ~ 150 km from a central grid cell, but is above that expected by random chance over almost all of

eastern North America, indicating supra-regional scale extreme events that may be associated with a substantial perturbation of the regional climate.

- I have developed a framework for calculating climate indicators of aerosol properties that can be used to track and attribute changes in regional aerosol optical properties and hence direct climate forcing. Application of this framework to develop climate indices for sub-regions of the contiguous U.S.A. indicates reductions in anthropogenic emissions over the last three decades are associated with decreased AOD over most of the U.S.A., but natural emissions (e.g. wildfires) are strongly associated with AOD in remote regions, and changes in the manifestation of synoptic scale meteorological patterns may have already offset some of the changes in AOD associated with anthropogenic emissions reductions due in part to the Clean Air Act and other measures designed to improve air quality.
- The detailed evaluation of WRF-Chem simulations of AOD and AE over eastern North America that I have collaborated on has addressed key aspects of diagnosing and attributing model skill. We quantify the value added by enhanced spatial resolution in simulations of the drivers of aerosol direct radiative forcing by applying Weather Research and Forecasting model with coupled Chemistry (WRF-Chem) over eastern North America at different resolutions. Using Brier Skill Scores and other statistical metrics, it is shown that enhanced resolution (from 60 to 12 km) improves model performance for both mean and extreme AOD in three wavelengths in the visible relative to satellite observations, principally via bias reduction. Some of the enhanced model performance appears to be attributable to improved simulation of

specific humidity and the resulting impact on aerosol hygroscopic growth/hysteresis, and thus AOD.

- Research objective 2:
    - In my research I have demonstrated that NPF at five sites across North America exhibits positive one-day autocorrelation. However, there is considerable spatial variability in NPF frequency, formation and growth rates, survival probabilities, and ultrafine particle concentrations. This may imply the need for the development of more sophisticated nucleation mechanisms for inclusion in numerical models. Typically, most model parameterizations that have been developed and applied to date use a single mechanism to predict the characteristics of nucleation across regional and even global domains. My research is thus consistent with other related studies that have suggested that the precise nucleation mechanism (e.g. ternary, activation, and the specific third molecule involved in ternary nucleation) exhibits spatiotemporal variability.
    - Despite the caveat given above, my research has demonstrated that there is enhanced skill in satellite-based proxies of NPF occurrence/intensity by inclusion of satellite-based measurements of gas-phase atmospheric composition.
    - I integrated an existing NPF parameterization in to WRF-Chem v 3.6.1, and applied the modified model at 4 km resolution over the Midwestern U.S.A. The results of my numerical simulations suggest that, consistent with in situ observations and my satellite-based proxy, NPF occurs frequently and on regional scales. However, for the calendar month I simulated, NPF is not associated with enhancement of cloud albedo over the Midwestern U.S.A. Analyses of these simulations indicates that NPF

quenches ambient sulfuric acid concentrations sufficiently to inhibit growth of preexisting particles to CCN sizes. This reduction in CCN-sized particles reduces cloud albedo, resulting in a positive top of atmosphere cloud radiative forcing of up to ~ 50 W m^{-2} relative to a simulation in which NPF is excluded.

Possible areas of related future work include:

- Investigation of the generalizability of the satellite-based NPF proxy to regions outside of the U.S.A. that exhibit markedly different ambient aerosol and precursor gas phase concentrations. Due to uncertainties in satellite-based retrievals of surface trace gas and aerosol concentrations, the proxy should also be evaluated using in situ measurements of the predictors and predictands, and should integrate future, improved satellite-based instruments (e.g., increased spatial/temporal resolution, multi-angle polarimeters) and retrieval algorithms (e.g., using machine learning/artificial neural networks).
- Climate indicators (CI) are a key component of efforts to track changes in both physical and socio-economic aspects of the couple Earth System. Prior to my research, no aerosol-related CI had been proposed for use in the USGCRP CI system. There are many ways in which the aerosol-CI I propose can be further advanced, including: Application of the aerosol climate indicators framework to regions outside of the U.S.A., development of more comprehensive (and potentially synthetic) aerosol indicators, and develop an analogous set of climate indicators to track and attribute changes in regional cloud properties.
- Additional numerical simulations to quantify the impact of NPF on cloud radiative properties in different times of year and geographic locations, and test the sensitivity of our results to the NPF pathway scheme used and inclusion of a more comprehensive chemical scheme, and evaluation of responses to both future emissions and climate scenarios.

APPENDIX A

EVALUATING THE SKILL OF HIGH-RESOLUTION WRF-CHEM SIMULATIONS IN DESCRIBING DRIVERS OF AEROSOL DIRECT CLIMATE FORCING ON THE REGIONAL SCALE

Crippa, P., R. C. Sullivan, A. Thota, and S. C. Pryor (2016), Evaluating the skill of high-resolution WRF-Chem simulations in describing drivers of aerosol direct climate forcing on the regional scale, *Atmos. Chem. Phys.*, *16*, 397–416, doi:10.5194/acp-16-397-2016.

Atmos. Chem. Phys., 16, 397–416, 2016
www.atmos-chem-phys.net/16/397/2016/
doi:10.5194/acp-16-397-2016

Atmospheric Chemistry and Physics Open Access EGU

Evaluating the skill of high-resolution WRF-Chem simulations in describing drivers of aerosol direct climate forcing on the regional scale

P. Crippa[1], R. C. Sullivan[2], A. Thota[3], and S. C. Pryor[2,3]

[1]COMET, School of Civil Engineering and Geosciences, Cassie Building, Newcastle University, Newcastle upon Tyne, NE1 7RU, UK
[2]Department of Earth and Atmospheric Sciences, Bradfield Hall, 306 Tower Road, Cornell University, Ithaca, NY 14853, USA
[3]Pervasive Technology Institute, Indiana University, Bloomington, IN 47405, USA

Correspondence to: P. Crippa (paola.crippa@ncl.ac.uk)

Received: 29 July 2015 – Published in Atmos. Chem. Phys. Discuss.: 8 October 2015
Revised: 4 December 2015 – Accepted: 7 December 2015 – Published: 18 January 2016

Abstract. Assessing the ability of global and regional models to describe aerosol optical properties is essential to reducing uncertainty in aerosol direct radiative forcing in the contemporary climate and to improving confidence in future projections. Here we evaluate the performance of high-resolution simulations conducted using the Weather Research and Forecasting model with coupled with Chemistry (WRF-Chem) in capturing spatiotemporal variability of aerosol optical depth (AOD) and the Ångström exponent (AE) by comparison with ground- and space-based remotely sensed observations. WRF-Chem is run over eastern North America at a resolution of 12 km for a representative year (2008). A systematic positive bias in simulated AOD relative to observations is found (annual mean fractional bias (MFB) is 0.15 and 0.50 relative to MODIS (MODerate resolution Imaging Spectroradiometer) and AERONET, respectively), whereas the spatial variability is well captured during most months. The spatial correlation of observed and simulated AOD shows a clear seasonal cycle with highest correlation during summer months ($r = 0.5$–0.7) when the aerosol loading is large and more observations are available. The model is biased towards the simulation of coarse-mode aerosols (annual MFB for AE $= -0.10$ relative to MODIS and -0.59 for AERONET), but the spatial correlation for AE with observations is 0.3–0.5 during most months, despite the fact that AE is retrieved with higher uncertainty from the remote-sensing observations. WRF-Chem also exhibits high skill in identifying areas of extreme and non-extreme aerosol loading, and its ability to correctly simulate the location and relative intensity of extreme aerosol events (i.e., AOD > 75th percentile) varies between 30 and 70 % during winter and summer months, respectively.

1 Introduction and Objectives

Atmospheric aerosol particles (aerosols) play a major role in dictating Earth's climate by both directly interacting with solar radiation (direct effect) and acting as cloud condensation nuclei and thus changing cloud properties (indirect effect) (Boucher et al., 2013). The global mean aerosol direct effect is estimated to be -0.27 (possible range of -0.77 to $+0.23$) $\mathrm{W\,m^{-2}}$, while the indirect effect is -0.55 (-1.33 to -0.06) $\mathrm{W\,m^{-2}}$ (Stocker et al., 2013). Therefore, their combined radiative forcing is likely a significant fraction of the overall net anthropogenic climate forcing since preindustrial times (i.e., 1.13–3.33 $\mathrm{W\,m^{-2}}$ (Stocker et al., 2013)) and a substantial source of uncertainty in quantifying anthropogenic radiative forcing.

Accurate quantification of direct aerosol radiative forcing is strongly dependent on aerosol precursor and primary aerosol emissions. Both have evolved over the past 2 decades in terms of their spatiotemporal distribution and absolute magnitude. Emissions have generally increased in emerging economies (Kurokawa et al., 2013), biogenic and

Published by Copernicus Publications on behalf of the European Geosciences Union.

anthropogenic emissions have altered in response to changing land use and land cover (Wu et al., 2012), and the implementation of pollution control strategies particularly in North America and Europe have resulted in declines in air pollutant emissions (Xing et al., 2015; Giannouli et al., 2011). Therefore, there is evidence that aerosol burdens and thus direct climate forcing has varied markedly in the past and may change substantially in the future. Further, although best estimates of global anthropogenic radiative forcing from the aerosol direct and indirect effect are -0.27 and $-0.55\,\mathrm{W\,m^{-2}}$ (Stocker et al., 2013), respectively, the short residence time and high spatiotemporal variability of aerosol populations mean that their impact on regional climates can be much larger than the global mean but that they are even more uncertain.

Long-term measurements of aerosol properties are largely confined to aerosol mass (total, PM_{10} or $PM_{2.5}$) in the near-surface layer which may or may not be representative of either the total atmospheric burden (Ford and Heald, 2013; Alston et al., 2012) or radiation extinction and hence climate forcing. Further, aerosol composition measurements are often a 24 h integrated sample taken only on 1 in 3 days and thus are subject to undersampling. Hence, they provide an incomplete description of temporal variability and mean aerosol burdens for model performance evaluation. Columnar remote-sensing measurements of aerosol optical properties are available from a range of ground-based and satellite-borne instrumentation but have only a relatively short period of record, are subject to nonzero measurement uncertainty (and bias), and undersample the range of atmospheric conditions due to cloud masking and infrequent satellite overpasses. Therefore, regional and global models are most commonly used to quantify historical and contemporary aerosol direct radiative forcing based on simulated properties such as the aerosol optical depth (AOD) and Ångström exponent (AE) (Boucher et al., 2013).

Most global models that include aerosol microphysics have been run at a fairly coarse resolution (spatial resolution of the order of 1–2.5°) (Table 1) usually for periods of a few years. The resulting fields of AOD (and less frequently AE) have been evaluated relative to ground-based and satellite-borne remote-sensing optical properties measurements (Table 1). However, aerosol populations (and dynamics) are known to exhibit higher spatial variability (and scales) than can be manifest in those models (Kovacs, 2006; Kulmala et al., 2011; Santese et al., 2007; Schutgens et al., 2013; Shinozuka and Redemann, 2011). Despite recent improvements in the sophistication of aerosol processes and properties within global models, there are still substantial regional and latitudinal discrepancies in both the magnitude of AOD and other aerosol properties which impact aerosol direct radiative forcing and the degree of model-to-model agreement (Myhre et al., 2013). Thus, the skill of these models in reproducing the spatiotemporal variability in the aerosol size distribution, composition, concentration and radiative properties is incompletely characterized. Further large model-to-model variability both in the global mean direct aerosol forcing and in the spatial distribution thereof exists (Kulmala et al., 2011; Myhre et al., 2013), leading to high uncertainty in the quantification of aerosol climate forcing. Although a direct comparison between the studies summarized in Table 1 is inherently very difficult due to the different performance metrics reported and variations in both the model resolution and aerosol descriptions, there is a consistent finding of high spatial variability in model bias, both in sign and magnitude. Correlation coefficients of monthly and seasonal mean AOD from model simulations versus satellite-based measurements are typically in a range of ~ 0.6–0.8 both in global (Colarco et al., 2010; Lee et al., 2015) and regional (Nabat et al., 2015) simulations. However, these correlations are largely reflective of the ability of the models to capture the seasonal cycle and columnar aerosol properties from remote sensing and thus ignore substantial variability on the synoptic scale (Sullivan et al., 2015) and on mesoscales (Anderson et al., 2003). A wider range of correlation coefficients is reported when comparisons are made to high-frequency observations of AOD on the hourly or daily timescale both in global (Sič et al., 2015) and regional (Rea et al., 2015) simulations ($r \sim 0.3$–0.8). The largest range of correlation coefficients ([−0.99, 0.9]; Table 1) is reported when simulated AOD is compared with observations from the AErosol RObotic NETwork (AERONET) and appears to be a function of temporal averaging, location of AERONET sites and model resolution. Correlations between time series of simulated AE versus AERONET observations are reported less frequently and, when conducted for monthly mean values, range from ~ 0.4 (Li et al., 2015) to ~ 0.8 (Colarco et al., 2010).

At least some of the variability in model performance, as indicated by the mutual variability with observations described by correlation coefficients, and model-to-model agreement shown in AeroCom (Aerosol Comparisons between Observations and Models) Phase II may be attributable to variations in model resolution, differences in gas and particle phase parameterizations, and aerosol descriptions. However, there are also variations in the way in which model skill is evaluated and divergent opinions regarding prioritization of future research directions. The direct effect remains poorly quantified on the regional scale, due to uncertainty in aerosol loading, uncertainty and spatiotemporal variability in aerosol physical properties (Colarco et al., 2014), and a relative paucity of rigorous model verification and validation exercises. Confidence in projections of possible future aerosol radiative forcing requires detailed assessment of skill in the current climate and the need for and benefits of regional downscaling and/or the use of high-resolution global models requires careful quantification.

Regional models represent an opportunity to assess whether running higher-resolution simulations over specific regions of interest improves the characterization of aerosol

Table 1. Synthesis of some recent prior studies comparing simulated aerosol optical properties from global or regional model simulations with remote-sensing products. The first column summarizes the model used, the second the domain and the time period simulated, and the third shows the model resolution and summarizes the description of the aerosol size distribution. Columns 4 to 9 summarize the evaluation statistics in terms of the overall correlation coefficient (R), bias (as described using the mean fractional error (MFE)), and root mean square error (RMSE) or mean absolute error (MAE) relative to satellite or AERONET observations as reported in the references shown in column 10.

Model	Domain, time	Resolution, aerosol approach	R AOD vs. satellite	Bias AOD vs. satellite	R AOD vs. AERONET	Bias AOD vs. AERONET	R AE vs. AERONET	RMSE, MAE AE vs. AERONET	Ref
TOMAS in GISS	Global, 2000–2003	2° × 2.5°, sectional: 15 bins from 3 nm to 10 µm	0.63 (average of monthly values from 2004 to 2006, MODIS). 0.73 average of monthly values from 2004 to 2006, MISR)	MFE: −29 % (average of monthly values from 2004 to 2006, MODIS), −34 % (average of monthly values from 2004 to 2006, MISR)	−0.7–0.99 (monthly, 28)	−77–72 % (monthly, 28)	NA	NA	Lee et al. (2015)
GOCART with GEOS DAS	CONUS, 2006–2009	1° × 1.25°, not specified	NA	NA	0.5 (2 h average at MISR overpass, 32)	NA	0.43 (2 h average at MISR overpass, 32)	NA	Li et al. (2015)
GEMS–MACC aerosol module in CNRM-GAME and CERFACS	Global, 1993–2012	1.4°, sectional, 12 bins	NA	Mean relative bias −41–(−52) % (monthly, MISR)	< 0–0.9 (monthly, 166)	NA	NA	NA	Michou et al. (2015)
CNRM-RCSM5	Mediterranean, summer 2012	50 km, sectional, 12 bins	0.64 (seasonal, MODIS), 0.77 (seasonal, MISR), 0.65 (seasonal, SEVIRI)	NA	0.7 (daily, 30)	RMSE ~ 1.75 (daily, 30)	NA	NA	Nabat et al. (2015)
CHIMERE chemical transport model with WRF meteorology	Europe, Mediterranean −10–40° E, 30–55° N, summer 2012	50 km, sectional: 5 bins 40 nm–40 µm	0.35–0.75 (hourly, MODIS)	RMSE: 0.04–0.1 (hourly, MODIS)	0.44–0.73 (hourly, 65)	RMSE: 0.8–0.11 (hourly, 65)	NA	NA	Rea et al. (2015)

Table 1. Continued.

Model	Domain, time	Resolution, aerosol approach	*R* AOD vs. satellite	Bias AOD vs. satellite	*R* AOD vs. AERONET	Bias AOD vs. AERONET	*R* AE vs. AERONET	RMSE, MAE AE vs. AERONET	Ref
MOCAGE	Global, 2007	2° × 2°, sectional: 6 bins per species	0.322 (daily MODIS)	Normalized mean bias 0.098 (daily MODIS)	NA	NA	NA	NA	Sič et al. (2015)
WRF-Chem	0–10° E, 50–55° N, −10–15° E, 46–57° N, −15–30° E, 36–62° N, 14–30 May 2008	Nested 2–30 km, modal	NA	0.38 ± 0.12 and 0.42 ± 0.10 domain average AOD from MODIS and model, respectively	NA	NA	NA	NA	Tuccella et al. (2015)
GOCART in GEOS	Global, 2000–2006	1° × 1.25°, dust (eight bins 0.1–10 µm), sea salt (five bins 0.03–10 µm), carbonaceous and sulfate aerosols, modal	0.747, 0.72 (eastern USA (monthly, MODIS)	NA	0.707 (monthly, 53)	rms: 0.133 (monthly, 53)	0.81 (monthly, 53)	rms: 0.285 (monthly, 53)	Colarco et al. (2010)
EMAC	Global, year 2006	1.1° × 1.1°, modal	NA	Negative (North America)	0.27–0.60 (North America)	RMSE = 0.1–0.2	> 0.5 (Europe)	NA	de Meij et al. (2012)
GEOS-Chem	North America, 6 Jul–14 August 2004	2° × 2.5°, modal	NA	NA	0.87 (study period mean, 24)	NA	NA	NA	Drury et al. (2010)
WRF-Chem	Europe and north Africa, year 2010	23 km, modal and sectional (four bins: 0.04–10 µm)	NA	NA	0.52 (mod) 0.51 (sect)	NMB = −0.06 (mod) NMB = −0.21 (sect) (daily, 12 stations)	NA	NA	Balzarini et al. (2014)
RegCM4	South Asia, 2005–2007	50 km, sectional (four bins: 0.01–20 µm)	NA	NA	0.47–0.71 monthly, 6	NA	NA	NA	Nair et al. (2012)

optical properties of relevance to direct radiative forcing. The assessment of value added (or lack thereof) from high-resolution regional versus global coarse-resolution models has not been clearly quantified in previous studies (Table 1). Although high-resolution simulations, comparable to those presented herein, have been run, they cover a small temporal and spatial domain (e.g., Tuccella et al., 2015) or lack quantitative assessment of aerosol optical properties (e.g., Tessum et al., 2014). Thus, the quantification of the skill of high-resolution modeling of aerosol optical properties is presented here along with a preliminary analysis of model performance as a function of spatial aggregation. Forthcoming work will include a direct comparison to coarser-resolution simulations to quantify the value added (or lack thereof) from increased model resolution.

We evaluate the skill of state-of-the-art high-resolution regional model simulations of climate-relevant aerosol properties using a range of descriptive statistics and investigate possible sources of discrepancies with observations. The impact of aerosols on climate and human health are strengthened under conditions of enhanced aerosol concentrations; thus, it is necessary to study and diagnose causes of "extreme aerosol events" (Chu, 2004; Gkikas et al., 2012) and to evaluate the ability of numerical models to simulate their occurrence, intensity, spatial extent and location. Prior analyses of Level-3 (1° resolution) MODIS (MODerate resolution Imaging Spectroradiometer) AOD over the eastern half of North America have indicated that extreme AOD values (> local 90th percentile) are coherent on regional scales ($\sim$ 150 km) (Sullivan et al., 2015). Thus, our evaluation exercise also includes an analysis of the spatiotemporal coherence of extreme events.

We applied the Weather Research and Forecasting model coupled with Chemistry (WRF-Chem version 3.6.1) at high resolution (12×12 km) over eastern North America during the year 2008, in the context of a pseudo type-2 downscaling exercise in which the high-resolution model is nested within reanalysis boundary conditions (Castro et al., 2005). The choice of this spatial resolution is taken in part to match the resolution of the North American Mesoscale model that is used for the meteorological lateral boundary conditions and to ensure we capture some mesoscale variability while keeping it computationally feasible.

Our evaluation is designed to investigate spatiotemporal variability of aerosol optical properties (i.e., AOD and AE) in their mean and extreme values. Thus, we conduct our evaluation of the simulations using

1. high-frequency, disjunct time series data from point measurements at AERONET stations;

2. relatively high-resolution spatial data from lower-frequency (once daily or lower) data from polar-orbiting satellites (i.e., MODIS and MISR (Multi-angle Imaging Spectroradiometer)).

We also include intercomparison with daily mean $PM_{2.5}$ concentrations from 1230 surface stations and near-surface $PM_{2.5}$ composition using data from 123 IMPROVE (Interagency Monitoring of Protected Visual Environments) sites. The $PM_{2.5}$ concentrations data for 2008 were obtained from the US Environmental Protection Agency (EPA) AirData web site and represent all available outdoor near-surface 24 h mean $PM_{2.5}$ measurements in the model domain. Most of these stations report values on a 1 day in 3 schedule. Daily average $PM_{2.5}$ chemical compositions are also available for 1 day in 3 and were accessed online through the IMPROVE data wizard. We further evaluate the WRF-Chem simulations of a key meteorological parameter – precipitation – relative to observations from the Delaware gridded data set (Matsuura and Willmott, 2009). This data set includes monthly accumulated precipitation data on a $0.5 \times 0.5°$ grid which is estimated by interpolating station observations from the Global Historical Climatology Network using the spherical version of Shepard's distance-weighting method (Shepard, 1968; Willmott et al., 1985).

This paper is structured as follows. We first describe the settings used in our WRF-Chem simulations and introduce the remote-sensing and other data used for model evaluation (Sect. 2). A description of statistical metrics used for the evaluation is also provided. Section 3 presents results of the evaluation of simulated AOD and AE versus observations, as well as findings on extreme AOD values. In Sect. 4 we summarize our findings and draw conclusions.

2 Methods

2.1 WRF-Chem simulations

The WRF-Chem (Grell et al., 2005; Fast et al., 2006) is used to simulate aerosol processes over eastern North America during the whole of 2008. The simulation domain comprises 300×300 grid points with a 12 km resolution and is centered on southern Indiana (86° W, 39° N). The calendar year 2008 was selected because it is representative of average climate and aerosol conditions in the center of the model domain (near Indianapolis, IN). In 2008, mean T_{max}, T_{min}, precipitation and wind speed as measured at the National Weather Service Automated Surface Observing Systems (NWS ASOS) station at Indianapolis International Airport are within ± 0.25 standard deviations (σ) of the 2000–2013 seasonal means. Further, mean seasonal AOD from Level-3 MODIS retrievals is within $\pm 0.2\sigma$ of 2000–2013 mean values. Additionally, the choice of this year ensures the availability of multiple sources of ground- and space-based measurements of aerosol properties for the evaluation of the simulations.

Table 2 provides details of the WRF-Chem simulations. In brief, we used 32 vertical levels up to 50 hPa with telescoping to allow for a good vertical resolution in the boundary layer (i.e., approximately 10 layers below 1 km for

Table 2. Physical and chemical schemes adopted in the WRF-Chem simulations presented herein.

Simulation settings	Values
Domain size	300 × 300 cells
Horizontal resolution	12 km
Vertical resolution	32 levels up to 50 hPa
Time step for physics	72 s
Time step for chemistry	5 s
Physics option	**Adopted scheme**
Microphysics	WRF Single-Moment 5-class
Longwave radiation	Rapid radiative transfer model (RRTM)
Shortwave radiation	Goddard
Surface layer	Monin–Obhukov similarity
Land surface	Noah land surface model
Planetary boundary layer	Mellor–Yamada–Janjić
Cumulus parameterizations	Grell 3
Chemistry option	**Adopted scheme**
Photolysis	Fast J
Gas phase chemistry	RADM2
Aerosols	MADE/SORGAM
Anthropogenic emissions	NEI (2005)
Biogenic emissions	Guenther, from USGS land use classification

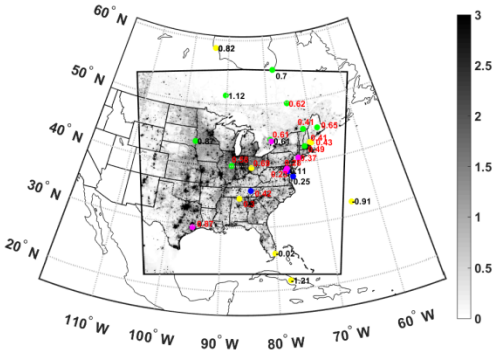

Figure 1. Location of the AERONET stations (colored dots) used in this study and mean daily $PM_{2.5}$ emissions (mg m^{-2} day^{-1}) during 2008 (gray shading). Colors indicate the AERONET site classification based on Kinne et al., 2013: polluted (magenta), land (green), coastal (blue), unclassified (yellow). The numbers are mean fractional bias (MFB) for WRF-Chem vs. AERONET stations (red numbers indicate that WRF-Chem vs. AERONET has a larger MFB than WRF-Chem vs. MODIS, whereas black numbers indicate a lower bias in the comparison with AERONET).

non-mountainous regions). Meteorological lateral boundary conditions are provided every 6 h from the North American Mesoscale (NAM) model applied at a 12 km resolution. The initial and boundary chemical conditions are based on output from the offline global chemical transport model MOZART-4 (Model for OZone And Related chemical Tracers, version 4), driven by meteorology from NCEP–NCAR reanalysis (Pfister et al., 2011; Emmons et al., 2010). Anthropogenic emissions are from the POET (Precursors of Ozone and their Effects in the Troposphere) and the EDGAR (Emissions Database for Global Atmospheric Research) databases. The land cover is specified based on the USGS 24-category data at 3.7 km resolution (Anderson et al., 1976). Anthropogenic point and area emissions at 4 km resolution are input hourly from the US National Emissions Inventory (NEI-05) (US-EPA, 2009) and specified for 19 vertical levels (see Fig. 1 for an overview of the primary aerosol emissions). Biogenic emissions of isoprene, monoterpenes, other biogenic volatile organic compounds (VOCs), oxygenated VOCs (OVOCs), and nitrogen gas emissions from the soil are described as a function of simulated temperature and photosynthetic active radiation (for isoprene) using the model of Guenther (Guenther et al., 1993, 1994; Simpson et al., 1995). Aerosol and gas phase chemistry are described using the second generation Regional Acid Deposition Model (RADM2) chemical mechanism (Stockwell et al., 1990) and the Modal Aerosol Dynamics model for Europe (MADE) which incorporates the Secondary Organic Aerosol Model (SORGAM) (Ackermann et al., 1998; Schell et al., 2001). The correct characterization of aerosol optical properties is dependent on model skill in describing particle composition and mixing state (Li et al., 2015; Curci et al., 2014). With this in mind, it is worthy of note that aerosol components are assumed to be internally mixed within each mode (although the composition differs by mode). The standard deviation on the lognormal Aitken and accumulation modes are fixed at 1.6 and 2, respectively. The choice of a modal representation of aerosol size distribution is dictated by the high computational demand of more sophisticated approaches (e.g., sectional description of the aerosol size distribution) for long-term simulations. With the current settings, the 1-year run was completed without restart in 9.5 days (230 h) on the Cray XE6/XK7 supercomputer (Big Red II) owned by Indiana University using 256 processors distributed on eight nodes, thus indicating the feasibility of this configuration for climate-scale simulations. Aerosol and gas phase concentrations and meteorological properties are saved once hourly. AE from the WRF-Chem simulations is computed using

$$\mathrm{AE} = \frac{\ln \frac{\mathrm{AOD}_{400\mathrm{nm}}}{\mathrm{AOD}_{600\mathrm{nm}}}}{\ln \frac{600\,\mathrm{nm}}{400\,\mathrm{nm}}}. \quad (1)$$

AOD at wavelengths (λ) of 500 and 550 nm for comparison with MODIS and MISR, respectively, are derived using the

Ångström power law:

$$\mathrm{AOD}_\lambda = \mathrm{AOD}_{300} \times \frac{\lambda}{300}^{(-\mathrm{AE})}. \quad (2)$$

We investigated the wavelength dependence on the AE calculation using λ at 300 and 1000 nm as proposed in Kumar et al. (2014) and found that, although AOD estimates are independent of the wavelength range selected, $\mathrm{AE}_{400-600\mathrm{nm}}$ is systematically lower than $\mathrm{AE}_{300-1000\mathrm{nm}}$. Analyses of AE reported in this study are obtained using $\lambda = 400$ and 600 nm since they are closer to those used in AE satellite retrievals.

2.2 Remotely sensed data

Consistent with previous research (Sect. 1 and Table 1), we evaluate the WRF-Chem simulations using four primary remote-sensing products – three are drawn from instruments on the Aqua and Terra satellites, while the fourth is from ground-based radiometers operated as part of the AERONET network. The data sets are as follows:

1. The MODIS instruments aboard the polar-orbiting Terra ($\sim$ 10:30 overpass local solar time (LST)) and Aqua ($\sim$ 13:30 LST) satellites. They have measured atmospheric aerosol optical properties since 2000 and 2002, respectively, with near-global daily coverage (Remer et al., 2005). Herein we use the Level 2 (L2; 10 km resolution) "dark-target" products of AOD at 550 nm and AE at 470 and 660 nm (Collection 5.1; Levy et al., 2010). The L2 AOD uncertainty is $\pm 0.05 \pm 0.15 \times$ AOD over land relative to global sun photometer measurements from AERONET; even when no spatiotemporal averaging is used in the comparison (i.e., all combinations of MODIS retrievals within 30 km of an AERONET site and all AERONET retrievals within 30 min of the satellite overpass), 71 % of MODIS retrievals fall within a $\pm 0.05 \pm 0.2 \times$ AOD envelope relative to AERONET over East CONtiguous US (E. CONUS) (Hyer et al., 2011). AE is retrieved with higher uncertainty, and tends to exhibit a bimodality in retrieved values (Levy et al., 2010; Remer et al., 2005) (see Fig. S1 in the Supplement). For this reason, where we compare WRF-Chem-simulated AE with values from MODIS, we treat AE as a binary variable, wherein AE < 1 is taken as representing coarse-mode-dominated aerosol populations and AE > 1 indicates fine-mode-dominated populations (Pereira et al., 2011; Valenzuela et al., 2014).

2. The MISR instrument is also aboard the Terra satellite and measures radiances at four wavelengths from 446 to 886 nm at nine viewing angles from nadir to 70.5°. MISR (L2, 17.6 km resolution) retrieves AOD with lower uncertainty than MODIS ($\pm 0.05 \times$ AOD relative to AERONET) but with lower temporal resolution (global coverage in $\sim$ 1 week) (Kahn et al., 2010, 2005). Herein, we use the $0.5° \times 0.5°$ gridded Level 3 (Ver. 31) AOD (at 555 nm) and AE (calculated from AOD at 443 and 670 nm).

3. Ground-based sun photometer measurements from 22 AERONET (Holben et al., 1998) stations are also used in this study (Fig. 1). This network is highly spatially inhomogeneous, but under cloud-free conditions the observations are available at multiple times during daylight hours. AOD is measured directly by the AERONET sun photometers at seven wavelengths (340, 380, 440, 500, 670, 870 and 1020 nm) with high accuracy (i.e., AOD uncertainty of < 0.01 for $\lambda > 440$ nm (Holben et al., 2001)). The AE is calculated for all available wavelengths within the AOD range. The AE 870–440 nm includes the 870, 670, 500 and 440 nm AOD data. Level-2 aerosol products from AERONET (i.e., cloud screened and quality assured) have been used extensively in satellite and model validation studies (including many of those summarized in Table 1) and are used herein.

To avoid the discontinuity in the MODIS retrieval algorithm due to different assumed aerosol types (Levy et al., 2007), we confine our analyses of model skill to longitudes east of 98° W. Only WRF grid cells with cloud fraction equaling 0 during the satellite over pass of each grid cell are used in comparison to MODIS and MISR observations, and only grid cells with at least five valid observations (both from MODIS and MISR and cloud-screened WRF) during a given month are included in the analyses presented herein. It is worth noting that setting a threshold of 10 observations does not significantly affect the results. For a uniform assessment, L2 MODIS and L3 MISR data have been interpolated from their native grids (and resolutions of 10 km and $0.5° \times 0.5°$, respectively) to the WRF-Chem 12 km resolution grid by computing the mean of pixels with valid data within 0.1° and 0.3° for MODIS and MISR, respectively, from the model centroids. The choice of averaging over a slightly larger area than model resolution is dictated by the sparsity of valid satellite retrievals. For AERONET vs. MODIS comparison, we only use the nearest MODIS data (after regridding to WRF) to each site. Where hourly WRF-Chem output is compared with data from AERONET sites, a station is only included if there are at least 20 simultaneous estimates available, and each AERONET measurement is compared to the nearest WRF-Chem time step and to the grid cell containing the station.

2.3 Statistical methods used in the model evaluation

The primary error metric of overall model performance used herein is the mean fractional bias (MFB) (Boylan and Russell, 2006):

$$\mathrm{MFB} = \frac{1}{N} \sum_{1}^{N} \frac{C_\mathrm{m} - C_\mathrm{o}}{\frac{C_\mathrm{m} + C_\mathrm{o}}{2}}. \quad (3)$$

Table 3. Spatial mean fractional bias (MFB) over the entire year. Recall MFB $= \frac{1}{N}\sum_1^N \frac{C_m - C_0}{\frac{C_m + C_0}{2}}$, where C_m is the monthly mean AOD or AE simulated by WRF-Chem at a specific location and C_0 refers to the same quantity from MODIS, MISR and AERONET. Thus, a negative value indicates that the model is negatively biased relative to the observations. The total sample size N is 358 048 and 359 633 when comparing WRF-Chem with MODIS onboard Terra and Aqua, respectively. The comparison between MODIS and AERONET is affected by a few outlier sites, so the MFB when the three most biased sites are removed is given in parentheses. The mean domain-averaged AOD and AE from WRF-Chem (after applying the cloud screen and selecting only MODIS overpass hours) are 0.222 and 1.089, respectively.

Comparisons	MFB AOD	MFB AE
WRF-MODIS (Terra)	0.15	−0.09
WRF-MODIS (Aqua)	0.14	−0.11
WRF-MISR (Terra)	0.16	−0.11
WRF-AERONET	0.50	−0.59
MODIS (Terra)-AERONET	−1.23 (−0.91)	−0.13 (−0.11)

Table 4. Contingency table used to compare the fraction of grid cells classified as fine, F (AE > 1), and coarse, C (AE < 1), by MODIS and WRF-Chem (indicated in the table by M and W, respectively).

		MODIS	
		Fine	Coarse
WRF-Chem	Fine	WF/MF	WF/MC
	Coarse	WC/MF	WC/MC

MFB is a useful model performance indicator since it weights positive and negative biases equally. It varies between +2 and −2 and has a value of 0 for an ideal model. Where MFB is reported for WRF-Chem versus MODIS, MISR and AERONET, C_m is the monthly mean AOD or AE simulated by WRF-Chem at a specific location, C_0 refers to the same quantify from remote-sensing data (Table 3) and N is the sample size.

The evaluation of WRF-Chem simulations of AOD and AE relative to satellite retrievals (MODIS and MISR) is also summarized using Taylor diagrams (Taylor, 2001) produced from the monthly means for the grid cells with simultaneous data availability. Taylor diagrams synthesize three aspects of model skill focused on evaluations of the spatial fields of the parameter of interest: the correlation coefficient of the modeled vs. observed field which is expressed by the azimuthal position; the root mean squared difference which is proportional to the distance between a point and the reference point on the x axis (at 1, 0); and the ratio of simulated and observed spatial standard deviation which is proportional to the radial distance from the origin.

To investigate model performance at given locations through time, empirical quantile–quantile (EQQ) plots are constructed using high-frequency realizations of AOD and AE at individual locations (AERONET sites) relative to WRF-Chem values simulated in the grid cell containing the measurement site. EQQ plots are thus generated for each of the AERONET stations using all hours when there are simultaneous estimates available from the direct observations and from the numerical simulations. The advantage of EQQ plots is that they make no assumptions regarding the underlying form of the data and can be readily used to determine which parts of the modeled distribution deviate from the observations (and thus fall away from a 1 : 1 line).

The validity of AE estimates is a function of both the absolute magnitude of AOD and the uncertainty in the wavelength-dependent AOD. AE provides information regarding the relative abundance of fine to coarse particles. Thus, here we quantify the model skill in reproducing spatial patterns of fine- and coarse-mode particles observed by MODIS (Terra) by comparing the frequency distribution of AE lower and higher than 1 to distinguish populations dominated by coarse and fine aerosols, respectively, in WRF-Chem and MODIS (Valenzuela et al., 2014; Pereira et al., 2011). The choice of this threshold reflects the AE distribution. AE simulated by WRF-Chem generally conforms to a single normal distribution centered on 1 during January–April and on 1.3 from May–June to December; AERONET time series also tend to conform to a single mode, while MODIS estimates typically are bimodally distributed (see Fig. S1). We therefore consider the data in the form of a contingency table (Table 4) and compute a χ^2 test to assess whether the frequency distribution of fine and coarse particles is the same between MODIS and WRF-Chem. The χ^2 statistic is applied with 1 degree of freedom and a 99% confidence limit.

As described above, the impact of aerosols on climate and human health is strengthened under conditions of enhanced aerosol concentrations; thus, two analyses were undertaken to evaluate the ability of the WRF-Chem simulations to represent extreme AOD values:

1. Evaluation of the spatial patterns of extreme events. Using daily estimates of AOD in each grid cell and month, we identified the 75th percentile value across space (i.e., p75) as a threshold for extreme AOD for WRF-Chem and MODIS separately. Grid cells with AOD exceeding that threshold were classified as exhibiting extreme values. The consistency in the spatial distribution of extreme values as simulated by WRF-Chem relative to MODIS is quantified using three skill statistics: the accuracy, hit rate (HR) and threat score (TS) defined in Eqs. (4)–(6). In these equations, WE, ME, WN and MN correspond to the frequency of extreme conditions in WRF-Chem (WE) or MODIS (ME) or neither (WN or

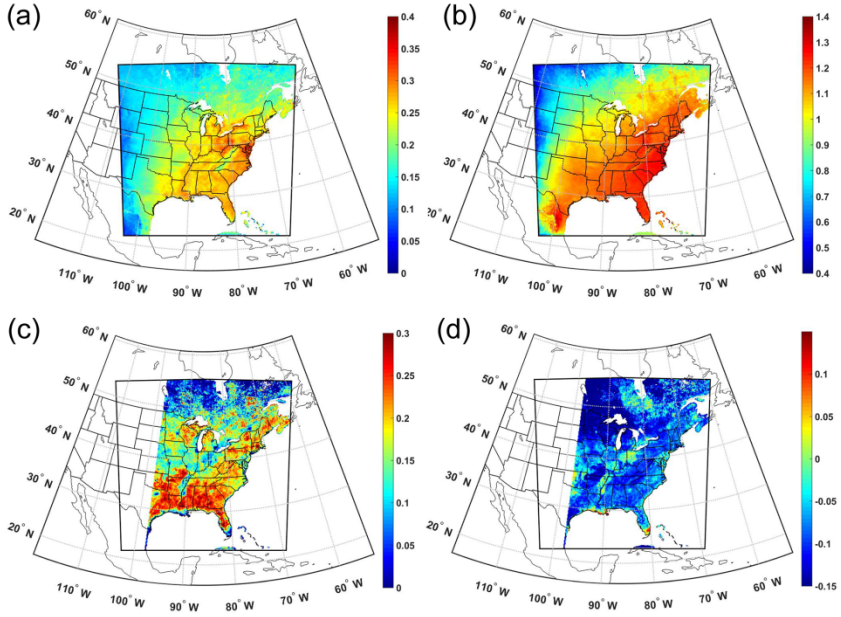

Figure 2. Mean **(a)** AOD and **(b)** AE simulated by WRF-Chem during the year 2008. The mean values are computed after applying a cloud mask and are for the Terra overpass time. Mean fractional bias (MFB) for **(c)** AOD and **(d)** AE for WRF-Chem relative to MODIS (Terra) (similar results are found for Aqua). The inner black frame indicates the entire model domain, while as stated in the text, model evaluation is only undertaken for longitudes east of 98° W.

MN):

$$\text{Accuracy} = \frac{\text{WE/ME} + \text{WN/MN}}{\text{WE/ME} + \text{WE/MN} + \text{WN/ME} + \text{WN/MN}}, \quad (4)$$

$$\text{HR} = \frac{\text{WE/ME}}{\text{WE/ME} + \text{WN/ME}}, \quad (5)$$

$$\text{TS} = \frac{\text{WE/ME}}{\text{WE/ME} + \text{WE/MN} + \text{WN/ME}}. \quad (6)$$

The Accuracy describes the fraction of grid cells co-identified as exceeding p75 or not in MODIS and WRF-Chem and thus weights event and non-event conditions equally. Since the accuracy quantifies model skill in correctly identifying both extreme and non-extreme aerosol loadings, it is thus indicative of model performance in capturing the overall AOD spatial variability. In this application, where extreme is identified as the 75th percentile, a value of 0.5 would indicate that none of the grid cells experiencing extreme events were reproduced by the model, while 1 would indicate perfect identification of events and non-events. The HR and TS metrics give "credit" only those grid cells identified as "extreme". For these metrics, a value of 0 indicates no correct identification of grid cells with extreme values, while a perfect model would exhibit a value of 1.

2. Evaluation of the scales of coherence of extreme AOD. For each day during the overpass time and hours of clear-sky conditions, we determine whether AOD simulated at our reference location (i.e., the center of the domain, in southern Indiana) is equal to or larger than the local p75 for that grid cell and season and then identify all grid cells in the domain that also satisfy the condition of AOD $\geq$ local p75. The reference location represents the center of gravity of the domain and was previously used by Sullivan et al. (2015) for assessing scales of coherence. In that work they also found that the spatial scales of coherence are not sensitive to the precise choice of reference location. For each season, we thus compute the probability of extreme AOD co-occurrence at our reference site and any other grid cell as the frequency of co-occurrence divided by the number of extreme occurrences at the reference location. The spatial

scales of extreme AOD are then estimated by binning the radial distance of each grid cell centroid from the domain center into 100 km distance classes. An analogous procedure is applied to L2 MODIS data to compare them with simulations.

3 Results

3.1 Evaluation of AOD

Overall WRF-Chem is positively biased relative to remotely sensed AOD. The spatial MFB is 0.15 (0.14) when computed using all available MODIS measurements from Terra (Aqua) and 0.50 relative to data from the AERONET stations (Table 3). The sign of this bias is consistent across the entire simulation domain (Fig. 2). These results agree with findings from previous regional studies that have also shown an overestimation of AOD by WRF-Chem over eastern North America and Europe (i.e., regions dominated by sulfate aerosols) and an underestimation in the western USA and most of the rest of the globe (Zhang et al., 2012; Colarco et al., 2010; Curci et al., 2014) (Table 1). Higher biases of WRF-Chem-simulated annual mean AOD are found in the southern portion of the domain (Fig. 2) where the model also exhibits a positive bias in daily mean near-surface $PM_{2.5}$ relative to observations from 1230 US EPA sites (see Figs. 3 and S2). We further investigated the bias in $PM_{2.5}$ by comparing WRF-Chem simulations with ground-based measurements of particle composition at 123 IMPROVE sites over our domain. We computed the MFB on a seasonal basis between sulfate and nitrate concentrations in fine-mode particles (i.e., Aitken and accumulation mode) versus observations (Fig. 4) and found sulfate concentrations are underestimated almost over the entire domain during winter, whereas a positive bias is present in the other seasons. Conversely, nitrates tend to be overestimated during winter and fall at most sites, whereas they are underestimated during summer. Thus, the positive bias in AOD and $PM_{2.5}$ mass particularly during the summer appears to be associated with excess sulfate concentrations.

The MFB of WRF-Chem relative to MODIS estimates of AOD is lower than the MFB relative to most of the AERONET stations except for a few sites located along the coast, one polluted site in the northeast and at a few land sites in the north or northwest (Figs. 1 and 5a). This is possibly a result of an inability of the model to capture variations in aerosol optical properties occurring on a local scale (below the resolution of 12 km). However, the evaluation statistics for WRF-Chem relative to AERONET did not vary consistently with the classification of AERONET stations. Indeed, the mean MFB for AOD at coastal, polluted and land sites varies between 0.26 (coastal) and 0.67 (land), whereas for AE it varies between −0.72 (coastal) and −0.50 (land). When MODIS is compared to the 22 AERONET stations the MFB is −1.23 suggesting an underestimation of AOD from AERONET relative to MODIS. The large bias can be explained noting that the number of co-samples in MODIS is quite small and that MFB is strongly impacted by a few outliers. When we remove the three most biased sites (one land site in the north and two sites along the east coast), the MFB decreases to −0.91.

Using very limited data, prior research indicated mesoscale variability (horizontal scales of 40–400 km and temporal scales of 2–48 h) is a common and perhaps universal feature of lower-tropospheric aerosol light extinction (Anderson et al., 2003). However, we are not aware of prior systematic attempts to quantify and test the universality of AOD scales of coherence over the contiguous USA. To test the sensitivity of the MFB in simulated AOD to spatial aggregation, we excluded the first 12 cells to the left and to the top of the simulated domain and averaged the remaining 12×12 km grid cells over the following scales: 24×24, 36×36, 48×48, 72×72, 96×96, 144×144, 192×192, 216×216, 288×288, 384×384, 432×432, 576×576, 864×864, 1152×1152, 1728×1728, 3456×3456 km. The last spatial average corresponds to a single grid cell encompassing the entire domain (excluding the outer 12 cells located to the west and north of the simulation domain). Each spatial average at a coarser resolution is computed as the mean of all valid 12×12 km grid cells within the averaging area. We then computed the MFB for the regridded WRF-Chem and MODIS data pair and found that, on a yearly basis, MFB is highest at 12 km (0.14 for Aqua and 0.15 for Terra) and reaches a first minimum at 72 km for Aqua (MFB = 0.13) and 384 km for Terra (MFB = 0.13) (see Fig. 6). However, the MFB, and hence systematic error in AOD relative to MODIS, exhibits only a weak dependence on the level of spatial aggregation. Spatial patterns of monthly mean AOD show the largest differences relative to MODIS during winter months in the southern states and near the coastlines, which show MFB up to 0.7, and lower spatial correlation (see Fig. 7a). This may be due to the larger uncertainty in MODIS retrievals near the coast (Anderson et al., 2013), the smaller sample size in the observations (particularly at high latitudes) during December to March or the lower overall AOD. Conversely, the spatial correlation is maximized during the summer ($r = 0.5$–0.7) for MODIS and August for MISR, when most data are available. The spatial variability of monthly mean AOD fields is also well simulated by WRF-Chem during the warm season (months May–August), as indicated by the ratio of the spatial standard deviation which is close to 1. However, σ (AOD) is usually higher in MODIS and/or MISR than in WRF-Chem. The root mean squared difference (RMSD) is largest and the spatial correlation is lowest during September and October, when MFB is also > 0.4 in part because WRF-Chem simulates high AOD and aerosol nitrate and sulfate concentrations over large regions in eastern North America (Figs. S3 and 4). The high positive bias in these months is also reflected in the near-surface $PM_{2.5}$ concentrations and its composition (Figs. S2

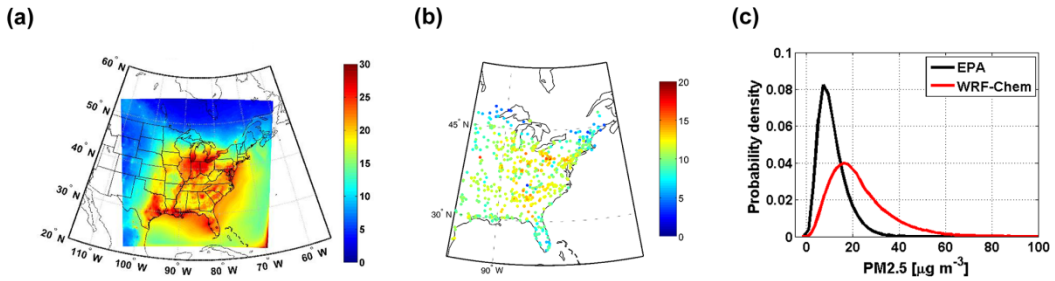

Figure 3. Mean daily $PM_{2.5}$ concentrations ($\mu g\,m^{-3}$) during 2008 as **(a)** simulated by WRF-Chem in the layer closest to the surface and **(b)** observed at 1230 EPA sites (note the different color bar). Panel **(c)** shows the probability density of daily mean $PM_{2.5}$ concentrations observed (black line) and simulated (red line) at the measurement stations.

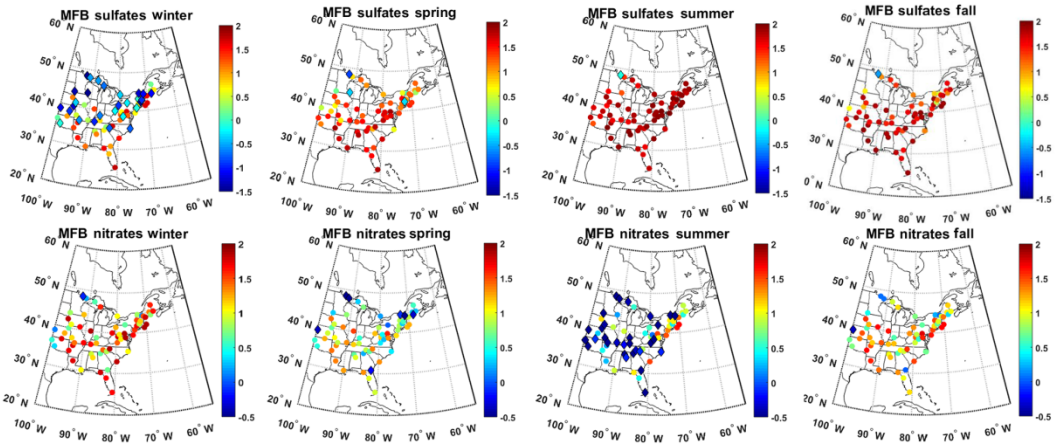

Figure 4. Mean fraction bias (MFB) of near-surface daily mean sulfate (first line) and nitrate (second line) concentrations in fine aerosol particles as simulated by WRF-Chem and observed in $PM_{2.5}$ measurements at 123 IMPROVE sites in different seasons. A positive MFB indicates that WRF-Chem overestimates the observations. Note that the scales differ between the frames shown for sulfate and nitrate MFB and dots and diamonds refer to positive and negative MFB, respectively.

and 4). A possible explanation for the relatively poor model performance during September and October may derive from the simulation of precipitation. During the majority of calendar months, domain-averaged precipitation as simulated by WRF-Chem is slightly positively biased relative to the gridded observational data. However, during September and October, the model exhibits a negative bias (of 8–10 % relative to observations) and a substantial underestimation of precipitation in regions of typically high AOD such as the Ohio River valley and along the east coast (Fig. S4). We also examined the impact of spatial aggregation (at 12, 24, 36, 48, 72 and 96 km resolution) on the seasonality of model performance. For AOD the spatial correlations are largest for most months when data are aggregated to a resolution of 24×24 km, and the ratio of spatial standard deviation is also closer to 1 when AOD are spatially aggregated, possibly indicating that the spatial patterns simulated by WRF-Chem on a fine scale do not always match those observed by MODIS (Fig. 8). For AE both spatial correlations and the ratio of standard deviations do not vary significantly when data are aggregated to a coarser resolution (Fig. S5). Empirical quantile–quantile plots of AOD at AERONET stations computed for both simultaneous MODIS observations and WRF-Chem with AERONET observations indicate that the positive bias in WRF-Chem-simulated values of AOD is evident across much of the probability distribution (5th to 95th percentile values) at most AERONET stations. However, it is worthy of note that WRF-Chem comparisons with

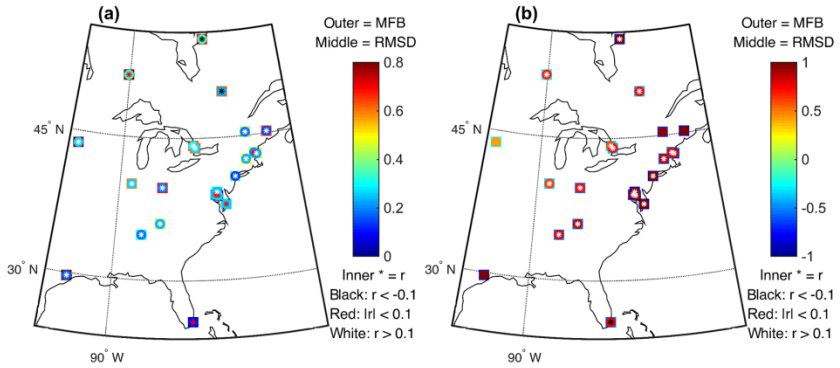

Figure 5. Summary statistics of comparisons of WRF-Chem simulations of **(a)** AOD and **(b)** AE relative to simultaneous observations at the AERONET sites. For a location to be included in this analysis at least 20 coincident observations and simulations must be available. The symbols at each AERONET station report MFB (outer square), root mean squared difference (RMSD, inner circle) and correlation coefficient (r, inner *). Note the different color bar for MFB and RMSD between the two frames. The correlation coefficient is displayed with different colors according with three classes: $r < -0.1$ (black), $|r| < 0.1$ (red) and $r > 0.1$ (white).

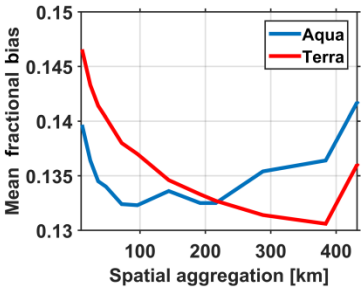

Figure 6. Mean fractional bias (MFB) on AOD from WRF-Chem as a function of spatial aggregation relative to observations from Terra (red line) and Aqua (blue line).

AERONET observations occupy much of the same observational range as simultaneous MODIS and AERONET observations at those sites (Fig. 9a), although the EQQ plot does not necessarily compare the same MODIS–AERONET and WRF-Chem–AERONET data pairs (i.e., the sample used to compare AERONET and MODIS may differ from that used to compare WRF-Chem and AERONET due to the cloud screening procedure). Thus, model simulations reproduce the range and probability of low-uncertainty AERONET measured AOD nearly as well as MODIS.

3.2 Evaluation of AE

Despite the low confidence in AE retrievals from MODIS, the comparison of WRF-Chem with the remote-sensing estimates indicates some degree of agreement. The overall

Table 5. Contingency table showing the fraction of grid cells simultaneously identified as fine(WF/MF)- or coarse(WC/MC)-mode particles by WRF-Chem and MODIS, as well as cells with different classification (columns 4 and 5). Recall a threshold of AE = 1 is used to define fine (AE > 1) and coarse-mode (AE < 1) dominance. Months in bold indicate that the distribution of observed and simulated fine- or coarse-mode fractions are significantly different (p value < 0.01) according to the χ^2 test described in Sect. 2.3.

Month	WF/MF	WC/MC	WF/MC	WC/MF
1	0.025	0.176	0.007	0.792
2	0.030	0.241	0.004	0.725
3	0.005	0.297	0.001	0.697
4	0.013	0.230	0.004	0.753
5	0.141	0.204	0.028	0.628
6	0.541	0.122	0.055	0.283
7	0.623	0.094	0.030	0.252
8	0.520	0.061	0.017	0.402
9	0.561	0.118	0.032	0.288
10	0.486	0.145	0.088	0.281
11	0.321	0.179	0.058	0.442
12	0.164	0.248	0.015	0.573
Mean	0.286	0.176	0.028	0.510

MFB of WRF-Chem vs. MODIS Terra is −0.09 (−0.11 vs. Aqua), and the correlation between WRF-Chem and MODIS monthly mean AE seems to be independent of season and lies between 0.20 and 0.54 for all months except April, May and November when it is lower, whereas r is always < 0.14 when compared to MISR (Fig. 7b). The AE RMSD relative to MODIS or MISR does not exhibit a clear seasonal pattern and the ratio of spatial standard deviations in the AE fields is always lower than 1, indicating more

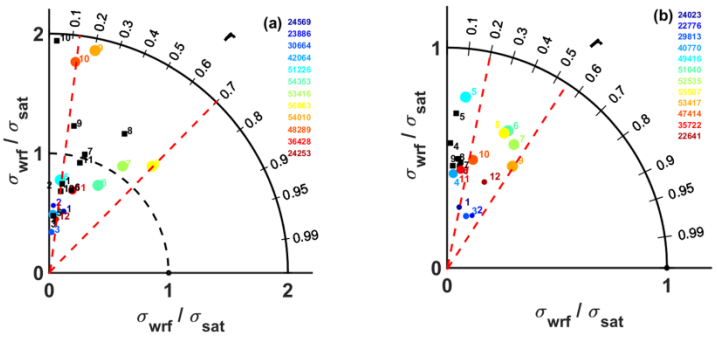

Figure 7. Taylor diagrams comparing the spatial fields of monthly mean **(a)** AOD and **(b)** AE from WRF-Chem vs. MODIS-Terra (color dots) or MISR (black squares). The numbers shown in the frames denote the month (e.g., 1 = January). The numbers shown in the legend indicate that the sample size of WRF-Chem data used for computing the monthly mean, and the scale of the dots is proportional to the sample size. Note the change in scale for the ratio of standard deviations between the frames. The red dashed lines define the sector with a Pearson correlation coefficient between **(a)** 0.12 and 0.70 for AOD and **(b)** 0.20 and 0.54 for AE, which comprise at least two thirds of the months. Each dot or square summarizes the statistics (i.e., RMSD, ratio of standard deviations and correlation coefficient) of the WRF-Chem vs. MODIS or WRF-Chem vs. MISR for a single month.

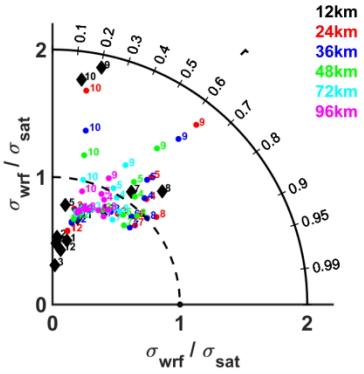

Figure 8. Taylor diagrams for AOD when MODIS observations and WRF-Chem simulations at 12 km are spatially aggregated to 24, 36, 48, 72 and 96 km. Numbers next to the colored dots and diamonds indicate different months (e.g., 1 = January).

spatial variability in the satellite retrievals than in WRF-Chem. The degree to which these results are symptomatic of the difficulties in retrieving AE from the remote-sensing observations is unclear. When the AE values are treated as binary samples (AE < 1 indicating that coarse-mode aerosols dominate, while AE > 1 indicating a dominance of the fine mode) and presented as a contingency table, WRF-Chem and MODIS simultaneously identify coarse-mode dominance (i.e., AE < 1) in 18 % of grid cells (Table 5). WRF-Chem simulates 31 % of grid cells as exhibiting annual mean AE > 1, while MODIS indicates a larger fraction of grid cells with AE > 1 (80 %, Table 5). Both WRF-Chem and MODIS indicate the highest prevalence of fine-mode particles during the warm months, with the highest agreement for co-identification (above 50 %) during June–September. Co-identification of coarse-mode particles is highest in the winter and spring months (above 20 % during February–May and December, Table 5). However, when a χ^2 test is applied to the frequency of fine and coarse particles identified by WRF-Chem and MODIS, for all months except January and April, the p value is < 0.01; thus, we reject the null hypothesis of equal distribution of fine- and coarse-mode particles identified by MODIS and WRF-Chem. The two data sets agree on 29 % of the cases when trying to identify fine-mode particles and approximately 53 % of the cells are misclassified, with MODIS usually identifying a higher prevalence of fine aerosols than WRF-Chem. AE from WRF-Chem is also negatively biased relative to AERONET observations, with MFB = −0.59 indicating a greater prevalence of coarse-mode aerosols in the simulations (Table 3, Fig. 2).

EQQ plots for all sites show good accord between WRF-Chem and AERONET observations, as indicated by the relatively consistent fractional error across the entire range of simulated and observed AE (Fig. 9b). Simulations from previous studies have also shown a systematic negative bias of simulated AE versus MODIS observations. AE is very difficult to derive from the MODIS measurements, and the uncertainty in AE scales with AOD (AE is very uncertain at AOD < 0.2). Further, AE is derived from wavelength-dependent AOD; thus, the uncertainties in the measurements are certainly correlated. As indicated in Fig. 5, for some AERONET sites there is evidence that positive bias in AOD is associated with a high negative bias in AE, but this does

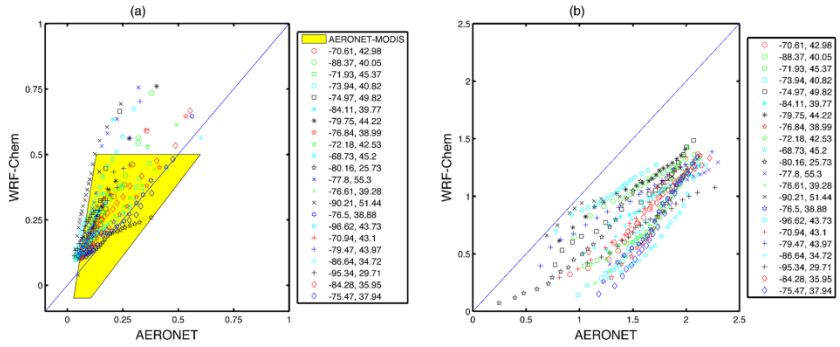

Figure 9. Empirical quantile–quantile (EQQ) plots of **(a)** AOD and **(b)** AE of the 5th to 95th percentile as simulated by WRF-Chem relative to 22 AERONET stations (their longitude (E) and latitude (N) is reported in the legend). The yellow shading shows the data envelope for EQQ plots of AERONET and MODIS. For inclusion in the analysis, a location must have at least 20 coincident observations and simulations in the grid cell containing the AERONET station. Note that MODIS uncertainty in the retrievals (± 0.05) in near-zero AOD conditions may lead to negative AOD values which are considered valid. The parameter space for MODIS–AERONET comparisons of AE is not shown because AE from the MODIS L2 data product are strongly bimodal (see examples given in Fig. S1 in the Supplement).

not uniformly occur over eastern North America (e.g., for the site at 77.8° W, 55.3° N, WRF-Chem exhibits a positive bias in AOD across the entire probability density function (pdf) while the simulated AE is negatively biased, but the site at 84.28° W, 35.95° N exhibits relatively good accord for AOD but is negatively biased in AE almost to the same amount as the northern station). Highest biases have been noted in regions dominated by dust aerosols or when the model overestimates the dust loading, since aerosol population mean diameter is inversely proportional to AE (Colarco et al., 2014; Balzarini et al., 2014). Sources of the biases in our study include the simplified treatment of the size distribution, weaknesses in the emission inventory or uncertainties in meteorological variables affecting particle growth (e.g., temperature and relative humidity). Future work will focus on examining these sensitivities.

3.3 AOD extremes

Averaged across the entire simulation period, WRF-Chem correctly identifies 70 % of locations with extreme and non-extreme AOD in the MODIS observations (i.e., Accuracy = 70 %, Table 6). The overall TS and HR also indicate that the geographic location of extreme AOD is similar between the model and satellite retrievals. The annual mean HR, which is defined as the proportion of grid cells with extreme AOD co-identified by WRF-Chem and MODIS relative to MODIS extremes, is 41 %. The annual mean TS, which also takes into account false alarms, is 27 % (Table 6).

For each month, the HR is significantly higher than the probability of co-identification of extremes by random chance (i.e., $p_0 = 0.25^2 = 0.0625$), since the test statistic $\frac{\mathrm{HR} - p_0^2}{\sqrt{\frac{p_0 \times (1-p_0)}{N}}}$ is always larger than the critical value at 1 % (i.e., 2.575). HR and TS vary seasonally, with highest skill during summer months (HR up to 70 % and TS up to 54 %) and lowest skill during winter and early spring (minimum HR = 29 % and minimum TS = 17 %) (Table 6 and Fig. 10). The relatively low skill in identifying the spatial occurrence of high AOD during winter and spring may reflect the relatively low AOD and low spatial variability during this season, which means "extreme" AOD may differ only marginally from the "non-extreme" areas (see Fig. S6 for monthly comparisons of extreme area identification).

The spatial distribution of extreme AOD also displays some seasonality, with areas of AOD > p75 concentrated over coastal regions and the southern states during summer months and smaller areas during winter and early spring (Fig. 10). Despite the relatively low simultaneous identification of extremes during cold seasons, the location of extremes moves from the coast to the Great Lakes region and Midwest states in both the model and MODIS (see Fig. S6). During winter and spring months, WRF-Chem simulates more areas with extreme AOD over coastal regions, whereas MODIS shows more spatial variability and predicts higher AOD in the Great Lakes area and in the states west of Illinois. Conversely, WRF-Chem underestimates areas of extreme AOD relative to MODIS in the northern regions of the domain, possibly due to the underestimation of sulfate aerosol. These two observations may be explained by noting that the mass fraction of aerosol nitrate in the accumulation and coarse mode predicted by WRF-Chem during most of the fall and winter months dominates the sulfate fraction over virtually all of the domain (see Fig. S3), whereas point observations indicate that aerosol nitrate mass fraction

Table 6. Synthesis of the skill with which WRF-Chem identifies the spatial distribution and location of extreme AOD values. Cells with extreme AOD are identified as exceeding the 75th percentile computed on a monthly basis across space from monthly averaged daily means. The second column reports the Accuracy, which indicates the spatial coherence of extremes and non-extremes between WRF-Chem and MODIS. The Accuracy metric is computed as the sum of cells co-identified as exceeding the 75th percentile and not exceeding that threshold by WRF-Chem and MODIS (Terra) relative to the total number of cells with valid data (fifth column, *N*). The third column reports the Threat Score (TS), which indicates the probability of correctly forecasting extreme AOD conditional upon either forecasting or observing extremes. The fourth column shows the hit rate (HR) (i.e., probability of correct forecast), which is the proportion of cells correctly identified as extremes by WRF-Chem relative to MODIS extremes. Values in parentheses refer to the same metrics when comparing WRF-Chem and MODIS onboard the Aqua satellite.

Month	Accuracy	TS	HR	*N*
January	0.664 (0.651)	0.196 (0.178)	0.328 (0.302)	14 899 (15 051)
February	0.654 (0.583)	0.182 (0.091)	0.308 (0.167)	13 721 (13 643)
March	0.656 (0.647)	0.185 (0.173)	0.312 (0.295)	16 641 (16 541)
April	0.645 (0.680)	0.169 (0.219)	0.289 (0.360)	25 265 (24 974)
May	0.664 (0.699)	0.196 (0.248)	0.327 (0.397)	32 770 (31 239)
June	0.796 (0.800)	0.420 (0.428)	0.592 (0.600)	36 148 (34 654)
July	0.850 (0.823)	0.538 (0.477)	0.700 (0.646)	36 055 (35 480)
August	0.834 (0.832)	0.500 (0.496)	0.667 (0.663)	39 173 (39 130)
September	0.667 (0.665)	0.200 (0.197)	0.333 (0.329)	35 883 (35 081)
October	0.656 (0.665)	0.185 (0.198)	0.311 (0.330)	29 662 (26 456)
November	0.703 (0.696)	0.254 (0.245)	0.405 (0.393)	21 630 (19 538)
December	0.648 (0.653)	0.173 (0.181)	0.295 (0.306)	14 914 (14 527)
Mean	0.703 (0.699)	0.266 (0.261)	0.406 (0.399)	26 397 (25 526)

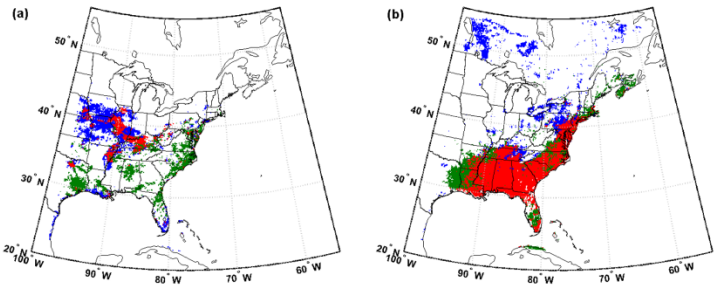

Figure 10. Spatial coherence in extreme AOD (i.e., the occurrence of AOD above the 75th percentile value) from WRF-Chem and MODIS Terra during **(a)** March 2008 and **(b)** July 2008. Green areas denote grid cells defined as experiencing extreme AOD only in the WRF-Chem simulations, blue pixels indicate extreme values as diagnosed using MODIS, while red pixels indicate areas where the occurrence of extreme values is indicated by both the WRF-Chem simulations and the MODIS observations.

is dominant only over the Central Great Plains (Hand et al., 2012). This may be related to an overestimation of aerosol nitrate in winter and fall (Fig. 4) as a result of the impact of air temperature and relative humidity on aerosol ammonium nitrate (NH_4NO_3) stability (Aksoyoglu et al., 2011), as well as an underestimation of aerosol sulfate, mostly during winter (Fig. 4) and likely due to an underestimation of the rate of SO_2 gaseous and aqueous (missing) oxidation or an underestimation of the nighttime boundary layer height which impacts sulfate formation near the surface (Tuccella et al., 2012). Localized negative biases in the model over the coast may be associated with the higher uncertainties in MODIS retrievals at coastlines (Anderson et al., 2013).

Extreme AOD exhibits relatively large spatial scales of coherence in both the WRF-Chem simulations and MODIS L2 observations (Fig. 11). Consistent with prior analyses of L3 MODIS data (Sullivan et al., 2015), the largest scales of coherence are found in fall. In all seasons except winter, the probability of the co-occurrence of extremes at the domain center and any other grid cell in the simulation domain is > 0.5 up to a distance of 300 km. The simulated mean seasonal scales of extreme coherence are comparable to L2 MODIS AOD (Fig. 11), despite the larger variability in the

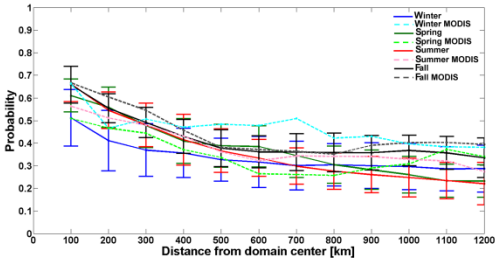

Figure 11. Mean and error bars (±1 standard deviation from the mean) of the probability of co-occurrence of extreme AOD (i.e., AOD > 75th percentile) at the reference location (i.e., domain center) and any other simulated grid cell during different seasons. The distance between the reference point and each grid cell centroid was binned using 100 km distance classes. Solid lines indicate mean seasonal spatial scales simulated by WRF-Chem, whereas dashed lines are observed means from L2 MODIS data (only the mean of the coherence ratios is plotted for the MODIS data).

MODIS data due to the limited retrievals with simultaneous extreme AOD at the reference location and at each other grid cell. Thus, consistent with prior research, this analysis indicates that extreme AOD occurs on large spatial scales and therefore may significantly impact regional climate.

4 Discussion and concluding remarks

Aerosol direct and indirect radiative forcing on the climate system are highly uncertain. A systematic assessment of the ability of global and regional models to reproduce aerosol optical properties in the contemporary climate is essential to increasing confidence in future projections. We contribute to this growing literature by presenting high-resolution (12 km) simulations from WRF-Chem conducted over eastern North America during a year representative of average meteorological and aerosol conditions. We evaluate the simulations relative to daily MODIS and MISR observations, high-frequency AERONET measurements of AOD, and AE and near-surface $PM_{2.5}$ mass and composition measurements. Results from this study show the following:

- After grid cells with any cloud presence are removed and considering only overpass hours, the domain-averaged simulated mean AOD is 0.22. Simulated AOD is positively biased relative to observations, with MFB = 0.14 when compared to MODIS-Aqua and MFB = 0.50 relative to AERONET (Figs. 1 and 2). A clear north–south gradient in AOD bias vs. MODIS is also observed. This positive bias is consistent across the entire probability distribution at most AERONET stations (Fig. 9) and is also evident in the comparison of modeled near-surface $PM_{2.5}$ mass relative to daily mean observations distributed at 1230 stations across the domain (Fig. 3).
- Model skill in reproducing the spatial fields of monthly mean AOD as measured by the spatial correlation and ratio of the spatial variability with MODIS is maximized during the summer months ($r \sim 0.5$–0.7, and ratio of $\sigma \sim 0.8$ to 1.2). During this season observed AOD is higher and more observations are available (Fig. 7). Lowest model–observation agreement is found in September and October and is at least partially attributable to a dry bias in precipitation from WRF-Chem (Fig. S4).
- In part because of the difficulties in retrieving robust estimates of AE, few previous studies have evaluated model-simulated AE values. We show that AE as simulated by WRF-Chem over eastern North America is negatively biased relative to MODIS (MFB = −0.10) and AERONET (MFB = −0.59). This bias indicates that WRF-Chem simulates a larger fraction of coarse-mode particles than is evident in the remote-sensing observations (see Tables 3 and 5). While some of the bias relative to MODIS may reflect high observational uncertainty, the large bias relative to AERONET is consistent with prior research (Table 1) and is symptomatic of substantial systematic error in the aerosol size distribution.
- Causes of the model error may include insufficiently detailed treatment of size distribution or inaccurate representation of aerosol composition and mixing state which affect the simulated size distribution and thus AE (Li et al., 2015; Curci et al., 2014). Further, weaknesses in the emission inventory (e.g., size resolution of primary emissions), as suggested by the systematic bias in simulated $PM_{2.5}$ concentrations relative to ground-based observations, and/or biases in the representation of meteorological conditions critical to determining aerosol nitrate concentrations may also affect model performance. Currently it is not possible to fully attribute the relative importance of these error sources.
- The majority of prior model evaluation exercises have tended to focus on mean AOD values. However, the climate and health impacts of aerosols are greater under high aerosol loadings. We demonstrate that WRF-Chem exhibits some skill in capturing the spatial patterns of extreme aerosol loading, especially during summer months. During this season, the hit rate for AOD > p75 reaches 70 %. Largest biases are found during winter months and near the coastlines where AOD from MODIS also exhibits largest retrieval uncertainty.

Despite the encouraging performance of WRF-Chem both in terms of simulation efficiency and in reproducing AOD (mean and extreme values) and the partial skill in reproducing AE over eastern North America, further investigations

are needed to properly quantify the value added by running high-resolution simulations by direct comparison with analogous runs at a coarser resolution. Future simulations will also involve the assessment of accuracy of different aerosol schemes (i.e., sectional vs. modal approaches) to represent the size distribution. The inclusion of a direct description of new particle formation processes within WRF-Chem may also improve estimates of ultrafine-particle concentrations and thus of simulated aerosol optical properties.

The Supplement related to this article is available online at doi:10.5194/acp-16-397-2016-supplement.

Acknowledgements. This research was supported in part by Lilly Endowment, Inc., through its support for the Indiana University Pervasive Technology Institute, and in part by the Indiana METACyt Initiative. The Indiana METACyt Initiative at IU is also supported in part by Lilly Endowment, Inc. Additional support was provided by the L'Oréal-UNESCO UK and Ireland Fellowship For Women In Science (to P. Crippa), the Natural Environmental Research Council (NERC) through the LICS project (ref. NE/K010794/1), the US NSF (grants no. 1102309 and 1517365 to S. C. Pryor) and a NASA Earth and Space Science Fellowship Program – Grant "14-EARTH14F-0207" (to R. C. Sullivan). The data used in this study were acquired as part of the NASA's Earth-Sun System Division and archived and distributed by the MODIS Level-1 and Atmosphere Archive and Distribution System (LAADS) and the Giovanni online data system, developed and maintained by the NASA Goddard Earth Sciences (GES) Data and Information Services Center (DISC). We thank the PIs and their staff for establishing and maintaining the 22 AERONET sites used in this investigation. $PM_{2.5}$ surface concentrations from the United States Environmental Protection Agency were obtained from http://www.epa.gov/airquality/airdata/ad_data_daily.html. Meteorological lateral boundary conditions from the North American Mesoscale model were obtained from the NOAA Operational Model Archive and Distribution System: ftp://nomads.ncdc.noaa.gov/NAM/analysis_only/.

Edited by: A. Perring

References

Ackermann, I. J., Hass, H., Memmesheimer, M., Ebel, A., Binkowski, F. S., and Shankar, U.: Modal aerosol dynamics model for Europe: development and first applications, Atmos. Environ., 32, 2981–2999, doi:10.1016/S1352-2310(98)00006-5, 1998.

Aksoyoglu, S., Keller, J., Barmpadimos, I., Oderbolz, D., Lanz, V. A., Prévôt, A. S. H., and Baltensperger, U.: Aerosol modelling in Europe with a focus on Switzerland during summer and winter episodes, Atmos. Chem. Phys., 11, 7355–7373, doi:10.5194/acp-11-7355-2011, 2011.

Alston, E. J., Sokolik, I. N., and Kalashnikova, O. V.: Characterization of atmospheric aerosol in the US Southeast from ground- and space-based measurements over the past decade, Atmos. Meas. Tech., 5, 1667–1682, doi:10.5194/amt-5-1667-2012, 2012.

Anderson, J. C., Wang, J., Zeng, J., Leptoukh, G., Petrenko, M., Ichoku, C., and Hu, C.: Long-term statistical assessment of Aqua-MODIS aerosol optical depth over coastal regions: bias characteristics and uncertainty sources, Tellus Series B-Chemical and Physical Meteorology, 65, ISSN 1600-0889, doi:10.3402/tellusb.v65i0.20805, 2013.

Anderson, J. R., Hardy, E. E., Roach, J. T., and Witmer, R. E.: A land use and land cover classification system for use with remote sensor data, Report 964, 1976.

Anderson, T. L., Charlson, R. J., Winker, D. M., Ogren, J. A., and Holmén, K.: Mesoscale Variations of Tropospheric Aerosols*, J. Atmos. Sci., 60, 119–136, doi:10.1175/1520-0469(2003)060<0119:MVOTA>2.0.CO;2, 2003.

Balzarini, A., Pirovano, G., Honzak, L., Žabkar, R., Curci, G., Forkel, R., Hirtl, M., San José, R., Tuccella, P., and Grell, G. A.: WRF-Chem model sensitivity to chemical mechanisms choice in reconstructing aerosol optical properties, Atmos. Environ., 115, 604–619, doi:10.1016/j.atmosenv.2014.12.033, 2014.

Boucher, O., Randall, D., Artaxo, P. C. B., Feingold, G., Forster, P., Kerminen, V.-M., Kondo, Y., Liao, H., Lohmann, U., Rasch, P., Satheesh, S. K., Sherwood, S., Stevens, B., and Zhang, X. Y.: Clouds and Aerosols, in: Climate Change 2013: The Physical Science Basis. Contribution of Working Group I to the Fifth Assessment Report of the Intergovernmental Panel on Climate Change, edited by: Stocker, T. F., Qin, D., Plattner, G.-K., Tignor, M., Allen, S. K., Boschung, J., Nauels, A., Xia, Y., Bex, V., and Midgley, P. M., Cambridge University Press, Cambridge, United Kingdom and New York, NY, USA, 33–115, 2013.

Boylan, J. W. and Russell, A. G.: PM and light extinction model performance metrics, goals, and criteria for three-dimensional air quality models, Atmos. Environ., 40, 4946–4959, doi:10.1016/j.atmosenv.2005.09.087, 2006.

Castro, C. L., Pielke, R. A., and Leoncini, G.: Dynamical downscaling: Assessment of value retained and added using the Regional Atmospheric Modeling System (RAMS), J. Geophys. Res.-Atmos., 110, D05108, doi:10.1029/2004JD004721, 2005.

Chu, S. H.: PM2.5 episodes as observed in the speciation trends network, Atmos. Environ., 38, 5237–5246, doi:10.1016/j.atmosenv.2004.01.055, 2004.

Colarco, P., da Silva, A., Chin, M., and Diehl, T.: Online simulations of global aerosol distributions in the NASA GEOS-4 model and comparisons to satellite and ground-based aerosol optical depth, J. Geophys. Res.-Atmos., 115, D14207, doi:10.1029/2009jd012820, 2010.

Colarco, P. R., Kahn, R. A., Remer, L. A., and Levy, R. C.: Impact of satellite viewing-swath width on global and regional aerosol optical thickness statistics and trends, Atmos. Meas. Tech., 7, 2313–2335, doi:10.5194/amt-7-2313-2014, 2014.

Curci, G., Hogrefe, C., Bianconi, R., Im, U., Balzarini, A., Baró, R., Brunner, D., Forkel, R., Giordano, L., Hirtl, M., Honzak, L., Jiménez-Guerrero, P., Knote, C., Langer, M., Makar, P. A., Pirovano, G., Pérez, J. L., San José, R., Syrakov, D., Tuccella, P., Werhahn, J., Wolke, R., Žabkar, R., Zhang, J., and Galmarini, S.: Uncertainties of simulated aerosol optical properties

induced by assumptions on aerosol physical and chemical properties: An AQMEII-2 perspective, Atmos. Environ., 115, 541–552, doi:10.1016/j.atmosenv.2014.09.009, 2014.

de Meij, A., Pozzer, A., Pringle, K. J., Tost, H., and Lelieveld, J.: EMAC model evaluation and analysis of atmospheric aerosol properties and distribution with a focus on the Mediterranean region, Atmo. Res., 114–115, 38–69, doi:10.1016/j.atmosres.2012.05.014, 2012.

Drury, E., Jacob, D. J., Spurr, R. J. D., Wang, J., Shinozuka, Y., Anderson, B. E., Clarke, A. D., Dibb, J., McNaughton, C., and Weber, R.: Synthesis of satellite (MODIS), aircraft (ICARTT), and surface (IMPROVE, EPA-AQS, AERONET) aerosol observations over eastern North America to improve MODIS aerosol retrievals and constrain surface aerosol concentrations and sources, J. Geophys. Res.-Atmos., 115, D14204, doi:10.1029/2009jd012629, 2010.

Emmons, L. K., Walters, S., Hess, P. G., Lamarque, J.-F., Pfister, G. G., Fillmore, D., Granier, C., Guenther, A., Kinnison, D., Laepple, T., Orlando, J., Tie, X., Tyndall, G., Wiedinmyer, C., Baughcum, S. L., and Kloster, S.: Description and evaluation of the Model for Ozone and Related chemical Tracers, version 4 (MOZART-4), Geosci. Model Dev., 3, 43–67, doi:10.5194/gmd-3-43-2010, 2010.

Fast, J. D., Gustafson, W. I., Easter, R. C., Zaveri, R. A., Barnard, J. C., Chapman, E. G., Grell, G. A., and Peckham, S. E.: Evolution of ozone, particulates, and aerosol direct radiative forcing in the vicinity of Houston using a fully coupled meteorology-chemistry-aerosol model, J. Geophys. Res.-Atmos., 111, D21305, doi:10.1029/2005JD006721, 2006.

Ford, B. and Heald, C. L.: Aerosol loading in the Southeastern United States: reconciling surface and satellite observations, Atmos. Chem. Phys., 13, 9269–9283, doi:10.5194/acp-13-9269-2013, 2013.

Giannouli, M., Kalognomou, E.-A., Mellios, G., Moussiopoulos, N., Samaras, Z., and Fiala, J.: Impact of European emission control strategies on urban and local air quality, Atmos. Environ., 45, 4753–4762, doi:10.1016/j.atmosenv.2010.03.016, 2011.

Gkikas, A., Houssos, E. E., Hatzianastassiou, N., Papadimas, C. D., and Bartzokas, A.: Synoptic conditions favouring the occurrence of aerosol episodes over the broader Mediterranean basin, Q. J. Roy. Meteorol. Soc., 138, 932–949, doi:10.1002/qj.978, 2012.

Grell, G. A., Peckham, S. E., Schmitz, R., McKeen, S. A., Frost, G., Skamarock, W. C., and Eder, B.: Fully coupled "online" chemistry within the WRF model, Atmos. Environ., 39, 6957–6975, doi:10.1016/j.atmosenv.2005.04.027, 2005.

Guenther, A. B., Zimmerman, P. R., Harley, P. C., Monson, R. K., and Fall, R.: Isoprene and monoterpene emission rate variability: model evaluations and sensitivity analyses, J. Geophys. Res.-Atmos., 98, 12609–12617, doi:10.1029/93jd00527, 1993.

Guenther, A., Zimmerman, P., and Wildermuth, M.: Natural volatile organic compound emission rate estimates for U.S. woodland landscapes, Atmos. Environ., 28, 1197–1210, doi:10.1016/1352-2310(94)90297-6, 1994.

Hand, J. L., Schichtel, B. A., Pitchford, M., Malm, W. C., and Frank, N. H.: Seasonal composition of remote and urban fine particulate matter in the United States, J. Geophys. Res.-Atmos., 117, D05209, doi:10.1029/2011JD017122, 2012.

Holben, B. N., Eck, T. F., Slutsker, I., Tanre, D., Buis, J. P., Setzer, A., Vermote, E., Reagan, J. A., Kaufman, Y. J., Nakajima, T., Lavenu, F., Jankowiak, I., and Smirnov, A.: AERONET – A federated instrument network and data archive for aerosol characterization, Remote Sens. Environ., 66, 1–16, doi:10.1016/s0034-4257(98)00031-5, 1998.

Holben, B. N., Tanre, D., Smirnov, A., Eck, T. F., Slutsker, I., Abuhassan, N., Newcomb, W. W., Schafer, J. S., Chatenet, B., Lavenu, F., Kaufman, Y. J., Castle, J. V., Setzer, A., Markham, B., Clark, D., Frouin, R., Halthore, R., Karneli, A., O'Neill, N. T., Pietras, C., Pinker, R. T., Voss, K., and Zibordi, G.: An emerging ground-based aerosol climatology: Aerosol optical depth from AERONET, J. Geophys. Res.-Atmos., 106, 12067–12097, doi:10.1029/2001jd900014, 2001.

Hyer, E. J., Reid, J. S., and Zhang, J.: An over-land aerosol optical depth data set for data assimilation by filtering, correction, and aggregation of MODIS Collection 5 optical depth retrievals, Atmos. Meas. Tech., 4, 379–408, doi:10.5194/amt-4-379-2011, 2011.

Kahn, R. A., Gaitley, B. J., Martonchik, J. V., Diner, D. J., Crean, K. A., and Holben, B.: Multiangle Imaging Spectroradiometer (MISR) global aerosol optical depth validation based on 2 years of coincident Aerosol Robotic Network (AERONET) observations, J. Geophys. Res.-Atmos., 110, D10S04, doi:10.1029/2004jd004706, 2005.

Kahn, R. A., Gaitley, B. J., Garay, M. J., Diner, D. J., Eck, T. F., Smirnov, A., and Holben, B. N.: Multiangle Imaging SpectroRadiometer global aerosol product assessment by comparison with the Aerosol Robotic Network, J. Geophys. Res.-Atmos., 115, D23209, doi:10.1029/2010jd014601, 2010.

Kinne, S., O'Donnel, D., Stier, P., Kloster, S., Zhang, K., Schmidt, H., Rast, S., Giorgetta, M., Eck, T. F., and Stevens, B.: MAC-v1: A new global aerosol climatology for climate studies, J. Adv. Model. Earth Syst., 5, 704–740, doi:10.1002/jame.20035, 2013.

Kovacs, T.: Comparing MODIS and AERONET aerosol optical depth at varying separation distances to assess ground-based validation strategies for spaceborne lidar, J. Geophys. Res.-Atmos., 111, D24203, doi:10.1029/2006JD007349, 2006.

Kulmala, M., Asmi, A., Lappalainen, H. K., Baltensperger, U., Brenguier, J.-L., Facchini, M. C., Hansson, H.-C., Hov, Ø., O'Dowd, C. D., Pöschl, U., Wiedensohler, A., Boers, R., Boucher, O., de Leeuw, G., Denier van der Gon, H. A. C., Feichter, J., Krejci, R., Laj, P., Lihavainen, H., Lohmann, U., McFiggans, G., Mentel, T., Pilinis, C., Riipinen, I., Schulz, M., Stohl, A., Swietlicki, E., Vignati, E., Alves, C., Amann, M., Ammann, M., Arabas, S., Artaxo, P., Baars, H., Beddows, D. C. S., Bergström, R., Beukes, J. P., Bilde, M., Burkhart, J. F., Canonaco, F., Clegg, S. L., Coe, H., Crumeyrolle, S., D'Anna, B., Decesari, S., Gilardoni, S., Fischer, M., Fjaeraa, A. M., Fountoukis, C., George, C., Gomes, L., Halloran, P., Hamburger, T., Harrison, R. M., Herrmann, H., Hoffmann, T., Hoose, C., Hu, M., Hyvärinen, A., Hõrrak, U., Iinuma, Y., Iversen, T., Josipovic, M., Kanakidou, M., Kiendler-Scharr, A., Kirkevåg, A., Kiss, G., Klimont, Z., Kolmonen, P., Komppula, M., Kristjánsson, J.-E., Laakso, L., Laaksonen, A., Labonnote, L., Lanz, V. A., Lehtinen, K. E. J., Rizzo, L. V., Makkonen, R., Manninen, H. E., McMeeking, G., Merikanto, J., Minikin, A., Mirme, S., Morgan, W. T., Nemitz, E., O'Donnell, D., Panwar, T. S., Pawlowska, H., Petzold, A., Pienaar, J. J., Pio, C., Plass-Duelmer, C., Prévôt, A. S. H., Pryor, S., Reddington, C. L., Roberts, G., Rosenfeld, D., Schwarz, J., Seland, Ø., Sellegri, K., Shen, X. J., Shiraiwa, M.,

Siebert, H., Sierau, B., Simpson, D., Sun, J. Y., Topping, D., Tunved, P., Vaattovaara, P., Vakkari, V., Veefkind, J. P., Visschedijk, A., Vuollekoski, H., Vuolo, R., Wehner, B., Wildt, J., Woodward, S., Worsnop, D. R., van Zadelhoff, G.-J., Zardini, A. A., Zhang, K., van Zyl, P. G., Kerminen, V.-M., S Carslaw, K., and Pandis, S. N.: General overview: European Integrated project on Aerosol Cloud Climate and Air Quality interactions (EUCAARI) – integrating aerosol research from nano to global scales, Atmos. Chem. Phys., 11, 13061–13143, doi:10.5194/acp-11-13061-2011, 2011.

Kumar, R., Barth, M. C., Pfister, G. G., Naja, M., and Brasseur, G. P.: WRF-Chem simulations of a typical pre-monsoon dust storm in northern India: influences on aerosol optical properties and radiation budget, Atmos. Chem. Phys., 14, 2431–2446, doi:10.5194/acp-14-2431-2014, 2014.

Kurokawa, J., Ohara, T., Morikawa, T., Hanayama, S., Janssens-Maenhout, G., Fukui, T., Kawashima, K., and Akimoto, H.: Emissions of air pollutants and greenhouse gases over Asian regions during 2000–2008: Regional Emission inventory in ASia (REAS) version 2, Atmos. Chem. Phys., 13, 11019–11058, doi:10.5194/acp-13-11019-2013, 2013.

Lee, Y. H., Adams, P. J., and Shindell, D. T.: Evaluation of the global aerosol microphysical ModelE2-TOMAS model against satellite and ground-based observations, Geosci. Model Dev., 8, 631–667, doi:10.5194/gmd-8-631-2015, 2015.

Levy, R. C., Remer, L. A., and Dubovik, O.: Global aerosol optical properties and application to Moderate Resolution Imaging Spectroradiometer aerosol retrieval over land, J. Geophys. Res.-Atmos., 112, 15, doi:10.1029/2006jd007815, 2007.

Levy, R. C., Remer, L. A., Kleidman, R. G., Mattoo, S., Ichoku, C., Kahn, R., and Eck, T. F.: Global evaluation of the Collection 5 MODIS dark-target aerosol products over land, Atmos. Chem. Phys., 10, 10399–10420, doi:10.5194/acp-10-10399-2010, 2010.

Li, S., Kahn, R., Chin, M., Garay, M. J., and Liu, Y.: Improving satellite-retrieved aerosol microphysical properties using GOCART data, Atmos. Meas. Tech., 8, 1157–1171, doi:10.5194/amt-8-1157-2015, 2015.

Matsuura, K. and Willmott, C. J.: Terrestrial precipitation: 1900–2008 gridded monthly time series, available at: http://climate.geog.udel.edu/~climate/html_pages/download.html (last access: July 2015), 2009.

Michou, M., Nabat, P., and Saint-Martin, D.: Development and basic evaluation of a prognostic aerosol scheme (v1) in the CNRM Climate Model CNRM-CM6, Geosci. Model Dev., 8, 501–531, doi:10.5194/gmd-8-501-2015, 2015.

Myhre, G., Samset, B. H., Schulz, M., Balkanski, Y., Bauer, S., Berntsen, T. K., Bian, H., Bellouin, N., Chin, M., Diehl, T., Easter, R. C., Feichter, J., Ghan, S. J., Hauglustaine, D., Iversen, T., Kinne, S., Kirkevåg, A., Lamarque, J.-F., Lin, G., Liu, X., Lund, M. T., Luo, G., Ma, X., van Noije, T., Penner, J. E., Rasch, P. J., Ruiz, A., Seland, Ø., Skeie, R. B., Stier, P., Takemura, T., Tsigaridis, K., Wang, P., Wang, Z., Xu, L., Yu, H., Yu, F., Yoon, J.-H., Zhang, K., Zhang, H., and Zhou, C.: Radiative forcing of the direct aerosol effect from AeroCom Phase II simulations, Atmos. Chem. Phys., 13, 1853–1877, doi:10.5194/acp-13-1853-2013, 2013.

Nabat, P., Somot, S., Mallet, M., Michou, M., Sevault, F., Driouech, F., Meloni, D., di Sarra, A., Di Biagio, C., Formenti, P., Sicard, M., Léon, J.-F., and Bouin, M.-N.: Dust aerosol radiative effects during summer 2012 simulated with a coupled regional aerosol–atmosphere–ocean model over the Mediterranean, Atmos. Chem. Phys., 15, 3303–3326, doi:10.5194/acp-15-3303-2015, 2015.

Nair, V. S., Solmon, F., Giorgi, F., Mariotti, L., Babu, S. S., and Moorthy, K. K.: Simulation of South Asian aerosols for regional climate studies, J. Geophys. Res.-Atmos., 117, D04209, doi:10.1029/2011JD016711, 2012.

Pereira, S. N., Wagner, F., and Silva, A. M.: Seven years of measurements of aerosol scattering properties, near the surface, in the southwestern Iberia Peninsula, Atmos. Chem. Phys., 11, 17–29, doi:10.5194/acp-11-17-2011, 2011.

Pfister, G. G., Parrish, D. D., Worden, H., Emmons, L. K., Edwards, D. P., Wiedinmyer, C., Diskin, G. S., Huey, G., Oltmans, S. J., Thouret, V., Weinheimer, A., and Wisthaler, A.: Characterizing summertime chemical boundary conditions for airmasses entering the US West Coast, Atmos. Chem. Phys., 11, 1769–1790, doi:10.5194/acp-11-1769-2011, 2011.

Rea, G., Turquety, S., Menut, L., Briant, R., Mailler, S., and Siour, G.: Source contributions to 2012 summertime aerosols in the Euro-Mediterranean region, Atmos. Chem. Phys., 15, 8013–8036, doi:10.5194/acp-15-8013-2015, 2015.

Remer, L. A., Kaufman, Y. J., Tanre, D., Mattoo, S., Chu, D. A., Martins, J. V., Li, R. R., Ichoku, C., Levy, R. C., Kleidman, R. G., Eck, T. F., Vermote, E., and Holben, B. N.: The MODIS aerosol algorithm, products, and validation, J. Atmos. Sci., 62, 947–973, doi:10.1175/jas3385.1, 2005.

Santese, M., De Tomasi, F., and Perrone, M. R.: AERONET versus MODIS aerosol parameters at different spatial resolutions over southeast Italy, J. Geophys. Res-Atmos. 112, D10214, doi:10.1029/2006JD007742, 2007.

Schell, B., Ackermann, I. J., Hass, H., Binkowski, F. S., and Ebel, A.: Modeling the formation of secondary organic aerosol within a comprehensive air quality model system, J. Geophys. Res.-Atmos., 106, 28275–28293, doi:10.1029/2001jd000384, 2001.

Schutgens, N. A. J., Nakata, M., and Nakajima, T.: Validation and empirical correction of MODIS AOT and AE over ocean, Atmos. Meas. Tech., 6, 2455–2475, doi:10.5194/amt-6-2455-2013, 2013.

Shepard, D.: A two-dimensional interpolation function for irregularly-spaced data, in: Proceedings of the 1968 23rd ACM National Conference (1968), pp. 517–524, doi:10.1145/800186.810616, 1968.

Shinozuka, Y. and Redemann, J.: Horizontal variability of aerosol optical depth observed during the ARCTAS airborne experiment, Atmos. Chem. Phys., 11, 8489–8495, doi:10.5194/acp-11-8489-2011, 2011.

Sič, B., El Amraoui, L., Marécal, V., Josse, B., Arteta, J., Guth, J., Joly, M., and Hamer, P. D.: Modelling of primary aerosols in the chemical transport model MOCAGE: development and evaluation of aerosol physical parameterizations, Geosci. Model Dev., 8, 381–408, doi:10.5194/gmd-8-381-2015, 2015.

Simpson, D., Guenther, A., Hewitt, C. N., and Steinbrecher, R.: Biogenic emissions in Europe. 1. estimates and uncertainties, J. Geophys. Res.-Atmos., 100, 22875–22890, doi:10.1029/95jd02368, 1995.

Stocker, T. F., Qin, D., and Plattner, G.-K., Alexander, L. V., Allen, S. K., Bindoff, N. L., Breion, F.-M., Church, J. A., Cubasch, U., Emori, S., Forster, P., Friedlingstein, P., Gillett, N., Gregory, J. M., Hartmann, D. L., Jansen, E., Kirtman, B., Knutti, R., Kr-

ishna Kumar, K., Lemke, P., Marotzke, J., Masson-Delmotte, V., Meehl, G. A., Mokhov, I. I., Piao, S., Ramaswamy, V., Randall, D., Rhein, M., Rojas, M., Sabine, C., Shindell, D., Talley, L. D., Vaughan, D. G., and Xie, S.-P.: Summary for Policymakers, in: Climate Change 2013: The Physical Science Basis. Contribution of Working Group I to the Fifth Assessment Report of the Intergovernmental Panel on Climate Change, Cambridge University Press, Cambridge, United Kingdom and New York, NY, USA, 33–115, 2013.

Stockwell, W. R., Middleton, P., Chang, J. S., and Tang, X.: The second generation regional acid deposition model chemical mechanism for regional air quality modeling, J. Geophys. Res.-Atmos., 95, 16343–16367, doi:10.1029/JD095iD10p16343, 1990.

Sullivan, R. C., Levy, R. C., and Pryor, S. C.: Spatiotemporal coherence of mean and extreme aerosol particle events over eastern North America as observed from satellite, Atmos. Environ., 112, 126–135, doi:10.1016/j.atmosenv.2015.04.026, 2015.

Taylor, K. E.: Summarizing multiple aspects of model performance in a single diagram, J. Geophys. Res.-Atmos., 106, 7183–7192, doi:10.1029/2000jd900719, 2001.

Tessum, C. W., Hill, J. D., and Marshall, J. D.: Twelve-month, 12 km resolution North American WRF-Chem v3.4 air quality simulation: performance evaluation, Geosci. Model Dev., 8, 957–973, doi:10.5194/gmd-8-957-2015, 2015.

Tuccella, P., Curci, G., Visconti, G., Bessagnet, B., Menut, L., and Park, R. J.: Modeling of gas and aerosol with WRF/Chem over Europe: Evaluation and sensitivity study, J. Geophys. Res.-Atmos., 117, D03303, doi:10.1029/2011JD016302, 2012.

Tuccella, P., Curci, G., Grell, G. A., Visconti, G., Crumeyrolle, S., Schwarzenboeck, A., and Mensah, A. A.: A new chemistry option in WRF-Chem v. 3.4 for the simulation of direct and indirect aerosol effects using VBS: evaluation against IMPACT-EUCAARI data, Geosci. Model Dev., 8, 2749–2776, doi:10.5194/gmd-8-2749-2015, 2015.

US-EPA: 2005 National Emissions Inventory (NEI), US Environmental Protection Agency, available at: ftp://aftp.fsl.noaa.gov/divisions/taq/emissions_data_2005/ (last access: July 2015), 2009.

Valenzuela, A., Olmo, F. J., Lyamani, H., Granados-Munoz, M. J., Anton, M., Guerrero-Rascado, J. L., Quirantes, A., Toledano, C., Perez-Ramirez, D., and Alados-Arboledas, L.: Aerosol transport over the western Mediterranean basin: Evidence of the contribution of fine particles to desert dust plumes over Alboran Island, J. Geophys. Res.-Atmos., 119, 14028–14044, doi:10.1002/2014jd022044, 2014.

Willmott, C. J., Rowe, C. M., and Philpot, W. D.: Small-Scale Climate Maps: A Sensitivity Analysis of Some Common Assumptions Associated with Grid-Point Interpolation and Contouring, The American Cartographer, 12, 5–16, doi:10.1559/152304085783914686, 1985.

Wu, S., Mickley, L. J., Kaplan, J. O., and Jacob, D. J.: Impacts of changes in land use and land cover on atmospheric chemistry and air quality over the 21st century, Atmos. Chem. Phys., 12, 1597–1609, doi:10.5194/acp-12-1597-2012, 2012.

Xing, J., Mathur, R., Pleim, J., Hogrefe, C., Gan, C.-M., Wong, D. C., Wei, C., Gilliam, R., and Pouliot, G.: Observations and modeling of air quality trends over 1990–2010 across the Northern Hemisphere: China, the United States and Europe, Atmos. Chem. Phys., 15, 2723–2747, doi:10.5194/acp-15-2723-2015, 2015.

Zhang, Y., Chen, Y., Sarwar, G., and Schere, K.: Impact of gas-phase mechanisms on Weather Research Forecasting Model with Chemistry (WRF/Chem) predictions: Mechanism implementation and comparative evaluation, J. Geophys. Res.-Atmos., 117, D01301, doi:10.1029/2011jd015775, 2012.

APPENDIX B

QUANTIFYING THE ROLES OF CHANGING ALBEDO, EMISSIVITY, AND ENERGY PARTITIONING IN THE IMPACT OF IRRIGATION ON ATMOSPHERIC HEAT CONTENT

Pryor, S. C., R. C. Sullivan, and T. Wright (2016), Quantifying the Roles of Changing Albedo, Emissivity, and Energy Partitioning in the Impact of Irrigation on Atmospheric Heat Content, *J. Appl. Meteorol. Climatol.*, *55*(8), 1699–1706, doi:10.1175/JAMC-D-15-0291.1.

Quantifying the Roles of Changing Albedo, Emissivity, and Energy Partitioning in the Impact of Irrigation on Atmospheric Heat Content

S. C. PRYOR AND R. C. SULLIVAN

Department of Earth and Atmospheric Sciences, Cornell University, Ithaca, New York

T. WRIGHT

Antorcha, LLC, Logan, Utah

(Manuscript received 14 October 2015, in final form 22 January 2016)

ABSTRACT

Introduction of irrigated agriculture changes the partitioning of the surface energy flux between sensible and latent heat (H vs LE) and alters the albedo α and emissivity ε. In the absence of changes in the radiation components of the surface energy balance, the change in the Bowen ratio due to irrigation typically suppresses the local air temperature T but increases the total near-surface atmospheric heat content (as measured using equivalent potential temperature θ_e). While the effect of irrigation on surface energy partitioning due to enhanced surface and subsurface water availability has long been acknowledged, the roles of associated changes in ε and α have received less attention, and the scales and magnitudes of these effects remain uncertain. A new methodology designed for application to in situ and remote sensing data is presented and used to demonstrate that the net impact of irrigation on T and θ_e is strongly dependent on the regional climate, land cover in surrounding areas, and the amount of irrigation in the upwind fetch. The results suggest that the impact of the radiative forcing terms on net available energy is not negligible and may amplify or offset the impact from changed energy partitioning on T and θ_e depending on the specific regional climate and land cover.

1. Introduction and motivation

Irrigation represents a substantial perturbation to the global hydrological cycle and delivers about 2600 km^3 of water to the global land surface each year (~2% of annual overland precipitation) (Sacks et al. 2009). It has been a growing part of U.S. agriculture for over 60 years and affects a substantial fraction of the country; the area of land under irrigation is projected to increase (Gollehon and Quinby 2006; Moore et al. 2015). Changes in land use and land cover, including adoption of irrigation, have been identified as important drivers of local and regional climate (Adegoke et al. 2007; Pielke et al. 2011) and an important source of uncertainty in climate change detection and attribution studies (Fall et al. 2010).

Corresponding author address: S. C. Pryor, Department of Earth and Atmospheric Sciences, Bradfield Hall, Cornell University, Ithaca, NY 14853.
E-mail: sp2279@cornell.edu.

DOI: 10.1175/JAMC-D-15-0291.1

Adoption of irrigation changes three components of the surface energy balance equation

$$S \times (1 - \alpha) + R_{li} - R_{lo} = H + \mathrm{LE} + G, \qquad (1)$$

where S = incoming solar radiation, α = albedo, R_{li} = counterradiated longwave radiation from the atmosphere, R_{lo} = outgoing longwave radiation from the surface ($R_{lo} = \varepsilon\sigma T_s^4$, where ε = emissivity, σ = Stefan Boltzmann's constant, and T_s = surface temperature), H = sensible heat transfer, LE = latent heat transfer, and G = ground heat transfer:

1) *Reflection of incoming solar radiation by the surface.* Typical α values for dark-colored wet rough soils lie in the range 0.05–0.10, those for crops are typically 0.15–0.25, and those for light-colored flat dry soil are frequently in the range 0.35–0.40 (Dobos 2006). Thus, α for irrigated crops can be 0.05–0.10 lower than for surrounding natural vegetation, bare rock, and dry soil (Dobos 2006; Evett 2000). However, there is tremendous variability in the α of different

surface types, and the difference in α due to irrigation (even the sign) is a complex function of crop, soil properties (e.g., organic carbon content or texture), surface roughness, and moisture content (Cierniewski et al. 2014).

2) *Emissivity of the surface for longwave radiation.* The ε of most soils is 0.88–0.94, while that of vegetation is ~0.94–0.98. The emissivity of vegetated surfaces, therefore, usually exceeds that of rocks and exposed soil (Evett 2000; Geiger et al. 2009; Pielke et al. 2011), and the ε of soils increases rapidly with increasing soil moisture (Alex and Behari 1998; Rees 2001).
3) *Partitioning of land surface energy transfer between sensible and latent heat fluxes (H vs* LE*) and thus the Bowen ratio (H/*LE*) (Hargreaves and Allen 2003; Pielke et al. 2011).* The presence of irrigation generally increases LE and thus the specific humidity q but differentially affects air temperature T during the day and night. Daily maximum temperatures are generally reduced by the increase in both LE and surface thermal energy storage [the specific heat of water ($4190\,\mathrm{J\,kg^{-1}\,K^{-1}}$) is higher than that for dry soil ($420–2510\,\mathrm{J\,kg^{-1}\,K^{-1}}$) (Geiger et al. 2009)]. Conversely, nighttime temperatures are typically increased by release of energy during condensation/deposition of water, the action of water vapor as a greenhouse gas (increasing R_{li}), and release of thermal energy absorbed during the day (Adegoke et al. 2007).

However, uncertainty remains regarding the scales of the effect and relative importance of impacts on the atmospheric heat content resulting from changes in the partitioning of H and LE, versus those that derive from changed α and ε.

Air temperature T provides an incomplete representation of lower atmospheric energy content, so equivalent potential temperature θ_e, which accounts for the contributions to static energy from both air temperature and specific humidity, is also used here as a response variable (Davey et al. 2006):

$$\theta_e = T\left(\frac{1000}{P}\right)^{\mathrm{Rd/Cpd}} + \frac{L(T)}{\mathrm{Cpd}}q, \qquad (2)$$

where T = air temperature, P = pressure, Rd = specific gas constant for air, Cpd = specific heat for dry air, $L(T)$ = latent heat of vaporization [$f(T)$], and q = specific humidity.

We present a new methodology designed for application to in situ and remote sensing data in which paired stations that are differentially influenced by irrigation are used to quantify the impact of irrigation on α, ε, T, and θ_e. The methodology is illustrated using high-quality meteorological data from the Automated Surface Observing System (ASOS; Sun et al. 2005) and U.S. Climate Reference Networks (CRN; Diamond et al. 2013), and estimates of irrigation and surface α and ε from the Moderate Resolution Imaging Spectroradiometer (MODIS).

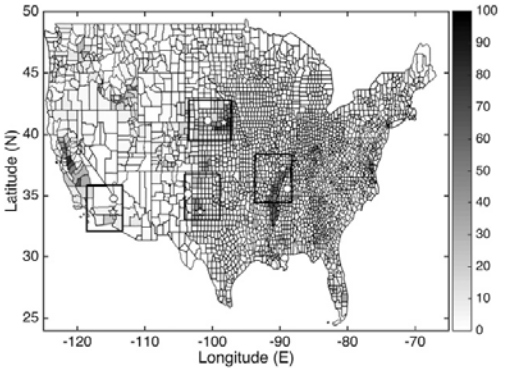

FIG. 1. USGS county-level irrigation (percentage of total land area) for 2010 based on data from http://waterdata.usgs.gov/nwis/wu. The boxes denote the four study regions. The irrigated and nonirrigated ASOS stations used herein are shown by the stars and circles, respectively.

2. Methods and data

An empirical methodology designed to quantify the theorized impacts of irrigation on changed land surface properties and the variability of changes in the energy balance components in space is illustrated using examples from four study regions: (i) California Mojave desert (CA), (ii) Mississippi River valley (MO), (iii) Nebraska central plains (NE), and (iv) Texas high plains (TX) (Fig. 1; Table 1). These regions represent some of the variation in climate, land surface characteristics, crop types and irrigation scales and mechanisms across the contiguous United States (Fig. 2).

For each ASOS station pair hourly measurements (1995–2014) of T are corrected to a common height above sea level (elevation of the lower measurement station) using a lapse rate of $6.5\,\mathrm{K\,km^{-1}}$ (T_{lap}), and θ_e is calculated from measured q, T, and P. Daily average S from measurements at CRN stations are assumed to be equal at each pair of stations within a region and are used in the analysis to estimate the impact of changing α on absorbed shortwave radiation [a key determinant of net radiation (NR), the left-hand side of Eq. (1)]. The quantity R_{lo} is not measured at ASOS or CRN stations so a first-order

TABLE 1. Monthly mean differences in air temperature dT (K), temperature adjusted for differences in station elevation dT_{lap} (K), and equivalent potential temperature $d\theta_e$ (K), based on data from the period 1995–2014. All differences are irrigated site − nonirrigated site. Data are shown by calendar month (rows) and study region (CA, MO, NE, and TX). Months for which a paired-sample t test leads to rejection of the null hypothesis that the mean difference T_{lap} and/or θ_e from the irrigated and nonirrigated site is equal to 0 at a significance level of 98% after the Bonferroni correction for the application of multiple tests (Simes 1986) is applied are shown in boldface type. Dominant crop types in the counties in which the meteorological stations are located are provided in the second row from the USDA 2014 National Agricultural Statistics Service report (http://www.nass.usda.gov/Charts_and_Maps/Crops_County/#db). Shown within the irrigated and nonirrigated stations blocks are their geographical location (lat and lon), elevation (m), and irrigation fetch Γ (s).

	CA			MO			NE			TX		
Dominant crop types	Alfalfa hay, durum wheat			Soybeans, corn; also cotton and rice			Corn, soybeans; also hay			Cotton, sorghum, and winter wheat		
Irrigated station	33.617°N, 114.717°W			37.233°N, 89.567°W			40.967°N, 98.317°W			33.650°N, 101.817°W		
	119			103			561			992		
	1866			2522			5239			2788		
Nonirrigated station	34.767°N, 114.617°W			35.600°N, 88.917°W			41.133°N, 100.683°W			35.183°N, 103.600°W		
	302			132			846			1237		
	77			74			1661			96		
Distance between stations (km)	130			190			200			236		
	dT (K)	dT_{lap} (K)	$d\theta_e$ (K)	dT (K)	dT_{lap} (K)	$d\theta_e$ (K)	dT (K)	dT_{lap} (K)	$d\theta_e$ (K)	dT (K)	dT_{lap} (K)	$d\theta_e$ (K)
Jan	0.36	**−0.83**	**−1.03**	2.75	**2.57**	**4.31**	0.05	**−1.81**	**−2.77**	1.25	**−0.34**	**−0.44**
Feb	0.38	**−0.80**	**−0.70**	2.36	**2.17**	**3.72**	0.36	**−1.49**	**−2.26**	1.34	**−0.25**	**−0.10**
Mar	0.31	**−0.88**	**−0.47**	2.00	**1.81**	**3.27**	0.59	**−1.26**	**−1.70**	1.40	**−0.19**	**1.33**
Apr	−0.18	**−1.37**	**−0.87**	1.45	**1.26**	**2.58**	1.46	**−0.39**	**−0.25**	1.67	0.08	**2.02**
May	−0.84	**−2.02**	**−1.08**	0.91	**0.73**	**2.20**	1.70	**−0.15**	**0.62**	1.24	**−0.35**	**3.70**
Jun	−1.36	**−2.55**	**−0.42**	0.31	**0.12**	**1.97**	1.53	**−0.32**	**0.76**	0.33	**−1.27**	**4.42**
Jul	−1.37	**−2.56**	**−0.22**	0.24	0.06	**1.50**	0.85	**−1.00**	**0.34**	0.02	**−1.57**	**0.56**
Aug	−0.84	**−2.03**	**0.38**	0.66	**0.47**	**1.81**	0.86	**−1.00**	**0.33**	0.58	**−1.02**	**1.10**
Sep	−0.40	**−1.59**	**1.33**	1.34	**1.15**	**3.29**	1.33	**−0.52**	**−0.03**	0.43	**−1.17**	**1.81**
Oct	−0.06	**−1.25**	**−0.43**	1.23	**1.04**	**3.18**	1.86	0.01	0.08	1.21	**−0.38**	**2.46**
Nov	0.15	**−1.04**	**−1.03**	1.46	**1.27**	**2.73**	1.72	−0.13	**−0.29**	1.25	**−0.34**	**0.98**
Dec	0.25	**−0.94**	**−1.24**	2.43	**2.24**	**3.87**	1.02	**−0.83**	**−1.34**	1.37	−0.22	**−0.37**
Annual	−0.30	−1.49	−0.49	1.43	1.24	2.87	1.11	−0.74	−0.54	1.01	−0.59	1.46

estimate of the change in R_{lo} due to the difference in emissivity dε is derived using Stefan–Boltzmann's law applied under the assumption that T measurements at 2 m are equal to the skin temperature T_s.

The influence of irrigation at a given station is a function of the time an upwind air parcel travels over irrigation. For each region one site defined as "irrigated" and one as "nonirrigated" were selected to make up a station pair. A site is defined as irrigated if >25% of land in either a 10- or 50-km radius in the prevailing upwind direction is irrigated. Conversely, a site is defined as nonirrigated if <15% of land in either a 10- or 50-km radius in the prevailing wind direction is irrigated. The overirrigation fetch time scale Γ is the equivalent mean number of seconds over irrigation:

$$\Gamma = \sum_{i=1}^{16}\left[\left(\frac{50\,000\text{ m}}{||U_i||}\right)(I_i)(f_i)\right], \quad (3)$$

where $||U_i||$ = mean wind speed at 10 m in one of 16 direction sectors i (m s^{-1}), f_i = frequency of winds in that sector, and I_i = fraction of area within 50 km of the station in that sector that is irrigated according to the MODIS Irrigated Agriculture Dataset. In this dataset, MODIS pixels with highest peak normalized difference vegetation index are sequentially classified as irrigated until the area of irrigation is approximately equal to that in U.S. Department of Agriculture (USDA) county-level statistics (Brown and Pervez 2014).

Station pairs are selected to maximize the difference in Γ, while seeking to maintain a reasonable separation distance to allow an implicit assumption of a similar base climate (Table 1). For each region, the stations that are defined as being influenced by irrigation have estimated Γ that exceeds those of the nonirrigated sites by at least a factor of 3 (Table 1).

MODIS visible (0.3–0.7 μm) white-sky albedo (MCD43A3) is generated every 16 days at 0.5-km resolution using surface reflectances at viewing angles from all 16 orbital paths (Schaaf et al. 2002; Taberner et al. 2010). The estimated α is likely accurate to within ±0.01–0.03 (Pinty et al. 2011). Emissivity estimates are based on irradiance in the infrared (band 31; 10.78–11.28 μm; MOD11A2). The

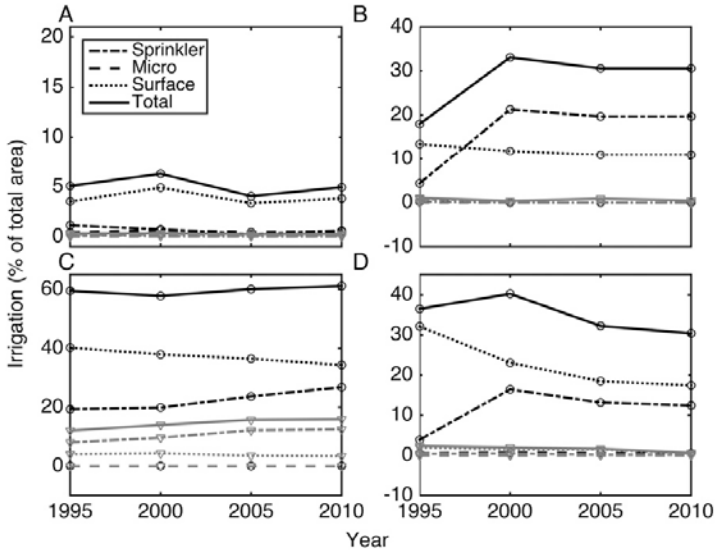

FIG. 2. Percentage of total area in the county containing the ASOS stations under irrigation (and by irrigation mechanism shown in legend) for (a) CA, (b) MO, (c) NE, and (d) TX. Black lines (circles) are the irrigated stations; gray lines (inverted triangles) are the nonirrigated stations. Locations of sites are given in Fig. 1. Data are from http://waterdata.usgs.gov/nwis/wu. Note the scales of the ordinate axes differ in each of the panels.

dataset includes 8-day ε estimates at 1 km (Hulley et al. 2012; Wan 2008) that are reported to have an accuracy of ± 0.015 (Hulley et al. 2012; Jacob et al. 2004). Herein, we use an average of all α and ε retrievals within 1 km of each ASOS station during June–August of 2000–14 to derive an average α and ε for the nonirrigated and irrigated sites and generate an average difference (dX; irrigated site − nonirrigated site) for those parameters (Table 2). Naturally, the representativeness of these estimates is a function of the number of cloud-free pixels, and, as discussed further below, the mean difference in these surface properties must be viewed with caution.

3. Results

Table 1 shows the monthly mean difference between paired air temperature measurements (both T, and those adjusted to a common elevation above sea level,

TABLE 2. Summary of data for June–August 2000–14 in each region. Note all difference values are irrigated site − nonirrigated site. T = mean June–August temperature (K) of the paired sites, S = daily mean measured incoming solar radiation (W m^{-2}), R_{lo} = daily mean outgoing longwave radiation (W m^{-2}) calculated under the assumption that the air temperature measured at 2 m is equal to the skin temperature (T_s); α = mean summer albedo at the nonirrigated site, dα = difference in albedo, and dFα = difference in net radiation due to the difference in albedo (note positive values indicate increased NR); ε = mean emissivity (nonirrigated site), dε = difference in emissivity, and dFε = difference in net radiation due to the difference in emissivity (W m^{-2}); dF = total difference in net radiation due to the differences in both albedo and emissivity (W m^{-2}); dT_s is an approximation of the response of skin temperature (K) to the difference in NR, computed using the mean T and ε from the nonirrigated site. The final two columns show dT_{lap} = difference in observed air temperature (June–August 2000–14) corrected to a common elevation (K), and dθ_{eobs} = difference in equivalent potential temperature (K).

	Mean values			Mean α and ε, difference in paired stations, radiative forcing, and thermal response								Observations	
Region	T (K)	S (W m^{-2})	R_{lo} (W m^{-2})	α	dα (10^{-2})	dFα (W m^{-2})	ε	dε (10^{-3})	dFε (W m^{-2})	dF (W m^{-2})	dT_s (K)	dT_{lap} (K)	dθ_{eobs} (K)
CA	308.3	308	498	0.12	−3.05	9.40	0.97	−0.28	0.14	9.54	1.35	−2.52	−0.32
MO	298.4	254	441	0.06	−0.70	1.78	0.98	0.44	−0.19	1.58	0.19	0.21	1.77
NE	296.1	255	427	0.07	−0.77	1.96	0.98	0.01	−0.004	1.96	0.44	−0.78	0.53
TX	299.4	280	448	0.11	−0.31	0.87	0.98	2.34	−1.05	−0.18	−0.28	−1.15	2.31

T_{lap}) and equivalent potential temperature θ_e at stations close to irrigation versus stations not affected by irrigation. According to a paired-sample t test, the hypothesis that the mean difference is equal to 0 is rejected at a 98% confidence level for virtually all calendar months for each of the paired stations (Table 1). As expected, the differences in T_{lap} and θ_e at irrigated versus nonirrigated sites are generally (though not uniformly) of largest magnitude during the growing season, when S and irrigation use are highest. For this reason the attribution analyses presented below focus on the climatological summer months (June–August), although it must be acknowledged that the growing and crop peak water demand seasons for some of the crops prevalent in the study regions extend greatly beyond these calendar months (Döll and Siebert 2002; Steduto et al. 2012).

In the paired samples from CA, NE, and TX, T_{lap} is uniformly lower at the irrigated sites. The mean monthly dT_{lap} is about −1.5 K in the paired sample from CA. Estimates for the growing season indicate larger impacts, with mean dT_{lap} from −2 to −3 K. Mean dT_{lap} from TX and NE are from approximately −0.5 to −0.8 K and thus are of lower magnitude than the data from CA. But, like the CA paired sites, the irrigation-impacted stations in NE and TX exhibit lower T_{lap} in virtually all calendar months (Table 1). Results for the paired stations in MO indicate slightly higher T_{lap} at the irrigated station, possibly because of a difference in the base climate of the stations, but dT_{lap} is smallest in the summer, consistent with cooling due to irrigation. Results for this station pair emphasize the difficulty in quantifying the impact of irrigation on local to regional climates and illustrate an important confounding factor—the potential for upstream regional-scale irrigation to affect the nonirrigated sites. The area of irrigated land in the prevailing winds during the growing season in NE and MO are far greater than either TX or CA (Fig. 1), potentially meaning that sites considered herein as nonirrigated may be contaminated by irrigation more than 50 km upstream.

The higher LE and resulting increase in q due to irrigation is manifest as higher θ_e at the irrigated sites during the growing season in MO, NE, and TX ($d\theta_e$ during June–August ranges from 0.3 to 4.4 K). A priori expectations were that the lower q and larger regional vapor pressure deficits (Gaffen and Ross 1999) in CA would cause a greater impact of irrigation on LE and therefore θ_e. However, although $d\theta_e$ is generally less negative than dT_{lap}, $d\theta_e$ for the CA paired stations is generally negative (indicating the nonirrigated site has higher θ_e) (Table 1). A partial explanation for this finding may be that Γ for the CA irrigation-impacted site is smaller than in the other three regions (Table 1). However, it may also reflect compensating forcing deriving from modification of albedo and/or emissivity (see below).

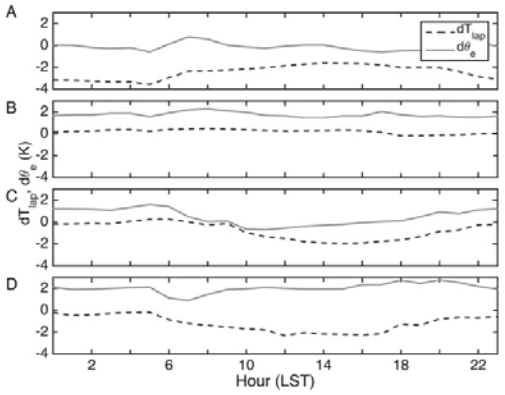

FIG. 3. Hourly mean difference in summer (June–August 1995–2014) air temperature corrected for difference in site elevation (dT_{lap}) and equivalent potential temperature ($d\theta_e$) between irrigated and nonirrigated stations in (a) CA, (b) MO, (c) NE, and (d) TX. Note that all times are expressed in local standard time (LST). The sites are located in the central time zone except for those in (a), which are in the Pacific time zone.

In addition to the clear seasonality in dT and $d\theta_e$ (Table 1), these variables also exhibit diurnal signatures (Fig. 3). The quantity $d\theta_e$ is of very small magnitude or positive in all hours of the day, whereas dT_{lap} in MO, NE, and TX is, as expected, most negative during the afternoon. CA is an exception in that dT_{lap} is negative throughout the day but of smallest magnitude during the afternoon. This may be due to confounding influences such as changes in α and/or ε or in the timing, extent, or type of irrigation (surface flooding vs sprinkler; Fig. 2).

In all regions mean summertime α at both the irrigated and nonirrigated sites is relatively low (0.05–0.13; Table 2). In accord with our expectations, the presence of irrigation is generally associated with lower α (Table 2). Using S from the nearest CRN stations and the difference in mean α at the irrigated versus nonirrigated sites, an estimate for the resulting increase in available NR is obtained. For CA this calculation results in considerably higher NR (9.4 W m^{-2}) at the irrigated station, while in the other regions the impact is more modest (NR increased by up to 2 W m^{-2}). This change in α thus acts as a positive forcing on T, that is largest at the CA paired stations where $d\alpha$ is about 20% of the nonirrigated site mean summertime α (Table 2). In CA, MO and NE the impact of $d\varepsilon$ on NR is smaller than that deriving from $d\alpha$ (from −0.19 to +0.14 W m^{-2}), while in TX it is of comparable magnitude. The combined impact of the difference in α and ε on NR is strongly positive in

CA, and weakly positive in MO and NE leading to enhanced surface energy availability and thus higher "predicted" air temperatures (by 0.2–1.5 K; Table 2). Conversely, in TX the combined effect of $d\alpha$ and $d\varepsilon$ is to slightly reduce NR and thus predicted T_{lap} at the irrigated site.

4. Discussion

The purpose of this article is to highlight the need for deeper understanding the total impact of irrigation on climate change at the regional scale, and specifically for the need to include the impacts on parameters relating to shortwave and longwave radiation. We further seek to propose an approach that maybe applied to empirically quantify the impact of irrigation on the different terms in the energy balance in different climate regions. The results of our limited proof of principle must be considered only *very approximate* estimates of the possible thermal response to changes in NR due to the assumptions applied in their generation (e.g., that the 2-m air temperature is equal to the skin temperature) and the high uncertainty in $d\alpha$ and $d\varepsilon$. However, the results shown in Table 2 imply that irrigation may substantially alter NR in some regions and may act to greatly confound interpretation of T and θ_e time series in regions with substantial irrigation. Observations indicate summer air temperatures are lower (on average) at sites impacted by irrigation in CA, NE, and TX (by 0.78–2.4 K). Thus it appears that the change in flux partitioning dominates the net impact on air temperatures in these regions. However, the impacts of changes in α and ε due to irrigation in CA, MO, and NE generally act to offset some fraction of the cooling of air temperatures due to changes in the surface energy partitioning. For example, the observed summertime dT_{lap} is −2.5 K in CA, while the NR forcing is estimated to result in dT_s of nearly +1.4 K. Thus it may be that changes in surface properties are masking up to one-third of the cooling due to enhanced water availability. However, the magnitude of these effects is regionally specific, and indeed the impact of $d\alpha$ and $d\varepsilon$ on NR is of the opposite sign in TX and indicates the change in surface properties may enhance surface cooling in some regions. A comprehensive analysis of region-to-region variations in the magnitude of the irrigation-induced changes in the components of the surface energy balance would have high scientific value. However, there are a number of challenges to such a meta-analysis, including 1) the limited availability of paired sites with similar base climates, elevation, and cropping that have long, complete time series derived from identical instrumentation but different fetch characteristics in terms of irrigation coverage, and 2) the uncertainty associated with the remote sensing estimates of surface properties [see further details below, and prior discussions regarding data needs for land surface–atmosphere coupling studies (Sellers et al. 1995)]. It should also be acknowledged that both California and Texas have experienced severe, long-lasting droughts during the study period, and in recent years both Missouri and Nebraska have experienced a number of growing seasons with above-average precipitation (Lehmann and Coumou 2015; Shukla et al. 2015; Trepanier et al. 2015). Year-to-year variations in crop selection (or the relative fraction of area under the dominant crops shown in Table 1) and in precipitation receipt may have greatly influenced the amount of water used in irrigation in individual years within individual counties. Such effects are difficult to quantify with the once-every-5-yr county-level irrigation data available from the USDA and therefore are neglected in the current analysis.

It is important to acknowledge that the methodology proposed herein is subject to a range of caveats and uncertainties, and that further research is necessary to test the generalizability of our findings and to refine the technique to increase the signal-to-noise ratio. The correction of the air temperature time series to a common altitude introduces potential errors in the dT_{lap} and $d\theta_e$ estimates. Further, the differences in α and ε at the irrigated versus nonirrigated sites are of very small magnitude and therefore are difficult to detect using currently available remote sensing measurements. Satellite-derived global surface albedo products are of high value to studies such as that presented herein and are being increasingly well quantified. However, they are subject to uncertainties including those challenges inherent in the measurement (e.g., reradiation of the earth's surfaces is not Lambert distributed, and atmospheric attenuation) and related to ground truthing (including spatial scaling errors between satellite and field measurements; Mira et al. 2015). Further, α is a function of irradiance conditions and thus varies as a function of hour of the day in a way that differs between soil and crops (Kimes et al. 1987), while the MODIS satellite overpasses only once per day. Despite these important caveats that pertain to the currently available data, the approach we propose may be useful in deconvoluting the impact of irrigation on surface properties and energy exchange, providing observational constraints on numerical attribution studies of the atmospheric impacts of irrigation, and can be readily applied in other regions or to other datasets. For example, it could be applied to higher-resolution (and higher

accuracy) remote sensing data as they become available or to meteorological data from mesonets to examine station pairs that are less separated geographically and thus are less vulnerable to variations in base climate.

Acknowledgments. We acknowledge grants to SCP from NSF (1339629 and 1502400) to RCS from NASA (14-EARTH14F-0207); useful conversations with R. J. Barthelmie, G. Olyphant, and J. T. Schoof; and the many scientists who developed the data sets used herein. The comments of three reviewers improved the quality and clarity of this manuscript.

REFERENCES

Adegoke, J. O., R. Pielke, and A. M. Carleton, 2007: Observational and modeling studies of the impacts of agriculture-related land use change on planetary boundary layer processes in the central US. *Agric. For. Meteor.*, **142**, 203–215, doi:10.1016/j.agrformet.2006.07.013.

Alex, Z. C., and J. Behari, 1998: Laboratory evaluation of emissivity of soils. *Int. J. Remote Sens.*, **19**, 1335–1340, doi:10.1080/014311698215478.

Brown, J. F., and M. S. Pervez, 2014: Merging remote sensing data and national agricultural statistics to model change in irrigated agriculture. *Agric. Syst.*, **127**, 28–40, doi:10.1016/j.agsy.2014.01.004.

Cierniewski, J., A. Karnieli, C. Kaźmierowski, and J. Ceglarek, 2014: A tool for predicting diurnal soil albedo variation in Poland and Israel. *EARSeL eProc.*, **13**, 36–40, doi:10.12760/02-2014-1-07.

Davey, C. A., R. A. Pielke Sr., and K. P. Gallo, 2006: Differences between near-surface equivalent temperature and temperature trends for the eastern United States: Equivalent temperature as an alternative measure of heat content. *Global Planet. Change*, **54**, 19–32, doi:10.1016/j.gloplacha.2005.11.002.

Diamond, H. J., and Coauthors, 2013: U.S. Climate Reference Network after one decade of operations status and assessment. *Bull. Amer. Meteor. Soc.*, **94**, 485–498, doi:10.1175/BAMS-D-12-00170.1.

Dobos, E., 2006: Albedo. *Encyclopedia of Soil Science*, R. Lal, Ed., CRC Press, 64–66.

Döll, P., and S. Siebert, 2002: Global modeling of irrigation water requirements. *Water Resour. Res.*, **38**, doi:10.1029/2001WR000355.

Evett, S. R., 2000: Energy and water balances at soil–plant–atmosphere interfaces. *Handbook of Soil Science*, M. E. Sumner, Ed., CRC Press, A129–A182.

Fall, S., D. Niyogi, A. Gluhovsky, R. A. Pielke, E. Kalnay, and G. Rochon, 2010: Impacts of land use land cover on temperature trends over the continental United States: Assessment using the North American Regional Reanalysis. *Int. J. Climatol.*, **30**, 1980–1993, doi:10.1002/joc.1996.

Gaffen, D. J., and R. J. Ross, 1999: Climatology and trends of U.S. surface humidity and temperature. *J. Climate*, **12**, 811–828, doi:10.1175/1520-0442(1999)012<0811:CATOUS>2.0.CO;2.

Geiger, R., R. H. Aron, and P. Todhunter, 2009: *The Climate near the Ground*. Rowman and Littlefield, 584 pp.

Gollehon, N., and W. Quinby, 2006: Irrigation resources and water costs. *Agricultural Resources and Environmental Indicators*, Economic Research Service/USDA, 24–32.

Hargreaves, G. H., and R. G. Allen, 2003: History and evaluation of Hargreaves evapotranspiration equation. *J. Irrig. Drain. Eng.*, **129**, 53–63, doi:10.1061/(ASCE)0733-9437(2003)129:1(53).

Hulley, G., S. Hook, and C. Hughes, 2012: MODIS MOD21 land surface temperature and emissivity Algorithm Theoretical Basis Document. Jet Propulsion Laboratory, California Institute of Technology, JPL Publ. 12–17, 102 pp. [Available online at http://emissivity.jpl.nasa.gov/downloads/examples/documents/MOD21_LSTE_ATBD_Hulley_v2.0_20121116_pmbv1.pdf.]

Jacob, F., F. Petitcolin, T. Schmugge, E. Vermote, A. French, and K. Ogawa, 2004: Comparison of land surface emissivity and radiometric temperature derived from MODIS and ASTER sensors. *Remote Sens. Environ.*, **90**, 137–152, doi:10.1016/j.rse.2003.11.015.

Kimes, D. S., P. J. Sellers, and W. W. Newcomb, 1987: Hemispherical reflectance variations of vegetation canopies and implications for global and regional energy budget studies. *J. Climate Appl. Meteor.*, **26**, 959–972, doi:10.1175/1520-0450(1987)026<0959:HRVOVC>2.0.CO;2.

Lehmann, J., and D. Coumou, 2015: The influence of mid-latitude storm tracks on hot, cold, dry and wet extremes. *Sci. Rep.*, **5**, 17491, doi:10.1038/srep17491.

Mira, M., M. Weiss, F. Baret, D. Courault, O. Hagolle, B. Gallego-Elvira, and A. Olioso, 2015: The MODIS (collection V006) BRDF/albedo product MCD43D: Temporal course evaluated over agricultural landscape. *Remote Sens. Environ.*, **170**, 216–228, doi:10.1016/j.rse.2015.09.021.

Moore, B., A. Coleman, M. Wigmosta, R. Skaggs, and E. Venteris, 2015: A high spatiotemporal assessment of consumptive water use and water scarcity in the conterminous United States. *Water Resour. Manage.*, **29**, 5185–5200, doi:10.1007/s11269-015-1112-x.

Pielke, R. A., Sr., and Coauthors, 2011: Land use/land cover changes and climate: Modeling analysis and observational evidence. *Wiley Interdiscip. Rev.: Climate Change*, **2**, 828–850, doi:10.1002/wcc.144.

Pinty, B., M. Taberner, V. R. Haemmerle, S. R. Paradise, E. Vermote, M. M. Verstraete, N. Gobron, and J.-L. Widlowski, 2011: Global-scale comparison of MISR and MODIS land surface albedos. *J. Climate*, **24**, 732–749, doi:10.1175/2010JCLI3709.1.

Rees, W. G., 2001: *Physical Principles of Remote Sensing*. 2nd ed. Cambridge University Press, 343 pp.

Sacks, W. J., B. I. Cook, N. Buenning, S. Levis, and J. H. Helkowski, 2009: Effects of global irrigation on the near-surface climate. *Climate Dyn.*, **33**, 159–175, doi:10.1007/s00382-008-0445-z.

Schaaf, C. B., and Coauthors, 2002: First operational BRDF, albedo nadir reflectance products from MODIS. *Remote Sens. Environ.*, **83**, 135–148, doi:10.1016/S0034-4257(02)00091-3.

Sellers, P., and Coauthors, 1995: Remote sensing of the land surface for studies of global change: Models—algorithms—experiments. *Remote Sens. Environ.*, **51**, 3–26, doi:10.1016/0034-4257(94)00061-Q.

Shukla, S., A. Steinemann, S. F. Iacobellis, and D. R. Cayan, 2015: Annual drought in California: Association with monthly precipitation and climate phases. *J. Appl. Meteor. Climatol.*, **54**, 2273–2281, doi:10.1175/JAMC-D-15-0167.1.

Simes, R. J., 1986: An improved Bonferroni procedure for multiple tests of significance. *Biometrika*, **73**, 751–754, doi:10.1093/biomet/73.3.751.

Steduto, P., T. C. Hsiao, D. Raes, and E. Fereres, 2012: Crop yield response to water. Food and Agriculture Organization of the United Nations, 505 pp. [Available online at http://www.fao.org/docrep/016/i2800e/i2800e.pdf.]

Sun, B. M., C. B. Baker, T. R. Karl, and M. D. Gifford, 2005: A comparative study of ASOS and USCRN temperature measurements. *J. Atmos. Oceanic Technol.*, **22**, 679–686, doi:10.1175/JTECH1752.1.

Taberner, M., B. Pinty, Y. Govaerts, S. Liang, M. Verstraete, N. Gobron, and J. L. Widlowski, 2010: Comparison of MISR and MODIS land surface albedos: Methodology. *J. Geophys. Res.*, **115**, D05101, doi:10.1029/2009JD012665.

Trepanier, J. C., M. J. Roberts, and B. D. Keim, 2015: Trends and spatial variability in dry spells across the south-central United States. *J. Appl. Meteor. Climatol.*, **54**, 2261–2272, doi:10.1175/JAMC-D-14-0319.1.

Wan, Z., 2008: New refinements and validation of the MODIS land-surface temperature/emissivity products. *Remote Sens. Environ.*, **112**, 59–74, doi:10.1016/j.rse.2006.06.026.

APPENDIX C

EMPIRICAL ESTIMATES OF SIZE-RESOLVED PRECIPITATION SCAVENGING COEFFICIENTS FOR ULTRAFINE PARTICLES

Pryor, S. C., V. M. Joerger, and R. C. Sullivan (2016), Empirical estimates of size-resolved precipitation scavenging coefficients for ultrafine particles, *Atmos. Environ.*, *143*, 133–138, doi:http://dx.doi.org/10.1016/j.atmosenv.2016.08.036.

Atmospheric Environment 143 (2016) 133–138

Contents lists available at ScienceDirect

Atmospheric Environment

journal homepage: www.elsevier.com/locate/atmosenv

Short communication

Empirical estimates of size-resolved precipitation scavenging coefficients for ultrafine particles

S.C. Pryor*, V.M. Joerger, R.C. Sullivan

Department of Earth and Atmospheric Sciences, Cornell University, Ithaca, NY 14853, USA

HIGHLIGHTS

- Below-cloud scavenging coefficients derived from long-term particle measurements.
- Scavenging coefficients decline by three as diameter goes from 15 nm to 100 nm.
- Good agreement with empirical parameterization of Laakso et al. (2003).

ARTICLE INFO

Article history:
Received 10 June 2016
Received in revised form
21 July 2016
Accepted 9 August 2016
Available online 11 August 2016

Keywords:
Below-cloud
Particle removal
Wet scavenging
Observational
Aerosol particles

ABSTRACT

Below-cloud scavenging coefficients for ultrafine particles (UFP) exhibit comparatively large uncertainties in part because of the limited availability of observational data sets from which robust parameterizations can be derived or that can be used to evaluate output from numerical models. Long time series of measured near-surface UFP size distributions and precipitation intensity from the Midwestern USA are used here to explore uncertainties in scavenging coefficients and test both the generalizability of a previous empirical parameterization developed using similar data from a boreal forest in Finland (Laakso et al., 2003) and whether a more parsimonious formulation can be developed. Scavenging coefficients (λ) over an ensemble of 95 rain events (with a median intensity of 1.56 mm h^{-1}) and 104 particle diameter (D_p) classes (from 10 to 400 nm) indicate a mean value of 3.4×10^{-5} s^{-1} (with a standard error of 1.1×10^{-6} s^{-1}) and a median of 1.9×10^{-5} s^{-1} (interquartile range: -2.0×10^{-5} to 7.5×10^{-5} s^{-1}). The median scavenging coefficients for D_p: 10–400 nm computed over all 95 rain events exhibit close agreement with the empirical parameterization proposed by (Laakso et al., 2003). They decline from ~4.1×10^{-5} s^{-1} for D_p of 10–19 nm, to ~1.6×10^{-5} s^{-1} for D_p of 80–113 nm, and show an increasing tendency for $D_p > 200$ nm.

1. Introduction and motivation

Below-cloud scavenging of aerosol particles by hydrometeors plays an important role in defining their atmospheric lifetimes and in situ particle size distributions (Andronache, 2003; Pruppacher and Klett, 1997). Full numerical treatment of below-cloud scavenging in atmospheric chemistry models is computationally demanding and is subject to large uncertainties due to non-linear dependencies of scavenging efficiencies with hydrometeor diameter spectra and phase, precipitation intensity, atmospheric turbulence and particle diameters (Andronache, 2003; Pruppacher and Klett, 1997). Thus, some atmospheric chemistry models continue to use scavenging coefficients expressed as a function of rainfall rate for specific particle diameters or modes (Feng, 2007) to represent this process (e.g. the EMEP MSC-W Eulerian chemical transport model (Simpson et al., 2012), DEHM (Frohn et al., 2001), and MATCH (Robertson et al., 1999)).

A number of previous publications have explained the mechanisms and theorized dependencies of below-cloud scavenging (e.g. (Andronache, 2003; Pruppacher and Klett, 1997; Wang et al., 2010)), so they are described only briefly here. The rate at which particles are scavenged by rain droplets depends on the collision and collection efficiency (where the latter term is often assumed to be 1 for particles with diameters much smaller than the rain droplet diameter), and is thus a function of the rainfall intensity and rain droplet size distribution, as well as the size distribution and composition of the in situ particles. The collision efficiency

* Corresponding author.
E-mail address: sp2279@cornell.edu (S.C. Pryor).

http://dx.doi.org/10.1016/j.atmosenv.2016.08.036
1352-2310/

($E(D,D_p)$) between a falling raindrop of a given diameter (D) and an in situ particle (of diameter, D_p) is theorized to decrease with increasing particle diameter in the D_p range ~1–100 nm, to remain fairly constant (i.e. within a factor of approximately 2–5) in the D_p range ~100 nm to 1 μm, and then to exhibit a rapid increase with increasing D_p (Wang et al., 2010). $E(D,D_p)$ for the smallest D_p is dominated by Brownian diffusion with additional contributions from thermophoresis and electrostatic forces (Andronache, 2004), and atmospheric turbulence (Quérel et al., 2014). For larger D_p interception and impaction play a larger role in dictating collision efficiency (Pruppacher and Klett, 1997; Wang et al., 2010). $E(D,D_p)$ increases with D, so given rainfall events with lower intensities (rainfall rates) are typically characterized by smaller rain droplet diameters than those with higher intensities (Marshall and Palmer, 1948), the *a priori* expectation is that higher rainfall rates are typically associated with a larger number of larger rain droplets, and thus higher particle scavenging efficiencies. This expectation has largely been realized in observational analyses e.g. (Castro et al., 2010; Chate, 2005; Laakso et al., 2003; Maria and Russell, 2005; Volken and Schumann, 1993; Zhao et al., 2015). However, there are large event-to-event and site-to-site variations in experimentally derived scavenging efficiencies (Andronache et al., 2006). Of the observational studies of below-cloud scavenging of ultrafine particles (UFP, particles with diameters (D_p) less than 100 nm) that have been conducted to date, only two (Laakso et al., 2003; Zikova and Zdimal, 2016) have considered sufficient rain event sample sizes ($n \approx 100$) to generate statistically robust estimates of size-resolved scavenging coefficients, and only one (Laakso et al., 2003) sought to develop an empirical parameterization of size-resolved scavenging coefficients. Herein, we use a 30-month time series of measured near-surface UFP size distributions and precipitation intensity to explore the generalizability of the empirical parameterization of Laakso et al. (2003), and to evaluate whether alternative, more parsimonious formulations can be advanced.

2. Data and methods

The meteorological and particle size distribution (PSD) data analyzed herein were collected at an AmeriFlux site in southern Indiana (in the Morgan Monroe State Forest (MMSF), 39°19′ N, 86°25′ W, 275 m a.s.l (Schmid et al., 2000)) from December 2006 to April 2009. Precipitation at this site is fairly evenly distributed across the year and has an average occurrence of approximately 1 day in 3 (see précis description of the meteorological conditions in Fig. 1). Size-resolved particle number concentrations in 104 size classes over the D_p range: 10–400 nm were obtained using a TSI scanning mobility particle sizer (SMPS3936) system comprising an electrostatic classifier (TSI-3080), long differential mobility analyzer (TSI-DMA3081) and a condensation particle counter (TSI-3025A). A second SMPS3936 system was also operated on the same manifold and comprised an electrostatic classifier (TSI-3080), nano-DMA (TSI-DMA3085) and a condensation particle counter (TSI-3786) and for which particle concentrations for D_p in the range 6–100 nm are reported. The sampling protocol was such that air was drawn from a height of 46-m (above a forest canopy with a mean height ~26–28 m) through copper tubing for 10-min in each half-hour period, with sampling at two other heights via a common manifold in each 30-min period (Pryor et al., 2010). Copper was chosen for the sampling lines because it was available at very long sections reducing the number of connections to two, is malleable (meaning all bends could be relatively smooth) and is relatively inert and resistant to acquisition of charge, but with such long sampling lines particle losses are inevitable. Thus, transmission efficiencies derived experimentally (which for $D_p = 10$ nm are

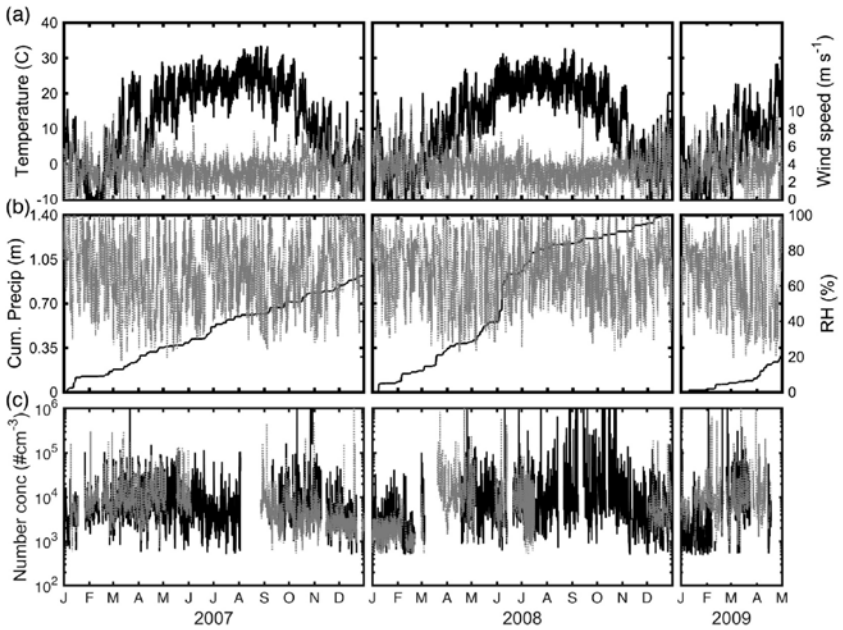

Fig. 1. Overview of meteorological conditions and particle number concentrations at MMSF during January 2007–April 2009. (a) Hourly average air temperature (°C) (black) and wind speed (m s^{-1}) (gray) at 46-m. (b) Cumulative precipitation (Cum. Precip, m) in each year (black) and hourly average relative humidity (RH, %) again at 46-m. (c) Total number particle concentrations (# cm^{-3}) at 46-m (Number conc) from an SMPS with a nano-DMA (D_p: 6–100 nm) (black) and an SMPS with a long-DMA (D_p: 10–400 nm) (gray).

below 0.3, but increase to over 0.5 for $D_p > 20$ nm) were used to determine empirical correction factors (Pryor et al., 2010) that have been applied to the observed PSD. We assume the particle losses in the copper sampling lines are independent of variations in humidity and other environmental conditions.

Rainfall rates derive from measurements using a Texas Electronics TE525 tipping bucket rain gauge also deployed at 46 m (Fig. 1b). Since this instrument is deployed without a wind-shield it is subject to under-capture during high wind events. The modal correction factor computed using the approach of Hildebrandt et al. (2007) and wind speed data from a sonic anemometer deployed at 46-m is ~1.1 (Fig. 2b). Frozen hydrometeors (snow, ice and hail) differ greatly from liquid droplets both in terms of the particle capture efficiencies (Sparmacher et al., 1993) and the accuracy of their measurement by tipping bucket rain gauges (Savina et al., 2012). To avoid inclusion of snow events in the analysis, METAR reports from the National Weather Service station KIND-Indianapolis, IN (located approximately 45 km to the north of MMSF) are used to screen out periods when snow or hail was observed. The procedure used is as follows; any event during which precipitation is reported by the TE525 at MMSF and for which snow/ice/hail were reported at KIND during that hour or the two hours prior to or subsequent to that time stamp are excluded from consideration. The resolution of the tipping bucket rain gauge is 0.254 mm (equal to one tip). To be consistent with the analysis of Laakso et al. (2003) and avoid inclusion of very light and comparatively poorly quantified rain events, events were only included in the analysis if the precipitation intensity $\geq$0.4 mm h^{-1}.

The in situ measured PSDs and rainfall rates are used to derive size-resolved scavenging coefficients ($\lambda(D_p)$) using:

$$\lambda(D_p) = -\frac{1}{t_1 - t_0}\ln\left(\frac{c_1(D_p)}{c_0(D_p)}\right) \quad (1)$$

where D_p is the particle diameter, $t_1 - t_0$ is the length of the rain event in seconds, and $c_0(D_p)$ and $c_1(D_p)$ are the average number concentration of particles in each size bin in the 30-min periods before and after the rain event, respectively.

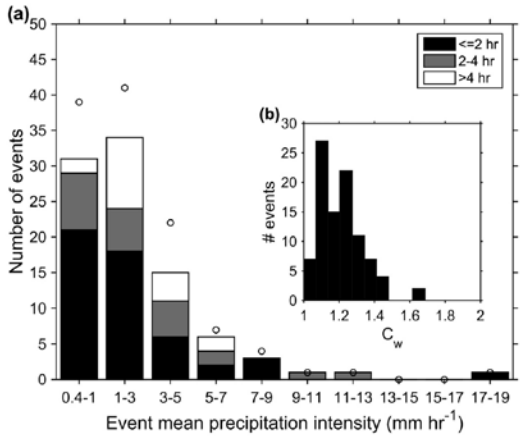

Fig. 2. (a) Summary of the intensity (in mm h^{-1}) and duration of the 95 rain events from which scavenging coefficients are computed for the SMPS3936 with the long-DMA (shown by the bars). Also shown are the intensities of the rainfall events (dots) included in the analysis of data from the SMPS with a nano-DMA (n = 121). (b) Histogram of the correction factor (C_w) for wind-related under-catch by the rain gauge computed from $C_w = exp[-0.001 \times \ln(R) - 0.0122 \times U \times \ln(R) + 0.034 \times U + 0.0077]$, where U is the wind speed (m s^{-1}), and R is the measured rainfall rate (mm h^{-1}) (Hildebrandt et al., 2007).

A premise of the empirical approach to determining size-resolved scavenging efficiencies is that with the exception of removal by below-cloud scavenging the particle population is stationary over the course of the rain event. To avoid strongly non-stationary conditions such as frontal passages or new particle formation occurrence, events are only included in the analysis if two criteria are met: (i) the wind direction (as measured using a 03001-5 R.M. Young Wind Sentry Set deployed at 46-m) at the start and end of the rain event did not differ by more than 90° and (ii) new particle formation (NPF) was not observed in the hour following cessation of rain (i.e. particle concentrations $<1 \times 10^3$ cm^{-3} for $D_p = 10$–15 nm, inclusive and visual inspection of plots of the time evolution of PSD did not show evidence of NPF (see a detailed description of robust subjective and objective ways to detect NPF given in Kulmala et al. (2012)). To avoid unstable estimates of the concentration ratio, an individual diameter class was only included in the analysis of a specific rain event if both $c_0(D_p)$ and $c_1(D_p)$ exceeded 10 cm^{-3}.

Laakso et al. (2003) proposed the following functional form for the relationship between the median $\lambda(D_p)$ (for each of the 29 logarithmically distributed size channels (D_p) in the diameter space 10–500 nm) and precipitation rate:

$$\log_{10}\left(\frac{\lambda}{\lambda_0}\right) = a + b \times d_p^4 + c \times d_p^3 + d \times d_p^2 + e \times d_p^1 + f \times \left(\frac{p}{p_0}\right)^{0.5} \quad (2)$$

where λ_0 is 1 s^{-1}, $d_p = \log_{10}(D_p/D_{p0})$, $D_{p0} = 1$ m, p is the rain rate in mm hr^{-1}, p_0 is 1 mm h^{-1}, and *a*-*f* are the fitted coefficients.

In this analysis, we evaluate the degree of agreement between the empirical coefficients (*a*-*f*) as derived by Laakso et al. (2003) and observational estimates of $\lambda(D_p)$ as derived from the MMSF data set. We also use the framework described by (2) to develop least squares best-fit estimates from our observations. Our fitting procedure is as follows: the coefficient *f* (which describes the scaling term for precipitation intensity) is first derived by conditionally sampling the scavenging coefficients in three precipitation intensity classes (light (0.4–2 mm h^{-1}), moderate (2–5 mm h^{-1}), and heavy (>5 mm h^{-1})) in addition to treating the whole sample ensemble (i.e. all rainfall intensities). Then *f* and the median value of p is used with the estimates of $\log_{10}(\lambda/\lambda_0)$ as a composite dependent variable to generate the other fitting coefficients in Equation (2). Application of regression to fit complex (multi-predictor) equations (such as (2)) to small data sets can lead to model over-fitting. Hence we use stepwise regression to examine if a more parsimonious fit can be derived. In this analysis we use stepwise regression with a threshold minimum p-value of 0.1 for a term to be removed.

There are four primary potential sources of discrepancies between empirically derived $\lambda(D_p)$ from different studies:

a) Variations in the methodology used to select the cases (e.g. the stationarity criteria) and those used to compute the scavenging coefficients (e.g. the discretization of the precipitation data). The precipitation data at the MMSF site are reported with hourly discretization, while Laakso et al. (2003) had precipitation rates discretized at 15-min intervals and they included all events with a duration >0.5 h. The hourly discretization of precipitation data from MMSF will inevitably result in lower precipitation intensities than if

the precipitation data were discretized at higher frequency. Also, herein we compare UFP concentrations before and after rain events to capture the net effect of the precipitation event. That is we compare distributions at t = 0, prior to the commencement of precipitation, and at time t = n, after precipitation and thus each individual event results in a single estimate of λ for each particle diameter so each event is equally weighted in the estimation of median and mean λ(D_p) regardless of the event duration. However, previous authors calculated λ from the UFP concentrations during rain events and thus compare the PSD at time t = 0, just prior to precipitation and at time = t + n, and at t + n and t + 2n, (where n is the temporal discretization of the PSD measurements) during the rain event (Laakso et al., 2003; Zikova and Zdimal, 2016).

b) Variations in the sampling system. Here we present data that were sampled well above a forest canopy to avoid local contamination of the PSD, and thus used long sampling lines that result in large corrections for tubing losses. Other sampling locations may not require use of long sampling lines.
c) Differences in particle instrumentation both in terms of operating principle (e.g. SMPS versus Fast Mobility Particle Sizers (Hornsby and Pryor, 2014)) and the discretization of the PSD. Also differences in instrument maintenance and deployment protocols (e.g. the presence of a wind shielding on, or heating of, rain gauges).
d) Differences in the type and intensity of precipitation and thus the rain droplet size distribution.

To address some of these sources of uncertainty we compute λ(D_p) from two different SMPS3936 systems connected to the same sampling lines and manifold system. One SMPS was operated with a long-DMA in order to capture a wide range of particles diameters (10–400 nm), and one with a short-DMA to provide estimates of scavenging coefficients for D_p < 100 nm for a larger event sample (i.e. more rain events), and also undertake an assessment of λ(D_p) for the diameter range 10–100 nm for rainfall events sampled by both SMPS systems.

3. Results

The rain events used to compute the scavenging coefficients from the SMPS3936 with a long-DMA exhibit a mean duration of almost 3 h (median of 2 h) and a mean intensity of 2.47 mm h^{-1} (median of 1.57 mm h^{-1}) (Fig. 2 and Table 1). Thus, the average rain intensities are higher than those reported in (Laakso et al., 2003) (median value of 0.8 mm h^{-1}), but cover the same range of values.

Although a substantial fraction of the scavenging coefficients (λ) from (1) are close to (or below) zero, the mean-λ is significantly different from zero and positive. We postulate that the negative λ values (that have also been observed in previous studies (Laakso et al., 2003; Zikova and Zdimal, 2016)) reflect causes such as the uncertainty in PSD measurements and inclusion cases where the PSD was non-stationary events (although the event passed our selection criteria). The empirical cumulative density function of λ over the ensemble of rain events and 104 diameter classes indicate a mean value of 3.4×10^{-5} s^{-1} (with a standard error of 1.1×10^{-6} s^{-1}), a median of 1.9×10^{-5} s^{-1}, and an interquartile range of -2.0×10^{-5} to 7.5×10^{-5} s^{-1} (Fig. 3a, Table 1). To provide further context for these estimates of λ an analysis was conducted in which number concentrations from the 104 size classes were sampled across 95 randomly sampled "no rain" events (that have the same characteristics in terms of duration and stationarity conditions applied above) and used to compute scavenging coefficients. The results indicate a mean value (computed over all diameters and all events) of 4.8×10^{-6} s^{-1} (with a standard error of 2.8×10^{-6} s^{-1}), and a median of -1.0×10^{-7} s^{-1} (interquartile range: -7.7×10^{-6} to 1.0×10^{-5} s^{-1}). Thus, the mean-λ for non-rain events is almost an order of magnitude below that obtained for our rain event ensemble, and the median is over an order of magnitude smaller than that computed for the rain events. This analysis thus further indicates that, while there is considerable event-to-event variability in derived λ estimates, the estimates derived herein are likely reflective of physical removal of particles by below-cloud scavenging. Further, although as in the study of Zikova and Zdimal (2016) the interquartile range of λ(D_p) spans an order of magnitude for virtually all diameters considered (Fig. 3b), only two measured D_p exhibit mean-λ values that are negative and they are confined to diameters (10.9 nm and 399.5 nm) near the edges of the measured interval for this SMPS where the instrument has lower precision, and for the smaller diameter where the correction for tubing losses is largest.

The magnitude of median-λ(D_p) agree with previously reported theoretical predictions (Wang et al., 2010) for the range of rainfall intensities represented in the data set. Also in accord with theoretical considerations and prior experimental research (Andronache et al., 2006; Wang et al., 2010), median scavenging coefficients by particle diameter computed over all 95 rain events decline from ~4.1×10^{-5} s^{-1} for D_p of 10–19 nm to ~1.6×10^{-5} s^{-1} for D_p of 80–113 nm, and then show an increasing tendency for D_p > 200 nm (Fig. 3b).

Scavenging coefficients for all D_p were conditionally sampled by rainfall intensity (Fig. 3a) to derive an estimate of the coefficient *f* in (2) as the slope of the fit between median-λ and rainfall intensity. The results indicate a value of 0.185 (versus 0.244984 in (Laakso et al., 2003)). The other coefficients in (2) were then determined by first averaging the median λ estimates across three size channels (so median λ(D_p) is the average value of λ(D_p(n − 1), λ(D_p(n), and λ(D_p(n + 1)) and then fitting (2) using least squares regression (Fig. 4). The resulting fit has an adjusted variance explanation (adjusted-r^2) of 0.46, and all values of the coefficients have p-values <0.10. No more parsimonious model could be found using stepwise

Table 1
Summary of the data sets from which scavenging coefficients were computed for MMSF and the resulting statistics.

Statistic	Instrument			
	SMPS3936: Long-DMA	SMPS3936: Nano-DMA	Common events long-DMA	Common events nano-DMA
D_p range (nm)	10–400	6–100	10–100	
# Rainfall events	95	121	87	
Mean rainfall intensity (mm h^{-1}) (median)	2.47 (1.56)	2.46 (1.59)	2.55 (1.48)	
Mean-λ (10^{-5} s^{-1}) (standard error)	3.4 (0.11)	3.5 (0.32)	4.6 (0.25)	3.2 (0.28)
Median-λ (10^{-5} s^{-1}) (IQR)	1.9 (−2.0 to 7.5)	5.7 (−1.7 to 11)	2.6 (−1.5 to 8.8)	2.2 (−2.3 to 8.1)
RMSE of median-λ(D_p) versus fit (10^{-5} s^{-1})	1.23	1.26		
RMSE of median-λ(D_p) versus fit of Laakso et al., 2003 (10^{-5} s^{-1})	1.63	3.95		

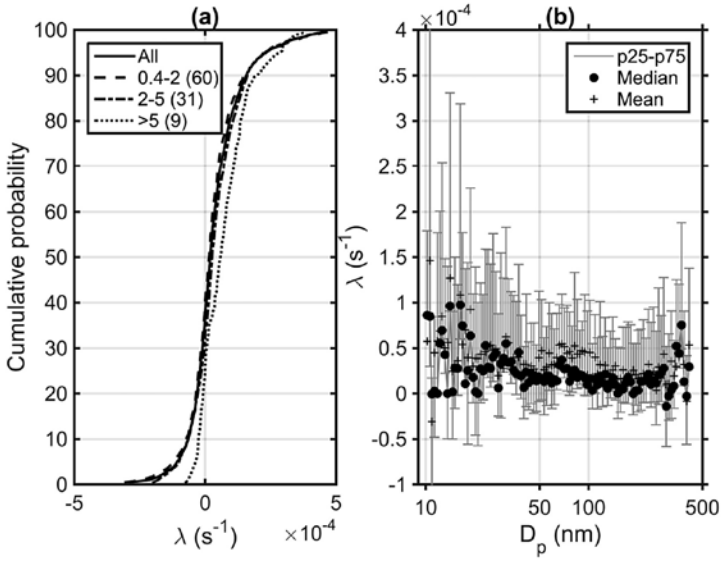

Fig. 3. (a) Empirical cumulative distribution plot of scavenging coefficients (λ) for each of the 104 diameters (D_p) reported by the SMPS3936 with the long-DMA for the ensemble of 95 rain events at MMSF (denoted by All in the legend). Also shown are cumulative distributions of λ values conditionally sampled by three rain intensity classes (in mm h^{-1}). The numbers shown in parentheses are the fraction of the total number of valid λ values in that rainfall intensity class. Thus, results from the highest rainfall intensity class are the least robust since they derive from a small sample size. (b) Mean, median and inter-quartile range of scavenging coefficients (λ) for each of the 104 diameters (D_p) reported by the SMPS fitted with the long-DMA.

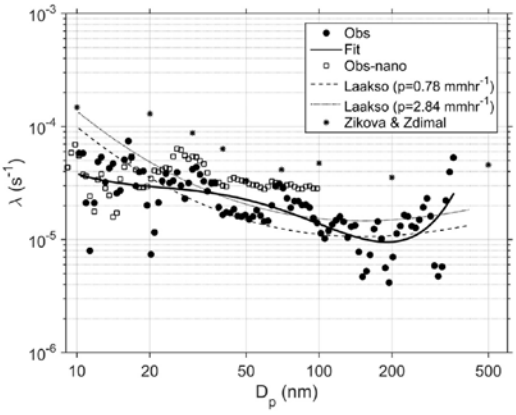

Fig. 4. Median scavenging coefficients (λ) as a function of particle diameter (D_p) at MMSF as used in the fitting procedure (i.e. averaged over three adjacent size classes) (Obs). Also shown is a fit from Equation (2) (the adjusted variance explanation (r^2) for this fit is 0.46), and the median scavenging coefficients as computed from the SMPS with the nano-DMA (Obs-nano). The lines denote results of the parameterization of Laakso et al. (2003) for two different precipitation rates (p = 0.78 mm h^{-1} and 2.84 mm h^{-1}). The asterisks show median scavenging coefficients as presented for 311 rain events by Zikova and Zdimal (2016) for selected particle diameters. The fitting coefficients for Equation (2) from MMSF and those from Laakso et al. (2003) (shown in parentheses in the format provided in the original reference) are as follows: a = 3.4549076 × 10^3 (274.35758), b = 1.0040252 × 10^7 (332839.59273), c = 5.484421066 × 10^6 (226656.57259), d = 1.12147496 × 10^6 (58005.91340), e = 1.01768617 × 10^5 (96588.38582), f = 0.185 (0.244984).

regression. Thus it appears that all the terms in Equation (2) contribute to the overall quality of the fit.

Although the fitting coefficients from MMSF exhibit marked discrepancies from those developed by Laakso et al. (2003), the median λ(D_p) values computed from the MMSF data set also exhibit good agreement with the parameterization of Laakso et al. (2003) (Fig. 4). The root mean squared error (RMSE) between λ from the fit derived herein and the observations for the 104 diameter classes is 1.23 × 10^{-5} s^{-1} (for the median precipitation intensity of 1.56 mm h^{-1}), while for the Laakso et al. (2003) parameterization is only slightly higher (1.63 × 10^{-5} s^{-1}). Thus, the parameterization of median λ(D_p) derived by Laakso et al. (2003) appears to be broadly applicable. Interestingly, in contrast to the convergence with estimates from the boreal forest site in Finland (Laakso et al., 2003), for all diameters data from MMSF indicate substantially smaller λ(D_p) than were derived using data from a site in the Czech Republic (Zikova and Zdimal, 2016) (Fig. 4). This discrepancy may reflect the occurrence of higher rainfall intensities at the site in the Czech Republic, differences due to the criteria used for event selection with regards to stationarity, and/or difference in the way in which scavenging coefficients are calculated (described above).

Median-λ(D_p) computed from the SMPS3936 with the nano-DMA for a larger set of rainfall events at MMSF (n = 121, see Table 1) generally exceed those from the SMPS with a long-DMA (Fig. 4). The λ estimates from the nano-DMA SMPS data set at MMSF are also smaller than those from the site in the Czech Republic, but by a lower margin than those from the SMPS with a long-DMA (Fig. 4). This may be in part due to the inclusion of more summertime rainfall events in the sample used to compute λ(D_p) from the SMPS with the nano-DMA (see Fig. 1c). To provide a context for these results computed independently from the two SMPS systems at MMSF (over different rain events), λ estimates for

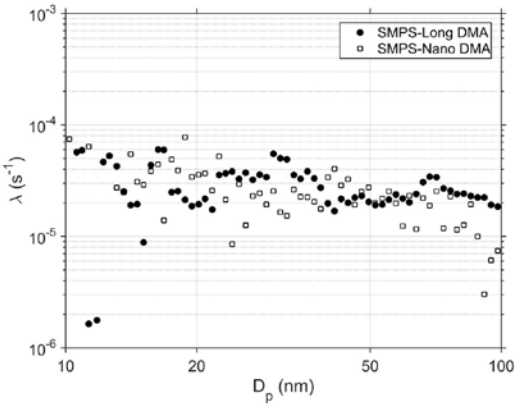

Fig. 5. Median scavenging coefficients (λ) as a function of particle diameter (D_p) for diameters between 10 and 100 nm, for all 87 events for which data from the SMPS with the Long-DMA (SMPS-Long DMA) and SMPS with nano-DMA (SMPS-Nano DMA) are both available. See Table 1 for the statistics of these events.

D_p 10–100 nm from the two systems for 87 common rainfall events were also computed. The results indicate relatively good agreement between $\lambda(D_p)$ estimates from the two systems (Table 1, Fig. 5) adding support to the inference that the discrepancies shown in Fig. 4 reflect differences in the nature of the rainfall events.

4. Concluding remarks

Below cloud scavenging is an important removal process for atmospheric aerosol particles and plays a key role in determining particle concentrations and size distributions. The magnitude of the effect remains uncertain in part because there remain very few robust observational data sets with which to evaluate numerical models of scavenging efficiencies. In situ measurements of particle size distributions and rainfall intensities collected over a 30-month period are used to develop a data set of rain events from which scavenging efficiencies for particle diameters between 10 and 400 nm are derived. The ensemble mean scavenging efficiency is $3.4 \times 10^{-5}\ s^{-1}$ (and has a standard error of $1.1 \times 10^{-6}\ s^{-1}$), while the median is $1.9 \times 10^{-5}\ s^{-1}$ (interquartile range: -2.0×10^{-5} to $7.5 \times 10^{-5}\ s^{-1}$). The median scavenging coefficients by particle diameter exhibit good agreement with the empirical expression formulated by Laakso et al. (2003).

Acknowledgments

This work was supported by a grant to SCP from NSF (1517365). RCS acknowledges funding from NASA (14-EARTH14F-0207). The comments and suggestions of two reviewers and Prof. R. Barthelmie are gratefully acknowledged. The PSD data from MMSF analyzed herein can be downloaded from http://www.geo.cornell.edu/eas/PeoplePlaces/Faculty/spryor/ or can be requested by email (sp2279@cornell.edu). The AmeriFlux data used herein (available at: http://ameriflux.ornl.gov/) were collected under funding from the Office of Science, U.S. Department of Energy, and from the AmeriFlux Management Project, Lawrence Berkeley National Laboratory. Observations of meteorological conditions from the NWS station in Indianapolis are available from the National Centers for Environmental Information (ftp://ftp.ncdc.noaa.gov/pub/data/).

References

Andronache, C., 2003. Estimated variability of below-cloud aerosol removal by rainfall for observed aerosol size distributions. Atmos. Chem. Phys. 3, 131–143.
Andronache, C., 2004. Diffusion and electric charge contributions to below-cloud wet removal of atmospheric ultra-fine aerosol particles. J. Aerosol Sci. 35, 1467–1482.
Andronache, C., Grönholm, T., Laakso, L., Phillips, V., Venäläinen, A., 2006. Scavenging of ultrafine particles by rainfall at a boreal site: observations and model estimations. Atmos. Chem. Phys. 6, 4739–4754.
Castro, A., Alonso-Blanco, E., González-Colino, M., Calvo, A.I., Fernández-Raga, M., Fraile, R., 2010. Aerosol size distribution in precipitation events in León, Spain. Atmos. Res. 96, 421–435.
Chate, D.M., 2005. Study of scavenging of submicron-sized aerosol particles by thunderstorm rain events. Atmos. Environ. 39, 6608–6619.
Feng, J., 2007. A 3-mode parameterization of below-cloud scavenging of aerosols for use in atmospheric dispersion models. Atmos. Environ. 41, 6808–6822.
Frohn, L.M., Christensen, J.H., Brandt, J., Hertel, O., 2001. Development of a high resolution integrated nested model for studying air pollution in Denmark. Phys. Chem. Earth Part B Hydrol. Oceans Atmos. 26, 769–774.
Hildebrandt, A., Al Aufi, M., Amerjeed, M., Shammas, M., Eltahir, E.A.B., 2007. Eco-hydrology of a seasonal cloud forest in Dhofar: 1. Field experiment. Water Resour. Res. 43 (n/a-n/a).
Hornsby, K.E., Pryor, S.C., 2014. A laboratory comparison of real-time measurement methods for 10–100-nm particle size distributions. Aerosol Sci. Technol. 48, 571–582.
Kulmala, M., et al., 2012. Measurement of the nucleation of atmospheric aerosol particles. Nat. Protoc. 7, 1651–1667.
Laakso, L., Gronholm, T., Rannik, Ü., Kosmale, M., Fiedler, V., Vehkamaki, H., Kulmala, M., 2003. Ultrafine particle scavenging coefficients calculated from 6 years field measurements. Atmos. Environ. 37, 3605–3613.
Maria, S.F., Russell, L.M., 2005. Organic and inorganic aerosol below-cloud scavenging by suburban New Jersey precipitation. Environ. Sci. Technol. 39, 4793–4800.
Marshall, J.S., Palmer, W.M.K., 1948. The distribution of raindrops with size. J. Meteorol. 5, 165–166.
Pruppacher, H.R., Klett, J.D., 1997. Cloud chemistry. Microphysics of Clouds and Precipitation. Kluwer Academic Publishers, Dordrecht, pp. 700–791 (Chapter 17).
Pryor, S., Spaulding, A., Barthelmie, R., 2010. New particle formation in the Midwestern USA: event characteristics, meteorological context and vertical profiles. Atmos. Environ. 44, 4413–4425.
Quérel, A., Monier, M., Flossmann, A.I., Lemaitre, P., Porcheron, E., 2014. The importance of new collection efficiency values including the effect of rear capture for the below-cloud scavenging of aerosol particles. Atmos. Res. 142, 57–66.
Robertson, L., Langner, J., Engardt, M., 1999. An Eulerian limited-area atmospheric transport model. J. Appl. Meteorol. 38, 190–210.
Savina, M., Schäppi, B., Molnar, P., Burlando, P., Sevruk, B., 2012. Comparison of a tipping-bucket and electronic weighing precipitation gage for snowfall. Atmos. Res. 103, 45–51.
Schmid, H.P., Grimmond, C.S.B., Cropley, F., Offerle, B., Su, H.-B., 2000. Measurements of CO_2 and energy fluxes over a mixed hardwood forest in the mid-western United States. Agric. For. Meteorol. 103, 357–374.
Simpson, D., Coauthors, 2012. The EMEP MSC-W chemical transport model – technical description. Atmos. Chem. Phys. 12, 7825–7865.
Sparmacher, H., Fülber, K., Bonka, H., 1993. Below-cloud scavenging of aerosol particles: Particle-bound radionuclides—Experimental. Atmos. Environ. 27, 605–618.
Volken, M., Schumann, T., 1993. A Critical review of below-cloud aerosol scavenging results on Mt. Rigi. Water Air Soil Pollut. 68, 15–28.
Wang, X., Zhang, L., Moran, M.D., 2010. Uncertainty assessment of current size-resolved parameterizations for below-cloud particle scavenging by rain. Atmos. Chem. Phys. 10, 5685–5705.
Zhao, S., Yu, Y., He, J., Yin, D., Wang, B., 2015. Below-cloud scavenging of aerosol particles by precipitation in a typical valley city, northwestern China. Atmos. Environ. 102, 70–78.
Zikova, N., Zdimal, V., 2016. Precipitation scavenging of aerosol particles at a rural site in the Czech Republic. Tellus B 68, 27343 doi: 27310.23402/tellusb.v27368.27343.

APPENDIX D

THE IMPACT OF RESOLUTION ON METEOROLOGICAL, CHEMICAL AND AEROSOL PROPERTIES IN REGIONAL SIMULATIONS WITH WRF-CHEM

Crippa, P., R. C. Sullivan, A. Thota, and S. C. Pryor (2017), The impact of resolution on meteorological, chemical and aerosol properties in regional simulations with WRF-Chem, *Atmos. Chem. Phys.*, *17*(2), 1511–1528, doi:10.5194/acp-17-1511-2017.

Atmos. Chem. Phys., 17, 1511–1528, 2017
www.atmos-chem-phys.net/17/1511/2017/
doi:10.5194/acp-17-1511-2017

Atmospheric Chemistry and Physics Open Access EGU

The impact of resolution on meteorological, chemical and aerosol properties in regional simulations with WRF-Chem

Paola Crippa[1], Ryan C. Sullivan[2], Abhinav Thota[3], and Sara C. Pryor[2,3]

[1]COMET, School of Civil Engineering and Geosciences, Cassie Building, Newcastle University, Newcastle upon Tyne, NE1 7RU, UK
[2]Department of Earth and Atmospheric Sciences, Bradfield Hall, 306 Tower Road, Cornell University, Ithaca, NY 14853, USA
[3]Pervasive Technology Institute, Indiana University, Bloomington, IN 47405, USA

Correspondence to: Paola Crippa (paola.crippa@ncl.ac.uk)

Received: 26 May 2016 – Published in Atmos. Chem. Phys. Discuss.: 31 May 2016
Revised: 6 January 2017 – Accepted: 11 January 2017 – Published: 31 January 2017

Abstract. Limited area (regional) models applied at high resolution over specific regions of interest are generally expected to more accurately capture the spatiotemporal variability of key meteorological and climate parameters. However, improved performance is not inevitable, and there remains a need to optimize use of numerical resources and to quantify the impact on simulation fidelity that derives from increased resolution. The application of regional models for climate forcing assessment is currently limited by the lack of studies quantifying the sensitivity to horizontal spatial resolution and the physical–dynamical–chemical schemes driving the simulations. Here we investigate model skill in simulating meteorological, chemical and aerosol properties as a function of spatial resolution, by applying the Weather Research and Forecasting model with coupled Chemistry (WRF-Chem) over eastern North America at different resolutions. Using Brier skill scores and other statistical metrics it is shown that enhanced resolution (from 60 to 12 km) improves model performance for all of the meteorological parameters and gas-phase concentrations considered, in addition to both mean and extreme aerosol optical depth (AOD) in three wavelengths in the visible relative to satellite observations, principally via increase of potential skill. Some of the enhanced model performance for AOD appears to be attributable to improved simulation of meteorological conditions and the concentration of key aerosol precursor gases (e.g., SO_2 and NH_3). Among other reasons, a dry bias in the specific humidity in the boundary layer and a substantial underestimation of total monthly precipitation in the 60 km simulations are identified as causes for the better performance of WRF-Chem simulations at 12 km.

1 Motivation and objectives

Aerosols alter Earth's radiation balance primarily by scattering or absorbing incoming solar radiation (direct effect, dominated by accumulation mode – diameters ~ wavelength (λ), where total extinction is often quantified using aerosol optical depth, or AOD), or regulating cloud formation/properties by acting as cloud condensation nuclei (CCN) (indirect effect, dominated by diameters ≥ 100 nm, magnitude $= f$, composition). Most aerosols (excluding black carbon) have a larger scattering cross section than absorption cross section and act as CCN thus enhancing cloud albedo and lifetimes. Hence increased aerosol concentrations are generally (but not uniformly) associated with surface cooling (offsetting a fraction of greenhouse gas warming) (Boucher et al., 2013; Myhre et al., 2013b) to a degree that is principally dictated by the aerosol concentration, size and composition, in addition to the underlying surface and height of the aerosol layer (McComiskey et al., 2008). Despite major advances in measurement and modeling, both the current global mean aerosol direct effect (possible range: -0.77 to $+0.23\,W\,m^{-2}$) and the indirect effect (possible range: -1.33 to $-0.06\,W\,m^{-2}$) remain uncertain (Stocker et al., 2013), as does their future role in climate forcing (Rockel et al., 2008) and regional manifestations (Myhre et al., 2013a).

Published by Copernicus Publications on behalf of the European Geosciences Union.

Specific to our current study region (eastern North America), one analysis using the NASA GISS global model found that the "regional radiative forcing from US anthropogenic aerosols elicits a strong regional climate response, cooling the central and eastern US by 0.5–1.0 °C on average during 1970–1990, with the strongest effects on maximum daytime temperatures in summer and fall. Aerosol cooling reflects comparable contributions from direct and indirect radiative effects" (Leibensperger et al., 2012). A recent comparison of multiple global models conducted under the AEROCOM-project indicated that this is also a region that exhibits very large model-to-model variability in simulated AOD ($<\mathrm{AOD}> \sim 0.5$, $\sigma(\mathrm{AOD}) \sim 1$) (Myhre et al., 2013a).

Major reasons why aerosol radiative forcing on both the global and regional scales remains uncertain include short atmospheric residence times, high spatiotemporal variability of aerosol populations, and the complexity of the processes that dictate aerosol concentrations, composition and size distributions (Seinfeld and Pandis, 2016). Although aerosol processes and properties are increasingly being treated in the global Earth system models (ESMs) (Long et al., 2015; Tilmes et al., 2015) applied in the Coupled Model Intercomparison Project Phase 6 (CMIP-6) (Meehl et al., 2014), the scales on which such models are applied remain much coarser than those on which aerosol population properties are known to vary (Anderson et al., 2003). Therefore, limited area atmospheric models (regional models) applied at higher resolution over specific regions of interest are expected to "add value" (i.e., improve the fidelity) of the physical–dynamical–chemical processes that induce extreme events and dictate climate forcing. There is empirical evidence to suggest a strong resolution dependence in simulated aerosol particle properties. For example, WRF-Chem simulations with spatial resolution enhanced from 75 to 3 km exhibited higher correlations and lower bias relative to observations of aerosol optical properties over Mexico likely due to more accurate description of emissions, meteorology and of the physicochemical processes that convert trace gases to particles (Gustafson et al., 2011; Qian et al., 2010). This improvement in the simulation of aerosol optical properties implies a reduction of the uncertainty in associated aerosol radiative forcing (Gustafson et al., 2011). Further, WRF-Chem run over the United Kingdom and northern France at multiple resolutions in the range of 40–160 km, underestimated AOD by 10–16 % and overestimated CCN by 18–36 % relative to a high resolution run at 10 km, partly as a result of scale dependence of the gas-phase chemistry and differences in the aerosol uptake of water (Weigum et al., 2016).

However, debate remains regarding how to objectively evaluate model performance, how to quantify the value added by enhanced resolution (Di Luca et al., 2015; Rockel et al., 2008) and possible limits to the improvement of climate representation in light of errors in the driving "imperfect lateral boundary conditions" (Diaconescu and Laprise, 2013). Nevertheless, although "it is unrealistic to expect a vast amount of added values since models already perform rather decently" (Di Luca et al., 2015) and global ESMs are now run at much higher resolution than in the past, it is generally assumed that high-resolution regional models will add value via more realistic representation of spatiotemporal variability than global coarser-resolution simulations. Further, "the main added value of a regional climate model is provided by its small scales and its skill to simulate extreme events, particularly for precipitation" (Diaconescu and Laprise, 2013).

It is particularly challenging to assess the added value from enhanced resolution in the context of climate-relevant aerosol properties since they are a complex product of the fidelity of the simulation of meteorological parameters, gas-phase precursors, emissions and the treatment of aerosol dynamics. Here we quantify the value added by enhanced resolution in the description of physical and chemical atmospheric conditions using year-long simulations from WRF-Chem over eastern North America, and investigate how they impact AOD. The primary performance evaluation of aerosol properties focuses on AOD at different wavelengths ($\lambda = 470$, 550 and 660 nm, where the AOD at different λ is used as a proxy of the aerosol size distribution (Tomasi et al., 1983), see details in Sect. 2.3) and is measured relative to observations from satellite-borne instrumentation. Thus the term "value added" is used here in the context of columnar aerosol properties to refer to an improvement of model performance in simulation of wavelength-specific AOD as measured by the MODerate resolution Imaging Spectroradiometer (MODIS) instrument aboard the polar-orbiting Terra satellite. To attribute sources of the enhanced fidelity of AOD, our analysis also incorporates evaluation of the value added by enhanced resolution in terms of key meteorological and gas-phase drivers of aerosol concentrations and composition and is conducted relative to the Modern-Era Retrospective analysis for Research and Applications (MERRA-2) reanalysis product for the physical variables and columnar gas concentrations from satellite observations (see details of the precise data sets used given below). The meteorological parameters considered are air temperature at 2 m ($T_{2\,\mathrm{m}}$), total monthly precipitation (PPT), planetary boundary layer height (PBLH) and specific humidity in the boundary layer (Q_{PBL}). The gas-phase concentrations considered are sulfur dioxide (SO_2), ammonia (NH_3), nitrogen dioxide (NO_2) and formaldehyde (HCHO).

We begin by quantifying the performance of WRF-Chem when applied over eastern North America at a resolution of 60 km (WRF60) ($\sim$ finest resolution likely to be employed in CMIP-6 global simulations) and then compare the results to those from simulations conducted at 12 km (WRF12) (simulation details are given in Table 1). Quantification of model skill is undertaken by mapping the WRF12 output to the WRF60 grid (WRF12-remap) and computing Brier skill scores (BSS) using MODIS as the target, WRF60 as the reference forecast and WRF12-remap as the forecast to be evaluated. We also evaluate the performance of the WRF-Chem

Table 1. Physical and chemical schemes adopted in the WRF-Chem simulations presented herein.

Simulation settings	Values
Domain size	300×300 (60×60) grid points
Horizontal resolution	12 km (60 km)
Vertical resolution	32 levels up to 50 hPa
Timestep for physics	72 s (300 s)
Timestep for chemistry	5 s
Physics option	**Adopted scheme**
Microphysics	WRF Single-Moment 5-class (Hong et al., 2004)
Longwave radiation	Rapid Radiative Transfer Model (RRTM) (Mlawer et al., 1997)
Shortwave radiation	Goddard (Fast et al., 2006)
Surface layer	Monin–Obhukov similarity (Janjić, 1994, 2002)
Land surface	Noah Land Surface Model (Chen and Dudhia, 2001)
Planetary boundary layer	Mellor–Yamada–Janjić (Janjić, 1994)
Cumulus parameterizations	Grell 3-D (Grell and Dévényi, 2002)
Chemistry option	**Adopted scheme**
Photolysis	Fast J (Wild et al., 2000)
Gas-phase chemistry	RADM2 (Stockwell et al., 1990)
Aerosols	MADE/SORGAM (Ackermann et al., 1998; Schell et al., 2001)
Anthropogenic emissions	NEI (2005) (US-EPA, 2009)
Biogenic emissions	Guenther, from USGS land use classification (Guenther et al., 1993, 1994; Simpson et al., 1995)

simulations of 2008 relative to climatology as represented by MODIS observations for 2000–2014. We additionally assess the impact of simulation resolution on extreme AOD values that are associated with enhanced impacts on climate and human health. This analysis uses both accuracy and hit rate (HR) as the performance metrics and focuses on the co-occurrence of extreme values in space from the model output and MODIS.

Based on the performance evaluation of the WRF-Chem simulations that indicate substantial dry bias in the WRF60 simulations and large seasonality in the skill scores for AOD as a function of resolution, we conducted two further year-long simulations at 60 km. In the first we held all other simulation conditions constant but selected a different cumulus parameterization. In the second, we held all simulation conditions constant but employed a different set of lateral boundary conditions for the meteorology. In the context of the precipitation biases reported herein it is worthy of note that discrepancies in simulated precipitation regimes are key challenges in regional modeling (both physical and coupled with chemistry). Although the Grell 3-D scheme has been successfully applied in a number of prior analysis wherein the model was applied at resolutions in the range of 1–36 km (e.g., Grell and Dévényi, 2002; Lowrey and Yang, 2008; Nasrollahi et al., 2012; Sun et al., 2014; Zhang et al., 2016), the North American Regional Climate Change Assessment Program (NARCCAP) simulations with WRF at 50 km were also dry biased in the study domain (Mearns et al., 2012). Although there have been a number of studies that have sought to evaluate different cumulus schemes over different regions at different resolutions, no definitive recommendation has been made regarding the dependence of model skill on resolution and cumulus parameterization (Arakawa, 2004; Jankov et al., 2005; Nasrollahi et al., 2012; Li et al., 2014). Hence, further research is needed to identify the optimal cumulus scheme for use over North America at coarser resolution. Thus, we performed a sensitivity analysis on the cumulus scheme at 60 km by applying the Grell–Freitas parameterization (Grell and Freitas, 2014), which is the next generation of the Grell 3-D scheme.

2 Materials and methods

2.1 WRF-Chem simulations

WRF-Chem (version 3.6.1) simulations were performed for the calendar year 2008 over eastern North America, in a domain centered over southern Indiana (86° W, 39° N) at two resolutions, one close to the finest resolution designed for CMIP-6 global model runs (i.e., 60 km, WRF60) and the other one at much higher resolution (12 km, WRF12). Simulation settings are identical for the two runs except for the time step used for the physics (Table 1). Physical and chemical parameterizations were chosen to match previous work using WRF-Chem at 12 km on the same region, which showed good performance relative to observations,

and the year 2008 was selected because it is representative of average climate and aerosol conditions during 2000–2014 (Crippa et al., 2016). More specifically the simulations adopted the RADM2 chemical mechanism (Stockwell et al., 1990) and a modal representation of the aerosol size distribution (MADE/SORGAM, Ackermann et al., 1998; Schell et al., 2001) with three lognormal modes and fixed geometric standard deviations (i.e., 1.7, 2 and 2.5 for Aitken, accumulation and coarse mode, respectively; Ackermann et al., 1998; Grell et al., 2005). Aerosol direct feedback was turned on and coupled to the Goddard shortwave scheme (Fast et al., 2006). A telescoping vertical grid with 32 model layers from the surface to 50 hPa and 10 layers up to 800 hPa was selected. Meteorological initial and boundary conditions from the North American Mesoscale Model at 12 km resolution (NAM12) are applied every 6 h, while initial and chemical boundary conditions are taken from MOZART-4 (Model for Ozone and Related chemical Tracers, version 4) with meteorology from NCEP/NCAR reanalysis (Emmons et al., 2010). Anthropogenic emissions are specified for both WRF60 and WRF12 from the US National Emission Inventory 2005 (NEI-05) (US-EPA, 2009) which provides hourly point and area emissions at 4 km on 19 vertical levels. The simulation settings and specifically the use of a modal representation of the aerosol size distribution were selected to retain computational tractability. Accordingly, the 60 km simulations for the year 2008 completed in 6.4 h whereas the 12 km simulations completed in 9.5 days (230 h) on the Cray XE6/XK7 supercomputer (Big Red II) owned by Indiana University, using 256 processors distributed on eight nodes.

As described in detail below, in the WRF60 simulations configured as described in Table 1, simulated precipitation during the summer months exhibits substantial dry bias, and the analysis of value added by enhanced simulation resolution exhibited strong seasonality. We performed a sensitivity analysis to the cumulus scheme, by conducting an additional year-long simulation at 60 km using the Grell–Freitas parameterization (Grell and Freitas, 2014), which is an evolution of Grell 3-D that is scale-aware and treats some aspects of aerosol-cloud interactions. We also tested the sensitivity of the simulation results to the meteorological boundary conditions, by repeating the WRF60 simulations using output from the Global Forecast System (GFS) at 0.5° resolution every 6 h to provide the lateral boundary conditions.

2.2 Observations

Model aerosol optical properties are evaluated relative to the MODIS Collection 6 dark-target land aerosol product from aboard the Terra satellite (~1030 overpass local solar time, LST) (Levy et al., 2013). To provide a consistent assessment of model skill, the evaluation of AOD is conducted only on land areas since the MODIS dark-target ocean aerosol product is based on a retrieval algorithm different from the one over land (Levy et al., 2013). Trace gas concentrations are evaluated relative to measurements from the Ozone Monitoring Instrument (OMI; version 3) (Chance, 2002) and the Infrared Atmospheric Sounding Interferometer (IASI; NN version 1) (Whitburn et al., 2016) aboard the Aura (~13:45 LST) and MetOp satellites (~09:30 LST), respectively. MODIS retrieves AOD at multiple λ including 470, 550 and 660 nm, and the MODIS algorithm removes cloud-contaminated pixels prior to spatial averaging over 10×10 km (at nadir). OMI and IASI have nadir resolutions of 13×24 and 12 km (circular footprint), respectively, and have been filtered to remove retrievals with cloud fractions > 0.3 (Fioletov et al., 2011; McLinden et al., 2014; Vinken et al., 2014) and OMI pixels affected by the row anomalies. MODIS, OMI and IASI provide near daily global coverage, although the row anomalies render portions of the OMI viewing swath unusable. Uncertainty in AOD from MODIS is spatially and temporally variable. It has been estimated as $\pm$ (0.05 + 15 %) for AOD over land (Levy et al., 2013), and prior research has reported 71 % of MODIS Collection 5 retrievals fall within 0.05 ± 20 % for AOD relative to AERONET in the study domain (Hyer et al., 2011). The accuracy of OMI ("root sum of the square of all errors, including forward model, inverse model and instrument errors"; Brinksma et al., 2003) is 1.1 DU or 50 % for SO_2, 2×10^{14} cm^{-2}/30 % for background/polluted NO_2 conditions and 35 % for HCHO. This uncertainty is typically reduced by spatial and temporal averaging, as employed herein (Fioletov et al., 2011; Krotkov et al., 2008). IASI NH_3 retrievals do not use an a priori assumption of emissions, vertical distribution, or lifetime of NH_3 (i.e., no averaging kernel); therefore, NH_3 accuracy is variable (Whitburn et al., 2016), and thus only retrievals with uncertainty lower than the retrieved concentrations are used herein.

For the model evaluation, satellite observations for each day are regridded to the WRF-Chem discretization. This is done by averaging all valid retrievals within 0.1 and 0.35° of the WRF-Chem grid-cell center for the 12×12 km and 60×60 km resolutions, respectively, for MODIS; $0.125° \times 0.18°$ (along-track/latitudinal $\times$ cross-track/longitudinal) and $0.365° \times 0.42°$ for OMI; 0.12 and 0.36° for IASI. To avoid issues from undersampling, we require at least 10 valid MODIS granules for the 60×60 km daily average to be computed and at least five daily averages to compute a monthly average for each grid cell. Model evaluation of gaseous species is performed on a seasonal basis using standard scores (z scores), which are computed as the difference between the seasonal mean within a grid cell and the seasonal spatial mean, divided by the seasonal spatial standard deviation. Use of z scores allows comparison of the spatial patterns of satellite observations and model output in terms of standard deviation units from the mean.

The simulated meteorological properties are evaluated using MERRA-2 reanalysis data as the target. MERRA-2 is a homogenized and continuous in time description of atmospheric properties on a 3-D global grid (horizontal resolu-

tion of 0.5° × 0.625°, L72), developed by NASA and was released in fall 2015 (Molod et al., 2015). MERRA-2 provides hourly values of $T_{2\,\mathrm{m}}$ and PBLH, as well as vertical profile of 3-D variables every 3 h on a large number of pressure levels. Here we compute the total specific humidity (Q_{PBL}) of the lowest eight pressure levels (i.e., in the boundary layer approximated as the layer from 1000 to 825 hPa) in MERRA-2, assuming an average air density in the PBL of 1.1 kg m^{-3}. For the evaluation of simulated precipitation we use accumulated monthly total values.

2.3 Spectral dependence of AOD

Three properties dictate the actual aerosol direct radiative forcing: AOD, single scattering albedo and asymmetry factor, all of which are a function of the wavelength (λ) of incident radiation. The first property is related to the total columnar mass loading, typically dominates the variability of direct aerosol effect (Chin et al., 2009) and is the focus of the current research. The relationship between the aerosol size distribution and spectral dependence of AOD is described by a power law function:

$$\beta(\lambda_1) = \beta(\lambda_2) \times \left(\frac{\lambda_1}{\lambda_2}\right)^{-\alpha}, \quad (1)$$

where β is the particle extinction coefficient at a specific wavelength λ and α is the Ångström exponent (Ångström, 1964), which describes the wavelength dependence of AOD (and is inversely proportional to the average aerosol diameter):

$$\alpha = \frac{\ln \frac{\mathrm{AOD}(\lambda_1)}{\mathrm{AOD}(\lambda_2)}}{\ln \frac{\lambda_2}{\lambda_1}}. \quad (2)$$

The aerosol volume distribution usually conforms to a multilognormal function with n modes:

$$\frac{\mathrm{d}V(r)}{d\ln r} = \sum_{i=1}^{n} \frac{C_i}{\sqrt{2\pi}\sigma_i} \exp\left[\frac{-(\ln r - \ln R_i)^2}{2\sigma_i^2}\right], \quad (3)$$

where r is the particle radius and C_i, R_i and σ_i are the particle volume concentration, the geometric mean radius and the standard deviation in the mode i, respectively.

We can thus compute AOD for a polydisperse distribution of aerosols with refractive index m in an atmospheric column of height Z as

$$\mathrm{AOD}(\lambda) = \int \frac{3\beta(m, r, \lambda)}{4r} \frac{dV(r)}{\mathrm{d}\ln r} \mathrm{d}\ln r \mathrm{d}Z. \quad (4)$$

As indicated in Schuster et al. (2006), "the spectral variability of extinction diminishes for particles larger than the incident wavelength"; thus fine mode particles contribute more to AOD in the visible ($\lambda \sim 0.5\,\mu\mathrm{m}$) than at longer wavelengths, whereas coarse mode particles provide a similar AOD both at short and long wavelengths. This is reflected in the Ångström parameter which can be thus used as a proxy for the fine mode fraction or fine mode radius (Schuster et al., 2006).

2.4 Quantification of model performance and added value

Taylor diagrams summarize three aspects of model performance relative to a reference: the spatial correlation coefficient (i.e., Pearson correlation of the fields, r), the ratio of spatial standard deviations of the two spatial fields ($\sigma_{\mathrm{wrf}}/\sigma_{\mathrm{sat}}$) and the root mean squared difference (RMSD) (Taylor, 2001). Here Taylor diagrams are presented for monthly mean AOD from WRF60, WRF12 and WRF12-remap relative to MODIS at different wavelengths (Fig. 1d–f). Because AOD is not normally distributed, Spearman's rank correlation coefficients (ρ) of the mean monthly AOD spatial fields are also computed to reduce the impact of a few outliers and the small sample size during cold months (Table 2). To assess the significance of ρ while accounting for multiple testing, we apply a Bonferroni correction (Simes, 1986), in which for m hypothesis tests the null hypothesis is rejected if $p \leq \frac{\alpha}{m}$, where p is the p value and α is the confidence level (0.05 is used here).

We further quantify the value added (or lack of thereof) of the high-resolution simulations using the following metrics:

i. Brier skill score

   Value added is quantified using BSS and is evaluated in two ways: first by evaluating the model performance as a function of simulation resolution and then using climatology as the reference "forecast". In these analyses the hourly output from the 12 km resolution simulation is degraded (averaged) to 60 km (hereafter WRF12-remap) as follows: the 12 km domain is resized excluding 2 grid cells at the border to exactly match the 60 km resolution domain. For example, in the analysis of AOD each coarse grid cell thus includes 5 × 5 12 km resolution cells and its value is the mean of all valid 12 km grid cells inside it if at least half of those cells contain valid AOD (i.e., no cloud cover), otherwise the whole coarse cell is treated as missing. In all comparisons of AOD only cells with simultaneous (i.e., model and MODIS) clear sky conditions are considered. A daily value from WRF-Chem is computed as an instantaneous value for the hour nearest to the satellite overpass time. When the comparison is done on a monthly basis, a monthly mean value is computed from the daily values obtained under clear sky conditions, only if there are at least five valid observations in the month.

   The primary metric used to quantify the added value of WRF12-remap versus WRF60 is the BSS (Murphy and Epstein, 1989):

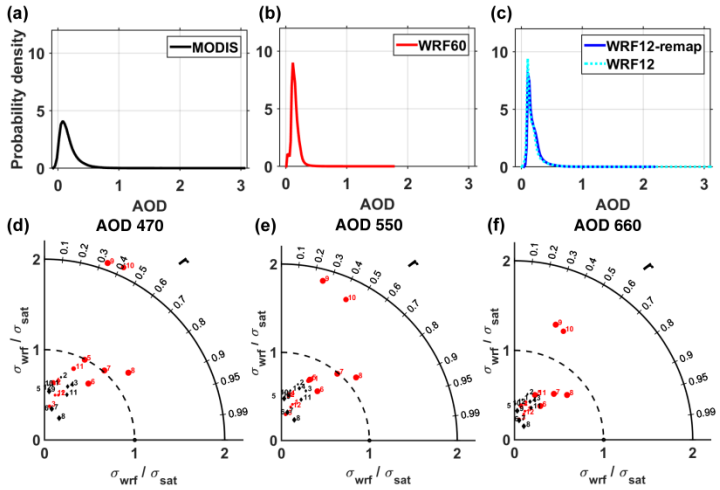

Figure 1. Probability density function of once daily AOD at a wavelength (λ) of 550 nm for **(a)** MODIS, **(b)** WRF60 and **(c)** WRF12 and WRF12-remap during the year 2008. **(d–f)** Taylor diagrams of mean monthly AOD at wavelengths (λ) of **(d)** 470, **(e)** 550 and **(f)** 660 nm as simulated by WRF-Chem at different resolutions (black diamonds = WRF60 and red dots = WRF12-remap) relative to MODIS observations. The numbers by each symbol denote the calendar month (e.g., 1 = January).

Table 2. Spearman correlation coefficients (ρ) between AOD at wavelengths (λ) of 470, 550 and 660 nm from MODIS observations averaged over 12 or 60 km and WRF-Chem simulations conducted at 60 km (WRF60, shown in the table as -60), at 12 km (WRF12, shown in the table as -12), and from WRF-Chem simulations at 12 km but remapped to 60 km (WRF12-remap, shown in the table as remap). Given WRF12-remap is obtained by averaging WRF12 when at least half of the 5×5 12 km resolution cells contain valid data, ρ from WRF60 and WRF12-remap may be computed on slightly different observations and sample size. The bold text denotes correlation coefficients that are significant at $\alpha = 0.05$ after a Bonferroni correction is applied (i.e., $p \leq \frac{0.05}{9 \times 12} = 4.63 \times 10^{-4}$ is significant). The italic typeface is a visual guide that shows for each month and λ the model output that has highest ρ with MODIS.

Month→ / Variable↓	Jan	Feb	Mar	Apr	May	Jun	Jul	Aug	Sep	Oct	Nov	Dec
470–12	**0.238**	**0.150**	**0.137**	**0.147**	**0.377**	**0.581**	**0.610**	**0.723**	**0.352**	**0.306**	**0.259**	**0.212**
470–60	0.156	***0.226***	***0.438***	***0.412***	**−0.219**	**−0.146**	**0.379**	**0.601**	0.087	−0.051	***0.500***	−0.059
470–remap	***0.295***	**0.197**	**0.250**	**0.182**	***0.516***	***0.637***	***0.675***	***0.777***	***0.368***	***0.441***	**0.315**	***0.274***
550–12	**0.223**	**0.124**	**0.142**	**0.146**	**0.349**	**0.541**	**0.580**	**0.689**	**0.275**	**0.301**	**0.280**	**0.215**
550–60	**0.179**	***0.244***	***0.429***	***0.332***	**−0.288**	**−0.188**	**0.324**	0.567	0.073	−0.077	***0.491***	0.002
550–remap	***0.297***	0.164	**0.261**	**0.199**	***0.493***	***0.605***	***0.651***	***0.747***	***0.286***	***0.437***	**0.352**	***0.309***
660–12	**0.217**	**0.136**	**0.165**	**0.152**	**0.324**	**0.476**	**0.540**	**0.644**	**0.183**	**0.290**	**0.292**	**0.221**
660–60	**0.191**	***0.230***	***0.437***	***0.402***	**−0.305**	**−0.189**	**0.389**	**0.616**	0.099	**−0.137**	***0.536***	0.049
660–remap	***0.356***	**0.211**	**0.289**	**0.208**	***0.480***	***0.624***	***0.669***	***0.772***	***0.371***	***0.432***	**0.393**	***0.368***

$$\mathrm{BSS} = \frac{r_{F'P'}^2 - \left(r_{F'P'} - \frac{\sigma_{F'}}{\sigma_{P'}}\right)^2 - \left(\frac{\langle P' \rangle - \langle F' \rangle}{\sigma_{P'}}\right)^2 + \left(\frac{\langle P' \rangle}{\sigma_{P'}}\right)^2}{1 + \left(\frac{\langle P' \rangle}{\sigma_{P'}}\right)^2}, \quad (5)$$

where F is the "forecast" (i.e., the 12 km simulations mapped to 60 km, WRF12-remap), P is the "target" (i.e., for AOD this is MODIS at 60 km) and output from WRF60 is used as the reference forecast, F' the difference between 12 km estimates regridded to 60 km and MODIS, and P' the difference between the 60 km simulation and the "target" (i.e., for the AOD MODIS observations regridded to 60 km). In the analysis of BSS relative to the long-term (15-year) climatology of AOD from MODIS, the monthly mean climatological value of AOD is used as the reference forecast, while

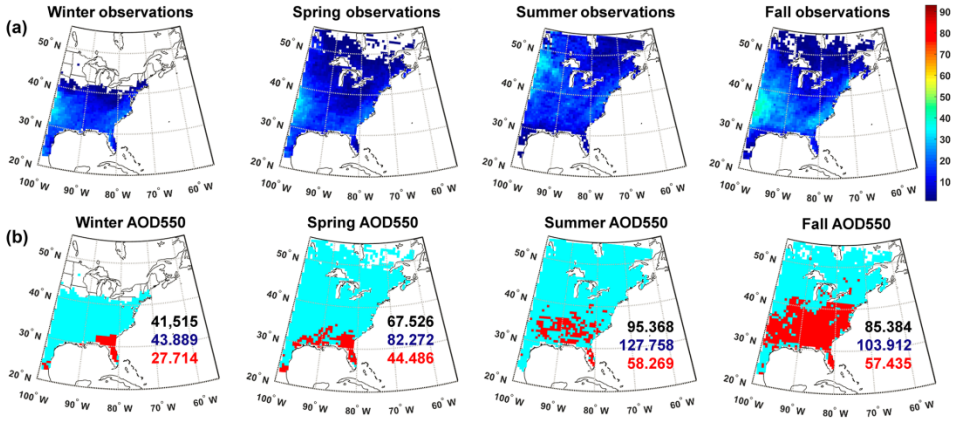

Figure 2. First line: number of paired AOD observations at a wavelength (λ) of 550 nm (i.e., simultaneous values as output from WRF-Chem and observed by MODIS) used to perform a t test designed to evaluate whether the difference computed for each grid cell as WRF60-MODIS differs from that computed as WRF12-remap-MODIS on a seasonal basis (columns show winter, DJF, spring, MAM, summer, JJA, and fall, SON). Second line: results of the t test. Pixels that have p values that are significantly different at $\alpha = 0.10$ are indicated in red and have been corrected for multiple testing using a false discovery rate approach. The number of observations of cloud-free conditions summed across all days in each season and all grid cells is also reported (black = MODIS, blue = WRF60, red = WRF12-remap).

WRF60 and WRF12-remap are used as the forecasts, and monthly mean AOD from MODIS at 60 km is the target.

BSS measures by how much a test simulation (WRF12-remap) more closely (or poorly) reproduces observations (from MODIS, MERRA-2 or other satellite products) relative to a control (WRF60) run. For example, a BSS > 0 indicates that WRF12, even when regridded to 60 km, does add value. The first term in Eq. (5) ranges from 0 to 1, is described as the potential skill and is the square of the spatial correlation coefficient between forecast and reference anomalies to MODIS. It is the skill score achievable if both the conditional bias (second term) and overall bias (third term) were zero, and for most of the variables considered herein (particularly AOD) it contributes to a positive BSS in most calendar months (and seasons). The second term (the conditional bias, > 0) is the square of the difference between the anomaly correlation coefficient and the ratio of standard deviation of the anomalies and is small when, for all points, F' is linear to P'. The third term is referred to as the forecast anomaly bias and is the ratio of the difference between the mean anomalies of WRF12-remap and the observations relative to WRF60 and the standard deviation of WRF60 anomaly relative to observed values. The fourth term is the degree of agreement and appears in both the numerator and denominator. It is computed as the square of the ratio of the mean anomaly between WRF60 and observations and the standard deviation of the anomalies.

ii. Pooled paired t test

To identify which areas in space contribute most to the AOD added value, we compare daily mean AOD fields from WRF-Chem at different resolutions and MODIS. We perform a pooled paired t test to evaluate the null hypothesis that those differences come from normal distributions with equal means and equal but unknown variances (the test statistic has a Student's t distribution with $df = n + m - 2$, and the sample standard deviation is the pooled standard deviation, where n and m are the two sample sizes). The test is conducted by climatological season (e.g., winter = DJF) since there are fewer than 20 valid AOD observations in most 60 km grid cells for each calendar month (Fig. 2). Given the large number of hypothesis tests performed (i.e., one for each 60 km grid cell), we adjust the p values using the false discovery rate (FDR) approach (Benjamini and Hochberg, 1995). In this approach, p values from the t tests are ranked from low to high ($p_1, p_2, \ldots, p_m$), then the test with the highest rank, j, satisfying

$$p_j \leq \frac{j}{m}\alpha \tag{6}$$

is identified. Here all p values satisfying Eq. (6) with $\alpha = 0.1$ are considered significant.

iii. Accuracy and HR in identification of AOD extremes

For each month we identify grid cells in which the wavelength-specific AOD exceeds the 75th percentile value computed from all grid cells and define that as an extreme. Thus grid cells with extreme AOD are independently determined for MODIS and WRF-Chem at different resolutions. The spatial coherence in identification of extremes in the fields is quantified using two metrics: the accuracy and the HR. The accuracy indicates the overall spatial coherence and is computed as the number of grid cells co-identified as extreme and non-extreme between WRF-Chem and MODIS relative to the total number of cells with valid data. The HR weights only correct identification of extremes in MODIS by WRF-Chem.

3 Results

3.1 Model performance as a function of spatial resolution

When WRF-Chem is applied at 60 km resolution the degree of association of the resulting spatial fields of mean monthly AOD at the three wavelengths with MODIS varies seasonally. Smallest RMSD and highest Spearman spatial correlations (ρ) with MODIS observations generally occur during months with highest mean AOD (i.e., during summer, Figs. 1d–f and 3) and reach a maximum in August ($\rho = 0.60$, Table 2). However, while the patterns of relative AOD variability are well captured, the absolute magnitudes and spatial gradients of AOD during the summer are underestimated by WRF60 (Figs. 1d–f and 3, Table S1 in the Supplement). High spatial correlations ($\rho > 0.40$) are also observed in March, April and November (Table 2), when the ratio of spatial standard deviations is closer to 1 (Fig. 1d–f, Table S1). Only a weak wavelength dependence is observed in the performance metrics as described on Taylor diagrams. The spatial variability is generally more negatively biased for AOD at 660 nm (Table S1), indicating that WRF60 simulations tend to produce larger diameter aerosols homogeneously distributed over the domain, whereas MODIS observations indicate more spatial variability.

The performance of WRF60 simulations relative to MODIS contrasts with analyses of WRF12 and WRF12-remap. WRF12 and WRF12-remap indicate highest spatial correlations with MODIS observations throughout the summer months ($\rho = 0.5$–0.7, Table 2), although the bias towards simulation of more coarse aerosols than are observed is consistent across the two simulations and with prior research (see details provided in Crippa et al., 2016). However, simulations at 12 km (WRF12) show positive ρ with MODIS for all λ in all calendar months, while mean monthly spatial fields of AOD from WRF60 show low and/or negative correlations with MODIS during May, June, September, October and December, indicating substantial differences in the degree of correspondence with MODIS AOD in the two simulations and higher fidelity of the enhanced resolution runs (Tables 2 and S1).

Monthly mean spatial fields of AOD(λ) as simulated by WRF12 or WRF12-remap exhibit positive Spearman correlation coefficients (ρ) with MODIS observations for all calendar months and range from ~ 0.25 for WRF12-remap (0.20 for WRF12) during winter to ~ 0.70 and 0.64, respectively, during summer (Table 2). Spearman's ρ is uniformly higher in WRF12-remap than WRF12 indicating a mismatch in space in the high-resolution simulation (i.e., that grid cells with high AOD are slightly displaced in the 12 km simulations possibly due to the presence of sub-grid scale aerosol plumes; Rissman et al., 2013). Mean monthly fields of AOD (all λ) from both WRF12 and WRF12-remap exhibit lower ρ with MODIS in February–April and November than the 60 km runs (Table 2). These discrepancies appear to be driven by conditions in the south of the domain. For example, differences between WRF60/WRF12-remap and MODIS during all seasons are significant according to the paired t test over Florida and along most of the southern coastlines (Fig. 2). This region of significant differences extends up to $\sim 40^\circ$ N during summer and fall, reflecting the stronger north–south gradient in AOD from MODIS and WRF12-remap that is not captured by WRF60 (see example for $\lambda = 550$ nm, Fig. 3). These enhancements in the latitudinal gradients from WRF12-remap are also manifest in the physical variables (particularly specific humidity as discussed further below).

The differences in the absolute values of mean monthly AOD deriving from differences in the resolution at which WRF-Chem was applied are of sufficient magnitude (a difference of up to 0.2 in regions with a mean AOD value of 0.4), particularly in the summer months (Fig. 4), to raise concerns. However, detailed investigation of the simulations settings and repetition of the 60 km simulation resulted in virtually identical results, indicating no fault can be found in the analysis. Further, we note that the eastern half of North America was also identified as a region of high discrepancy in global ESM (Myhre et al., 2013a).

To further investigate differences in the simulation output due to spatial discretization we computed BSS. In this analysis AOD for each λ from WRF12-remap is used as the "forecast", output from WRF60 is used as the reference forecast and MODIS observations at 60 km are used as the target. BSS exceed 0 during all months except for September and October, and largest BSS (> 0.5) for AOD (all λ) is found during most months between December and July (Fig. 5a–c). This indicates that running WRF-Chem at 12 km resolution yields higher skill in simulated AOD relative to WRF60, even when the WRF12 output is remapped to 60 km. BSS do not strongly depend on λ, indicating that the added value from enhanced resolution similarly affects aerosol particles of different sizes. Inspecting the terms defining the BSS provides information about the origin of the added value (Fig. 5a–

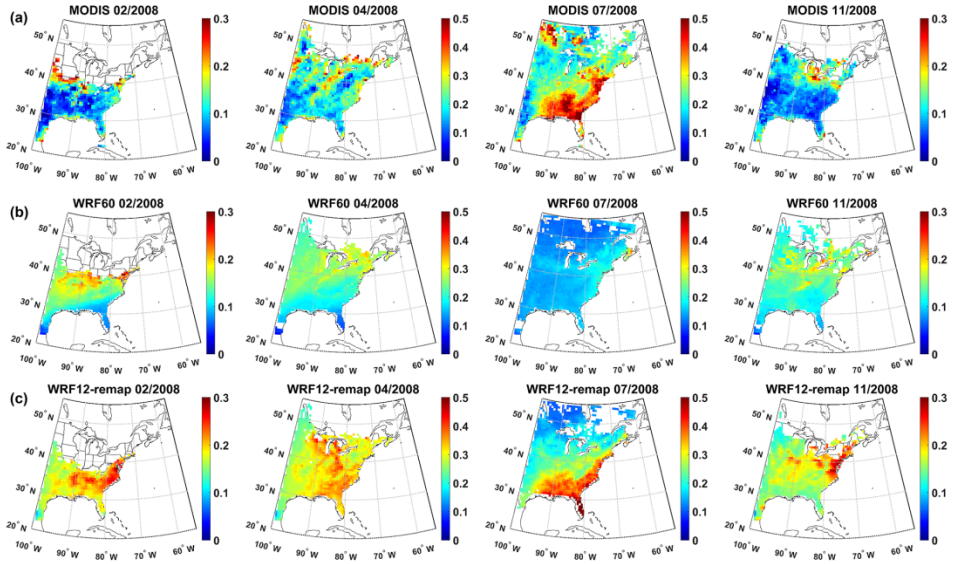

Figure 3. Monthly mean AOD at a wavelength (λ) of 550 nm from MODIS (first line) and WRF-Chem at different resolutions (WRF60 and WRF12-remap, second and third line) during a representative month in each climatological season (columns). Note that a different color scale is applied for different months. For a monthly mean value for a grid cell to be shown, there must be at least five simultaneous daily values (for the time of the satellite overpass) available.

c). The positive BSS derives principally from the potential skill (first term in Eq. 5), which demonstrates a reduction in bias and/or more accurate representation of the spatial gradients in WRF12-remap. This term exhibits weak seasonality with values below 0.5 only during August and fall months. The second and third terms are close to zero during most months, although bigger biases are found during August–October. The substantial conditional bias during late summer and early fall is the result of the large ratio of standard deviations (> 1, i.e., the spatial variability of the anomaly relative to MODIS is larger for WRF12-remap than WRF60; Table S1). It thus contributes to the negative BSS found in September and October, which are also identified as outlier months in WRF12-remap from the Taylor diagram analysis (Fig. 1). Output for these months show modest spatial correlations with AOD from MODIS and higher ratio of standard deviations than in WRF60-MODIS comparisons (Fig. 1, Table S1). Previous work showed that the lower model skill (in WRF12) during September and October may be partially attributable to a dry bias in precipitation from WRF-Chem relative to observations. As a result, simulated AOD and near-surface aerosol nitrate and sulfate concentrations are positively biased over large parts of the domain (Crippa et al., 2016). Although the effects of the boundary conditions appear in some variables (e.g., in Figs. 4 and S1–S3 in the Supplement), the BSS results do not significantly change even when those cells are removed from the analysis.

When the BSS is used to assess the skill of each model relative to MODIS AOD climatological mean over the years 2000–2014, WRF12-remap is found to add value relative to the climatology (i.e., BSS > 0) during summer months and November–January whereas BSS for WRF60 is positive from late fall to early spring (Fig. 5d). The fact that WRF-Chem does not always outperform the climatology is expected since the model is based on time-invariant emissions and skill is assessed relative to a year selected to be representative of the AOD climatology. Mean seasonal AOD from MODIS retrievals over the study region during 2008 lie within ± 0.2 standard deviations of the climatology (Crippa et al., 2016). Interestingly, BSS for most months (excluding September) are higher for the WRF60 simulations conducted using lateral boundary conditions from NAM12 than GFS.

Model resolution also affects the accuracy and HR for identification of areas of extreme AOD (AOD > 75th percentile). Highest coherence in the identification of extreme AOD in space identified in WRF12-remap (and WRF12) relative to MODIS is found during May–August (HR = 53–77 %) vs. WRF60 (HR = 17–54 %; Table 3). Conversely highest HR are found for WRF60 and MODIS during winter and early spring and indeed exceed those for WRF12 and WRF12-remap (Table 3, e.g., February: HR = 0.78 for

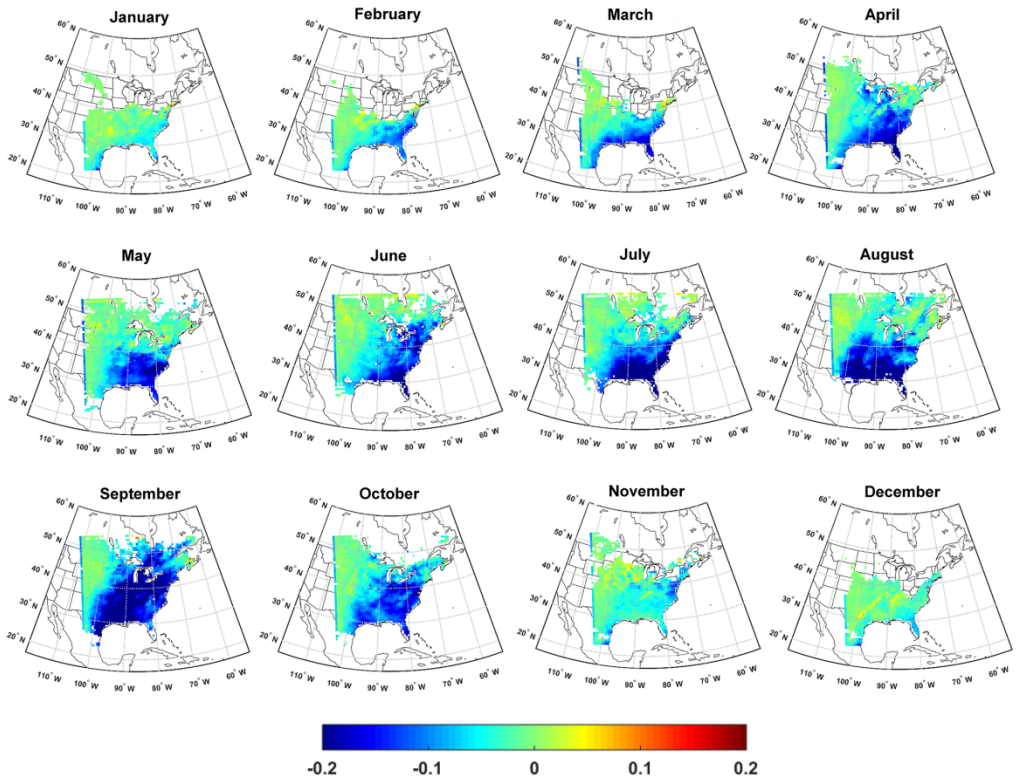

Figure 4. Difference in monthly mean AOD at a wavelength (λ) of 550 nm between WRF-Chem simulations conducted at 60 km resolution (WRF60) and output from WRF-Chem simulations conducted with a resolution of 12 km but remapped to 60 km (WRF12-remap). Differences are computed as WRF60 minus WRF12-remap. Similar spatial patterns and magnitudes of differences are found for λ of 470 and 660 nm. The calendar months of 2008 are shown in the titles of each panel.

Table 3. Spatial coherence in the identification of extreme AOD values (i.e., areas with AOD > 75th percentile over space for each month) between WRF-Chem at different resolutions relative to MODIS. No significant wavelength dependence is found for model skill in identifying extreme AOD so results are only shown for $\lambda = 550$ nm. The different model output is denoted by 60 for simulations at 60 km, 12 for simulations at 12 km resolution and as remap for simulations at 12 km but with the output remapped to 60 km. The accuracy (Acc) indicates the fraction of grid cells co-identified as extremes and non-extremes between WRF-Chem and MODIS relative to the total number of cells with valid data. The Hit Rate (HR) is the probability of correct forecast and is the proportion of cells correctly identified as extremes by both WRF-Chem and MODIS. The italic typeface indicates the model resolution with highest skill in each month for AOD at 550 nm.

Month→ / Metric↓	Jan	Feb	Mar	Apr	May	Jun	Jul	Aug	Sep	Oct	Nov	Dec
Acc-12	0.673	0.665	0.659	0.638	0.710	0.800	0.855	*0.839*	0.666	0.679	0.723	0.661
Acc-60	*0.707*	*0.778*	*0.735*	*0.730*	0.600	0.587	0.658	0.769	0.661	0.637	0.729	*0.681*
Acc-remap	0.674	0.680	0.694	0.640	*0.766*	*0.824*	*0.887*	0.837	*0.667*	*0.699*	*0.767*	0.641
HR-12	0.346	0.331	0.319	0.275	0.421	0.599	0.711	*0.678*	0.333	0.358	0.447	0.323
HR-60	*0.417*	*0.558*	*0.471*	*0.460*	0.200	0.173	0.315	0.538	0.321	0.274	0.458	*0.364*
HR-remap	0.350	0.361	0.387	0.281	*0.532*	*0.649*	*0.775*	0.674	*0.333*	*0.399*	*0.535*	0.284

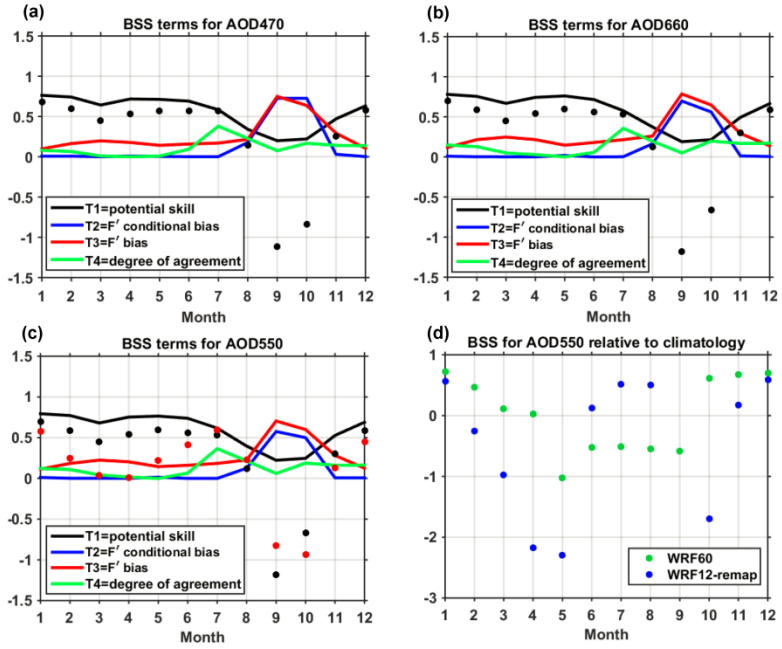

Figure 5. (a–c) Brier skill scores (BSS, black dots) for monthly mean AOD by calendar month (1 = January) for AOD at 470, 550 and 660 nm. In this analysis of model skill WRF12 output is mapped to the WRF60 grid (WRF12-remap) and BSS are computed using MODIS as the target, WRF60 (driven by NAM12 meteorological boundary conditions) as the reference forecast and WRF12-remap as the forecast. Also shown by the color lines are the contributions of different terms to BSS. In panel **(c)** the red dots indicate BSS when the reference forecast is WRF60 driven by GFS meteorological boundary conditions. **(d)** BSS of monthly mean AOD from WRF60 (green dots) and WRF12-remap (blue dots) relative to MODIS monthly mean climatology during 2000–2014 (reference forecast). Monthly mean AOD from MODIS are used as the target. BSS for WRF12-remap in September is −6.1.

WRF60, and 0.67 and 0.68 for WRF12 and WRF12-remap, respectively). These differences are consistent with the observation that WRF12-remap overestimates the scales of AOD coherence and AOD magnitude during the cold season along coastlines and over much of the domain in April (Fig. 3).

The synthesis of these analyses is thus that the higher-resolution simulation increases the overall spatial correlation and decreases overall bias in AOD close to the peak of the solar spectrum relative to MODIS observations, and therefore the higher-resolution simulations better represent aerosol direct climate forcing. However, WRF12-remap exhibits little improvement over WRF60 in terms of reproducing the spatial variability of AOD in the visible wavelengths and further that WRF12-remap tends to be more strongly positively biased in terms of mean monthly AOD outside of the summer months (Figs. 2 and 3). Also the improvement in detection of areas of extreme AOD in the higher-resolution simulations (WRF12-remap) is manifest only during the warm season.

3.2 Investigating sources of error in simulated AOD

As documented above, WRF-Chem applied at either 60 or 12 km resolution over eastern North America exhibits some skill in reproducing observed spatial fields of AOD and the occurrence of extreme AOD values. However, marked discrepancies both in space and time are found, and at least some of them show a significant dependence on model resolution. Thus, we investigated a range of physical conditions and gas-phase concentrations known to be strongly determinant of aerosol dynamics in terms of the BSS as a function of model resolution and also in terms of the mean monthly spatial patterns.

WRF12 even when remapped to 60 km provides more accurate description of key meteorological variables such as specific humidity (Q) within the boundary layer, PBLH, surface temperature and precipitation (see Figs. 6, S1, S2 and S3) when compared to MERRA-2, as indicated by the positive BSS during almost all months (Fig. 7a). Good qualitative agreement is observed for the spatial patterns and abso-

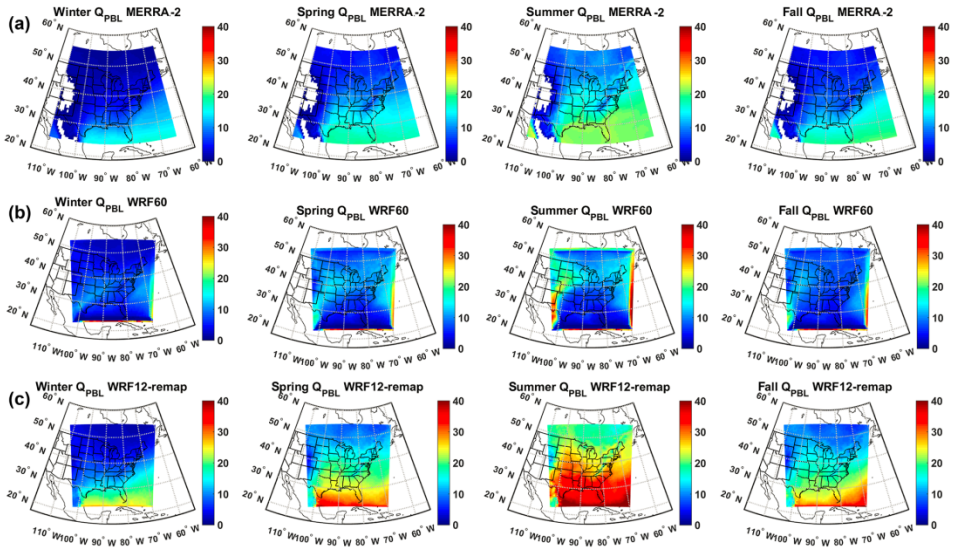

Figure 6. Seasonal mean specific humidity (kg m^{-2}) integrated from the surface to 825 hPa (Q_{PBL}) from MERRA-2 (first row) assuming an average air density in the PBL of 1.1 kg m^{-3}, WRF60 (second row) and WRF12-remap (third row). The data are 3-hourly and show only cloud-free hours in all three data sets.

lute magnitude of $T_{2\,m}$ in both WRF60 and WRF12-remap relative to MERRA-2 for all seasons (Fig. S1), leading to only modest magnitude of BSS (i.e., value added by the higher-resolution simulations; Fig. 7a). The aerosol size distribution and therefore wavelength-specific AOD exhibits a strong sensitivity to Q (Santarpia et al., 2005) due to the presence of hygroscopic components in atmospheric aerosols and thus the role of water uptake in determining aerosol diameter, refractivity and extinction coefficient (Zieger et al., 2013). For example, the hygroscopic growth factor, which indicates the change of aerosol diameter due to water uptake, is ~ 1.4 for pure ammonium sulfate with dry diameter of 532 nm at relative humidity of 80 %; thus biases in representation atmospheric humidity may lead to big errors in simulated aerosol size and AOD (Flores et al., 2012). Our previous analyses of the 12 km resolution simulations indicated overestimation of sulfate aerosols (a highly hygroscopic aerosol component, and one which in many chemical forms exhibits strong hysteresis; Martin et al., 2004) relative to observed near-surface $PM_{2.5}$ concentrations during all seasons except for winter (Crippa et al., 2016), leading to the hypothesis that simulated AOD and discrepancies therein may exhibit a strong dependence on Q. Consistent with that postulate, Q_{PBL} from WRF12-remap exhibits a moist bias in cloud-free grid cells mostly during warm months, whereas WRF60 is characterized by a dry bias during all seasons (Fig. 6). Despite the positive bias, WRF12-remap better captures the seasonal spatial patterns of Q_{PBL} in MERRA-2, leading to positive BSS for this variable in all calendar months. Thus, there is added value by higher-resolution simulations in representation of one of the key parameters dictating aerosol particle growth and optical properties. Spatial patterns of differences in Q_{PBL} from WRF60 and WRF12-remap relative to MERRA-2 (Fig. 6) exhibit similarities to differences in AOD (Fig. 4). WRF60 is dry-biased relative to WRF12 particularly during the summer (and fall) and underestimates Q_{PBL} relative to MERRA-2 during all seasons over the southern states and over most of continental US during summer and fall. Conversely, WRF12-remap overestimates Q_{PBL} over most of continental US during summer and fall relative to MERRA-2.

PBLH is a key variable for dictating near-surface aerosol concentrations but is highly sensitive to the physical schemes applied, and biases appear to be domain and resolution dependent. However, this parameter is comparatively difficult to assess because differences in PBLH from WRF-Chem and MERRA-2 may also originate from the way they are computed (i.e., from heat diffusivity in MERRA-2, as in Jordan et al., 2010, and from turbulent kinetic energy in WRF-Chem, as in Janjić, 2002, and von Engeln and Teixeira, 2013). Nevertheless, the Mellor–Yamada–Janjić PBL scheme combined with the Noah Land Surface Model applied in this work was found to produce lower PBL heights (Zhang et al., 2009) than other parameterizations. Thus, the positive bias in simulated

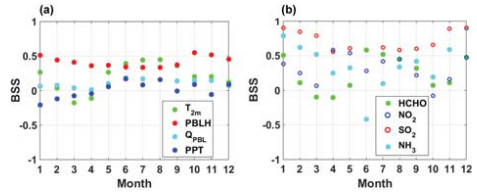

Figure 7. Brier skill scores (BSS) for key (**a**) meteorological and (**b**) chemical variables. BSS are computed using hourly data of T at 2 m ($T_{2\,\mathrm{m}}$) and PBLH, 3-hourly estimates of specific humidity in the boundary layer (Q_{PBL}) and z scores of monthly total precipitation (PPT) and of monthly mean columnar gas-phase concentrations.

AOD and surface $PM_{2.5}$ concentrations (reported previously in Crippa et al., 2016) may be linked to the systematic underestimation of PBLH simulated by WRF12-remap over continental US relative to MERRA-2 during all seasons (except winter) with greatest bias over regions of complex topography (Fig. S2). A positive bias (of several hundred meters) in terms of PBLH for WRF simulations using the MYJ parameterization was previously reported for high-resolution simulations over complex terrain (Rissman et al., 2013), and a positive bias in PBLH is also observed in the 60 km simulations presented herein (Fig. S2). This may provide a partial explanation for the large negative bias in AOD in WRF60 during summer (Fig. 3). In general, the BSS indicate improvement in the simulation of PBLH in WRF12-remap than in WRF60 (Fig. 7a).

Consistent with the dry bias in Q_{PBL} in WRF60, total accumulated precipitation is also underestimated in WRF60, while WRF12-remap captures the absolute magnitudes and the spatial patterns therein (Fig. S3). Analyses of hourly precipitation rates also show higher skill for WRF12-remap than WRF60 in simulating precipitation occurrence (HR) relative to MERRA-2 (Table S2). More specifically, WRF12-remap correctly predicts between 40 and 70 % of precipitation events in MERRA-2 with highest skill during winter months, whereas WRF60 output exhibits lower HR ($\sim$ 6 % during summer and 30 % during winter). This result thus confirms our expectation of a strong sensitivity of model performance to resolution due to the inherent scale dependence in the cumulus scheme. Use of the Grell–Freitas parameterization in the WRF60 simulations did not lead to substantially different magnitude and/or spatial patterns of precipitation compared to WRF60 applied with the Grell 3-D scheme or to improvement in agreement with output from MERRA2. The findings of a negative bias in precipitation amounts in WRF60 simulations without a corresponding overestimation of AOD may appear counterintuitive since aerosol concentrations (and thus AOD) are dependent on aerosol residence times and analyses of 16 global models from the AeroCom project indicate wet scavenging is the dominant removal process for most aerosol species in the study area (Hand et al., 2012; Textor et al., 2006). However, the negative precipitation bias in WRF60 simulations appears to also be linked to poor representation of surface moisture availability, boundary layer humidity (Fig. 6) and ultimately aerosol water content (and hence AOD).

Gas-phase concentrations (transformed into z scores) from WRF12-remap show higher agreement with satellite observations during almost all months, as indicated by the positive BSS (Fig. 7b). However, given the limited availability of valid satellite observations (especially during months with low radiation intensity), the BSS are likely only robust for the summer months for all species. Nevertheless, with the exception of NH_3 during June, BSS for all months are above or close to zero indicating that on average, the enhanced resolution simulations do exhibit higher skill in the simulation of the gas-phase species even when remapped to 60 km resolution. Further, the seasonal average spatial patterns of the total columnar concentrations, expressed in terms of z scores, also exhibit qualitative agreement with the satellite observations (Figs. S4–S7).

4 Concluding remarks

This analysis is one of the first to quantify the impact of model spatial resolution on the spatiotemporal variability and magnitude of meteorological and chemical parameters and how representation of these variables impact AOD, and it does so using simulations for a full calendar year. Application of WRF-Chem at two different resolutions (60 and 12 km) over eastern North America for a representative year (2008) leads to the following conclusions:

- Higher-resolution simulations improve the representation of key meteorological variables such as temperature, near-surface specific humidity, boundary layer height and the occurrence and amount of precipitation. Both spatial patterns and precipitation occurrence are better captured by WRF12-remap, and particularly during the summer months the specific humidity within the boundary layer exhibits closer agreement with a reanalysis product when WRF is applied at higher resolution. The dry bias in the low-resolution WRF-Chem simulations (60 km) is consistent with previous research over eastern North America and is manifest in simulations with two different cumulus parameterizations and two different data sets for the lateral boundary conditions (GFS and NAM12).

- More accurate representation of spatial patterns and concentration of gaseous species that either play a key role in particle formation and growth or are indicators of primary aerosol emissions is also achieved by running WRF-Chem at high resolution.

- Partly/largely due to the improved fidelity of key meteorological parameters and gas-phase aerosol precursor species, higher-resolution simulations enhance the fidelity of AOD representation at and near to the peak in the solar spectrum relative to a coarser run. At least some of the improvement in the accuracy with which AOD is reproduced in the higher-resolution simulations may be due to improved fidelity of specific humidity and thus more accurate representation of hygroscopic growth of some aerosol components. Spatial correlations of AOD from WRF12 and WRF12-remap with observations from MODIS are higher than AOD from a simulation conducted at 60 km during most months. WRF12 show positive spatial correlations with MODIS for all λ in all calendar months, and particularly during summer ($\rho = 0.5$–0.7). However, the improvement in model performance is not uniform in space and time.

- Output from WRF12 and WRF12-remap exhibit highest accord with MODIS observations in capturing the frequency, magnitude and location of extreme AOD values during summer when AOD is typically highest. During May–August WRF12-remap has HRs for identification of extreme AOD of 53–78 %.

It is worthy of note that even the 12 km resolution WRF-Chem simulations exhibit substantial differences in AOD relative to MODIS over eastern North America, and the agreement varies only slightly with wavelength. This may be partially attributable to use of the modal approach to represent the aerosol size distribution in order to enhance computational tractability. In this application each mode has a fixed geometric standard deviation (σ_g), which can lead to biases in simulated AOD in the visible wavelengths by up to 25 % (Brock et al., 2016) (with the model overestimating observations if the prescribed σ_g is larger than the observed one). Setting $\sigma_g = 2$ for the accumulation mode (the default in WRF-Chem) may lead to an overestimation of the number of particles at the end of the accumulation mode tail, and there is evidence that a value of $\sigma_{g,acc} = 1.40$ leads to higher agreement with observations (Mann et al., 2012). Further possible sources of the AOD biases reported herein derive from selection of the physical schemes (e.g., PBL schemes and land-surface model; Misenis and Zhang, 2010, and Zhang et al., 2009). Further, it is worth mentioning that NEI emissions are specified based on an average summertime weekday, so enhanced model performance might be achieved if seasonally varying emissions were available.

Naturally, there is a need for more research regarding the sensitivity of WRF-Chem simulations of climate relevant aerosol properties to the parameterizations used, the lateral boundary conditions employed and the resolution at which the simulations are conducted. Further, attribution of added value in the simulation of AOD by enhanced spatial resolution is necessary and will be facilitated by identifying simulation settings that minimize bias in the variables affecting AOD. This research will be part of future investigations.

5 Data availability

Data are available from MODIS and OMI (NASA, http://reverb.echo.nasa.gov/reverb, last access: May 2016), IASI NH3 (L. Clarisse, lclariss@ulb.ac.be) and MERRA-2 (https://gmao.gsfc.nasa.gov/reanalysis/MERRA-2/, last access May 2016).

The Supplement related to this article is available online at doi:10.5194/acp-17-1511-2017-supplement.

Competing interests. The authors declare that they have no conflict of interest.

Acknowledgements. This research was supported in part by a L'Oréal-UNESCO UK and Ireland Fellowship For Women In Science (to PC), the Natural Environmental Research Council (NERC) through the LICS project (ref. NE/K010794/1), grants to SCP from US NSF (grant no. 1517365) and NASA (NNX16AG31G) and a NASA Earth and Space Science Fellowship Program grant "14-EARTH14F-0207" (to R. C. Sullivan). Further support was provided by the Lilly Endowment, Inc., through its support for the Indiana University Pervasive Technology Institute and the Indiana METACyt Initiative. We gratefully acknowledge the NASA scientists responsible for MERRA-2 and MODIS products, the developers of WRF-Chem, and Lieven Clarisse, Simon Whitburn, and Martin Van Damme for producing and sharing the NH_3 retrievals. The clarity and content of this paper was substantially improved by the comments of two reviewers.

Edited by: P. Stier
Reviewed by: two anonymous referees

References

Ackermann, I. J., Hass, H., Memmesheimer, M., Ebel, A., Binkowski, F. S., and Shankar, U.: Modal aerosol dynamics model for Europe: development and first applications, Atmos. Environ., 32, 2981–2999, doi:10.1016/S1352-2310(98)00006-5, 1998.

Anderson, T. L., Charlson, R. J., Winker, D. M., Ogren, J. A., and Holmén, K.: Mesoscale Variations of Tropospheric Aerosols, J. Atmos. Sci., 60, 119–136, doi:10.1175/1520-0469(2003)060<0119:MVOTA>2.0.CO;2, 2003.

Ångström, A.: The parameters of atmospheric turbidity, Tellus, 16, 64–75, doi:10.1111/j.2153-3490.1964.tb00144.x, 1964.

Arakawa, A.: The Cumulus Parameterization Problem: Past, Present, and Future, J. Climate, 17, 2493–2525, doi:10.1175/1520-0442(2004)017<2493:RATCPP>2.0.CO;2, 2004.

Benjamini, Y. and Hochberg, Y.: Controlling the False Discovery Rate: A Practical and Powerful Approach to Multiple Testing, J. Roy. Stat. Soc. B Met., 57, 289–300, 1995.

Boucher, O., Randall, D., Artaxo, P., Bretherton, C., Feingold, G., Forster, P., Kerminen, V.-M., Kondo, Y., Liao, H., Lohmann, U., Rasch, P., Satheesh, S. K., Sherwood, S., Stevens, B., and Zhang, X. Y.: Clouds and Aerosols, in: Climate Change 2013: The Physical Science Basis. Contribution of Working Group I to the Fifth Assessment Report of the Intergovernmental Panel on Climate Change, edited by: Stocker, T. F., Qin, D., Plattner, G.-K., Tignor, M., Allen, S. K., Boschung, J., Nauels, A., Xia, Y., Bex, V., and Midgley, P. M., Cambridge University Press, Cambridge, UK and New York, USA, 33–115, 2013.

Brinksma, E. J., Boersma, K. F., Levelt, P. F., and McPeters, R. D.: OMI validation requirements document, Version 1, Rep. RS-OMIE-KNMI-345, 66, 2003.

Brock, C. A., Wagner, N. L., Anderson, B. E., Beyersdorf, A., Campuzano-Jost, P., Day, D. A., Diskin, G. S., Gordon, T. D., Jimenez, J. L., Lack, D. A., Liao, J., Markovic, M. Z., Middlebrook, A. M., Perring, A. E., Richardson, M. S., Schwarz, J. P., Welti, A., Ziemba, L. D., and Murphy, D. M.: Aerosol optical properties in the southeastern United States in summer – Part 2: Sensitivity of aerosol optical depth to relative humidity and aerosol parameters, Atmos. Chem. Phys., 16, 5009–5019, doi:10.5194/acp-16-5009-2016, 2016.

Chance, K.: OMI algorithm theoretical basis document, volume IV: OMI trace gas algorithms, available at: https://eospso.gsfc.nasa.gov/sites/default/files/atbd/ATBD-OMI-04.pdf (last access: May 2016), 2002.

Chen, F. and Dudhia, J.: Coupling an advanced land surface–hydrology model with the Penn State–NCAR MM5 modeling system. Part I: model implementation and sensitivity, Mon. Weather Rev., 129, 569–585, doi:10.1175/1520-0493(2001)129<0569:CAALSH>2.0.CO;2, 2001.

Chin, M., Kahn, R. A., and Schwartz, S. E.: Atmospheric Aerosols Properties and Climate Impacts. A Report by the U.S. Climate Change Science Program and the Subcommittee on Global Change Research, available at: http://irina.eas.gatech.edu/EAS8802_Spring2011/Report2009-aerosol-climate.pdf (last access: May 2016), National Aeronautics and Space Administration, Washington, DC, USA, 128, 2009.

Crippa, P., Sullivan, R. C., Thota, A., and Pryor, S. C.: Evaluating the skill of high-resolution WRF-Chem simulations in describing drivers of aerosol direct climate forcing on the regional scale, Atmos. Chem. Phys., 16, 397–416, doi:10.5194/acp-16-397-2016, 2016.

Di Luca, A., de Elía, R., and Laprise, R.: Challenges in the Quest for Added Value of Regional Climate Dynamical Downscaling, Curr. Clim. Change Rep., 1, 10–21, doi:10.1007/s40641-015-0003-9, 2015.

Diaconescu, E. and Laprise, R.: Can added value be expected in RCM-simulated large scales?, Clim. Dynam., 41, 1769–1800, doi:10.1007/s00382-012-1649-9, 2013.

Emmons, L. K., Walters, S., Hess, P. G., Lamarque, J.-F., Pfister, G. G., Fillmore, D., Granier, C., Guenther, A., Kinnison, D., Laepple, T., Orlando, J., Tie, X., Tyndall, G., Wiedinmyer, C., Baughcum, S. L., and Kloster, S.: Description and evaluation of the Model for Ozone and Related chemical Tracers, version 4 (MOZART-4), Geosci. Model Dev., 3, 43–67, doi:10.5194/gmd-3-43-2010, 2010.

Fast, J. D., Gustafson, W. I., Easter, R. C., Zaveri, R. A., Barnard, J. C., Chapman, E. G., Grell, G. A., and Peckham, S. E.: Evolution of ozone, particulates, and aerosol direct radiative forcing in the vicinity of Houston using a fully coupled meteorology-chemistry-aerosol model, J. Geophys. Res.-Atmos., 111, D21305, doi:10.1029/2005JD006721, 2006.

Fioletov, V. E., McLinden, C. A., Krotkov, N., Moran, M. D., and Yang, K.: Estimation of SO_2 emissions using OMI retrievals, Geophys. Res. Lett., 38, L21811, doi:10.1029/2011GL049402, 2011.

Flores, J. M., Bar-Or, R. Z., Bluvshtein, N., Abo-Riziq, A., Kostinski, A., Borrmann, S., Koren, I., Koren, I., and Rudich, Y.: Absorbing aerosols at high relative humidity: linking hygroscopic growth to optical properties, Atmos. Chem. Phys., 12, 5511–5521, doi:10.5194/acp-12-5511-2012, 2012.

Grell, G. A. and Dévényi, D.: A generalized approach to parameterizing convection combining ensemble and data assimilation techniques, Geophys. Res. Lett., 29, 38-31–38-34, doi:10.1029/2002GL015311, 2002.

Grell, G. A., Peckham, S. E., Schmitz, R., McKeen, S. A., Frost, G., Skamarock, W. C., and Eder, B.: Fully coupled "online" chemistry within the WRF model, Atmos. Environ., 39, 6957–6975, doi:10.1016/j.atmosenv.2005.04.027, 2005.

Grell, G. A. and Freitas, S. R.: A scale and aerosol aware stochastic convective parameterization for weather and air quality modeling, Atmos. Chem. Phys., 14, 5233–5250, doi:10.5194/acp-14-5233-2014, 2014.

Guenther, A., Zimmerman, P., and Wildermuth, M.: Natural volatile organic compound emission rate estimates for U.S. woodland landscapes, Atmos. Environ., 28, 1197–1210, doi:10.1016/1352-2310(94)90297-6, 1994.

Guenther, A. B., Zimmerman, P. R., Harley, P. C., Monson, R. K., and Fall, R.: Isoprene and monoterpene emission rate variability: model evaluations and sensitivity analyses, J. Geophys. Res.-Atmos., 98, 12609–12617, doi:10.1029/93jd00527, 1993.

Gustafson, W. I., Qian, Y., and Fast, J. D.: Downscaling aerosols and the impact of neglected subgrid processes on direct aerosol radiative forcing for a representative global climate model grid spacing, J. Geophys. Res.-Atmos., 116, D13303, doi:10.1029/2010JD015480, 2011.

Hand, J. L., Schichtel, B. A., Pitchford, M., Malm, W. C., and Frank, N. H.: Seasonal composition of remote and urban fine particulate matter in the United States, J. Geophys. Res.-Atmos., 117, doi:10.1029/2011jd017122, 2012.

Hong, S.-Y., Dudhia, J., and Chen, S.-H.: A Revised Approach to Ice Microphysical Processes for the Bulk Parameterization of Clouds and Precipitation, Mon. Weather Rev., 132, 103–120, doi:10.1175/1520-0493(2004)132<0103:ARATIM>2.0.CO;2, 2004.

Hyer, E. J., Reid, J. S., and Zhang, J.: An over-land aerosol optical depth data set for data assimilation by filtering, correction, and aggregation of MODIS Collection 5 optical depth retrievals, Atmos. Meas. Tech., 4, 379–408, doi:10.5194/amt-4-379-2011, 2011.

Janjić, Z. I.: The Step-Mountain Eta Coordinate Model: Further Developments of the Convection, Viscous Sublayer, and Turbulence Closure Schemes, Mon. Weather Rev., 122, 927–945, doi:10.1175/1520-0493(1994)122<0927:TSMECM>2.0.CO;2, 1994.

Janjić, Z. I.: Nonsingular implementation of the Mellor–Yamada level 2.5 scheme in the NCEP Meso model, NCEP office note, 437, 61, 2002.

Jankov, I., Gallus, A. W., Segal, M., Shaw, B., and Koch, E. S.: The Impact of Different WRF Model Physical Parameterizations and Their Interactions on Warm Season MCS Rainfall, Weather Forecast., 20, 1048–1060, doi:10.1175/WAF888.1, 2005.

Jordan, N. S., Hoff, R. M., and Bacmeister, J. T.: Validation of Goddard Earth Observing System-version 5 MERRA planetary boundary layer heights using CALIPSO, J. Geophys. Res.-Atmos., 115, D24218, doi:10.1029/2009jd013777, 2010.

Krotkov, N. A., McClure, B., Dickerson, R. R., Carn, S. A., Li, C., Bhartia, P. K., Yang, K., Krueger, A. J., Li, Z., Levelt, P. F., Chen, H., Wang, P., and Lu, D.: Validation of SO_2 retrievals from the Ozone Monitoring Instrument over NE China, J. Geophys. Res.-Atmos., 113, D16S40, doi:10.1029/2007JD008818, 2008.

Leibensperger, E. M., Mickley, L. J., Jacob, D. J., Chen, W.-T., Seinfeld, J. H., Nenes, A., Adams, P. J., Streets, D. G., Kumar, N., and Rind, D.: Climatic effects of 1950–2050 changes in US anthropogenic aerosols – Part 1: Aerosol trends and radiative forcing, Atmos. Chem. Phys., 12, 3333–3348, doi:10.5194/acp-12-3333-2012, 2012.

Levy, R. C., Mattoo, S., Munchak, L. A., Remer, L. A., Sayer, A. M., Patadia, F., and Hsu, N. C.: The Collection 6 MODIS aerosol products over land and ocean, Atmos. Meas. Tech., 6, 2989–3034, doi:10.5194/amt-6-2989-2013, 2013.

Li, L. F., Li, W. H., and Jin, J. M.: Improvements in WRF simulation skills of southeastern United States summer rainfall: physical parameterization and horizontal resolution, Clim. Dynam., 43, 2077–2091, doi:10.1007/s00382-013-2031-2, 2014.

Long, M. S., Yantosca, R., Nielsen, J. E., Keller, C. A., da Silva, A., Sulprizio, M. P., Pawson, S., and Jacob, D. J.: Development of a grid-independent GEOS-Chem chemical transport model (v9-02) as an atmospheric chemistry module for Earth system models, Geosci. Model Dev., 8, 595–602, doi:10.5194/gmd-8-595-2015, 2015.

Lowrey, M. R. K. and Yang, Z. L.: Assessing the Capability of a Regional-Scale Weather Model to Simulate Extreme Precipitation Patterns and Flooding in Central Texas, Weather Forecast., 23, 1102–1126, doi:10.1175/2008waf2006082.1, 2008.

Mann, G. W., Carslaw, K. S., Ridley, D. A., Spracklen, D. V., Pringle, K. J., Merikanto, J., Korhonen, H., Schwarz, J. P., Lee, L. A., Manktelow, P. T., Woodhouse, M. T., Schmidt, A., Breider, T. J., Emmerson, K. M., Reddington, C. L., Chipperfield, M. P., and Pickering, S. J.: Intercomparison of modal and sectional aerosol microphysics representations within the same 3-D global chemical transport model, Atmos. Chem. Phys., 12, 4449–4476, doi:10.5194/acp-12-4449-2012, 2012.

Martin, S. T., Hung, H.-M., Park, R. J., Jacob, D. J., Spurr, R. J. D., Chance, K. V., and Chin, M.: Effects of the physical state of tropospheric ammonium-sulfate-nitrate particles on global aerosol direct radiative forcing, Atmos. Chem. Phys., 4, 183–214, doi:10.5194/acp-4-183-2004, 2004.

McComiskey, A., Schwartz, S. E., Schmid, B., Guan, H., Lewis, E. R., Ricchiazzi, P., and Ogren, J. A.: Direct aerosol forcing: Calculation from observables and sensitivities to inputs, J. Geophys. Res.-Atmos., 113, D09202, doi:10.1029/2007JD009170, 2008.

McLinden, C. A., Fioletov, V., Boersma, K. F., Kharol, S. K., Krotkov, N., Lamsal, L., Makar, P. A., Martin, R. V., Veefkind, J. P., and Yang, K.: Improved satellite retrievals of NO_2 and SO_2 over the Canadian oil sands and comparisons with surface measurements, Atmos. Chem. Phys., 14, 3637–3656, doi:10.5194/acp-14-3637-2014, 2014.

Mearns, L. O., Arritt, R., Biner, S., Bukovsky, M., Stain, S., and NARCCAP team: The North American Regional Climate Change Assessment Program: Overview of Phase I Results, B. Am. Meteorol. Soc., 93, 1337–1362, 2012.

Meehl, G. A., Moss, R., Taylor, K. A., Eyring, V., Stouffer, R. J., Sandrine, B., and Stevens, B.: Climate model intercomparisons: preparing for the next phase, Eos, Transaction, American Geophysical Union, 95, 77–84, doi:10.1002/2014EO09, 2014.

Misenis, C. and Zhang, Y.: An examination of sensitivity of WRF/Chem predictions to physical parameterizations, horizontal grid spacing, and nesting options, Atmos. Res., 97, 315–334, doi:10.1016/j.atmosres.2010.04.005, 2010.

Mlawer, E. J., Taubman, S. J., Brown, P. D., Iacono, M. J., and Clough, S. A.: Radiative transfer for inhomogeneous atmospheres: RRTM, a validated correlated-k model for the longwave, J. Geophys. Res.-Atmos., 102, 16663–16682, doi:10.1029/97JD00237, 1997.

Molod, A., Takacs, L., Suarez, M., and Bacmeister, J.: Development of the GEOS-5 atmospheric general circulation model: evolution from MERRA to MERRA2, Geosci. Model Dev., 8, 1339–1356, doi:10.5194/gmd-8-1339-2015, 2015.

Murphy, A. H. and Epstein, E. S.: Skill scores and correlation-coefficients in model verification, Mon. Weather Rev., 117, 572–581, doi:10.1175/1520-0493(1989)117<0572:ssacci>2.0.co;2, 1989.

Myhre, G., Samset, B. H., Schulz, M., Balkanski, Y., Bauer, S., Berntsen, T. K., Bian, H., Bellouin, N., Chin, M., Diehl, T., Easter, R. C., Feichter, J., Ghan, S. J., Hauglustaine, D., Iversen, T., Kinne, S., Kirkevåg, A., Lamarque, J.-F., Lin, G., Liu, X., Lund, M. T., Luo, G., Ma, X., van Noije, T., Penner, J. E., Rasch, P. J., Ruiz, A., Seland, Ø., Skeie, R. B., Stier, P., Takemura, T., Tsigaridis, K., Wang, P., Wang, Z., Xu, L., Yu, H., Yu, F., Yoon, J.-H., Zhang, K., Zhang, H., and Zhou, C.: Radiative forcing of the direct aerosol effect from AeroCom Phase II simulations, Atmos. Chem. Phys., 13, 1853–1877, doi:10.5194/acp-13-1853-2013, 2013a.

Myhre, G., Shindell, D., Bréon, F.-M., Collins, W., Fuglestvedt, J., Huang, J., Koch, D., Lamarque, J.-F., Lee, D., Mendoza, B., Nakajima, T., Robock, A., Stephens, G., Takemura, T., and Zhang, H.: Anthropogenic and Natural Radiative Forcing, in: Climate Change 2013: The Physical Science Basis. Contribution of Working Group I to the Fifth Assessment Report of the Intergovernmental Panel on Climate Change, edited by: Stocker, T. F., Qin, D., Plattner, G.-K., Tignor, M., Allen, S. K., Boschung, J., Nauels, A., Xia, Y., Bex, V., and Midgley, P. M., Cambridge University Press, Cambridge, UK, NY, USA, 659–740, 2013b.

Nasrollahi, N., AghaKouchak, A., Li, J. L., Gao, X. G., Hsu, K. L., and Sorooshian, S.: Assessing the Impacts of Different WRF Pre-

cipitation Physics in Hurricane Simulations, Weather Forecast., 27, 1003–1016, doi:10.1175/waf-d-10-05000.1, 2012.

Qian, Y., Gustafson Jr., W. I., and Fast, J. D.: An investigation of the sub-grid variability of trace gases and aerosols for global climate modeling, Atmos. Chem. Phys., 10, 6917–6946, doi:10.5194/acp-10-6917-2010, 2010.

Rissman, J., Arunachalam, S., Woody, M., West, J. J., BenDor, T., and Binkowski, F. S.: A plume-in-grid approach to characterize air quality impacts of aircraft emissions at the Hartsfield-Jackson Atlanta International Airport, Atmos. Chem. Phys., 13, 9285–9302, doi:10.5194/acp-13-9285-2013, 2013.

Rockel, B., Castro, C. L., Pielke, R. A., von Storch, H., and Leoncini, G.: Dynamical downscaling: Assessment of model system dependent retained and added variability for two different regional climate models, J. Geophys. Res.-Atmos., 113, D21107, doi:10.1029/2007JD009461, 2008.

Santarpia, J. L., Gasparini, R., Li, R. J., and Collins, D. R.: Diurnal variations in the hygroscopic growth cycles of ambient aerosol populations, J. Geophys. Res.-Atmos., 110, D03206, doi:10.1029/2004jd005279, 2005.

Schell, B., Ackermann, I. J., Hass, H., Binkowski, F. S., and Ebel, A.: Modeling the formation of secondary organic aerosol within a comprehensive air quality model system, J. Geophys. Res.-Atmos., 106, 28275–28293, doi:10.1029/2001jd000384, 2001.

Schuster, G. L., Dubovik, O., and Holben, B. N.: Angstrom exponent and bimodal aerosol size distributions, J. Geophys. Res.-Atmos., 111, D07207, doi:10.1029/2005JD006328, 2006.

Seinfeld, J. H. and Pandis, S. N.: Atmospheric chemistry and physics: from air pollution to climate change, John Wiley & Sons, 1152 pp., 2016.

Simes, R. J.: An improved Bonferroni procedure for multiple tests of significance, Biometrika, 73, 751–754, doi:10.2307/2336545, 1986.

Simpson, D., Guenther, A., Hewitt, C. N., and Steinbrecher, R.: Biogenic emissions in Europe. 1. estimates and uncertainties, J. Geophys. Res.-Atmos., 100, 22875–22890, doi:10.1029/95jd02368, 1995.

Stocker, T. F., Qin, D., Plattner, G.-K., Alexander, L. V., Allen, S. K., Bindoff, N. L., Bréon, F.-M., Church, J. A., Cubasch, U., Emori, S., Forster, P., Friedlingstein, P., Gillett, N., Gregory, J. M., Hartmann, D. L., Jansen, E., Kirtman, B., Knutti, R., Krishna Kumar, K., Lemke, P., Marotzke, J., Masson-Delmotte, V., Meehl, G. A., Mokhov, I. I., Piao, S., Ramaswamy, V., Randall, D., Rhein, M., Rojas, M., Sabine, C., Shindell, D., Talley, L. D., Vaughan, D. G., and Xie, S.-P.: Summary for Policymakers, in: Climate Change 2013: The Physical Science Basis. Contribution of Working Group I to the Fifth Assessment Report of the Intergovernmental Panel on Climate Change, Cambridge University Press, Cambridge, UK, NY, USA, 33–115, 2013.

Stockwell, W. R., Middleton, P., Chang, J. S., and Tang, X.: The second generation regional acid deposition model chemical mechanism for regional air quality modeling, J. Geophys. Res.-Atmos., 95, 16343–16367, doi:10.1029/JD095iD10p16343, 1990.

Sun, Y., Yi, L., Zhong, Z., and Ha, Y.: Performance of a New Convective Parameterization Scheme on Model Convergence in Simulations of a Tropical Cyclone at Grey-Zone Resolutions, J. Atmos. Sci., 71, 2078–2088, doi:10.1175/JAS-D-13-0285.1, 2014.

Taylor, K. E.: Summarizing multiple aspects of model performance in a single diagram, J. Geophys. Res.-Atmos., 106, 7183–7192, doi:10.1029/2000jd900719, 2001.

Textor, C., Schulz, M., Guibert, S., Kinne, S., Balkanski, Y., Bauer, S., Berntsen, T., Berglen, T., Boucher, O., Chin, M., Dentener, F., Diehl, T., Easter, R., Feichter, H., Fillmore, D., Ghan, S., Ginoux, P., Gong, S., Grini, A., Hendricks, J., Horowitz, L., Huang, P., Isaksen, I., Iversen, I., Kloster, S., Koch, D., Kirkevåg, A., Kristjansson, J. E., Krol, M., Lauer, A., Lamarque, J. F., Liu, X., Montanaro, V., Myhre, G., Penner, J., Pitari, G., Reddy, S., Seland, Ø., Stier, P., Takemura, T., and Tie, X.: Analysis and quantification of the diversities of aerosol life cycles within AeroCom, Atmos. Chem. Phys., 6, 1777–1813, doi:10.5194/acp-6-1777-2006, 2006.

Tilmes, S., Lamarque, J.-F., Emmons, L. K., Kinnison, D. E., Ma, P.-L., Liu, X., Ghan, S., Bardeen, C., Arnold, S., Deeter, M., Vitt, F., Ryerson, T., Elkins, J. W., Moore, F., Spackman, J. R., and Val Martin, M.: Description and evaluation of tropospheric chemistry and aerosols in the Community Earth System Model (CESM1.2), Geosci. Model Dev., 8, 1395–1426, doi:10.5194/gmd-8-1395-2015, 2015.

Tomasi, C., Caroli, E., and Vitale, V.: Study of the Relationship between Ångström's Wavelength Exponent and Junge Particle Size Distribution Exponent, J. Clim. Appl. Meteorol., 22, 1707–1716, doi:10.1175/1520-0450(1983)022<1707:SOTRBW>2.0.CO;2, 1983.

US-EPA: 2005 National Emissions Inventory (NEI), US Environmental Protection Agency in, available at: ftp://aftp.fsl.noaa.gov/divisions/taq/emissions_data_2005/, 2009.

Vinken, G. C. M., Boersma, K. F., van Donkelaar, A., and Zhang, L.: Constraints on ship NOx emissions in Europe using GEOS-Chem and OMI satellite NO2 observations, Atmos. Chem. Phys., 14, 1353–1369, doi:10.5194/acp-14-1353-2014, 2014.

von Engeln, A. and Teixeira, J.: A Planetary Boundary Layer Height Climatology Derived from ECMWF Reanalysis Data, J. Climate, 26, 6575–6590, doi:10.1175/JCLI-D-12-00385.1, 2013.

Weigum, N., Schutgens, N., and Stier, P.: Effect of aerosol subgrid variability on aerosol optical depth and cloud condensation nuclei: implications for global aerosol modelling, Atmos. Chem. Phys., 16, 13619–13639, doi:10.5194/acp-16-13619-2016, 2016.

Whitburn, S., Van Damme, M., Clarisse, L., Bauduin, S., Heald, C., Hadji-Lazaro, J., Hurtmans, D., Zondlo, M. A., Clerbaux, C., and Coheur, P.-F.: A flexible and robust neural network IASI-NH_3 retrieval algorithm, J. Geophys. Res.-Atmos., doi:10.1002/2016JD024828, in press, 2016.

Wild, O., Zhu, X., and Prather, M. J.: Fast-J: Accurate Simulation of In- and Below-Cloud Photolysis in Tropospheric Chemical Models, J. Atmos. Chem., 37, 245–282, doi:10.1023/a:1006415919030, 2000.

Zhang, X., Chen, Z. M., Wang, H. L., He, S. Z., and Huang, D. M.: An important pathway for ozonolysis of alpha-pinene and beta-pinene in aqueous phase and its atmospheric implications, Atmos. Environ., 43, 4465–4471, doi:10.1016/j.atmosenv.2009.06.028, 2009.

Zhang, Y., He, J., Zhu, S., and Gantt, B.: Sensitivity of simulated chemical concentrations and aerosol-meteorology interactions to aerosol treatments and biogenic organic emissions in WRF/Chem, J. Geophys. Res.-Atmos., 121, 6014–6048, doi:10.1002/2016JD024882, 2016.

Zieger, P., Fierz-Schmidhauser, R., Weingartner, E., and Baltensperger, U.: Effects of relative humidity on aerosol light scattering: results from different European sites, Atmos. Chem. Phys., 13, 10609–10631, doi:10.5194/acp-13-10609-2013, 2013.

APPENDIX E

MODELING THE CONTRIBUTIONS OF GLOBAL AIR TEMPERATURE, SYNOPTIC-SCALE PHENOMENA AND SOIL MOISTURE TO NEAR-SURFACE STATIC ENERGY VARIABILITY OVER THE EASTERN USA

SC Pryor, RC Sullivan, and JT Schoof, submitted.

Modeling the contributions of global air temperature, synoptic-scale phenomena and soil moisture to near-surface static energy variability over the eastern USA.

S.C. Pryor[1], R.C. Sullivan[1] and J.T. Schoof[2]

[1]Department of Earth and Atmospheric Sciences, Cornell University, Ithaca, NY 14853, USA.

[2]Department of Geography and Environmental Resource, Southern Illinois University, Carbondale, IL 62901, USA.

Correspondence to: S.C. Pryor (sp2279@cornell.edu)

Abstract. The static energy content of the atmosphere is increasing at the global scale, but exhibits important sub-global and sub-regional scales of variability and is a useful parameter for integrating the net effect of changes in the partitioning of energy at the surface and for improving understanding of the causes of so-called 'warming-holes' (i.e. locations with decreasing daily maximum air temperatures (T) or increasing trends of lower magnitude than the global mean). Further, measures of the static energy content (herein the equivalent potential temperature, θ_e) are more strongly linked to excess human mortality and morbidity than air temperature alone, and have great relevance in understanding causes of past heat-related excess mortality and making projections of possible future events that are likely to be associated with negative human health and economic consequences. New non-linear statistical modela for summertime daily maximum and minimum θ_e are developed and used to advance understanding of drivers of historical change and variability over the eastern USA. It is shown that soil moisture (SM) is particularly important in determining the magnitude of θ_e over regions that have previously been identified as exhibiting 'warming holes' confirming the key importance of SM in dictating the partitioning of net radiation into sensible and latent heat and dictating trends in near-surface T and θ_e. Consistent with our *a priori* expectations, transfer functions built using Artificial Neural Networks (ANN) out-perform linear models that do not permit interaction of the predictor variables (global T, synoptic-scale meteorological conditions and SM). This is particularly marked in regions with high variability in min- and max-θ_e, where more complex models built using ANN with multiple hidden layers are better able to capture the day-to-day variability in θ_e and the occurrence of extreme max-θ_e. Over the entire domain the ANN with 3 hidden layers exhibits high accuracy in predicting max-θ_e > 347 K. The median hit rate for max-θ_e > 347 K is > 0.60, while the median false alarm rate ≈ 0.08.

1 Motivation and objectives

Extreme heat is associated with significant societal and environmental impacts, and a number of prior studies have elaborated the drivers of extreme air temperatures (T) and made projections of extreme T and the associated human health impacts and socioeconomic consequences (Sanderson and Ford, 2017;de'Donato et al., 2015;O'Neill and Ebi, 2009;Garcia-Herrera et al., 2010). For example, research has suggested that warming of the United States of

America by 5°C by 2100 would be associated with annual welfare losses of $57 billion largely due to negative human health impacts (including those due to heat-stress) (Mansur et al., 2008).

Many previous studies have sought to quantify the predictability of extreme T as a function of lead-time and variables describing teleconnections to remote sea-surface temperature anomalies (McKinnon et al., 2016) and/or local soil moisture (Brabson et al., 2005). However, surface temperature (enthalpy) is only one component of the energy content of the surface atmosphere (Pielke et al., 2004), and analyses that also integrate other components of atmospheric energetics (latent heat and kinetic energy) have greater diagnostic value particularly in understanding changes in energy partitioning at the atmosphere-surface boundary (Peterson et al., 2011). Further, physiological stress and hence excess human mortality and morbidity is maximized under the co-occurrence of elevated T and specific humidity (Q) (Zhang et al., 2014). Thus to understand spatiotemporal variability in heat-related mortality and/or morbidity there is a need to consider integrative variables derived from both T and Q, such as equivalent potential temperature (θ_e):

$$\theta_e = T\left(\frac{1000}{P}\right)^{R_d/C_{pd}} + \frac{L(T)}{C_{pd}}Q, \quad (1)$$

Where T = air temperature, P = pressure, R_d = specific gas constant for air, C_{pd} = specific heat for dry air, $L(T)$ = latent heat of vaporization ($f(T)$), Q = specific humidity.

As shown in equation (1), θ_e increases linearly with T and by ~2.5K for each gKg^{-1} change in Q. Thus, specific humidity makes the largest contribution to θ_e during the summer months (Fall et al., 2010), and while T is responsive only to changes in the sensible heat flux from the surface, θ_e responds to changes in both the sensible and latent heat flux terms within the surface energy balance (i.e. the balance between net radiation, left hand side of Eq 2, and the sensible, latent and ground heat fluxes, right hand side of Eq 2):

$$S(1-\alpha) + R_{li} - R_{lo} = H + LE + G \quad (2)$$

Where S = incoming solar radiation, α = albedo, R_{li} = counter-radiated longwave radiation from the atmosphere, R_{lo} = outgoing longwave radiation from the surface, H = sensible heat transfer, LE = latent heat transfer, and G = ground heat transfer.

While daytime maximum T tends to be enhanced when soils dry out leading to an increase in the partitioning of positive daytime net radiation into sensible heat, wetter soils increase latent heat fluxes and θ_e. Thus, although events such as the 2003 European summer heat wave are associated with dry soils enhancing the sensible heat flux leading to extreme T (Garcia-Herrera et al., 2010), at least over the study region considered herein (the eastern United States of America (USA)) the majority of high mortality events have been associated with the combined occurrence of elevated T and Q and thus high θ_e (Vanos et al., 2015).

There is evidence that the total static energy of the lower atmosphere (θ_e) at the global scale has significantly increased since the 1970s consistent with the increase in net radiation (Peterson et al., 2011) and in response to both increased air temperature and the associated response in the atmospheric water vapor content (Ribera et al., 2004;Willett et al., 2007). However, climate modes cause inter-annual variability in global (Huang et al., 2017) and regional (Llamedo et al., 2017) air temperature (T) and specific humidity (Q) anomalies, and there is substantial regional and sub-regional variability in absolute magnitude of static energy and temporal trends therein (Fall et al.,

2010;Pryor and Schoof, 2016;Pryor et al., 2016). Research presented herein is designed to develop a new statistical downscaling model for summertime daily maximum and minimum equivalent potential temperature (θ_e) (Davey et al., 2006) (Eq. 1) and use it to advance understanding of drivers of historical change and variability in summertime θ_e over the eastern USA.

De-convoluting causes of regional variability and trends in θ_e through time is challenging, and the driving mechanisms are not independent. The following is a précis of the scales and processes we seek to explore and include in our statistical model:

- Global scale forcing due to enhanced greenhouse gas concentrations and internal climate variability (e.g. the occurrence of climate modes of variability such as El Niño-Southern Oscillation (ENSO) (Mann et al., 1998)). As T increases the atmospheric water vapor content responds in proportion to the saturation vapor pressure (Willett et al., 2007;Allen and Ingram, 2002). Thus, both components (T and Q) of static energy (θ_e) are enhanced in years and seasons with high global mean air temperatures. Previous research has indicated that variability in equivalent temperature (T_e, i.e. the temperature computed from (1) but excluding the correction for bringing the air parcel adiabatically to a reference pressure of 1000 hPa) in the North Atlantic is strongly linked to the North Atlantic Oscillation (NAO) (Ribera et al., 2004), and the probability of 'heat waves' across the US is linked to hemispheric waves (Teng et al., 2013) and thus large-scale climate modes of variability (such as the Pacific North American mode (PNA) (Trenberth, 1990)).
- Synoptic scale forcing (Grotjahn et al., 2016). Much of the eastern USA broke records for heat indices during the summer of 2012 in part due to persistent anticyclonic conditions over the region (Peterson et al., 2013). Further, variability and temporal trends in summertime moist static energy and dew point temperatures (T_d) in the Midwestern USA appear to be linked to enhanced horizontal atmospheric moisture advection due in part to northward expansion of the southeast summertime anticyclone and thus changes in the synoptic circulation (Kalkstein et al., 1998;Rogers et al., 2007;Pryor and Schoof, 2016;Ford and Schoof, 2017).
- Local-regional changes in water availability and energy partitioning at the surface, due to factors such as land cover change and soil moisture modification as a result of irrigation of cropland, strongly impact local and regional static energy content (Davey et al., 2006;Pryor et al., 2016). Recall that while dry soils tend to be associated with the occurrence of extreme air T (Garcia-Herrera et al., 2010), this is not the case for T_e or θ_e, which tend to be enhanced by the presence of moist soils (Ford and Schoof, 2016).

Observed tendencies in T, Q and θ_e are naturally a product of a combination of these drivers (Horton et al., 2016). The expression of internal climates modes (.e.g. ENSO, PNA and NAO) influences the frequency and intensity of different synoptic scale phenomena (Sheridan, 2003;Weaver, 2013), which has been found to be partly responsible for an increase in the number of oppressively hot days in many urban areas across the USA over recent decades (Sheridan et al., 2009). Further, there are important feedbacks between the land-atmosphere coupling, the synoptic scale circulation patterns and boundary-layer structure (Lee et al., 2016). Thus, for example, extreme T_d (and by association elevated Q) in the Midwestern USA is associated with (a) development and propagation of low pressure from the High Plains to through the upper Great Lakes, (b) healthy crops and sufficient surface soil moisture, and (c) restricted vertical mixing (Bentley and Stallins, 2008).

The overall objectives of this research are:

1) To use non-linear (machine learning) models applied to a three-tiered suite of predictors: (a) An index of the daily global mean temperature, (b) indices of the conditions at the synoptic scale based on principal components analysis (PCA) of upper-air variables, and (c) soil moisture estimates, to investigate spatiotemporal variations in θ_e and enhance mechanistic understanding of the causes of variability and change in θ_e over the eastern USA.
2) To examine whether the performance of the statistical models used to predict daily maximum and minimum θ_e is enhanced by inclusion of additional hidden layers in the artificial neural networks (ANNs) used to relate the predictors to near-surface θ_e.

2 Data and Methods

2.1 Study region

The eastern USA (Figure 1a) is the focus of this research because:

- It is characterized by high summertime T_e (and θ_e) and in situ data have indicated trends in T_e exceed those in T alone (Schoof et al., 2015), and largely congruent with an area of coherence for extreme T events in prior research (McKinnon et al., 2016).
- It encompasses many major urban areas that have experienced a number of past extreme heat events associated with substantial excess mortality and morbidity (see summary in (Vanos et al., 2015) and also (Anderson and Bell, 2011)). Further, a range of reanalyses exhibit a consistent signal of increasing frequency of both dry (i.e. high T but low Q) and humid (i.e. combined high T and Q) heat wave days over the study region (Schoof et al., 2017). Therefore, historical and projected tendencies in T and Q may offset some of the risk-reduction benefits from development/deployment of heat wave impact mitigation strategies (O'Neill et al., 2010).
- It exhibits strong spatial gradients in terms of the nature of land cover and rate of change of both land management and soil moisture (Figure 1a and g, (Pryor et al., 2016;Pryor and Schoof, 2016;Ellenburg et al., 2016)). Parts of the region were identified in the global land–atmosphere coupling experiments (GLACE) as exhibiting atypically strong atmosphere-surface coupling in some global climate models, and soil moisture makes a large contribution to sub-seasonal forecast skill for air temperatures and precipitation in this region (Koster et al., 2011;Koster et al., 2006).
- The study region also incorporates two areas of reduced daily maximum T during parts or all of the twentieth century. One is located along the border of Iowa (IA)-Nebraska (NE)-South Dakota (SD) and one is centered on Mississippi (MS) and Alabama (AL) (locations shown in Figure 1h). The lack of warming in both regions has been attributed to changing land-surface characteristics and enhanced soil moisture availability (Kalnay and Cai, 2003;Pan et al., 2009;Ellenburg et al., 2016), and in the case of Mississippi (MS) and Alabama (AL) upto 60% of the variance of summer temperatures has been ascribed to soil moisture (and thus an increase in the LE at the surface at the expense of H, Eq. 2) and cloud cover (reducing the net radiation) (Ellenburg et al., 2016). However, it must be acknowledged that additional factors may account for these regions of slow or absent warming including large scale climate modes such as the Interdecadal Pacific Oscillation and the associated sea

surface temperature anomalies in the tropical Pacific (Meehl et al., 2015), and aerosol radiative forcing (Leibensperger et al., 2012;Yu et al., 2014).

2.2 Data set

All variables used herein derive from the MERRA-2 reanalysis data set (Molod et al., 2015;Reichle et al., 2017). This minimizes uncertainty in transfer functions linking our predictors to near-surface static energy resulting from use of different data sets to derive the predictor suite and/or the response variables (daily minimum and maximum θ_e). The MERRA-2 reanalysis product assimilates an unprecedented array of remote sensing and in situ data streams, but does not assimilate in situ observations of near-surface T or Q. MERRA-2 output is available at a resolution of 0.625°× ~0.5° (longitude-by-latitude). We use MERRA-2 output for all summer days (JJA) during 1980-2015 to compute the following variables that are used in this analysis:

1) A globally averaged daily mean air temperature computed using hourly 2-m T from all MERRA-2 grid cells. This predictor (Figure 1b) is intended to represent the long-term tendency in global mean temperatures and interannual/interdecadal variability caused by internal climate modes (Huang et al., 2017).
2) Indices of synoptic scale meteorology. Air temperature (T_{850}) and specific humidity (Q_{850}) at 850 hPa along with 500 hPa geopotential heights (Z_{500}) in the domain (25.5-50°N, 97.5-65°W) for 20:00 UTC are converted to z-scores (that indicates how many standard deviations an individual value is from the mean) and used in a rotated principal components analysis (PCA) to generate daily principal component scores (PCs) that represent the proximity of each day to the major modes of synoptic-scale variability. Fifteen components are retained based on a scree plot analysis (Cattell, 1966) and are subject to Varimax rotation (Richman, 1986). Daily PC scores for all 15 PCs are used as predictors in the statistical models, to allow each day to exhibit partial membership of multiple synoptic types. Spatial fields of the three variables sampled once per day are used in the PCA due to the high temporal autocorrelation present in these variables, and 20:00 UTC is selected to coincide with approximately the timing of the afternoon peak in surface air temperature over the eastern USA. Figure 2 shows centroids of synoptic modes of variability as defined using the PCA (so-called key days) as represented by the spatial patterns of T_{850}, Q_{850} and Z_{500} computed as the mean conditions on the seven days that exhibit highest PC scores on each PC. As shown, many of the synoptic types thus identified are readily interpretable as representing a diversity of zonal versus meridional circulation (cf. type 9 and 5 and 6), and some are characterized by conditions known to be associated with strong low-level advection of T and Q into the region (e.g. types 1, 3, and 15) (Pryor and Schoof, 2016;Weaver, 2013). Further, most types exhibit a high degree of similarity with other synoptic-scale classifications derived for the region (e.g. type 7 is very similar to one that is associated with summertime precipitation over the southeastern USA (Diem, 2006)).
3) An index of soil moisture (SM). Following previous research (Ford and Schoof, 2016), we use a time and spatially integrated metric of SM. Specifically we use a 90-day running mean estimate of antecedent SM in 3×3 grid cells centered on the grid cell in question (see Figure 1g). Soil moisture is an extremely

challenging variable to characterize both observationally and in numerical models (Pryor and Schoof, 2016;Knist et al., 2017;Su et al., 2016). Nevertheless, it is a key determinant of the surface energy balance and static energy over the region (Pryor et al., 2016;Ellenburg et al., 2016) since it critically determines the partitioning of net radiation into sensible and latent heat (Eq. 2) and also modifies the net radiation due to the influence on soil emissivity and albedo (Pryor et al., 2016). The MERRA-2 data set *SM* output has been extensively evaluated relative to in situ measurements of surface and root-zone soil moisture and exhibits an unbiased root mean square error (RMSE) of 0.05 m^3m^{-3} and a variance explanation (R^2) value of the average root-zone soil moisture anomaly of 0.56 (Reichle et al., 2017).

4) An estimate of (i) daily maximum θ_e and (ii) daily minimum θ_e in each grid cell across the eastern USA (see Figure 1c and d) derived using Eq(1) along with hourly T at 2-m, Q at 2-m and surface pressure (P) from MERRA-2. The domain used to compute the gridded fields of the predictands (daily minimum and maximum θ_e) is truncated by one grid cell on each boundary of the domain used to generate the predictors to accommodate the spatial averaging used to generate the soil moisture predictor. The range of gridcell θ_e estimates are consistent with those derived from station observations within the study region (Pryor and Schoof, 2016), and in accord with *a priori* expectations both daily max-θ_e and min-θ_e exhibit primarily latitudinal variability (Figure 1c and d). Mean max-θ_e decreases from values of ~350 K (~80°C) in the south of the domain to approximately 320 K (~50°C) in the north. The states of Missouri (MO) and Iowa (IA) exhibit anomalously high mean max-θ_e compared with grid cells at the same latitudes (Figure 1c), reflecting the advection of air with high temperatures and specific humidity from the south by the Great Plains Low Level Jet (GPLLJ) (Weaver, 2013;Pryor and Schoof, 2016;Schoof et al., 2015), and the presence of abundant *SM* (Figure 1g). There are also important spatial patterns of the day-to-day variability of daily max-θ_e and min-θ_e that provide key context for considering the performance of different transfer functions (i.e. statistical models linking indices of the global mean T, synoptic scale meteorology and soil moisture (the predictors) to the response variables; max-θ_e and min-θ_e). The variance (and standard deviation) of daily max-θ_e values (i.e. a measure of the dispersion of individual days around the mean values of min- and max-θ_e shown in Figures 1c and 1d) is largest over Iowa (IA)/southern Minnesota (MN) (Figure 1e), while the variance of min-θ_e is greatest over Illinois (IL) (Figure 1f). In both cases the day-to-day variability in these states as measured by the standard deviation is ~ 10 K. The standard deviation of daily max-θ_e and min-θ_e decreases with decreasing latitude and both variables exhibit lowest variability over he southern portions of the study domain (e.g. Florida (FL) has a standard deviation < 5 K) (Figure 1e,f).

Thus the time series of predictors 1) and 2) (global mean T and the 15 PC scores) are common to models built for all grid cells, but predictor 3) (*SM*) and the response variables (predictands, daily max-θ_e and min-θ_e) are grid-cell specific.

2.3 Methods

Artificial neural network (ANN) architectures are potentially highly useful in developing statistical transfer functions for response variables such as θ_e because ANN are trained on data, do not require any assumptions about the form of the relationship between individual predictors, between predictors and predictands (min- and max-θ_e), and can treat complex and non-linear term interactions. Our *a priori* expectation is that the different predictors of daily maximum and minimum θ_e will interact in complex, non-linear ways. Thus, we apply ANN to develop the transfer functions relating the global mean air temperature, PC scores of the synoptic-scale meteorology and antecedent *SM* to daily maximum or minimum θ_e in each grid cell. Because we seek to examine spatial variability in model performance, we build and test the ANNs at the grid-cell level and then examine the resulting spatial coherence of model skill. Although there is no single 'best-practice' regarding the number of hidden layers to use with ANN, there is evidence that a single hidden layer is sufficient for the large majority of problems (Toth et al., 2000). To test the dependence of model skill on the number of hidden-layers, three independent transfer functions are constructed for each MERRA-2 grid cell using:

1) No hidden layers, i.e. a linear regression model with no interaction between the predictors.
2) ANN with a single hidden layer.
3) ANN with three hidden layers.

To examine the importance of *SM* in determining the downscaling model skill, a fourth ANN model (with 3 hidden layers) is also built for each grid cell and each of the two predictands (daily maximum and minimum θ_e) that excludes *SM* from the input variables. Lastly, it is challenging to determine which measures of *SM* are most appropriate to use within statistical downscaling models. Therefore, in addition to developing models using the MERRA-2 variable 'PRMC', which is the 'Total profile soil moisture content' in m^3m^{-3} (and is summed across all six soil layers), a fifth ANN model (with 3 hidden layers) is also built that uses the variable 'GWETTOP' which is 'Top soil layer wetness'. This variable is unit-less and describes the *SM* content in the upper 5 cm of the soil (Reichle et al., 2017), and thus it best represents the *SM* that is readily available to the overlying atmosphere.

Table 1 summarizes the model abbreviations used herein, and a schematic of the model architecture for the downscaling models and data flows is given in Figure 3. For each model (and thus each grid cell) 70% of the data set is randomly selected to be used for training of the model, 15% is used for internal validation and 15% is withheld and used as an independent sample for model testing. A range of different learning algorithms can be employed in ANN. Herein the neural networks are constructed within Matlab using the Levenberg-Marquardt back-propagation algorithm (in which the sum of the squares of the deviations between the observations and model predictions is minimized) (Papageorgiou and Poczeta, 2017).

We use two primary metrics of model performance: RMSE and Pearson correlation coefficient (r) between observed and predicted daily minimum and maximum-θ_e in each grid cell on each day in the test data set (i.e. independent observations), summarized at both the grid cell level and also averaged over all 1962 MERRA-2 grid cells that have some land areas within them (i.e. a domain average). The correlation coefficient is thus used as a relative measure of model performance, while RMSE provides an absolute measure of degree of agreement between the model 'predictions' and the observed values (i.e. it is the typical value of the prediction error). Given the importance of

extreme heat to human health we further examine the ability of the transfer functions to capture the occurrence of very high θ_e. In this analysis we set a threshold of 347 K (73°C) to indicate extreme max-θ_e (based on information provided in (Buzan et al., 2015) for the eastern USA) and a threshold of 337 K for min-θ_e. A contingency table approach is used to evaluate the accuracy of the model predictions of extreme-θ_e using the hit rate (*HR*) (Wilks, 2011):

$$HR = \frac{\#hits}{\#hits+\#misses} \quad , \tag{3}$$

Where *#hits* = number of days in the independent data set where the observations and predictions both indicate exceedance of the threshold, and *#misses* is the number of days when the observations indicate an exceedance of the threshold but the model prediction does not.

And the false alarm rate (*FAR*) of each individual grid cell:

$$FAR = \frac{\#false\ alarms}{\#false\ alarms+\#correct\ non-events} \quad , \tag{4}$$

Where *#false alarms* = number of days in the independent data set where the observations did not indicate exceedance of the threshold but the prediction was for an exceedance, and *#correct non-events* is the number of days when the observations and predictions both indicate the threshold is not exceeded.

3 Results

For both daily maximum-θ_e and daily minimum-θ_e, the worst model performance statistics (highest RMSE as a fraction of the temporal variability θ_e, and lowest *r*) are associated with the linear models that do not include parameter interactions (MLR) (Table 1 and Figures 4 and 5). Nevertheless, output from all model architectures for min-θ_e and max-θ_e exhibit high correlation coefficients (r > 0.8) with independent data over most of the study domain. Correlation coefficients exceed 0.8 for 84% of grid cells for ANN-HL3-SM applied to max-θ_e and 81% for min-θ_e and RMSE < 5 K (92% of grid cells for ANN-HL3-SM exhibit a RMSE below this threshold for max-θ_e and 91% for min-θ_e) (Table 1, Figure 4 and 5). The grid cells that are characterized by highest RMSE for min-θ_e and max-θ_e are generally collocated with the regions that have highest variance (i.e. largest day-to-day variability). For example, Iowa (IA) exhibits highest variance and highest RMSE for max-θ_e (Figure 1e and Figure 4), and grid-cells within Illinois (IL) are generally characterized by large RMSE and variance of min-θ_e (Figure 1f and Figure 5). Thus, while noting the RMSE (i.e. typical prediction error) is largest over Iowa (IA) for max-θ_e (~ 5 K), it is less than half the standard deviation computed from the day-to-day variability in max-θ_e (~ 10 K).

Generally all of the transfer functions exhibit slightly worse performance across both measures (r and RMSE) for min-θ_e than max-θ_e at the grid-cell level and integrated over all land grid cells (Table 1 and Figures 4 and 5). The reduced model skill for min-θ_e may reflect use of output at 20:00 UTC values of the predictors used in the synoptic classification due to our particular focus on daytime max-θ_e.

Although performance differences between the five transfer function architectures for daily maximum-θ_e and daily minimum-θ_e are comparatively modest when averaged over the entire domain (Table 1), there are important regional variations in the performance of the different model functional forms. Over two-thirds of all grid cells (1332 of

1962) exhibit lower RMSE in the ANN model with 3 hidden layers and including *SM* (i.e. ANN-HL3-SM) than in any of the other transfer functions (e.g. in the linear model, MLR). The enhancement of model performance as measured by a decrease in RMSE for the more complex model of max-θ_e and min-θ_e is particularly marked in the west-central of the domain (over parts of Missouri (MO) and Iowa (IA), close to or within one of the 'warming holes') (Figure 4 and 5). This is a region for which prior research has indicated a substantial fraction of the temperature variance is explained by thermal and moisture advection by the GPLLJ (Weaver, 2013), where land-atmosphere coupling is particularly intense (Koster et al., 2011;Koster et al., 2006) and where there are strong horizontal gradients of *SM* (Figure 1g). Lowest correlations between predicted and observed min- and max-θ_e values occur over east Texas (TX) for all model formulations although the RMSE of model predictions are not particularly high in this area (Figure 4 and 5). The causes of this finding are not fully understood. However, the low RMSE may reflect the small day-to-day variability in min- and max-θ_e over eastern Texas (TX) (Figure 1e and f), possibly due to the proximity to the ocean, while the low correlation coefficients may indicate that the synoptic types derived herein are not able to represent mesoscale features such dry lines that play a key role in dictating day-to-day variability in θ_e over this sub-region. It is also worthy of note that this area was excluded from the eastern US in terms of the area of coherence for extreme *T* over the eastern USA (McKinnon et al., 2016) and that eastern Texas (TX) is on the southwestern boundary of the study domain. These two factors may indicate that the synoptic types derived herein do not fully represent the range of meteorological conditions associated with θ_e variability.

Interpreting weights from complex ANN is very challenging in the context of predictor relevance and the values (and sign) of the weights vary in space and with the complexity of the model architecture (number of hidden layers). However, it is worthy of note that the weights on the index of global temperatures (and thus expression of internal climate modes) in ANN-HL3-SM are uniformly close to zero across the grid-cells in the interior of the continent, but are of large magnitude in land grid cells close to the Gulf of Mexico (i.e. the south of the domain) and around the Great Lakes. Given this index is strongly influenced by global sea surface temperatures (SST), the implication is that this predictor contains important information about the SST and thus evaporation from the Great Lakes and the Gulf of Mexico.

Consistent with prior research that has indicated the importance of atmosphere-surface interactions (Cai et al., 2014) and specifically soil moisture (Pryor et al., 2016;Seneviratne et al., 2010) in surface energy partitioning and thus near-surface *T* and *Q* regimes and static energy, exclusion of *SM* from the ANN with 3 hidden layers (i.e. ANN-HL3) decreases model performance relative to the ANN-HL3-SM and increases the RMSE for max-θ_e in 70% of grid cells. The regions for which this impact is most strongly manifest are close to or within the 'warming holes' decribed above and/or are located downstream of regions of significant county-level irrigation and anthropogenic enhancement of *SM* (Pryor et al., 2016) (Figure 1g). For example, RMSE for max-θ_e is increased in transfer models excluding *SM* in all grid cells within Missouri (MO), and all but one grid cell each in Iowa (IA) and Illinois (IL) (Figure 4). This finding is also replicated in the second region of weak or negative air temperature trends described above and centered on Mississippi (MS) and Alabama (AL) (Ellenburg et al., 2016). The RMSE is lower in ANN-HL3-SM than ANN-HL3 over all but one grid cell in these two states. Thus this analysis strongly supports prior assertions that *SM* plays a key role in dictating the surface energy balance and in the suppression of daily maximum

T, while increasing max-θ_e.

The statistical transfer function (downscaling) models show similar dynamic range to independent observations, although there is some evidence that the transfer functions underestimate the total variance in max-θ_e leading to underestimation of extreme max-θ_e as is evident from the flattening of the scatterplots for very high values of daily maximum θ_e (see the upper row of panels in Figure 4). To examine this further we conduct an analysis of the *HR* and *FAR* for max-θ_e in excess of 347 K. This threshold is exceeded by daily maximum θ_e derived from the MERRA-2 reanalysis on an average of ~ 15% of summer days when all grid-cells are considered, but naturally exhibits a higher frequency of exceedance (of up to 75% of days) along the southeastern portion of the Texas (TX) gulf coast and is observed on nearly 50% of days over coastal portions of the Gulf coast states and Florida (FL) (Figure 6a). Conversely, it is seldom or never observed within grid cells in the north of the domain (Figure 6a). To ensure a sufficiently robust sample size on which to compute the *HR* for extreme max-θ_e we consider only grid cells where more than 40 days in the test period (i.e. 8%) exceed this threshold. The mean *HR* values for the linear model (MLR), the ANN with 3-hidden layers (ANN-HL3-SM), and the ANN with 3-hidden layers but excluding SM (ANN-HL3) computed over all these grid cells is 59, 60 and 56%, respectively (Figure 6b-d), indicating that over the entire study domain the role of SM and predictor interactions in explaining the occurrence of extreme max-θ_e is modest. All model forms perform least well in terms of predicting the occurrence of max-θ_e > 347 K over eastern Texas (TX) and South Carolina (SC) (Figure 6e-g). However, the model excluding *SM* exhibits particularly poor performance (low *HR*) in these regions. The causes of the poor model performance in eastern Texas (TX) and Southern Carolina are currently not fully understood, although it is worthy of note that data from MERRA-2 grid-cells in South Carolina (SC) exhibit a relatively low overall frequency of exceedance of this threshold and are also characterized by comparatively low 99th percentile θ_e in an analysis of heat indices derived from the Community Land Model v4.5 (Buzan et al., 2015). Grid cells along the Gulf coast and over the states of Missouri (MO), Iowa (IA) and Illinois (IL) exhibit high *HR* for prediction of extreme max-θ_e and substantial improvement in *HR* is noted in Iowa (IA), Illinois (IL) and Missouri (MO) (Figure 6e-g) in the ANN-HL3-SM relative to the other model forms. This is consistent with strong spatial gradients in *SM* (Figure 1e), findings of the GLACE projects of strong atmosphere-surface coupling (Koster et al., 2011;Koster et al., 2006), and analyses for stations in Illinois (IL) that also show a strong dependence of high T_e on soil moisture (Ford and Schoof, 2016). To contextualize the *HR* presented above it is important to note that they are associated with comparatively low false alarm rates (*FAR*). Indeed, *FAR* for the occurrence of min-θ_e > 342 K or max-θ_e > 347 K are very modest for all model formulations (Figure 6 and 7). For example, over 94% of grid cells indicate *FAR* for max-θ_e > 347 K that are below 0.25 for the ANN-HL3-SM transfer functions. Thus, the relatively high *HR* reported herein are not being artificially inflated by unrealistically high predictions of the occurrence of extreme θ_e. The inclusion of *SM* as a predictor greatly enhances *HR* in regions previously identified as exhibiting high variance in extreme θ_e without a concomitant increase in *FAR* (Figure 6 and 7). It should be acknowledged that even the ANN with 3 hidden layers and soil moisture (ANN-HL3-SM) exhibits a modal grid-cell *HR* of 0.6-0.7, and thus misses a substantial fraction of extreme θ_e. Nevertheless, these *HR* and *FAR* are indicative of positive Relative Operating Characteristics (ROC) (i.e. plots of the true positive

rate greatly exceeds false positive rates) (Wilks, 2011). Further, *HR* and *FAR* are comparable to (or better than) seasonal re-forecasts of summertime *T* at 2-m over the land areas of Southern Europe developed using the European Centre for Medium-Range Weather Forecasts (ECMWF) seasonal ensemble forecasting system (Weisheimer et al., 2011).

In contrast to the results for prediction of extreme max-θ_e the model architecture has virtually no impact on *HR* for min-θ_e > 342 K, and neither does the inclusion of *SM* in the model. In all cases the domain averaged *HR* = 59% and no region exhibits consistent improved or degraded performance for ANN-HL3-SM or ANN-HL3 over MLR (Figure 7). This finding is consistent with the overall results for models of min-θ_e that exhibit only modest decreases in model performance (increased RMSE and lower r) when *SM* is excluded from the predictor suite (Table 1 and Figure 5). Consistent with the interpretation of the surface energy balance (Eq 2) this re-emphasizes that *SM* more directly impacts near-surface *T* and *Q* during the daytime under conditions of positive net radiation.

Differences in model performance between ANN conditioned on total *SM* and using wetness only in the top soil layer (upper 5 cm) are very small when averaged across the domain (Table 1) and indeed for virtually all grid cells. Only 26 grid cells exhibited a Δ|RMSE| > 0.5 K for models using PRMC versus those using GWETTOP (out of a total of 1962), while 155 exhibited an increase in RMSE > 0.5 K when *SM* was excluded from the model. Thus, although the weights within the ANNs differ for use of the two *SM* parameters, the overall model skill is unchanged by use of the two *SM* estimates possibly due to the spatial and temporal averaging applied herein, or uncertainty in reanalysis-derived *SM* variables.

4 Conclusions

Very few statistical downscaling analyses focus on integrative variables such as θ_e that explicitly incorporate co-variability of *T* and *Q*, but such variables have direct applications to climate change impact analyses (such as analysis of heat waves (Buzan et al., 2015)). Further, this is an application of climate downscaling where statistical approaches may be particularly useful given evidence that even when nested within observed lateral boundary conditions Regional Climate Models (RCMs) have difficulty in capturing the joint probability distributions of *T* and *Q* and thus in accurately representing either the probability distribution of static energy or the spatio-temporal variability therein (Pryor and Schoof, 2016). Analyses of θ_e are also essential to advancing fundamental understanding of changes in the total static energy content of the lower atmosphere, and may reveal important information of relevance to both model performance analyses and attribution studies of global change.

The goal of this work is to develop a hierarchy of statistical models with increasing complexity and use them to determine the degree to which increased complexity enhances the skill of model predictions of θ_e and to attribute variability in min- and max-θ_e over eastern North America. Prior to discussing the results from application of this analysis framework to output from the EMRRA-2 reanalysis it is worthy of note that previous research on regional heat wave characteristics over the contiguous US using a suite of reanalyses indicated some important differences in the magnitude of derived equivalent temperature (T_e) between the reanalysis products (Schoof et al., 2017). Thus, there would be value in applying this framework to additional observationally constrained data sets to evaluate the

degree to which the findings of a key role of *SM* to determining the model skill for daily maximum θ_e in specific sub-regions are generalizable and spatially consistent between reanalyses and equally to determine if the partial truncation of the upper percentiles of daily maximum θ_e in the model predictions is also a generalizable finding when our model framework is applied to different data sets.

Consistent with our *a priori* expectations, transfer functions built using ANN out-perform those that do not permit interaction of the predictor variables. Domain averaged RMSE for min- and max-θ_e is smallest in the more complex models (i.e. for an ANN with 3 hidden layers, RMSE < 4 K and < 4.3 K, respectively, c.f. mean max-$\theta_e \approx$ 333 K and mean min-$\theta_e \approx$ 321 K). Particularly in regions with high variability in min- and max-θ_e the more complex models with multiple hidden layers are better able to capture the day-to-day variability in θ_e. Correlation coefficients exceed 0.8 for 84% of grid cells for ANN-HL3-SM applied to max-θ_e and 81% for min-θ_e and 92% of grid cells for ANN-HL3-SM exhibit a RMSE < 5 K for max-θ_e and 91% for min-θ_e. This is also true for the simulation of extreme min- and max-θ_e. The ANN with 3 hidden layers and that includes *SM* as a predictor exhibits a domain averaged median hit rate for max-θ_e > 347 K is > 0.60, while the median FAR $\approx$ 0.08. Results from the ANN models further indicate that max-θ_e and the occurrence of extreme max-θ_e appear to be considerably more sensitive to *SM* than min-θ_e which in turn exhibits a stronger dependence on the precise prevailing synoptic scale conditions.

We can not conclusively discount contributions from other phenomena to the occurrence of 'warming holes' (areas with declining or no-trends in *T*) (Meehl et al., 2015), or that these features are a complex response to multiple drivers. However, results presented herein are consistent with past work that has indicated the importance of soil moisture (*SM*) in determining partitioning of the surface energy budget, and thus the spatiotemporal patterns of θ_e over the eastern USA (Koster et al., 2011;Koster et al., 2006;Pryor and Schoof, 2016;Pryor et al., 2016;Ford and Schoof, 2016, 2017;McKinnon et al., 2016). Indeed, *SM* is particularly important in determining the surface energy partitioning and the magnitude of θ_e over regions that have previously been identified as exhibiting 'warming holes', and for all grid cells the RMSE for models including *SM* as a predictor is smaller than the temporal variability of θ_e as measured using the standard deviation of the daily θ_e values. Specifically, only a model including *SM* is able to predict the occurrence of extreme (and highly health-relevant) values of θ_e over the western portion of Midwestern states such as Iowa (IA), Missouri (MO) and Illinois (IL), and in the states of Mississippi (MS) and Alabama (AL). This research thus implies that *SM* has played and may continue to play a key role in dictating the presence and intensity of 'warming holes' that have been previously noted in analyses of near-surface air temperature data (from both in situ measurements and reanalysis products).

The primary purposes of this research are to enhance mechanistic understanding of the causes of variability and change in θ_e over the eastern USA and to propose a new downscaling approach to allow projections of daily minimum and maximum θ_e using variables commonly available from reanalyses and global and regional climate models. However, these analyses also may have applications to short-term forecasting of human-health relevant heat events (McKinnon et al., 2016;Weisheimer et al., 2011), since the methodological framework developed herein could be applied to observed antecedent *SM*, and modeled forecasts of the global mean *T* and conditions at the synoptic scale over the eastern USA.

5 Data availability

The MERRA-2 data used herein are available from http://disc.sci.gsfc.nasa.gov/daac-bin/FTPSubset2.pl (see (Bosilovich et al., 2015) for a detailed description of the file structures).

6 Acknowledgments

The authors gratefully acknowledge funding from the US National Science Foundation under grants 1339655 and 1502400, the US Department of Energy (DE-SC0016438) and the US National Aeronautics and Space Administration (14-EARTH14F-0207). Any opinions, findings, and conclusions or recommendations expressed in this material are those of the authors and do not necessarily reflect the view of the National Science Foundation, National Aeronautics and Space Administration or Department of Energy.

7 References

Allen, M., and Ingram, W.: Constraints on future changes in climate and the hydrologic cycle, Nature, 419, 224-232, 2002.

Anderson, G. B., and Bell, M. L.: Heat waves in the United States: Mortality risk during heat waves and effect modification by heat wave characteristics in 43 U.S. communities, Environmental Health Perspectives, 119, 210-218, 2011.

Bentley, M. L., and Stallins, J. A.: Synoptic evolution of Midwestern US extreme dew point events, International Journal of Climatology, 28, 1213-1225, 2008.

Bosilovich, M. G., Lucchesi, R., and Suarez, M.: MERRA-2: File Specification, GMAO Office Note No. 9 (Version 1.0), 73 pp, available from http://gmao.gsfc.nasa.gov/pubs/office_notes., 2015.

Brabson, B., Lister, D., Jones, P., and Palutikof, J.: Soil moisture and predicted spells of extreme temperatures in Britain, Journal of Geophysical Research: Atmospheres, 110, doi: 10.1029/2004JD005156, 2005.

Buzan, J. R., Oleson, K., and Huber, M.: Implementation and comparison of a suite of heat stress metrics within the Community Land Model version 4.5, Geoscientific Model Development, 8, 151-170, 10.5194/gmd-8-151-2015, 2015.

Cai, X., Yang, Z. L., Xia, Y., Huang, M., Wei, H., Leung, L. R., and Ek, M. B.: Assessment of simulated water balance from Noah, Noah-MP, CLM, and VIC over CONUS using the NLDAS test bed, Journal of Geophysical Research: Atmospheres, 119, 13,751-713,770, 2014.

Cattell, R. B.: The scree test for the number of factors, Multivariate Behavioral Research, 1, 245-276, 1966.

Davey, C. A., Pielke, R. A., Sr., and Gallo, K. P.: Differences between near-surface equivalent temperature and temperature trends for the Eastern United States - Equivalent temperature as an alternative measure of heat content, Global and Planetary Change, 54, 19-32, 10.1016/j.gloplacha.2005.11.002, 2006.

de'Donato, F. K., Leone, M., Scortichini, M., De Sario, M., Katsouyanni, K., Lanki, T., Basagana, X., Ballester, F., Astrom, C., Paldy, A., Pascal, M., Gasparrini, A., Menne, B., and Michelozzi, P.: Changes in the effect of heat on

mortality in the last 20 years in nine European cities. Results from the PHASE project, Int. J. Environ. Res. Public Health, 12, 15567-15583, 10.3390/ijerph121215006, 2015.

Diem, J. E.: Synoptic-scale controls of summer precipitation in the Southeastern United States, Journal of Climate, 19, 613-621, 10.1175/jcli3645.1, 2006.

Ellenburg, W. L., McNider, R. T., Cruise, J. F., and Christy, J. R.: Towards an understanding of the twentieth-century cooling trend in the southeastern United States: Biogeophysical impacts of land-use change, Earth Interactions, 20, Paper 20-018, doi: 010.1175/ei-d-1115-0038.1171, 2016.

Fall, S., Diffenbaugh, N. S., Niyogi, D., Pielke, R. A., Sr., and Rochon, G.: Temperature and equivalent temperature over the United States (1979-2005), International Journal of Climatology, 30, 2045-2054, 10.1002/joc.2094, 2010.

Ford, T. W., and Schoof, J. T.: Oppressive Heat Events in Illinois Related to Antecedent Wet Soils, Journal of Hydrometeorology, 17, 2713-2726, 2016.

Ford, T. W., and Schoof, J. T.: Characterizing extreme and oppressive heat waves in Illinois, Journal of Geophysical Research: Atmospheres, 122, 682-698, 2017.

Garcia-Herrera, R., Diaz, J., Trigo, R. M., Luterbacher, J., and Fischer, E. M.: A review of the European summer heat wave of 2003, Crit. Rev. Environ. Sci. Technol., 40, 267-306, 2010.

Grotjahn, R., Black, R., Leung, R., Wehner, M. F., Barlow, M., Bosilovich, M., Gershunov, A., Gutowski Jr, W. J., Gyakum, J. R., and Katz, R. W.: North American extreme temperature events and related large scale meteorological patterns: a review of statistical methods, dynamics, modeling, and trends, Climate Dynamics, 46, 1151-1184, 2016.

Horton, R. M., Mankin, J. S., Lesk, C., Coffel, E., and Raymond, C.: A review of recent advances in research on extreme heat events, Current Climate Change Reports, 24, 242-259, 2016.

Huang, J. P., Xie, Y. K., Guan, X. D., Li, D. D., and Ji, F.: The dynamics of the warming hiatus over the Northern Hemisphere, Climate Dynamics, 48, 429-446, 10.1007/s00382-016-3085-8, 2017.

Kalkstein, L. S., Sheridan, S. C., and Graybeal, D. Y.: A determination of character and frequency changes in air masses using a spatial synoptic classification, International Journal of Climatology, 18, 1223-1236, 1998.

Kalnay, E., and Cai, M.: Impact of urbanization and land-use change on climate, Nature, 423, 528-531, 2003.

Knist, S., Goergen, K., Buonomo, E., Christensen, O. B., Colette, A., Cardoso, R. M., Fealy, R., Fernandez, J., Garcia-Diez, M., Jacob, D., Kartsios, S., Katragkou, E., Keuler, K., Mayer, S., van Meijgaard, E., Nikulin, G., Soares, P. M. M., Sobolowski, S., Szepszo, G., Teichmann, C., Vautard, R., Warrach-Sagi, K., Wulfmeyer, V., and Simmer, C.: Land-atmosphere coupling in EURO-CORDEX evaluation experiments, Journal of Geophysical Research: Atmospheres, 122, 79-103, 2017.

Koster, R. D., Sud, Y., Guo, Z., Dirmeyer, P. A., Bonan, G., Oleson, K. W., Chan, E., Verseghy, D., Cox, P., and Davies, H.: GLACE: the global land–atmosphere coupling experiment. Part I: overview, Journal of Hydrometeorology, 7, 590-610, 2006.

Koster, R. D., Mahanama, S., Yamada, T., Balsamo, G., Berg, A., Boisserie, M., Dirmeyer, P., Doblas-Reyes, F., Drewitt, G., and Gordon, C.: The second phase of the global land–atmosphere coupling experiment: soil moisture contributions to subseasonal forecast skill, Journal of Hydrometeorology, 12, 805-822, 2011.

Lee, E., Bieda, R., Basara, H., and Shanmugasundaram, J.: Land surface and atmospheric conditions associated with heat waves over the Chickasaw Nation in the South Central United States, Journal of Geophysical Research: Atmospheres, 121, 6284-6298, 2016.

Leibensperger, E. M., Mickley, L. J., Jacob, D. J., Chen, W. T., Seinfeld, J. H., Nenes, A., Adams, P. J., Streets, D. G., Kumar, N., and Rind, D.: Climatic effects of 1950-2050 changes in US anthropogenic aerosols; Part 2: Climate response, Atmospheric Chemistry and Physics, 12, 3349-3362, 10.5194/acp-12-3349-2012, 2012.

Llamedo, P., Hierro, R., de la Torre, A., and Alexander, P.: ENSO-related moisture and temperature anomalies over South America derived from GPS radio occultation profiles, International Journal of Climatology, 37, 268-275, 10.1002/joc.4702, 2017.

Mann, M. E., Bradley, R. S., and Hughes, M. K.: Global-scale temperature patterns and climate forcing over the past six centuries, Nature, 392, 779-787, 1998.

Mansur, E. T., Mendelsohn, R., and Morrison, W.: Climate change adaptation: A study of fuel choice and consumption in the US energy sector, Journal of Environmental Economics and Management, 55, 175-193, 10.1016/j.jeem.2007.10.001, 2008.

McKinnon, K. A., Rhines, A., Tingley, M. P., and Huybers, P.: Long-lead predictions of eastern United States hot days from Pacific sea surface temperatures, Nature Geoscience, 9, 389-394, 10.1038/ngeo2687, 2016.

Meehl, G. A., Arblaster, J. M., and Chung, C. T. Y.: Disappearance of the southeast US "warming hole" with the late 1990s transition of the Interdecadal Pacific Oscillation, Geophysical Research Letters, 42, 5564-5570, 10.1002/2015gl064586, 2015.

Molod, A., Takacs, L., Suarez, M., and Bacmeister, J.: Development of the GEOS-5 atmospheric general circulation model: evolution from MERRA to MERRA2, Geoscientific Model Development, 8, 1339-1356, 2015.

O'Neill, M. S., and Ebi, K. L.: Temperature Extremes and Health: Impacts of Climate Variability and Change in the United States, Journal of Occupational and Environmental Medicine, 51, 13-25, 10.1097/JOM.0b013e318173et22, 2009.

O'Neill, M. S., Jackman, D. K., Wyman, M., Manarolla, X., Gronlund, C. J., Brown, D. G., Brines, S. J., Schwartz, J., and Diez-Roux, A. V.: US local action on heat and health: are we prepared for climate change?, International Journal of Public Health, 55, 105-112, 10.1007/s00038-009-0071-5, 2010.

Pan, Z. T., Segal, M., Li, X., and Zib, B.: Global climate change impact on the Midwestern USA - A summer cooling trend, in: Understanding Climate Change:Climate variability, predictability and change in the Midwestern United States, edited by: Pryor, S. C., Indiana University Press, Bloomington, IN, 29-41, 2009.

Papageorgiou, E. I., and Poczeta, K.: A two-stage model for time series prediction based on fuzzy cognitive maps and neural networks, Neurocomputing, 232, 113-121, 10.1016/j.neucom.2016.10.072, 2017.

Peterson, T. C., Willett, K. M., and Thorne, P. W.: Observed changes in surface atmospheric energy over land, Geophysical Research Letters, 38, doi: 10.1029/2011GL048442, 2011.

Peterson, T. C., Alexander, L. V., Allen, M. R., Anel, J. A., Barriopedro, D., Black, M. T., Carey-Smith, T., Castillo, R., Cattiaux, J., Chen, X. L., Chen, X. Y., Chevallier, M., Christidis, N., Ciavarella, A., de Vries, H., Dean, S. M., Deans, K., Diffenbaugh, N. S., Doblas-Reyes, F., Donat, M. G., Dong, B., Eilerts, G., Funk, C., Galu, G., Garcia-

Herrera, R., Germe, A., Gill, S., Gimeno, L., Guemas, V., Herring, S. C., Hoell, A., Hoerling, M. P., Huntingford, C., Husak, G., Imada, Y., Ishii, M., Karoly, D. J., Kimoto, M., King, A. D., Knutson, T. R., Lewis, S. C., Lin, R. P., Lyon, B., Massey, N., Mazza, E., Michaelsen, J., Mollard, J., Mori, M., Mote, P. W., Nieto, R., Otto, F. E. L., Park, J., Perkins, S. E., Rosier, S., Rowland, J., Rupp, D. E., Salas y Melia, D., Scherer, M., Shiogama, H., Shukla, S., Song, F. F., Sparrow, S., Scott, P. A., Sutton, R., Sweet, W., Tett, S. F. B., Trigo, R. M., van Oldenborgh, G. J., van Westrhenen, R., Verdin, J., Watanabe, M., Wittenberg, A. T., Woollings, T., Yiou, P., Zeng, F. R., Zervas, C., Zhang, R., and Zhou, T. J.: Explaining extreme events of 2012 from a climatic perspective, Bulletin of the American Meteorological Society, 94, S1-S74, 10.1175/bams-d-13-00085.1, 2013.

Pielke, R. A., Davey, C., and Morgan, J.: Assessing "global warming" with surface heat content, Eos, Transactions American Geophysical Union, 85, 210-211, 2004.

Pryor, S. C., and Schoof, J. T.: Evaluation of near-surface temperature, humidity, and equivalent temperature from regional climate models applied in type II downscaling, Journal of Geophysical Research: Atmospheres, 121, 3326-3338, 2016.

Pryor, S. C., Sullivan, R. C., and Wright, T.: Quantifying the roles of changing albedo, emissivity, and energy partitioning in the impact of irrigation on atmospheric heat content, Journal of Applied Meteorology and Climatology, 55, 1699-1706, 2016.

Reichle, R. H., Draper, C. S., Liu, Q., Griotto, M., Mahanama, S. P. P., Hoster, R. D., and Lannoy, G. J. M.: Assessment of MERRA-2 land surface hydrology estimates, Journal of Climate, In press: JCLI-D-16-0720, 2017.

Ribera, P., Gallego, D., Gimeno, L., Perez-Campos, J., García-Herrera, R., Hernández, E., de La Torre, L., Nieto, R., and Calvo, N.: The use of equivalent temperature to analyse climate variability, Studia Geophysica et Geodaetica, 48, 459-468, 2004.

Richman, M. B.: Rotation of principal components, Journal of Climatology, 6, 293-335, 1986.

Rogers, J. C., Wang, S. H., and Coleman, J. S. M.: Evaluation of a long-term (1882-2005) equivalent temperature time series, Journal of Climate, 20, 4476-4485, 2007.

Sanderson, M. G., and Ford, G. P.: Projections of severe heat waves in the United Kingdom, Climate Research, 71, 63-73, 10.3354/cr01428, 2017.

Schoof, J. T., Heern, Z. A., Therrell, M. D., and Remo, J. W. F.: Assessing trends in lower tropospheric heat content in the central United States using equivalent temperature, International Journal of Climatology, 35, 2828-2836, 2015.

Schoof, J. T., Ford, T., and Pryor, S. C.: Recent changes in United States heat wave characteristics derived from multiple reanalyses, Journal of Applied Meteorology and Climatology, In review, 2017.

Seneviratne, S. I., Corti, T., Davin, E. L., Hirschi, M., Jaeger, E. B., Lehner, I., Orlowsky, B., and Teuling, A. J.: Investigating soil moisture–climate interactions in a changing climate: A review, Earth-Science Reviews, 99, 125-161, 2010.

Sheridan, S. C.: North American weather-type frequency and teleconnection indices, International Journal of Climatology, 23, 27-45, 2003.

Sheridan, S. C., Kalkstein, A. J., and Kalkstein, L. S.: Trends in heat-related mortality in the United States, 1975–2004, Natural Hazards, 50, 145-160, 2009.

Su, C. H., Ryu, D., Dorigo, W., Zwieback, S., Gruber, A., Albergel, C., Reichle, R. H., and Wagner, W.: Homogeneity of a global multisatellite soil moisture climate data record, Geophysical Research Letters, 43, 11245-11252, 10.1002/2016gl070458, 2016.

Teng, H., Branstator, G., Wang, H., Meehl, G. A., and Washington, W. M.: Probability of US heat waves affected by a subseasonal planetary wave pattern, Nature Geoscience, 6, 1056-1061, 2013.

Toth, E., Brath, A., and Montanari, A.: Comparison of short-term rainfall prediction models for real-time flood forecasting, Journal of Hydrology, 239, 132-147, 2000.

Trenberth, K. E.: Recent observed interdecadal climate changes in the Northern Hemisphere, Bulletin of the American Meteorological Society, 71, 988-993, 1990.

Vanos, J., Kalkstein, L., and Sanford, T.: Detecting synoptic warming trends across the US Midwest and implications to human health and heat-related mortality, International Journal of Climatology, 35, 85-96, 2015.

Weaver, S. J.: Factors associated with decadal variability in Great Plains summertime surface temperatures, Journal of Climate, 26, 343-350, 10.1175/jcli-d-11-00713.1, 2013.

Weisheimer, A., Doblas-Reyes, F. J., Jung, T., and Palmer, T.: On the predictability of the extreme summer 2003 over Europe, Geophysical Research Letters, 38, doi: 10.1029/2010GL046455, 2011.

Wilks, D. S.: Statistical methods in the atmospheric sciences, International geophysics series, Academic press, Oxford, UK, 2011.

Willett, K. M., Gillett, N. P., Jones, P. D., and Thorne, P. W.: Attribution of observed surface humidity changes to human influence, Nature, 449, 710-712, 2007.

Yu, S., Alapaty, K., Mathur, R., Pleim, J., Zhang, Y., Nolte, C., Eder, B., Foley, K., and Nagashima, T.: Attribution of the United States “warming hole”: Aerosol indirect effect and precipitable water vapor, Scientific Reports, 4, Article # 6929, doi:6910.1038/srep06929, 2014.

Zhang, K., Li, Y., and Schwartz, J. D.: What weather variables are important in predicting heat-related mortality? A new application of statistical learning methods, Environmental Research, 132, 350-359, 2014.

Table 1. Domain averaged model performance statistics (root mean square error (RMSE) and Pearson correlation coefficient (r)) versus independent test data for daily maximum equivalent potential temperature (max-θ_e) and daily minimum equivalent potential temperature (min-θ_e). The results are shown for the five model formulations expressed in terms of the number of hidden layers in the ANN (where 0 hidden layers indicates results for a multiple linear regression model with no term interactions), the presence of absence of soil moisture as a predictor and whether the *SM* is total columnar (PRMC) or surface only (WGETTOP).

Abbreviation used herein	Model architecture	Soil moisture predictor	max-θ_e			min-θ_e		
			<RMSE> (K)	<r>	# grid cells with r>0.8 & RMSE < 5K	<RMSE> (K)	<r>	# grid cells with r>0.8 & RMSE < 5K
MLR	Multiple linear regression	PRMC	4.05	0.849	1575, 1727	4.39	0.836	1537, 1665
ANN-HL1-SM	ANN with 1 hidden layer	PRMC	4.03	0.850	1602, 1754	4.34	0.839	1572, 1750
ANN-HL3-SM	ANN with 3 hidden layers	PRMC	3.97	0.855	1621, 1798	4.29	0.844	1588, 1782
ANN-HL3	ANN with 3 hidden layers, but excluding *SM*	None	4.10	0.846	1549, 1675	4.33	0.843	1580, 1765
ANN-HL3-TOP	ANN with 3 hidden layers	WGETTOP	3.97	0.856	1623, 1802	4.29	0.844	1604, 1782

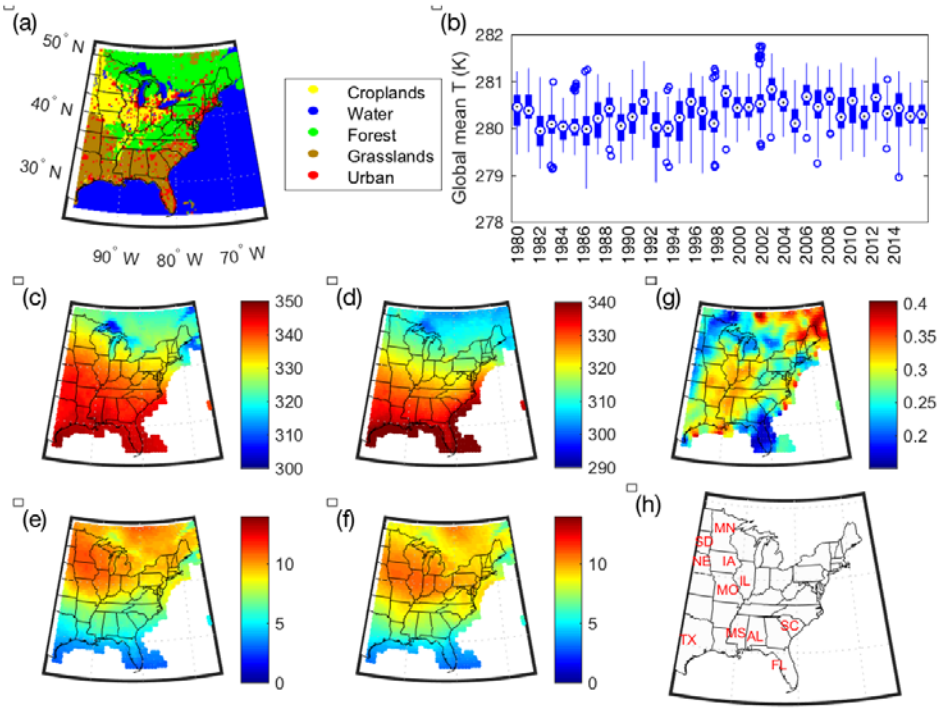

Figure 1. (a) The study domain used herein and five consolidated land use land-cover (LULC) classes as represented at a resolution of 0.05×0.05° from the MODIS land cover data set for 2014 (MCD12C). (b) A boxplot of daily global mean JJA temperature values (K) (1980-2014) as computed from the MERRA-2 output. (c) Mean summertime (JJA) maximum-θ_e and (d) minimum-θ_e (K) as computed from hourly T and Q at 2-m and surface pressure (P) in each MERRA-2 grid cell. Standard deviation of daily (e) maximum-θ_e and (f) minimum-θ_e (K). (g) Mean soil moisture estimates from MERRA-2 used as a predictor in the ANN and computed as follows: the daily mean value for total profile soil moisture content (PRMC) for each grid cell is averaged over a spatial area of 3×3 grid cells centered on the grid cell of interest, and used to compute a 90-day running JJA mean soil moisture (m^3m^{-3}). Panel (h) shows the location of states that are explicitly referred to herein.

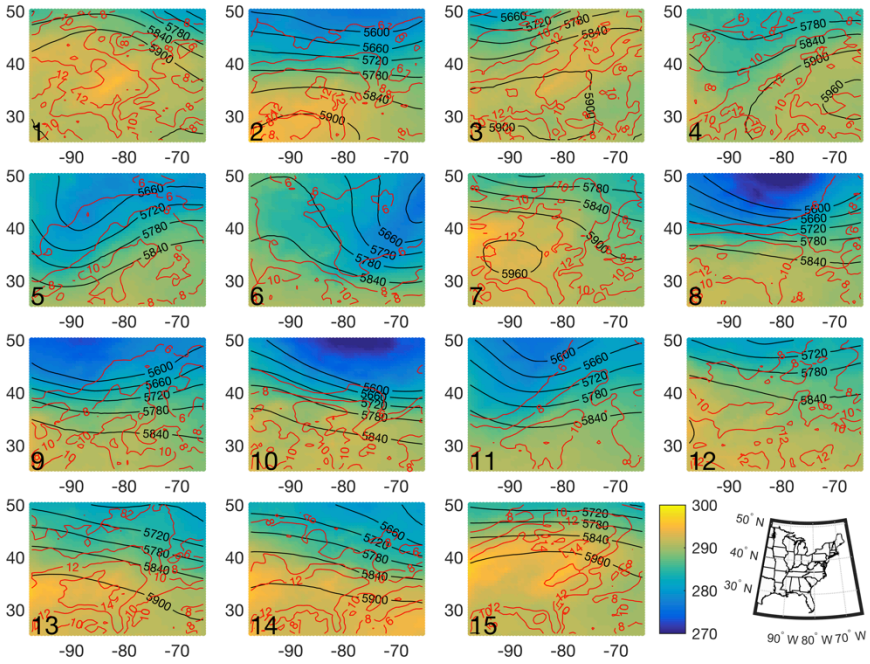

Figure 2. Summary of the conditions under each of the PCA-derived synoptic modes of variability. The panels show the "mode centroid" (i.e. mean of the 7 days that exhibit highest PC scores for the type). The color depicts T_{850} (K), the solid black lines show Z_{500} (gpm) and the red lines depict Q_{850} (gKg^{-1}). The PC number is shown in the lower left of each panel and the panels are arranged so that the first mode of variability is shown in the upper left panel, the fifth PC is shown in the second row in the left most panel and so forth. To aid legibility, the panels in this figure denote the study region as a rectangle, with state outlines excluded, thus also shown in the lower right of this figure is a map depicting the state outlines for the same domain as shown in the other panels but using a Plate Carree projection (i.e. the equi-rectangular projection) used in Figures 1, 4, 5, 6 and 7.

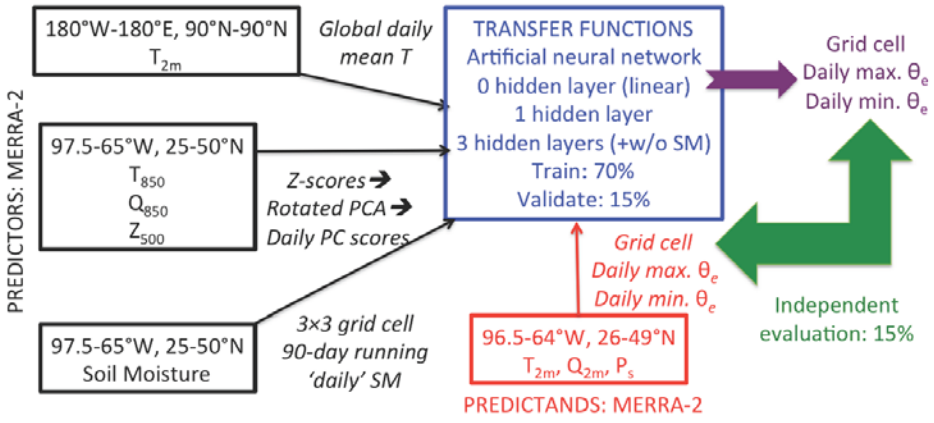

Figure 3. Schematic of the ANN model architecture, data flow, predictors and predictands.

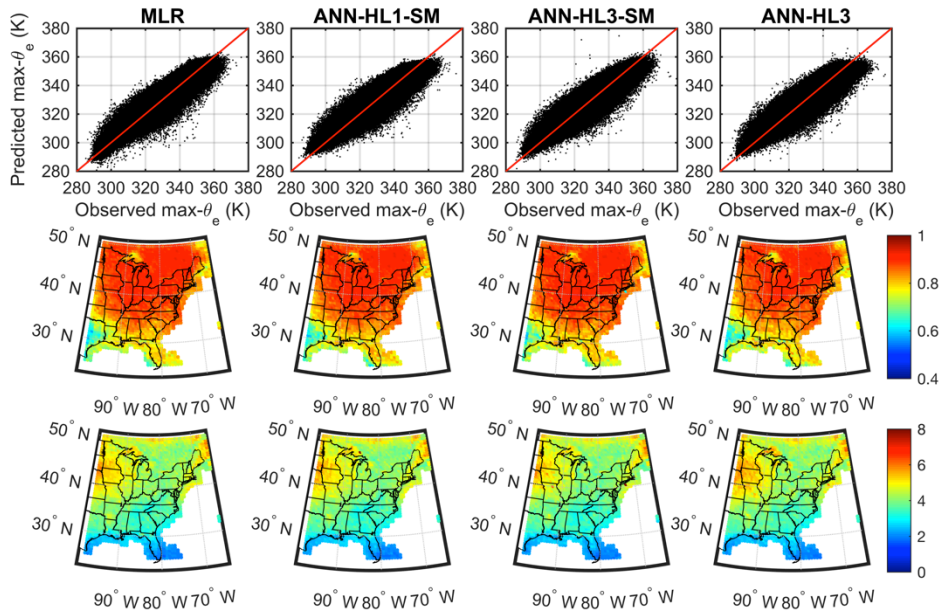

Figure 4. Précis of the downscaling model performance for daily maximum-θ_e (max-θ_e). The upper panels show scatterplots of observed and predicted max-θ_e for all grid cells and all days within the test (independent) data, along with a red 1:1 line. The columns show results for four model configurations: multiple linear regression (MLR, left), ANN with 1-hidden layer (ANN-HL1-SM, second column), ANN with 3-hidden layers (ANN-HL3-SM third column) and ANN with 3-hidden layers but excluding information regarding the soil moisture (ANN-HL3 right column). The second row shows the Pearson correlation (r) of predicted and observed max-θ_e values in the independent data for the four different models, while the third row shows the mean root mean square error (RMSE) (K) computed for independent data from each grid cell for the four models.

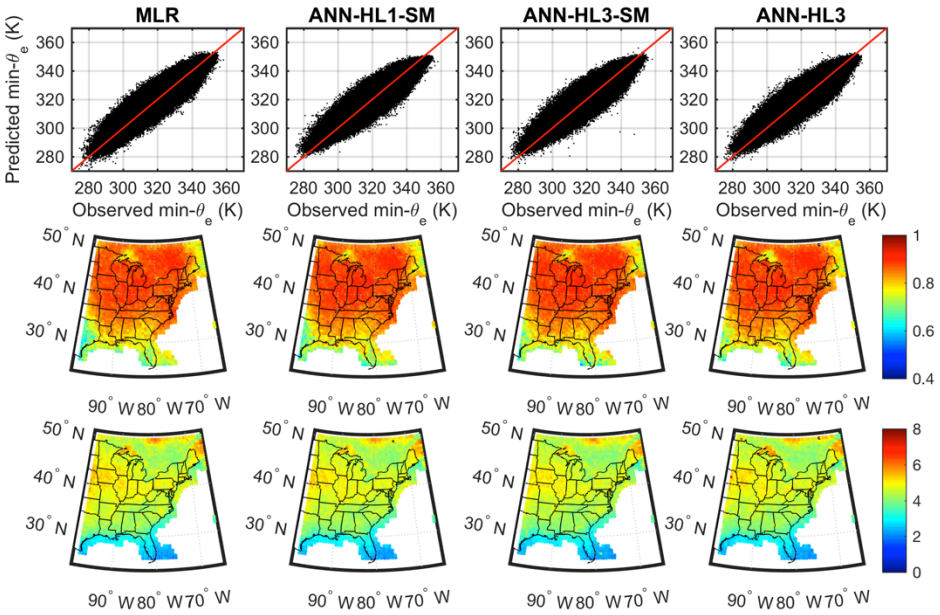

Figure 5. Précis of the downscaling model performance for daily minimum-θ_e (min-θ_e). The upper panels show scatterplots of observed and predicted min-θ_e for all grid cells and all days within the test (independent) data, along with a red 1:1 line. The columns show results for four model configurations: multiple linear regression (MLR, left), ANN with 1-hidden layer (ANN-HL1-SM, second column), ANN with 3-hidden layers (ANN-HL3-SM third column) and ANN with 3-hidden layers but excluding information regarding the soil moisture (ANN-HL3 right column). The second row shows the Pearson correlation (r) of predicted and observed min-θ_e values in the independent data for the four different models, while the third row shows the mean root mean square error (RMSE) (K) computed for independent data from each grid cell for the four models.

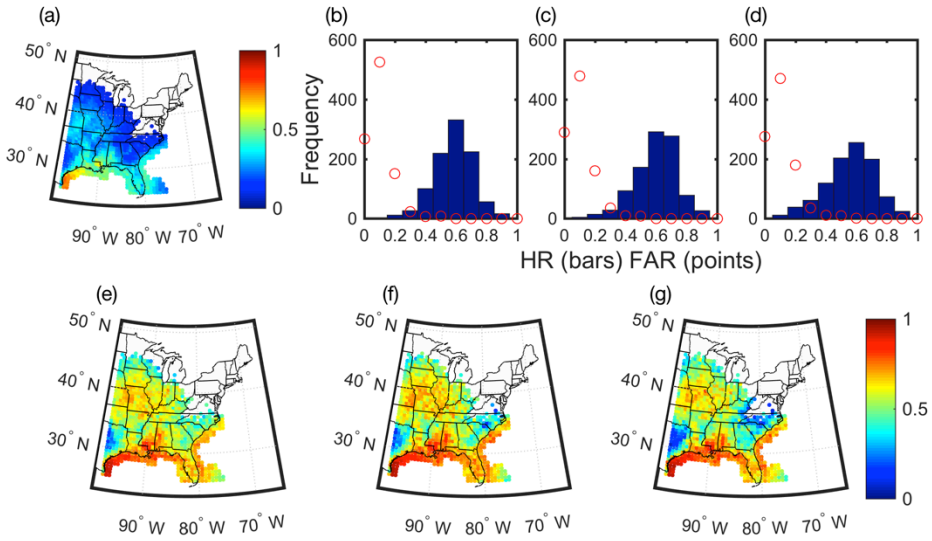

Figure 6. (a) Map of the fractional frequency of occurrence of max-θ_e > 347 K in each grid cell based on the independent (test) data set. (b) Histogram of hit rate (*HR*) and false alarm rate (*FAR*) for all grid cells and (e) spatial map for correct identification of max-θ_e>347 K for all grid cells where this threshold is exceeded by >8% of days in the independent data based on output from the multiple linear regression model (MLR). (c) and (f) As in panels (b) and (e) but for output from the ANN model with 3 hidden layers and including *SM* (ANN-HL3-SM). (d) and (g) As in panels (b) and (e) but for output from the ANN model with 3 hidden layers excluding *SM* (ANN-HL3).

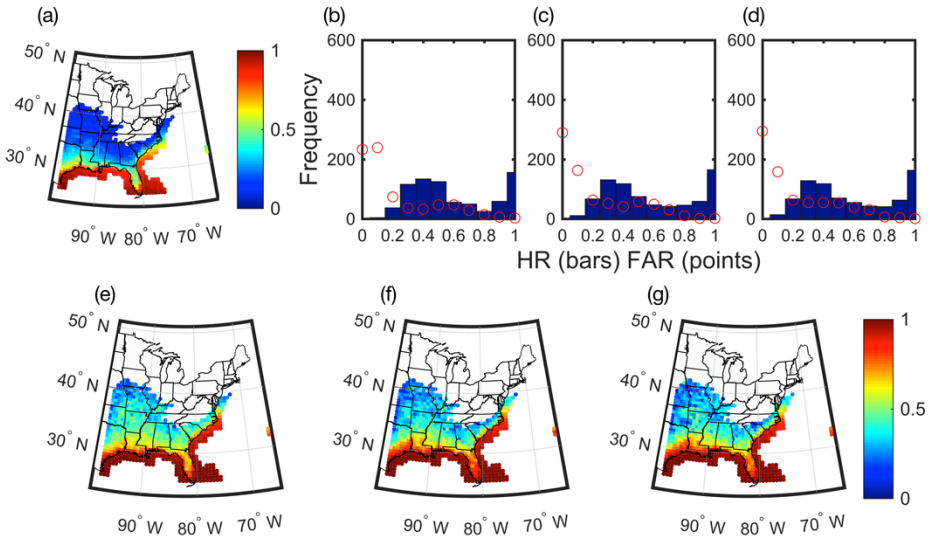

Figure 7. (a) Map of the fractional frequency of occurrence of min-θ_e > 337 K in each grid cell based on the independent (test) data set. (b) Histogram of hit rate (*HR*) and false alarm rate (*FAR*) for all grid cells and (e) spatial map for correct identification of min-θ_e>337 K for all grid cells where this threshold is exceeded by >8% of days in the independent data based on output from the multiple linear regression model (MLR). (c) and (f) As in panels (b) and (e) but for output from the ANN model with 3 hidden layers and including *SM* (ANN-HL3-SM). (d) and (g) As in panels (b) and (e) but for output from the ANN model with 3 hidden layers excluding *SM* (ANN-HL3).

APPENDIX F

ATMOSPHERIC CHEMISTRY

Pryor S. C., Crippa P., and **Sullivan, R. C.** (2015). Atmospheric chemistry. *In: Elsevier's Reference Module in Earth Systems and Environmental Sciences* (Available at http://www.sciencedirect.com/science/article/pii/B9780124095489091776). Edited by J.T. Schoof. doi:10.1016/B978-0-12-409548-9.09177-6.

Atmospheric Chemistry

SC Pryor, Cornell University, Ithaca, NY, USA
P Crippa, Newcastle University, Newcastle upon Tyne, UK
RC Sullivan, Cornell University, Ithaca, NY, USA

Atmospheric chemistry is the branch of atmospheric science focused on chemical processes within the Earth's atmosphere, including photochemistry of gas compounds; the formation and properties of airborne aerosol particles; gas–particle interactions; cloud processes; emission, transport, and dispersion of chemical tracers; and biogeochemical cycles (i.e., interaction with the underlying surface). The motivations to understand these processes include the relevance to climate forcing, implications for human health, and reciprocal interactions with (i.e., exchange of mass with) the biosphere and hence terrestrial and marine ecosystem health.

Atmospheric Gases

Although the majority of the gas molecules that comprise the Earth's atmosphere are nitrogen (N_2) and oxygen (O_2) (nearly 99% of the atmosphere by mass), hundreds of gas-phase species have been detected in the atmosphere. The concentration and environmental importance of these low abundance gases vary in space and time. However, it is these trace species that drive much of the chemistry of the atmosphere. As an example, the hydroxyl radical (OH) is responsible for a large fraction of all oxidation reactions in the atmosphere (and hence is often referred to as the 'atmosphere's detergent'). However, it is typically present at concentrations below 1×10^5 molecules per cm^3 (i.e., typically fewer than four in one quadrillion (10^{15}) gas molecules in the lower atmosphere are OH).

Gas molecules in the atmosphere are subject to physical removal processes (e.g., inclusion in cloud droplets and removal in precipitation), removal by contact with the surface (dry deposition), and/or chemical removal processes. Virtually, every gas that is emitted into the atmosphere will be chemically altered – either by photochemical processes (where sunlight strikes the molecule and has sufficient energy to break apart bonds within the molecule) or by interaction with another gas molecule and/or an aerosol particle. The likelihood of these interactions and the dominance of physical versus chemical removal are a function of the specific gas under consideration. Equally, the rate of removal of gases from the atmosphere to the Earth's land surface or oceans by physical processes is determined by properties such as the bonding structure of the gas molecule and the solubility. Hence, the atmospheric lifetime (residence time) of different gas molecules in the atmosphere ranges from fractions of a second to many thousands of years. The average atmospheric residence time for a given gas and/or aerosol particle of a given size is inversely related to removal rates and, in conjunction with the spatiotemporal variability and intensity of emission sources, determines the variability of the concentration of that atmospheric species in space and time (Figure 1). Gases with very low reactivity and solubility may become almost uniformly mixed throughout the Earth's atmosphere and even mix from the troposphere into the stratosphere (e.g., chlorofluorocarbons).

The environmental consequences of elevated concentrations of a particular gas are determined by factors such as atmospheric residence time, reactivity, toxicity, and the degree to which it interacts with radiation. For example, methane (CH_4) is the most abundant hydrocarbon (any compound that contains hydrogen and carbon atoms) in the Earth's atmosphere and is an important 'greenhouse gas' (i.e., a gas responsible for warming of Earth's atmosphere). Methane is responsible for anthropogenic (human-origin) radiative forcing of about 0.48 ± 0.05 W m^{-2}. For comparison, the radiative forcing from increased carbon dioxide (CO_2) (which is 200 times more abundant) is 1.82 ± 0.19 W m^{-2} (IPCC, 2013). The large contribution of CH_4 to anthropogenic 'global warming' is due to (i) its high radiative efficiency (i.e., the amount of radiation absorbed per unit mass of the gas), (ii) its relatively long atmospheric lifetime, and (iii) the rapid increase of atmospheric concentrations – from preindustrial concentrations of 722 ± 25 ppb to over 1800 ppb in 2011 (ppb, parts per billion; 1 ppb is equal to one in 10^9 molecules). Methane has a relatively long atmospheric lifetime (Figure 1) because it does not dissolve in water contained in clouds, rivers, and oceans (it is a nonpolar molecule), does not photochemically decompose, and has strong (saturated) chemical bonds that render it comparatively unreactive. Gases such as CH_4 are referred to as 'greenhouse gases' because they absorb passing infrared photons and convert

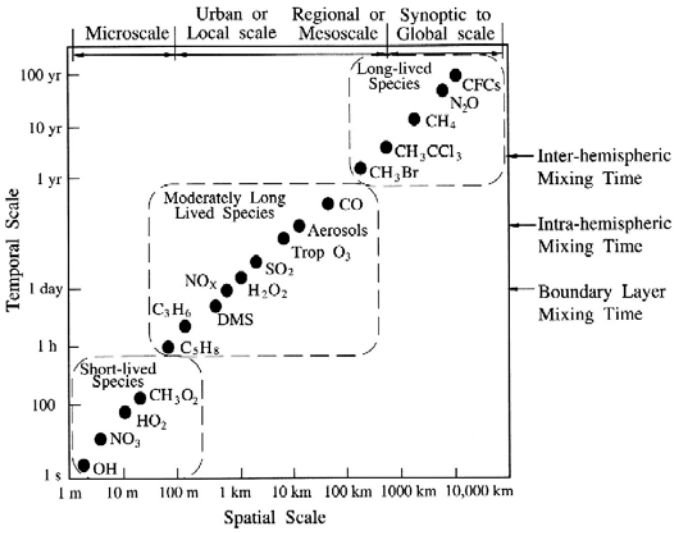

Figure 1 Spatial and temporal scales of variability of various atmospheric species. Reproduced from Seinfeld, J. H. and Pandis, S. N. (2006). *Atmospheric chemistry and physics: from air pollution to climate change* (2nd edn.). New York: Wiley. ISBN: 978-0-471-72018-8.

that energy into an excited vibrational state, thus trapping that energy in the atmosphere. A photon can only be absorbed by a molecule if the interaction between the radiation and the molecule leads to a transition from the molecule's original state to one of its other allowed states. Because of its molecular structure, CH_4 absorbs radiation at multiple wavelengths including 7.6 μm – which is a wavelength at which the Earth's surface emits a substantial amount of energy and that virtually no other atmospheric constituent absorbs. For this and other reasons, methane has a disproportionate impact on the climate of the Earth.

Atmospheric Aerosol Particles

Atmospheric aerosol particles are defined as any solid or liquid droplets suspended in the atmosphere. The size of aerosol particles ranges from diameters (Dp) of a few nanometers to diameters of several tens of micrometers (Figure 2), and hundreds of chemical compounds have been found in aerosol particles. Atmospheric aerosol particles, of both natural and anthropogenic origins, play a key role in the Earth's climate and human health impacts of decreased air quality. They are classified as being of primary origin if they are directly emitted into the atmosphere from either natural sources (e.g., volcano eruptions, sea spray, and erosion mechanisms) or anthropogenic processes (e.g., fuel combustion and industrial processes). Aerosol particles are referred to as secondary when formed in the atmosphere by chemical reactions. The chemical composition of atmospheric aerosol particles varies greatly by source. Primary aerosol particles from natural sources mostly comprise mineral dust and direct emissions from volcanoes (e.g., volcanic ash) and oceans (e.g., sea salt). Secondary natural aerosol particles are typically dominated by sulfate produced from reactions of dimethyl sulfide and other sulfur gases emitted by the oceans or volcanic sulfur dioxide (SO_2) oxidation and organic aerosol compounds formed from oxidation products of biogenic volatile organic compounds. Primary anthropogenic aerosol particles derive principally from combustion processes and are mostly black (elemental) carbon, whereas secondary anthropogenic aerosol particles tend to be dominated by sulfate and nitrate produced by oxidation of SO_2 and oxides of nitrogen (NO_x) emitted by human activities (often found in association with ammonium) and secondary organic components. The organic components comprise hundreds of different compounds formed when organic gases undergo reactions that typically lead to an increase in oxidation state and the products of which can partition to the aerosol particle phase depending on their volatility (Seinfeld and Pandis, 2006).

Most measurements indicate that sulfate, nitrate, and organic carbon constitute the majority of mass in both remote and urban areas. A key, and only partly understood, aspect of aerosol particle composition is whether atmospheric aerosol particle populations are largely externally or internally mixed – that is, does each particle in an ensemble have a similar composition comprising many chemical compounds (i.e., internally mixed), or are individual particles within a given population very different in terms of their composition (externally mixed) (Seinfeld and Pandis, 2006)? As described in the succeeding text, this 'mixing state' is extremely important to both the behavior of these aerosol particles in the atmosphere and their environmental effects.

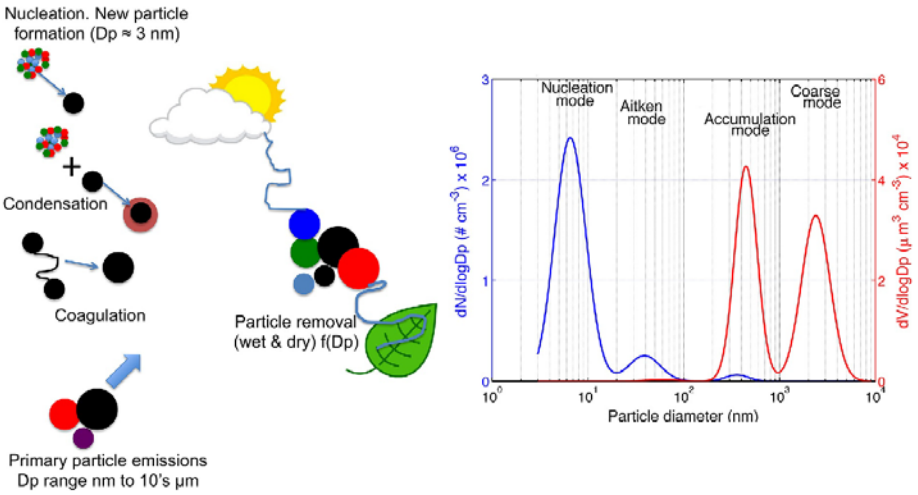

Figure 2 An overview of aerosol particle dynamics (left) and an example aerosol particle size distribution (right) expressed in terms of the number of particles in a given size interval per cm^3 of air (left-hand axis) and in terms of the volume of particles in a given size interval per cm^3 of air (right-hand axis).

Depending on their composition and size, aerosol particles alter the radiation balance of the Earth and thus its temperature, primarily by either scattering or absorbing the incoming radiation from the Sun (direct effect) and regulating cloud formation and properties by acting as cloud condensation nuclei (CCNs) (indirect effect). Generally, aerosol particles tend to be more efficient at scattering incoming sunlight (leading to an increase in the global albedo and cooling) than in absorbing radiation. An exception to this is black (or elemental) carbon aerosol particles that tend to have a larger absorption cross section than scattering cross section and hence generally act to absorb radiation and warm the atmosphere (Seinfeld and Pandis, 2006). The Intergovernmental Panel on Climate Change (IPCC) review indicates that radiative forcing due to the direct effect of aerosol particles (since 1750) is $-0.35\ W\ m^{-2}$ (with a possible range of -0.85 to $+0.15$), while the indirect effect is $-0.9\ W\ m^{-2}$ (-1.9 to -0.1) (IPCC, 2013).

Generally, observed aerosol particle size distributions conform to either a trimodal distribution with an Aitken mode characterized by particles with diameters <0.1 µm (100 nm), an accumulation mode characterized by particles with diameters >0.1 µm but <1 µm, and a coarse mode characterized by particles with diameters >1 µm or a bimodal distribution where the Aitken mode is absent. However, when nucleation occurs (i.e., new particles are produced from critical clusters of gas molecules), an additional nucleation mode can be present below the Aitken mode (Figure 2). The total number of aerosol particles in the atmosphere is typically (but not uniformly) dominated by the nucleation and Aitken mode, but the aerosol particle mass and volume tend to be dominated by the accumulation and coarse modes. The smallest particles, particularly those in the nucleation mode, are extremely mobile and numerous and grow rapidly by coagulation (collision and joining with other aerosol particles) and condensation (deposition of semivolatile gases on the surface of the aerosol particles). Some aerosol particles will ultimately reach a size (or will be emitted at a size) where they become climate-relevant. Aerosol particles become active in indirect climate forcing (by acting as CCN) at diameters (Dp) of about 100 nm. Aerosol particles with diameters approximately equal to the dominant wavelengths of incoming solar radiation (400–700 nm) are most relevant for direct climate forcing. Thus, accumulation mode particles are most important to the direct climate effect – although the precise composition and mixing state of the aerosol particles will determine the actual radiative properties of any given aerosol particle ensemble. Further, the 'mixing state' of the aerosol particles is extremely important to the ability of aerosol particles to act as CCN and thus to participate in the indirect climate forcing effect (Wang et al., 2010).

Air Quality

Some atmospheric species have a deleterious impact on human health, and exposure to elevated concentrations leads to increased mortality (premature death) and/or morbidity (excess illness). The term 'air quality' has been coined to reflect the presence (or absence) and abundance of chemical species known to have a negative impact on human health and/or welfare and/or have a deleterious impact on the environment. A range of regulatory approaches have been developed to reduce human exposure to unhealthy air quality. In the United States, the Clean Air Act requires the Environmental Protection Agency (EPA) to set National

Ambient Air Quality Standards (NAAQS) for six common (criteria) air pollutants for which there is evidence that exposure to elevated concentrations can cause human mortality and morbidity:

- Carbon monoxide (CO) is an odorless and colorless gas, emitted during combustion of all carbon-based materials. Exposure to elevated concentrations of CO negatively impacts human health by bonding with hemoglobin in the blood and thus reducing the oxygen supply to the body's organs and tissues. According to national emission inventory estimates for 2013 (note that the EPA produces annual estimates of emissions of the criteria pollutants; data quoted herein derive from a database available at http://www.epa.gov/ttn/chief/trends/trends06/national_tier1_caps.xlsx), ~54% of all CO emissions in the United States derive from the transportation sector, and the remainder derive principally from industrial processes, fossil fuel combustion in power plants, and wildfires. Measures designed to reduce CO emissions particularly from motor vehicles have decreased CO emissions in the United States by almost half over the last 20 years (see also review of emission reductions of the criteria pollutants and precursors for 1980–2005 given in Hidy et al. (2011)).
- Lead (Pb) in the air is typically present in aerosol particles. Although lead is a metal that is used in a wide array of industrial products and processes. When ingested lead is mistaken by the body for calcium and other essential nutrients, but it is actually toxic to many organs and tissues including the heart and nervous system. Emissions of lead from the transportation sector dramatically declined as a result of regulations that removed lead from fuel used by motor vehicles. Thus, airborne lead is now greatly reduced relative to past levels and high concentrations in the United States are usually associated with lead smelters.
- Nitrogen dioxide (NO_2) is one of a group of nitrogen-containing gases referred to as oxides of nitrogen (NO_x). These gases are emitted from high-temperature combustion of fossil fuels and are also released naturally into the atmosphere from soils and lightning events. Exposure to NO_2 concentrations exceeding those of EPA standards can cause respiratory failure. Elevated NO_2 concentrations are also responsible for enhanced production of ground-level ozone (O_3), decreases in visibility, eutrophication (or increase in algae formation) in freshwater bodies, increased aerosol particle formation, and acid rain effects. In the United States, ~60% of all anthropogenic emissions of NO_x come from the transportation sector. As in the case of CO, NO_x emissions in the United States have decreased by almost a factor of two over the last 20 years.
- Ozone (O_3) is a gas molecule that is beneficial in the upper layers of the atmosphere, where it is present in the 'ozone layer' that protects life on Earth from very short-wavelength ultraviolet radiation from the Sun. However, when it is produced at ground level, it can cause respiratory problems in humans (particularly those who suffer from asthma) and can also stifle the photosynthesis process in vegetation, causing decreases in agricultural yields. Unlike the other criteria pollutants, there are no direct emissions of O_3 to the atmosphere. Rather, O_3 is formed in the lower atmosphere (i.e., near ground level) by reactions between volatile organic compounds (VOCs) (hydrocarbons that will readily evaporate) and NO_x. Ozone production in any air parcel is a complex function of incident solar radiation (since many of the formation reactions are photolytic), the speciation of the VOCs (different VOCs vary greatly in terms of reactivity, with, e.g., CH_4 having rather low O_3 formation potential), and the precise VOC/NO_x ratios (Seinfeld and Pandis, 2006).
- Aerosol particles or particulate matter (PM) is a major contributor in the formation of haze and low-visibility conditions (via mechanisms similar to those involved in climate forcing) and when present in high concentrations can be detrimental to human health. Aerosol particles penetrate into the human body by inhalation, increasing human morbidity and mortality associated with respiratory and cardiovascular functions and affecting extrapulmonary organs and the lymphatic system. The EPA classifies atmospheric particles into two classes based on diameter (Dp): particulate matter 2.5 ($PM_{2.5}$) and particulate matter 10 (PM_{10}), where the number indicates the upper Dp of the particles measured in micrometers (microns, one-millionth of a meter). As shown by Figure 2 mass in these two size fractions tends to be dominated by the accumulation and coarse modes of the aerosol particle size distribution, respectively. Primary PM_{10} and $PM_{2.5}$ emissions in the United States are dominated by 'miscellaneous' – for example, area source emission sources such as windblown dust from agricultural activities. Emission estimates of PM in both size ranges are highly uncertain, and little or no trend is evident in the primary emission estimates.
- Sulfur dioxide (SO_2) is a toxic gas that is emitted to the atmosphere when fuels (such as coal) that contain sulfur are burnt. An excess of SO_2 in the atmosphere causes respiratory problems in humans and increases atmospheric aerosol particle formation and acidification of precipitation (more commonly known as 'acid rain') that can contribute to decreased agricultural yields and the corrosion of metals and structures. Nationally, SO_2 emissions derive mainly from fuel combustion at electrical utilities and other industrial facilities (82%). In 2013, estimates of SO_2 emissions decreased to one-quarter of the value in 1994.

Despite the enormous progress made in reducing the emissions of air pollutants the last 30 years, millions of people across the United States still live in counties that experience concentrations of one or more of the criteria pollutants (most commonly PM or O_3) above the EPA NAAQS. Further research is necessary to quantify and reduce the health burden associated with air quality degradation in high-population density megacities and to properly assess actual human exposure. Many cities have relatively few air quality measurement sites and therefore undersample the variability in concentrations of air pollutants, leading to uncertainty in human exposure and epidemiological consequences of reduced air quality.

In 2014, the World Health Organization (WHO) released documents indicating that in 2012, 7 million deaths worldwide were attributable to the joint effects of household and ambient air pollution (see documentation available at http://www.who.int/phe/health_topics/outdoorair/databases/en/). These health burdens are distributed unevenly across the globe with the majority of premature deaths occurring in the western Pacific and Southeast Asia. The relative importance of household versus ambient air pollutants also showed marked geographic variability with the WHO reporting that the overwhelming majority of the 4.3 million deaths attributed to household air pollution occurred in low- and middle-income countries. Thus, while much of the regulatory

activity and research to date has focused on outdoor air quality, degradation of indoor air quality plays a particularly important role in human health impacts. Indoor air quality is highly variable and is dependent on ambient outdoor air quality, air circulation in and out of the building (e.g., open vs. closed windows and quality of ventilation), lifestyle choices (e.g., smoking vs. nonsmoking), and domicile activities (e.g., heating and cooking practices). Almost 3 billion people (largely in low- and middle-income countries) use in-home combustion of solid fuels (wood, animal dung, charcoal, crop wastes, and coal) for cooking and heating, resulting in degraded indoor air quality and substantially elevated human mortality and morbidity (Lim et al., 2012).

Atmospheric Transport

Assuming a point source of a given air pollutant, concentrations near that release site will depend primarily on the rate of emission (how much is being introduced to the atmosphere per unit time) and the local meteorology. Key parameters are the wind speed, which determines the advection speed from the source, and the atmospheric stability (the change of temperature with height), which determines the characteristics of the 'plume' and dilution rates. For a pollutant released aloft from the surface in an unstable atmosphere, eddies in the atmosphere bring the pollutant down to the surface and mix in background air to dilute the plume, whereas in a stable atmosphere, the plume remains concentrated and aloft over comparatively long distances. At distances beyond a few tens to a hundred meters, mesoscale circulations – such as the presence of thermally or topographically driven flow – become increasingly important to determining the transport of the pollutants. Particularly in the midlatitudes, at scales beyond a few tens to a few hundreds of kilometers, transport is likely dictated by transient synoptic scale meteorological (i.e., weather) systems (Figure 1). Gases and aerosol particles with long residence times that thus are subject to transport within these systems may advect hundreds or thousands of kilometers away from the emission release point or their formation point in the atmosphere, resulting in 'long-range,' even transnational, transport (see Figure 3). During transport, primary pollutants are diluted, while secondary pollutants may be formed by chemical reactions. Thus, primary pollutants (e.g., CO) are typically most concentrated near the emission site, while secondary pollutants (e.g., ground-level O_3) exhibit the highest concentrations downwind (Seinfeld and Pandis, 2006).

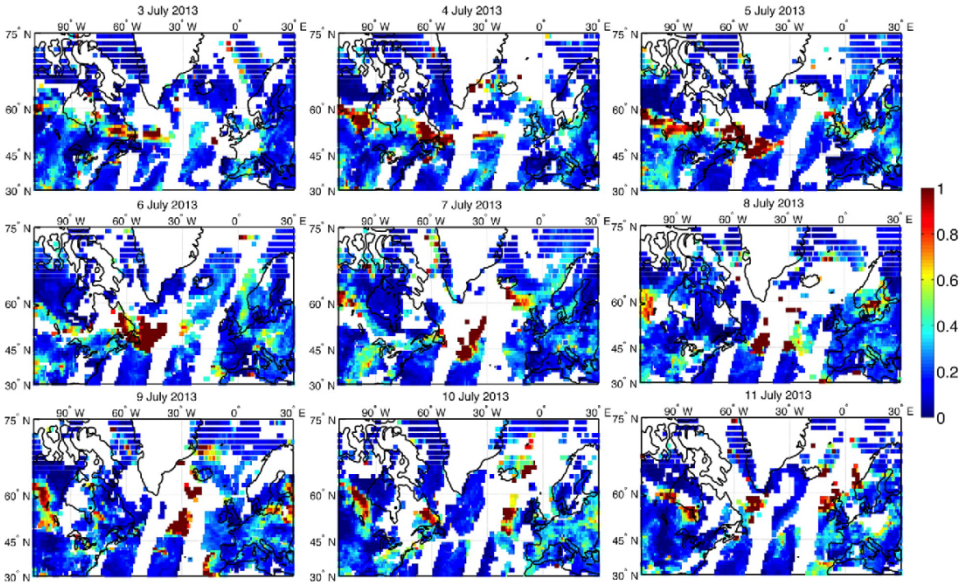

Figure 3 Once daily aerosol optical depth (AOD ∝ total columnar loading of aerosol particles) as reported in level 3 data from the MODIS instrument on the TERRA satellite during 9 days in July 2013. This sequence of images captures long-range transport of aerosol particle pollution from the eastern coast of North America across the Atlantic Ocean to Europe. A region with high AOD (values of approximately 1) is seen off the eastern coast of North America on 5 and 6 July 2013 and then moves eastward toward Europe across the North Atlantic over subsequent days and is evident over Great Britain on 11 July. White areas in each image denote regions of missing data.

New Frontiers

Atmospheric chemistry research has seen (and is seeing) a revolution spurred by rapid evolution of measurement technologies. Examples include use of condensation particle counters, ion spectrometers, and mass spectrometers to measure the concentrations and size distributions of ions, molecular clusters, and nanoparticles and to simultaneously obtain information about their chemical composition and interactions with trace gases and thus to yield new insights into the mechanisms leading to new particle formation (Kulmala et al., 2014). Other major innovations in in situ measurement technology include the use of aerosol mass spectrometers to provide quantitative size and chemical speciation in real time for nonrefractory (particles that volatize at or below 600 °C) aerosol particles. These systems measure inorganic components, such as nitrate, sulfate, and ammonium, and organics (including information about the functional groups and carbon to oxygen ratios), but cannot detect elemental carbon, sea salt, or dust (which are nonrefractory). Application of these systems allows higher temporal and size resolution than traditional (filter-based) methods and has greatly advanced understanding of gas–particle partitioning and aerosol particle speciation as a function of particle size. There have been similar innovations in measurements of gas-phase compounds – such that we now have unprecedented information about 'the air we breathe' and air pollutant emission rates (von der Weiden-Reinmüller et al., 2014). New techniques have been developed to provide high-frequency measurements of chemical concentrations to allow direct measurements of the flux (exchange of mass) between the atmosphere and underlying surface (Fowler et al., 2009). Measurement of the net ecosystem exchange of carbon dioxide is now virtually routine and has allowed more accurate quantification of the terrestrial carbon sink, and more exotic but highly important compounds such as ammonia (NH_3) are now being quantified using a range of approaches, including laser absorption spectroscopic techniques at rates (10 measurements per second) sufficient to allow application of eddy covariance approaches for direct measurement of the atmosphere–surface exchange.

Equally important are advances in remote sensing technologies that have enabled satellite-borne instrumentation to provide measurements over a large, nearly continuous spatial domain and thus to fill observational voids over parts of the globe not sampled by in situ measurement networks or aloft from the surface. The last decade has seen an explosion in terms of the number of gases for which columnar (or vertical resolved) concentrations can be measured via their interaction with radiation. Equally, a number of aerosol particle properties are now retrieved from both ground-based and satellite-borne instrumentation. Measurements from Earth-observing satellites have allowed investigation of a wide range of properties and phenomena (see examples in Table 1). The measurements have permitted unprecedented insights into the frequency and magnitude of transnational, and indeed transcontinental, advection of air pollution (Figure 3).

Advances in physical and chemical insights and computing resources have led to advances in atmospheric chemistry models designed to quantify the role played by gaseous and aerosol particle species in driving climate change (Lamarque et al., 2013) and air quality. Understanding the complex interactions between changing atmospheric composition and the biosphere (e.g., the mechanisms regulating fluxes between the atmosphere and the Earth's surface or the role of biogenic volatile emissions in aerosol processes) is crucial to more accurately quantifying potential climate feedbacks (Fowler et al., 2009). Earth system models (ESMs), run at the global scale and at increasingly higher spatial resolution (Lamarque et al., 2013), are unique tools employed to quantify not only reciprocal interactions with the surface (and biophysical feedbacks), but also the role of human activities in modifying the atmosphere, and critically to investigate and quantify uncertainties in these processes. ESMs have improved not only in spatial

Table 1 Examples of NASA satellite platforms, instrumentation, and measured properties from major current Earth-observing missions

Platform	*Instrumentation*	*Example measured properties*
Aura (NASA, 2014a)	Ozone monitoring instrument (OMI)	• Vertical concentration profiles of ozone (O_3) • Column average concentrations of nitrogen dioxide (NO_2), sulfur dioxide (SO_2), bromine oxide (BrO), formaldehyde (HCHO), chlorine dioxide (OClO), and aerosol particle characteristics
	Tropospheric emission spectrometer (TES)	• Vertical concentration profiles and column average concentrations of O_3, water vapor (H_2O), semi-heavy water (HDO), carbon monoxide (CO), and methane (CH_4) • Vertical profiles of NO_2 and nitric acid (HNO_3) • Column average concentrations of nitrous oxide (N_2O), ammonia (NH_3), carbon dioxide (CO_2), methanoic acid (CHOOH), and methanol (CH_3OH)
	High-resolution dynamics limb sounder (HIRDLS)	• Upper troposphere through stratosphere profiles of O_3, H_2O, CH_4, N_2O, NO_2, HNO_3, dinitrogen pentoxide (N_2O_5), trichlorofluoromethane (CFC11), dichlorodifluoromethane (CFC12), chlorine nitrate ($ClONO_2$), and aerosol particle properties
	Microwave limb sounder (MLS)	• Vertical profiles of chlorine monoxide (ClO), hydrogen chloride (HCl), hydroxyl radical (OH), hydroperoxy radical (HO_2), and BrO
Terra (NASA, 2014b)	Multiangle imaging spectroradiometer (MISR)	• Multiple viewing angles of column average atmospheric aerosol particle properties to distinguish natural and anthropogenic sources
	Measurement of pollution in the troposphere (MOPITT)	• Vertical profiles of CO
Terra and aqua (NASA, 2014c)	Moderate resolution imaging spectroradiometer (MODIS)	• Column average aerosol particle properties • Fire occurrence

resolution but also in the description of atmospheric chemical processes. In addition to atmospheric physics and dynamics, most ESMs specify anthropogenic and natural emissions, tropospheric and stratospheric gas chemistry, photolysis, and aerosol particle processes. Due to the complexity of reactions that occur in the atmosphere and the gas and aerosol particle compounds involved, simplified chemical schemes are implemented within ESMs. They usually include a reduced number of hydrocarbons and simplified radical chemistry that both play a major role in controlling aerosol particle formation and thus may strongly affect model output. Different approaches have been employed for aerosol particle treatment. Bulk schemes describe particle aerosols just in terms of their mass, whereas more complex approaches employ a number of assumptions regarding (and treatments of) the size distribution (e.g., modal vs. sectional) and chemical composition (Lamarque et al., 2013). The implementation of sophisticated aerosol particle mechanisms and their interaction with radiation within global ESMs poses great challenges in terms of computing power and time. Current research is directed to finding a balance between the required degree of complexity of atmospheric chemistry processes to provide reliable estimates of climate and air pollution impacts and demands on state-of-the-art computational facilities.

Acknowledgment

The authors acknowledge funding from NSF (1102309, 1517365), and a NASA ESSF (14-EARTH14F-0207).

References

Fowler D, Pilegaard K, Sutton MA, Ambus P, Raivonen M, Duyzer J, Simpson D, Fagerli H, Fuzzi S, Schjoerring JK, Granier C, Neftel A, Isaksen ISA, Laj P, Maione M, Monks PS, Burkhardt J, Daemmgen U, Neirynck J, Personne E, Wichink-Kruit R, Butterbach-Bahl K, Flechard C, Tuovinen JP, Coyle M, Gerosa G, Loubet B, Altimir N, Gruenhage L, Ammann C, Cieslik S, Paoletti E, Mikkelsen TN, Ro-Poulsen H, Cellier P, Cape JN, Horváth L, Loreto F, Niinemets Ü, Palmer PI, Rinne J, Misztal P, Nemitz E, Nilsson D, Pryor S, Gallagher MW, Vesala T, Skiba U, Brüggemann N, Zechmeister-Boltenstern S, Williams J, O'Dowd C, Facchini MC, de Leeuw G, Flossman A, Chaumerliac N, and Erisman JW (2009) Atmospheric composition change: ecosystems-atmosphere interactions. *Atmospheric Environment* 43: 5193–5267.

Hidy GM, Brook JR, and Demerjian KL (2011) Past examples of multipollutant air quality management and accountability. In: Hidy GM (ed.) *Technical challenges of multipollutant air quality management*. Dordrecht: Springer, http://dx.doi.org/10.1007/978-94-007-0304-9_12.

IPCC (2013) In: Stocker TF, Qin D, Plattner G-K, Tignor M, Allen SK, Boschung J, Nauels A, Xia Y, Bex V, and Midgley PM (eds.) *Climate change 2013: The physical science basis. Contribution of working group I to the fifth assessment report of the Intergovernmental Panel on Climate Change*. Cambridge/New York: Cambridge University Press, 1535 pp.

Kulmala M, Petäjä T, Ehn M, Thornton J, Sipilä M, Worsnop DR, and Kerminen V-M (2014) Chemistry of atmospheric nucleation: on the recent advances on precursor characterization and atmospheric cluster composition in connection with atmospheric new particle formation. *Annual Review of Physical Chemistry* 65: 21–37.

Lamarque JF, Shindell DT, Josse B, Young PJ, Cionni I, Eyring V, Bergmann D, Cameron-Smith P, Collins WJ, Doherty R, Dalsoren S, Faluvegi G, Folberth G, Ghan SJ, Horowitz LW, Lee YH, MacKenzie IA, Nagashima T, Naik V, Plummer D, Righi M, Rumbold ST, Schulz M, Skeie RB, Stevenson DS, Strode S, Sudo K, Szopa S, Voulgarakis A, and Zeng G (2013) The atmospheric chemistry and climate model intercomparison project (ACCMIP): overview and description of models, simulations and climate diagnostics. *Geoscientific Model Development* 6: 179–206.

Lim SS, Vos T, Flaxman AD, Danaei G, Shibuya K, and Adair-Rohani H (2012) A comparative risk assessment of burden of disease and injury attributable to 67 risk factors and risk factor clusters in 21 regions, 1990–2010: a systematic analysis for the global burden of disease study 2010. *Lancet* 380: 2224–2260.

National Aeronautics and Space Administration (2014a). *Reference handbook: Aura*. Available at http://eospso.gsfc.nasa.gov/sites/default/files/mission_handbooks/Aura.pdf.

National Aeronautics and Space Administration (2014b). *Reference handbook: Aqua*. Available at http://eospso.gsfc.nasa.gov/sites/default/files/mission_handbooks/Aqua.pdf.

National Aeronautics and Space Administration (2014c). *Reference handbook: Terra*. Available at http://eospso.gsfc.nasa.gov/sites/default/files/mission_handbooks/Terra.pdf.

Seinfeld JH and Pandis SN (2006) *Atmospheric chemistry and physics: from air pollution to climate change*, 2nd edn. New York: Wiley. ISBN :978-0-471-72018-8.

von der Weiden-Reinmüller SL, Drewnick F, Crippa M, Prévôt ASH, Meleux F, Baltensperger U, Beekmann M, and Borrmann S (2014) Application of mobile aerosol and trace gas measurements for the investigation of megacity air pollution emissions: the Paris metropolitan area. *Atmospheric Measurement Technique* 7: 279–299.

Wang J, Cubison MJ, Aiken AC, Jimenez JL, and Collins DR (2010) The importance of aerosol mixing state and size-resolved composition on CCN concentration and the variation of the importance with atmospheric aging of aerosols. *Atmospheric Chemistry and Physics* 10: 7267–7283.

APPENDIX G

CURRICULUM VITAE

Ryan Christopher Sullivan
Department of Earth and Atmospheric Sciences
Cornell University, Ithaca, NY 14853
rcs365@cornell.edu

Education:

2017	Ph.D. Atmospheric Sciences, Cornell University (CU), Ithaca, NY
	Minors in Fluid Dynamics and Environmental Engineering
2016	M.S. Atmospheric Sciences, Cornell University, Ithaca, NY
2014	M.S. Geological Sciences – Atmospheric Science, Indiana University (IU), Bloomington, IN
2012	B.S. Meteorology, *Summa Cum Lade*, Northern Illinois University (NIU), Dekalb, IL.
	Minor in Geography, Geographic Information Systems Certification
2010	A.S. William Rainey Harper College, Palatine, IL

Professional experience:

2014-2017	**NASA Earth and Space Science Fellow**, Project title: "Diagnosing Spatiotemporal Coherence and Variability of Aerosol Particle Concentrations Using a Satellite Proxy", Cornell University
Summer 2016	**Alternate Sponsored Fellow**, Atmospheric Sciences & Global Change Division, Pacific Northwest National Laboratory
2013-2014	**Research Assistant**, Indiana University
Summer 2013	**Quality Assurance Intern**, Indiana Department of Environmental Management, Office of Air Quality, Air Monitoring Branch
2012-2013	**Associate Instructor**, Indiana University
Summer 2012	**Student Research Aid**, Atmospheric Radiation Measurement (ARM) Climate Research Facility, Argonne National Laboratory
2011-2012	**Undergraduate Research Apprentice**, Northern Illinois University
Summer 2011	**Environmental Meteorologist Intern**, Environmental Applications Division, Murray & Trettel Inc.

Publications submitted:

Sullivan, R. C., Crippa, P., Matsui, H., Leung, L. Y. R., Zhao, C., Thota, A., and Pryor, S. C. New particle formation leads to cloud dimming. *Submitted*

Sullivan, R. C., Levy, R. C., da Silva, A. M., and Pryor, S. C. Developing and diagnosing climate change indicators of regional aerosol optical properties. *Submitted*.

Peer-reviewed publications:

Pryor, S. C., **Sullivan, R. C.**, and Schoof, J. T. (2017). Modeling the contributions of global air temperature, synoptic-scale phenomena and soil moisture to near-surface static energy variability

over the eastern USA. *Atmospheric Chemistry and Physics Discussions*, doi:10.5194/acp-2017-367.

Crippa, P., **Sullivan, R. C.**, Thota, A., and Pryor, S. C. (2017). The impact of resolution on meteorological, chemical and aerosol properties in regional simulations with WRF-Chem. *Atmospheric Chemistry and Physics, 17*, 1511–1528.

Sullivan, R. C., Crippa, P., Hallar A. G., Clarisse, L., Whitburn, S., Van Damme, M., Leaitch, W. R., Walker, J., Khlystov, A., and Pryor S. C. (2016). Using satellite-based measurements to explore spatiotemporal scales and variability of drivers of new particle formation. *Journal of Geophysical Research: Atmospheres, 121*, 12,217–12,235.

Pryor, S. C., Joerger, V. M., and **Sullivan, R. C.** (2016). Empirical estimates of size-resolved precipitation scavenging coefficients for ultrafine particles. *Atmospheric Environment, 143*, 133-138.

Sullivan, R. C. and Pryor, S. C. (2016). Dynamic and chemical controls on new particle formation occurrence and characteristics from in situ and satellite-based measurements. *Atmospheric Environment, 127*, 316-325.

Pryor, S. C., **Sullivan, R. C.**, and Wright, T. (2016). Quantifying the roles of changing albedo, emissivity, and energy partitioning in the impact of irrigation on atmospheric heat content. *Journal of Applied Meteorology and Climatology, 55*, 1699–1706.

Crippa, P., **Sullivan, R. C.**, Thota, A., and Pryor, S. C. (2016). Evaluating the skill of high-resolution WRF-Chem simulations in describing drivers of aerosol direct climate forcing at the regional scale. *Atmospheric Chemistry and Physics, 16*, 397–416.

Sullivan, R. C., Levy, R. C., and Pryor, S. C. (2015). Spatiotemporal coherence of mean and extreme aerosol particle events over eastern North America as observed from satellite. *Atmospheric Environment, 112*, 126-135.

Sullivan, R. C. and Pryor, S. C. (2014). Quantifying spatiotemporal variability of fine particles in an urban environment using combined fixed and mobile measurements. *Atmospheric Environment, 89*, 664-671.

Book chapters:

Pryor S. C., Crippa P., and **Sullivan, R. C.** (2015). Atmospheric chemistry. *In: Elsevier's Reference Module in Earth Systems and Environmental Sciences* (Available at http://www.sciencedirect.com/science/article/pii/B9780124095489091776). Edited by J.T. Schoof. doi:10.1016/B978-0-12-409548-9.09177-6.

Presentations:

Sullivan, R. C., Levy, R. C., da Silva, A. M., and Pryor, S. C. (2017): Developing and diagnosing climate change indictors of regional aerosol optical properties. PICO (Presenting Interactive Content) presentation at the *European Geosciences Union General Assembly 2017*. Vienna, Austria, April 26.

Pryor, S. C., Crippa, P., and **Sullivan, R. C.** (2016): Assessing value-added by high-resolution regional simulations of climate-relevant aerosol particle properties. Poster presented at the *International Conference on Regional Climate (ICRC) – COordinated Regional climate Downscaling Experiment (CORDEX) 2016*. Stockholm, Sweden, May 17 – 20.

Crippa, P., **Sullivan, R. C.**, Thota, A., Li, Z., and Pryor, S. C. (2015): Evaluating the spatiotemporal variability of WRF-Chem aerosol particle properties and extreme concentrations over eastern North America. Oral presentation at the *2015 European Aerosol Conference*, Milan, Italy, Sept. 9.

Pryor, S. C., Crippa P., and **Sullivan, R. C.** (2015): How skillfully can we simulate drivers of aerosol direct climate forcing? Oral presentation at the *Twelfth Informal Conference on Atmospheric and Molecular Science*, Aarhus University, Denmark, June 8.

Sullivan, R. C., Crippa, P., Thota, A., Levy, R. C., and Pryor, S. C. (2015): Quantifying the scales of coherence and causes of spatiotemporal variability of aerosol particle properties and extreme concentrations over eastern North America. Oral presentation at the *2015 Joint Assembly (AGU, CGU, GAC, and MAC)*, Montreal, Quebec, Canada, May 5.

Pryor, S.C., Barthelmie, R. J., and **Sullivan, R. C.** (2015): Mechanisms responsible for the size-dependence of, and bi-directionality of, ultrafine particle fluxes over forest. Oral presentation at the *2015 Joint Assembly (AGU, CGU, GAC, and MAC)*, Montreal, Quebec, Canada, May 4.

Sullivan, R. C., Levy, R. C., and Pryor, S. C. (2014): Spatial coherence of atmospheric particle properties over eastern North America as observed from satellites. Poster presentation at the *2014 Young Scientist Forum*, NASA Goddard Space Flight Center, Greenbelt, MD, June 26.

Sullivan, R. C., Pryor, S. C., Barthelmie, R. J., and Filippelli, G. M. (2014): Intra-urban variability of fine particle concentrations: A case study from Indianapolis. Oral presentation at the *Urban Health Conference*, Indiana University – Purdue University Indianapolis, April 1.

Sullivan, R. C. and Pryor, S. C., (2014): Spatial coherence of aerosol particle properties observed from satellites. Oral presentation at the *Crossroads Geology Conference*. Indiana University, Bloomington, March 28.

Sullivan, R. C., Pryor, S. C., Barthelmie, R. J., Filippelli, G. M., and Crippa, P. (2013): Understanding spatiotemporal variability of fine particulate matter in an urban environment using combined fixed and mobile measurements. Oral presentation at the *American Geophysical Union's 2013 Fall Meeting*. San Francisco, CA, Dec. 12.

Sullivan, R. C., Pryor, S. C., Filippelli, G. M., and Morrison, D. (2013): Understanding spatiotemporal variability of fine particulate matter concentrations in Indianapolis, Indiana. Oral presentation at the *Crossroads Geology Conference*. Indiana University, Bloomington, April 5.

Awards and grants:

2017 Atmospheric Chemistry Colloquium for Emerging Senior Scientists (ACCESS)

2014-7 NASA Earth and Space Science Fellowship: $90,000

2014-5 CU Department of Earth and Atmospheric Sciences Excellence in Research Award: $1000

2015 CU Graduate Conference Travel Grant to 2015 Joint Assembly Meeting: $235

2013-4 IU Office of Sustainability's Graduate Student Research Development Grant: $3000

2013 IU Department of Geological Science Travel Grant to AGU Fall 2013 Conference: $400

2013 IU Department of Geological Science Summer Research Grant-in-Aid: $500

2012 Nancy C. Wick Award for Outstanding Senior in Meteorology (NIU): $500

2010-2 Dean's List: Fall 2010, Spring 2011, Fall 2011, and Spring 2012 (NIU)

2010-1 National SMART Award (National Science & Mathematics Access to Retain Talent; NIU): $4000

2007 Distinguished Scholar Award (Harper College)

Professional affiliation and service:

- Member, American Geophysical Union, European Geosciences Union
- Peer Reviewer, *Atmospheric Environment*
- Volunteer, Tompkins County Society for the Prevention of Cruelty to Animals